UNIVERSITY OF SOUTHAMPTON

FACULTY OF ENGINEERING, SCIENCE AND MATHEMATICS

School of Ocean and Earth Science

Changes in shelf waters due to air-sea fluxes and their influence on the Arctic Ocean circulation as simulated in the OCCAM global ocean model

by

Richard Chaim Levine

Thesis for the Degree of Doctor of Philosophy

June 2005

CORRECTION SHEET

UNIVERSITY OF SOUTHAMPTON

ABSTRACT

FACULTY OF ENGINEERING, SCIENCE AND MATHEMATICS
SCHOOL OF OCEAN AND EARTH SCIENCE
Doctor of Philosophy

CHANGES IN SHELF WATERS DUE TO AIR-SEA FLUXES AND THEIR INFLUENCE ON THE ARCTIC OCEAN CIRCULATION AS SIMULATED IN THE OCCAM GLOBAL OCEAN MODEL

by Richard Chaim Levine

In this study we look at the ocean circulation of the Arctic Ocean in the high-resolution OCCAM global ocean model. The Arctic Ocean consists of deep basins surrounded by a large area of continental shelves, where cooling and ice formation play an important role in dense water formation. In the model these dense waters are transported by a circumpolar boundary current into the deep convection sites of the North Atlantic Ocean. The boundary current is thought to be a continuous feature in the real ocean, however the driving force is still unknown. We provide evidence that buoyancy fluxes that occur due to air-sea exchanges on the continental shelves are an important driving force for the boundary current in the model.

The formation area of the circumpolar boundary current is found in the Barents Sea, where there is a high pressure area associated with cooling of inflowing Atlantic Water (AW). The modified water, Barents Sea Water (BSW), is then able to pass through the Arctic Front as it sinks into the Arctic Basin via the St Anna Trough in a boundary current. The high density signal of these waters can be seen all around the continental slope of the Arctic Ocean as a continuous pressure gradient. The boundary pressure gradient continues into the North Atlantic, where a low pressure region is found off Cape Hatteras.

A time-dependent variant of an accurate particle tracking technique has been applied to calculate pathways of the dense waters using stored velocity fields of the OCCAM model. This technique has been extended with a representation of random motions due to diffusive effects. An expression for the random motions is derived using the theory of Brownian motion, and is chosen to match the Laplacian eddy viscosity terms in the momentum equations of the OCCAM model. The trajectories of the dense waters on the Barents Sea shelf follow the boundary current, and are guided around the slope by topographical contours. However the pathways are severely affected by large-scale wind-driven features as the Trans-Arctic drift and the Beaufort Gyre, which carry water masses out of the boundary current or trap them in the Canadian Basin. It is found that it takes approximately 30 years for the bulk of BSW to reach the North Atlantic, although the major signals complete the Arctic circumference within 10 years. The transport of the BSW through the Arctic into the North Atlantic can be accurately described by a 1D advection-diffusion model with a "diffusion" coefficient of $1.3 \cdot 10^9 cm^2/s$ and an "advection" coefficient of $2.9 cm/s$. This confirms that the diffusion of particles is caused by basin-scale features rather than meso-scale eddies. More dense water is formed on the Chukchi Sea shelf, which originates from the Bering Strait Outflow. There are signs that these dense waters provide forcing for eddies seen off North Alaska.

A new theory is presented for calculating the Available Potential Energy (APE) on the continental shelves for driving local currents in the Arctic Ocean, using the mean offshore density structure as a reference state. The air-sea fluxes in the Barents Sea are found to create a large amount of APE on the shelves, which is lost as the dense waters sink into the Arctic Basin. Although it is found the inflowing AW already has a large amount of APE which cannot fully be converted due to the Arctic Front in Fram Strait, therefore it appears the cooling in the Barents Sea is crucial to the forcing of the boundary current. This cooling in the prescribed model air-sea fluxes is likely to be caused by enormous heat losses to the atmosphere in large ice-free regions, which are created by the inflow of warm AW.

Contents

List of Figures

List of Tables

Acknowledgements

Special thanks to my supervisor Dr David J. Webb for his continuous help and motivation. Thanks to my co-supervisor Professor Harry L. Bryden for his help, and thanks to my other advisory panel members Professor Peter D. Killworth and Professor John W. Murray for their effort and suggestions. Thanks to Dr Yevgeny Aksenov, Dr Andrew C. Coward, and Mrs Beverly A. de Cuevas for their help with data and computing,

...and thanks for support from Joe, Nicholas, Bill, Dave, Rob, Hannah, and my parents.

This work was funded by the Natural Environment Research Council as part of the COAPEC (Coupled Ocean-Atmosphere Processes and European Climate) project. Reference number: NER/S/S/2001/06732.

List of abbreviations

ACW	Alaskan Coastal Water
AO	Arctic Oscillation
APE	Available Potential Energy
AW	Atlantic Water
BSO	Bering Strait Outflow
BSW	Barents Sea Water
ECMWF	European Centre for Medium range Weather Forecasting
KE	Kinetic Energy
NAC	North Atlantic Current
NCC	Norwegian Coastal Current
OCCAM	Ocean Circulation and Climate Advanced Model
PE	Potential Energy
PW	Pacific Water
RHS	Right-Hand Side

Chapter 1

Introduction

The Arctic Ocean circulation plays an important role in global climate and must be understood in order to understand global climate change. There are only sparse observations of the Arctic Ocean and therefore many processes are not understood. The Arctic Ocean consists of deep basins surrounded by a large area of continental shelves, which are important areas for dense water formation. Dense water is formed on the shelves due to cooling and ice formation, which leads to brine being rejected into the water column underneath. These processes are thought to be crucial in maintaining the current structure of the Arctic Ocean.

Permanent ice cover is currently made possible by a sharp halocline which underlies a shallow mixed layer. The dense waters are thought to help maintain the halocline, and provide waters for the intermediate and deep layers of the Arctic Ocean interior (Aagaard et al 1981). These waters also supply a large part of the overflows into the North Atlantic (Anderson et al 1999) and it has been suggested by Mauritzen (1996a,b) that these waters are dense enough to supply the deep equatorward return flow of the thermohaline circulation.

The dense waters are transported from the Arctic into the North Atlantic in a circumpolar boundary current, which is thought to be a continuous feature around the continental slope (Aagaard 1989). The boundary current could be an important flow feature for global climate. It provides waters that precondition the deep convection sites in the Nordic Seas, and it acts as a heat pump for Europe by drawing warm Atlantic Water northwards to high latitudes.

The boundary current has been observed at various locations along topography, and varies from a surface current on the Eurasian side of the Arctic, to a subsurface current further eastwards. Historically it has been thought that the boundary current starts as Atlantic Water (AW) enters the Arctic Ocean through Fram Strait. However recently it has been shown that another branch of AW that flows through Barents Sea and enters the Arctic Ocean further along the slope could be more important (Rudels et al 1994, Schauer et al 1997). It is still unknown how the boundary current is forced (Aagaard and Carmack 1994, Woodgate et al 2001), although Holloway (1987) has suggested a form of eddy-topography interaction, the Neptune effect, which produces along shore currents due to meso-scale eddies at the shelf break. The Neptune effect can only occur in ocean models if they resolve meso-scale eddies, or if a specific parameterization is used. Such model experiments have been performed by Nazarenko et al (1998) and Zhang and Zhang (2001), which have shown that the Neptune effect helps the cyclonic boundary circulation. Although it is found that the dense water formation on the Barents Sea shelf is also important. This will be discussed further in chapter 2.

Another meso-scale feature that affects water transport in the Arctic is the presence of small energetic eddies, which have been observed mostly in the Canadian Basin. These eddies are thought to last for several years, and to be formed near the slope of the basin (D'Asaro 1988), possibly by thermohaline forcing.

We aim to evaluate the effects of buoyancy forcing of the circumpolar boundary current and the meso-scale eddies due to air-sea fluxes on the continental shelves. We do this by looking at a recent run of the high-resolution, $1/8^\circ \times 1/8^\circ$ in the horizontal, OCCAM (Ocean Circulation and Climate Advanced Modelling) global ocean model (Aksenov and Coward 2001). This is the first such model to produce a seemingly continuous circumpolar boundary current around the continental slope, as very high-resolution is needed to resolve the Rossby radius of $5 - 10km$ in the Arctic Ocean. This version of the model does not include a parameterization for the Neptune effect.

Recently it has been found that the Arctic Ocean is subject to substantial inter-annual variability due to the Arctic Oscillation (Proshutinsky and Johnson 1997), which affects the structure of the wind-driven Beaufort Gyre and the position of the Trans-Arctic drift. It has been shown in model studies by Maslowski et al (2000) that this variability affects the distance with which Atlantic Water (AW) is able to flow into the Arctic. As the simulation of the OCCAM model was only run for two years it will show no evidence of this variability. Nevertheless it provides a good hypothesis of the circulation, which we can use to identify mechanisms of the Arctic Ocean circulation. Specifically here we look at the role played by dense water formation, due to air-sea fluxes, in driving energetic circulation features.

In order to investigate the effects of air-sea fluxes on shelf waters we first look at the pressure fields around the boundary in the OCCAM model simulation for evidence of intrusion of high density water along the continental slope. We then continue to look at pathways and time-scales of the dense shelf waters through the Arctic Ocean by applying a time-dependent variant, which includes diffusive effects, of an existing particle tracking technique to stored velocity fields of the OCCAM model. Finally we calculate the amount of Available Potential Energy (APE) on the continental shelves for driving local currents with a new definition, using a reference state in the Arctic Ocean interior. This allows us to estimate the gain in

APE due to the air-sea fluxes prescribed in the model.

Chapter 2

Arctic Ocean circulation and climate

2.1 Introduction

Currently there is a large interest in research of global climate change. The Arctic Ocean plays an important role in the global climate system, and needs to be understood in order for reliable predictions of rapid climate change.

The Arctic Ocean is thought to have two main effects on global climate through the surface heat balance and the thermohaline circulation (Aagaard and Carmack, 1994). The thermohaline circulation, or global conveyor belt, transports heat polewards in the surface layers of the North Atlantic which warms northern Europe. The deep southwards return flow of cold water is driven by deep convection in the Nordic and Labrador seas (Marshall and Schott, 1999). The waters in this region are conditioned by the outflow of water from the Arctic Ocean which exits through Fram Strait into the North Atlantic Ocean.

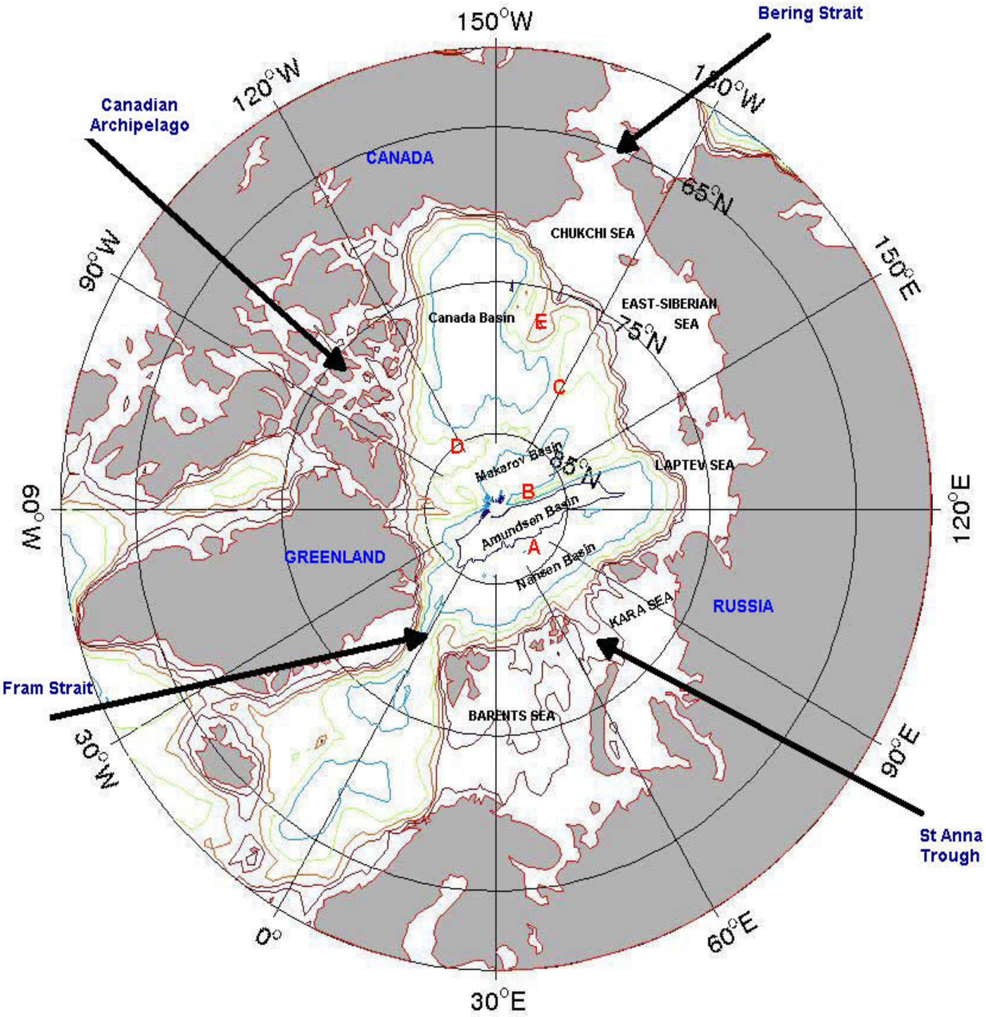

Figure 2.1: *The Arctic Ocean Basins, Shelf Seas, Ridges, and topography with contours at 250,500,1000,2000,3000,4000 metres. Ridges are marked as A: Nansen-Gakkel Ridge, B: Lomonosov Ridge. C: Mendeleyev Ridge. D: Alpha Ridge. E: Chukchi Plateau.*

The Arctic Ocean consists of a number of deep basins separated by ridges, and surrounded by a large area of continental shelves (see figure 2.1). The Nansen and Fram Basins, separated by the Nansen-Gakkel ridge, are sometimes referred to as the Eurasian Basin. The Fram and Makarov Basins are separated by the Lomonosov ridge, and the Makarov and Canada Basins are separated by the Mendeleyev and Alpha ridges.

The current understanding of the Arctic Ocean circulation has been derived from a sparse number of hydrographic measurements and ice motion observations. The main circulation features are described in Aagaard's (1989) synthesis, and consist of a large-scale boundary current, a wind-driven gyre in the Canadian Basin, and a strong eddy field on the western side of the Canadian Basin. These are all important energetic features of the otherwise weak flow field in the Arctic Ocean interior.

The most energetic flow feature is thought to be a continuous boundary current along the entire continental slope of the Arctic Ocean (Aagaard and Carmack 1994, Rudels et al 1994, 1999, 2000). It is directly important for European climate by drawing warm Atlantic Water northwards. The current is thought to transport Atlantic Water all around the Arctic Ocean before returning to the North Atlantic, mainly through Fram Strait. Mauritzen (1996a,b) has proposed that here it forms most of the dense overflow water over the Denmark Strait, together with AW that recirculates within Fram Strait. Therefore it is important to understand the water mass transformations that occur in the boundary current.

The most likely areas for water mass transformations of AW are on the continental shelves, which comprise a large area of the Arctic Ocean. This is likely to occur both through AW crossing the Barents Sea shelf before entering the Arctic deep basins (Loeng et al 1993, Rudels et al 1994), and through dense plumes sinking from the shelves into the boundary current (Schauer et al 1997). Anderson et al (1999) have estimated that 1/3 of the deep and intermediate waters flowing into the North Atlantic over the Greenland-Iceland-Scotland ridge originates on the Arctic continental shelves.

The continental shelves provide most of the ventilation for the Arctic Ocean, as the ocean interior is almost permanently covered in ice, although significant heat loss and freshwater fluxes are also possible in the central Arctic. There even small parts of open (or thinly covered) ocean can cause dense water formation (Aagaard and Carmack 1989). The permanent ice cover is due to the current thermohaline structure of the Arctic water column. There is a shallow mixed layer that consists of relatively cold and fresh water, with a strong halocline lying underneath at approximately 50-200m. This halocline insulates the warm Atlantic layer underneath at approximately 200-900m (Coachman and Aagaard 1974). The halocline also ensures that the surface water can be cooled to freezing point without the water column becoming unstable, enabling permanent ice cover in the Arctic.

The halocline is thought to be maintained by dense water flowing off the continental shelves. Traditionally (eg. Aagaard et al 1981) it is thought that dense (cold and salty) water is formed on the shelves due to ice formation, which is then advected into the deep basins. This water is then thought to mix in between a cold, fresh mixed surface layer (originating from river water inflow and the Pacific Water inflow) and the salty Atlantic layer, creating a cold halocline layer. Recently Rudels et al (1996) have proposed another mechanism, whereby dense (cold and fresh) water from the shelves is advected into the deep basins, that have a relatively deep winter mixed layer (cold and salty). Then subsequent convection within the mixed layer is proposed to lead to the formation of a cold halocline. Although the halocline has been thought to be a permanent feature, recently Steele and Boyd (1998) have shown that the halocline in the Eurasian Basin has retreated during the 1990s from the Amundsen Basin back into the Makarov Basin, possibly due to a change in atmospheric forcing.

If the halocline were to disappear there would be stronger atmospheric cooling necessary to maintain the permanent ice cover, and it would then be likely that the ice melt in summer would increase leading to an increase in freshwater export into the North Atlantic. It has been proposed that this could severely reduce the depth of the convection in the Nordic Seas (Aagaard and Carmack 1989). In that case even severe cooling would not create water dense enough to sink through the halocline as the density at cold temperatures is mainly controlled by salinity. Mauritzen (1996a,b) however has proposed that Arctic intermediate and deep waters are already dense enough to provide water for the deep return flow.

In the following sections we look at the most important aspects for this study: the inflows and outflows, the processes on the shelves creating dense water, and the flow features in the Arctic Ocean interior.

2.2 Interocean exchange

The Arctic Ocean exchanges waters with the Atlantic and the Pacific Oceans, as well as receiving a large input of freshwater from the Siberian and Canadian rivers.

The Atlantic Ocean provides relatively warm and salty water to the Arctic Ocean. The exchanges between the Atlantic and Arctic Oceans are thought to be driven by a combination of wind and thermohaline forcing (Proshutinsky and Johnson 1997). The Atlantic Water moves northwards across the eastern part of the Greenland-Scotland ridge into the Norwegian Sea in the North Atlantic Current (NAC), the extension of the Gulf Stream. As it flows northwards it is cooled and freshened due to net precipitation and cooling in the Nordic Seas. Along the coast of Norway the Norwegian Coastal Current (NCC) flows between the coast and the NAC, transporting relatively cold and fresh water northwards. The cold and fresh signal originates from the Baltic Sea, and is enhanced by mixing with waters from the fjords and rivers along the Norwegian coast. The AW continues northwards in the NAC and NCC, after which it is split into two separate pathways supplying the Arctic Ocean with relatively dense water.

One pathway continues along the continental slope towards Fram Strait in the West Spitsbergen Current. Another pathway flows eastwards into the Barents Sea (Rudels et al 1994, Schauer et al 1997). The Fram Strait is 500km wide and has a sill depth of 2500m. It is much wider than the Rossby radius in the Arctic Ocean (5-10km), and can therefore contain a complicated flow structure. Several branches of the Fram Strait pathway are deflected westwards before, and in, Fram Strait, and recirculate via the East Greenland Current (Manley 1995). Only a small part of the AW on this pathway makes it into the Arctic Ocean, and has been observed flowing eastwards along the continental slope (Schauer et al 1997). The transport through the approximately 500 km wide Fram Strait is difficult to estimate, because of the complicated flow field within the strait. Estimates for the transport vary widely. Model results indicate a transport between 3 and 11.2 Sv (Aksenov and Coward, 2001), although observations have shown that only approximately 1 Sv. ultimately enters the Arctic Ocean (Aagaard and Carmack 1989, Manley 1995).

The second pathway flows into Barents Sea through the Bear Island Channel, and via the Norwegian Coastal Current. The water is severely cooled and freshened in the Barents Sea before it reaches the Arctic Ocean, which is thought to occur through the St Anna Trough. The estimated volume flux into the Arctic Ocean via this pathway is 1-3 Sv. (Loeng et al 1993, Ingvaldsen et al 2004). The two pathways meet at the St Anna Trough, where the first pathway makes a small loop into the trough (Schauer et al 2002). They then continue to flow eastward along the continental slope of the Arctic Ocean, where their influence can be seen as far as the Canadian Basin (McLaughlin et al 1996, Woodgate et al 2001). It has been proposed by Rudels et al (1994) and Quadfasel et al (1993) that a branch of pure AW flows back towards Fram Strait in the Nansen Basin along the Nansen-Gakkel ridge, in order to explain the spread of heat in the interior. Swift et al (1997) however propose that the heating is caused by lateral spreading of heat from the boundary current, enhanced by double-diffusive mixing. Also Schauer et al (2002) found little evidence for such a return flow in observations.

The Pacific Ocean provides relatively fresh and cold water for the Arctic Ocean through the approximately 50 metre deep Bering Strait. This inflow is relatively well measured (Coachman and Aagaard 1988, Roach et al 1995), and is thought to be forced by a sea slope difference between either ends of the Bering Strait (Weingartner et al 1997, Proshutinsky and Johnson 1997), and could also play a significant role in forcing the Trans-Arctic drift. A slope in sea surface height (η) between the light water on the Pacific Ocean side (η high) and the relatively heavy water on the Arctic Ocean side ((η low) is also seen in the OCCAM global ocean model (D.J. Webb, personal communication). The mean transport through the Bering Strait has been measured to be around 1 Sv (Roach et al 1995), with a strong seasonal signal with maximum transport in July and minimum transport in March. Half of the freshwater content of the Canada Basin halocline is thought to be provided by this water mass (Aagaard and Carmack 1989), which is therefore a significant contributor to the freshwater budget of the Arctic Ocean.

The Bering Strait Outflow (BSO) is usually divided into two water masses (Steele et al 2004). The relatively fresher and warmer water mass is Alaskan Coastal Water (ACW), and flows through the eastern part of the Bering Strait. It contains a significant amount of river runoff from the Yukon river. The Yukon river flows into the Bering Sea from Alaska on the

Pacific Ocean side of the Bering Strait. The ACW enters the Arctic Ocean through Barrow Canyon on the Alaskan coast, and is thought to continue eastwards along the continental slope. As it continues in a boundary current some part of the ACW spins off into eddies (D'Asaro 1988b). Its properties have been observed on the slope north of Ellesmere Island (Newton and Sotirin 1997). Jones et al (1998) propose that this water mass makes up all of the outflow through the shallow straits of the Canadian Archipelago, although the outflow through Nares Strait (the passage between Greenland and Ellesmere Island) is also thought to contain water of Atlantic origin (Jones et al 2003).

The second water mass is saltier and colder, and is referred to as Bering Sea Water. This water mass is formed by mixing of water on the Bering Sea shelf with water in the Gulf of Andyr, which is on the Russian coast on the Pacific side of the Bering Strait. Steele et al (2004) distinguish between summer and winter variations of this water mass. The warmer summer Bering Sea Water flows through Herald and Hannah Canyons to enter the halocline of the Arctic Ocean. This water mass is found mostly in the Trans-Arctic drift and the northern part of the Beaufort Gyre. Jones et al (1998) propose that this branch flows westwards into the East-Siberian Sea. There is a strong front found at the Mendeleyev ridge as the Pacific Water meets Atlantic Water, and both water masses are thought to flow along the ridge towards Fram Strait.

It has been suggested by Martin and Drucker (1997) that topography plays an important role in steering the outflow from the Bering Strait. The outflow passes two shoals in the Chukchi Sea, where the mean sea floor is approximately at 50m depth. The Herald Shoal is 20 to 30m above the sea floor, and the Hannah Shoal is 10 to 20m above the sea floor. They show that during ice melt in summer ice remains mostly over the two shoals. They attribute this to the formation of Taylor columns over the shoals, which traps cold water and ice above them.

In winter the water masses on the Chukchi shelf become denser as the winds open large polynyas in the Chukchi Sea (Weingartner et al 1997). This water mass is found broadly distributed in the Canada Basin, underlying the ACW and summer Bering Sea Water (Steele et al 2004). The division of the pathways of the two water masses entering through Bering Strait is thought to be dependent on the Arctic Oscillation index, which will be discussed further on.

Another source providing freshwater into the Arctic is the river runoff from Siberian and Canadian rivers. The Ob and Yenisey rivers flow out into the Kara Sea, the Lena river flows into the Laptev Sea, and the MacKenzie river flows into the Beaufort Sea. These rivers produce an inflow of freshwater of the order of 0.1 Sv (Aagaard and Carmack 1989). There is also a smaller freshwater flux due to the net effect of precipitation over evaporation in the Arctic.

The only outflow of water from the Arctic Ocean is into the North Atlantic Ocean. In the Canadian Basin there is a small outflow of water through the shallow (75m) Canadian straits into the Labrador Sea, which is of the order of 1.4 Sv (Melling 1998). The largest outflow is through Fram Strait, where the East Greenland Current carries water southward into the Nordic Seas. This current transports Arctic deep and intermediate waters, that consist of cooled and freshened AW, as well as part of the recirculating water from the West Spitsbergen Current. It is thought to supply a large part of the Denmark Strait overflow (Mauritzen 1996a,b). Measurements of the transport in the East Greenland Current vary between 3-11Sv, however the net transport through Fram Strait is thought to be approximately 1-3Sv southwards into the North Atlantic (Aksenov and Coward 2001). Most of the water then continues via the Denmark Strait overflow, with a smaller part of dense water flowing via the

Faroe Bank Channel (Saunders 2001).

2.3 Arctic Shelf Seas

The Arctic shelves form a large area of the Arctic Ocean that is important for ventilating the ocean interior, and maintaining the halocline necessary for permanent ice cover. Dense water is formed on the continental shelves via a combination of cooling and ice formation. Ice formation leads to brine being rejected into the water column underneath creating dense bottom waters on the shelves. These dense waters then flow off the shelves, mixing with shallow and intermediate depth waters. The formation of dense waters on the shelves is one process that helps to maintain the halocline (Aagaard et al 2001). Another process is the cooling of the constant inflows into the Arctic Ocean. A significant amount of dense water contributing to the halocline is thought to be formed like this in the Barents Sea and Fram Strait (Steele et al 1995).

The most important shelf sea in the Arctic Ocean is the Barents Sea (Schauer et al 2002). It is the deepest (± 200m) of all Arctic shelf seas, and directly receives salty AW. The Barents Sea also receives little river input compared to other shelves. The most important dense water formed in the Barents Sea is due to the transformation of the through flow of AW. The AW is transformed into a cooler and fresher water mass, Barents Sea Water (BSW), by a combination of cooling, freezing and mixing with fresh surface water and dense bottom water (Middtun 1985). Recently Aagaard and Woodgate (2001) have proposed a feedback mechanism whereby the transformation of AW in the Barents Sea, which then helps to maintain the halocline, is caused by melting of ice exported from the Arctic Ocean. The BSW continues into the St Anna Trough, where it meets the Fram Strait pathway of AW that makes a short loop into the trough (Schauer et al 2002).

The properties of the two pathways are now quite distinct. As the AW enters the Arctic Ocean through Fram Strait its high temperature leads to melting of the sea ice above, which causes a large heat loss to the atmosphere (Rudels et al 1999). Then the melt water mixes with the upper part of AW, creating a fresh surface layer. As the AW flows further eastwards this layer, together with the ice cover, provides insulation for the warm AW underneath. Therefore the AW mainly retains its original properties, although it is slightly cooled (Swift et al 1997), and is quite different from the colder and fresher branch of BSW. There are also dense plumes seen to sink down the slope from the northern Barents Sea joining the current of AW (Schauer et al 1997).

As the BSW enters the Arctic Ocean it is confined to the slope by rotation (Schauer et al 1997). The denser part slides down the slope to depths up to 1000m, while the fresher part is confined to the upper part of the slope (Rudels et al 1999). The Fram Strait pathway of AW is deflected from the slope by the intrusion of BSW. Then the two branches flow side by side eastwards in the boundary current, where mixing between the two branches reduces the differences. Further along the slope approaching the Lomonosov ridge the warm signal of the AW has disappeared, for which there are two scenarios: either the warmest water of the AW water mass recirculates within the Nansen Basin (Rudels et al 1994, Quadfasel et al 1993), or the two water masses have been cooled by lateral mixing (Swift et al 1997, Schauer et al 2002).

After the BSW has joined, north of the Kara Sea, the water column is found to be less stratified at the slope than in the interior of the basin. Schauer et al (1997) explain this by the fact that the large volume flux of the BSW can only be accommodated by a downward displacement of the lower isopycnals on the slope. As the upper part of the boundary current is denser than interior water at the same depth, the deeper part is less dense than water at the same depth in the interior ocean. Therefore the velocity in the current must decrease with depth, and the flow direction of the deeper part of the current is determined by the variations in sea surface slope between the continental slope and the ocean interior. These variations can be caused by extra river discharge or atmospheric forcing.

As well as the constant input of BSW isolated dense plumes sinking off the shelves are also thought to contribute to Arctic intermediate and deep waters (Aagaard et al 1985). However there are only a few direct observations of such plumes, mostly at the Spitsbergen coast (Quadfasel et al 1988, Schauer et al 1995), where warm and saline plumes are found to sink down the slope. Modelling work has shown the possible importance of such plumes (Jungclaus et al 1995, Backhaus et al 1997, Anderson et al 1999). Also the existence of sinking plumes has also been derived from observations of water properties in the deep Arctic Basins (Aagaard et al 1985, Rudels et al 1994, Jones et al 1995). Schauer et al (1997) propose that there are shelf water intrusions at the northern Barents Sea slope, adding relatively fresh water to intermediate depths of the Nansen Basin. Also they found saltier outflows at the slope of the Kara Sea. They found that only the Barents and Kara Seas contribute to the ventilation of the Nansen Basin, while the Laptev Sea does not produce dense enough waters.

The formation of dense waters on the shelves through brine-rejection during ice formation is enhanced due to the formation of coastal polynyas. These are openings in ice cover near topographical obstacles forced by winds and tides, and allow dense water formation through intense cooling and ice formation. They have been shown to produce a significant amount of water for the halocline and deep waters on the Siberian and Chukchi shelves (Cavalieri and Martin 1994). Cavalieri and Martin (1994) estimate that 0.7-1.2 Sv of dense water is created on all Arctic shelves in polynyas, most of which enters the halocline. However they conclude that more is needed from other processes, such as general freezing and storms, for the 1-1.5 Sv necessary to maintain the halocline.

The process of the plume formation is described extensively by Backhaus et al (1997). In summer the shelves are covered by a cold and fresh surface layer (caused by river runoff or summer ice melt), overlying a halocline. Regular production of dense water on the shelves can only start in late winter when the water column has been sufficiently homogenised by cooling and brine rejection, which typically takes several months (Harms 1997). This is similar to the production of dense waters in polynyas. In that case the exposure of the surface causes severe heat loss, which together with brine-rejection from newly forming ice will homogenise the water column. The polynyas usually have a horizontal size of a few kilometres, similar to the internal Rossby radius. Eventually the polynya will be covered by sea ice, and the water column will re-stratify due to gravity and rotation. This leads to either the formation of a bottom plume or an eddy. In the case of a bottom plume it will move slowly towards the continental slope. There it sinks down to stable depth, while possibly entraining ambient waters. It ends up as an eastward flowing bottom plume that is almost in geostrophic equilibrium (Jungclaus et al 1995).

2.4 Interior circulation

Here we describe the circulation features in the Arctic Ocean interior, which have mainly been derived from observations of water mass properties. A summary of the circulation is seen in figure 2.2, which is based upon Aagaard's synthesis (1989) and more recent ideas of the boundary currents (Rudels et al 1999). It features the inflow pathways of Atlantic and Pacific Water, a strong boundary current of AW and BSW around the continental shelves and the Lomonosov ridge, the anti-cyclonic wind-driven Beaufort Gyre in the Canadian Basin, the Trans-Arctic drift, and a strong eddy field in the western part of the Canadian Basin.

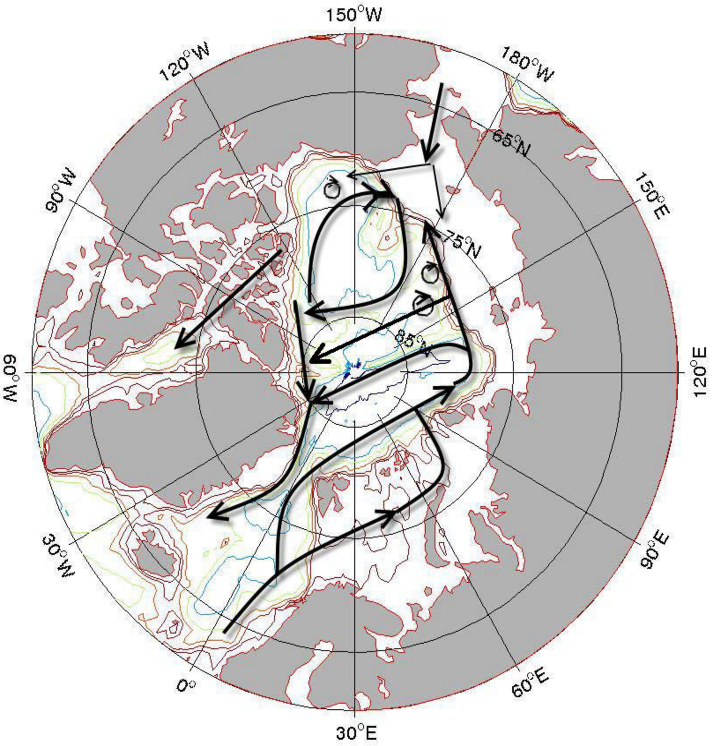

Figure 2.2: *Arctic Ocean circulation summary.*

2.4.1 Circumpolar boundary current

Strong eastward flowing boundary currents have been seen flowing along various sections of Eurasian and Canadian continental slopes, and are thought to be a continuous feature providing large-scale advection within the Arctic Ocean (Aagaard 1989, Rudels et al 1999, Woodgate et al 2001). The ocean interior only has a weak flow field, especially the Eurasian Basin, and the boundary current is therefore an important energetic flow feature. The cyclonic boundary current starts off as a surface current with two separate branches of AW flowing into the Arctic Ocean via Fram Strait and the Barents Sea. It is then split into separate streams, whereby one stream flows northwards along the Lomonosov ridge towards Fram Strait, the other stream continues eastwards into the Canadian Basin. More observations of an eastward flowing boundary current have been made in the Beaufort and Lincoln Seas (Aagaard 1984, Newton and Sotirin 1997).

The mechanism driving the boundary current is still unknown. Suggestions include a form of eddy-topography interaction (also known as the Neptune effect), which drives cyclonic currents over topographical lows and would lead to cyclonic circulation along the continental slope (Holloway 1987). Another suggestion is a form of thermohaline mechanism involving dense waters (Rudels et al 1994), whereby a buoyancy-driven current is formed due to dense shelf waters falling down the continental slope (Shapiro et al 2003). Woodgate et al (2001) found no evidence that the boundary currents are wind-driven, due to the lack of response of the currents to local wind forcing, however Nost and Isachsen (2003) find a good representation of cyclonic bottom currents in a simplified model. They conclude that their wind-forced model is dominated by topographic steering, and produces boundary currents due to the flow following f/H contours (approximate conservation of potential vorticity).

In ocean models the Neptune effect can only occur if they resolve meso-scale eddies, or they parameterize the effect. Nazarenko et al (1998) include such a parameterization of the Neptune effect and conclude that it may help the cyclonic circulation at intermediate levels around the Arctic Ocean to some degree. Specifically the parameterization helps the inflow of Atlantic Water into the Arctic Ocean, producing an in- and outflow through Fram Strait of 6 Sv with the Neptune parameterization, compared to 1 Sv without the parameterization. However in a similar model Zhang and Zhang (2001) identify both the Neptune effect and dense water formation on the shelf in the Barents Sea as important driving forces, and emphasize that they work in completely different ways. They find that the cold and dense Barents Sea shelf waters help to maintain the interior ocean stratification and to produce the correct cyclonic circulation, whereas the Neptune effect enhances the inflow of the warm AW through Fram Strait and produces an unrealistically high temperature of the Atlantic layer of the Arctic Ocean.

The locations of important measurements of the boundary current are shown in figure 2.3. The measurements from 1995-1996 by Woodgate et al (2001) provide the following properties of the boundary current in the Eurasian Basin. The results are from three mooring stations located on the slope near the junction of the Lomonosov Ridge with the Eurasian continent. Although eddies are found to affect the flow, the dominant flow is a cyclonic current along topography. The mean flow of the boundary current is found to be approximately 5 cm/s at 100 metre depth, and 1 cm/s at 1100 metres. Maximum currents of almost 40cm/s at the surface and 20 cm/s at 1100m are found. The transport of the boundary current was found to be 5 ± 1 Sv.

Further along the slope in the Lincoln Sea (north of Greenland) a cyclonic undercurrent has been observed by Newton and Sotirin (1997). Their observations show a boundary undercurrent, extending from about 30-600 metres depth, over the continental slope between the shelf break and the base of the slope. The width of the current is 50 km, and strengths were observed in the core of about 5-6 cm/s. The undercurrent was observed in each spring from 1989-1994, with the same water properties, characteristic of the Canadian Basin waters. The authors argue that their findings confirm the presence of a continuous boundary current system along the continental slope north of Alaska and Canada, as their observations match an undercurrent found in the Beaufort Sea (north of Alaska). They refer to measurements by Aagaard (1984), who finds a cyclonic undercurrent that is opposed to the anti-cyclonic surface current. These measurements show a flow that is directed along topography with a mean velocity of 10cm/s, and a width of 60-70km ranging from 40m to the bottom.

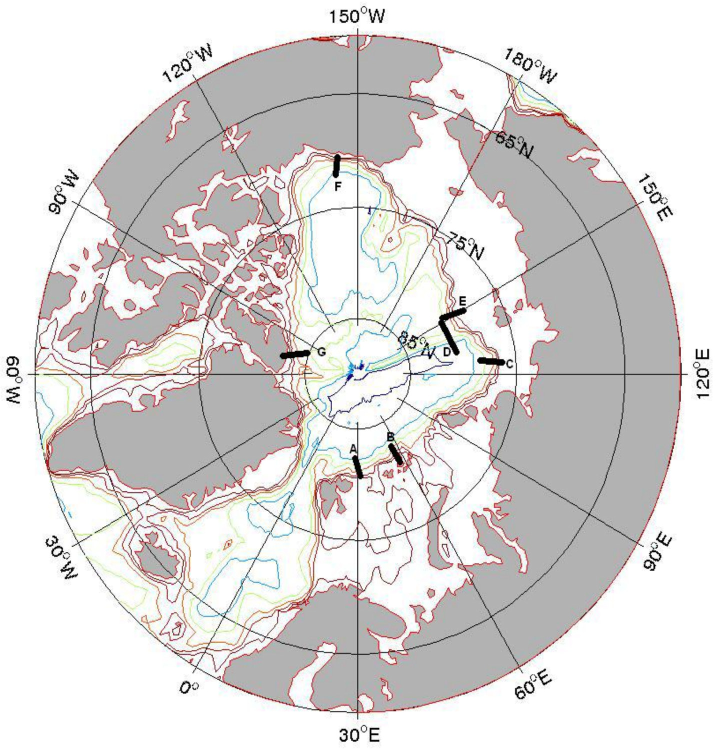

Figure 2.3: *Locations of various measurements of Arctic boundary current. A,B: Schauer et al (1997). C,D,E: Woodgate et al (2001). F: Aagaard (1984). G: Newton and Sotirin (1997)*

2.4.2 Wind-driven circulation

The surface circulation in the Arctic Ocean has been observed from various drifting ice stations and ships. Historically the circulation has been thought to be mostly anti-cyclonic, with the centre of an anti-cyclonic gyre (the Beaufort Gyre) in the Canadian Basin (Coachman and Aagaard 1974). Another feature is the Trans-Arctic drift which flows from the Laptev Sea across the Arctic towards Fram Strait. It is difficult to separate the roles of thermohaline and wind-driven circulation in the Arctic Ocean circulation, and it is currently thought that both driving forces are important (Proshutinsky and Johnson 1997).

Recently it has been found that the wind-driven circulation is subject to significant variability. The Arctic Oscillation (AO) consists of fluctuations in air mass between mid- and high-latitudes on the Northern Hemisphere. The AO index is highly correlated with the North Atlantic Oscillation (NAO) index, and the NAO is sometimes considered to be a regional representative of the AO (Delworth and Dixon 2000). During a positive AO index there is a weak Arctic high pressure corresponding to a cyclonic wind-driven ice drift circulation in the Eurasian Basin. During a negative AO index there is a strong Arctic high pressure corresponding to an anti-cyclonic wind-driven ice drift circulation in the Eurasian Basin (Proshutinsky and Johnson 1997, Kwok 2000). During a positive AO the size of the anti-cyclonic Beaufort Gyre is reduced, and the Trans-Arctic drift is slowed and shifted towards the Canadian Basin.

Proshutinsky and Johnson (1997) use a 2D coupled sea-ice model to present evidence of the two regimes. They show the presence of a cyclonic and an anti-cyclonic regime, which alternate at periods of 5-7 years. This suggests a negative AO index with an increased Beaufort Gyre during 1984-1988, and a positive AO index with a decreased Beaufort Gyre during 1989-1993. During a negative AO index it is found that more ice is exported into the North Atlantic from the Eurasian boundaries, where the ice is thinner than in the Canadian Basin, leading to a decrease in freshwater export. It is emphasized that more observations are needed to validate these theories, as most of the historical observations were conducted during a regime of negative AO index.

Steele et al (2004) have performed analysis of the AO index and conclude that 1979-1987 are years of a negative index, while 1988-1994 are years of a strong positive AO index. The following years 1995-2001 have a weakly positive index. They also find that the separation of the waters in the Bering Strait Outflow is more extreme in years of a positive AO, and during a negative AO index the wind-driven Beaufort Gyre is enlarged and plays an important role in trapping the transport of water masses through the Canadian Basin.

Maslowski et al (2000) have shown that the reach of AW in the Arctic is dependent on the atmospheric variability. They have compared trajectories of passive tracers in a regional high-resolution coupled ice-ocean model to assess the changes due to atmospheric variability. They calculated 'online' trajectories of both Atlantic Water and Pacific Water comparing constant annual atmospheric forcing for 1979 to annually varying forcing fields for 1979-1993 in their model integration. They find that in the constant forcing case there is an enlarged Beaufort Gyre, and the AW tracer flows mainly along the Eurasian side of the Lomonosov Ridge towards Fram Strait. However in the variable forcing case there is a reduced size Beaufort Gyre in the early 1990's, and the AW tracer crosses the Lomonosov Ridge and then flows towards Fram Strait along the Canadian side of the Lomonosov Ridge, and along the Mendeleyev Ridge.

2.4.3 Meso-scale eddies

Subsurface eddies are a major feature in the Canadian Basin of the Arctic Ocean. Also recently some have been observed in the Eurasian Basin (Woodgate et al 2001). The eddies are mostly anti-cyclonic, and have homogeneous temperature and salinity properties that differ from the surrounding waters.

Results from observations in 1972 by Newton et al (1974) using drifting ice camps in the Canadian Basin confirm the presence of small anti-cyclonic horizontal eddies within the pycnocline. The radius of these eddies was calculated to be of the order of 15 kilometres. The eddies appeared within the pycnocline at depths of 50-300 metres. The maximum speed observed was of the order of 35 cm/s.

Other observations by Manley and Hunkins (1985) suggested that eddies could fill a quarter of the Canadian Basin surface area, and produce ±30% of the kinetic energy found within the upper 200 metres of the Beaufort Sea. D'Asaro (1988a) showed that the eddies must originate on the Chukchi Shelf due to the water properties of the eddies. As water flows off the shelf through the Barrow Canyon into the Arctic Ocean it is suggested that instability forms eddies (D'Asaro 1988b).

Another formation mechanism for shallow eddies has been modelled by Chapman (1999), who showed that cold core eddies in the mixed layer and upper pycnocline are created via instabilities of the front between the dense waters formed in a wind-forced coastal polynya and the surrounding shelf waters. Woodgate et al (2001) suggested that larger eddies, extending over 1000m in depth, observed near the Lomonosov ridge in the Eurasian Basin are created by instabilities in the front between the AW and BSW branches.

Chapter 3

OCCAM global ocean model

3.1 Introduction

In this study we use results for the Arctic Ocean circulation from the OCCAM model (Webb et al 1998). The OCCAM model (from the Ocean Circulation and Climate Advanced Modelling Project) is a high-resolution fully global ocean model, based on the Bryan-Semtner-Cox primitive equations for the ocean, with an explicit free surface. There are two main problems for global models accurately simulating the Arctic Ocean circulation. Due to the small Rossby radius ($5-10km$) in the Arctic Ocean models must have a very high resolution in order to resolve the meso-scale circulation features. Another problem is the convergence of the meridians at the poles.

The OCCAM model simulation used in this study is described by Aksenov and Coward (2001). The model has a horizontal resolution of $1/8^\circ \times 1/8^\circ$, and uses two spherical (Arakawa B) grids to cover the full globe. The first grid is a standard latitude-longitude grid covering the Southern Atlantic, Pacific and Indian Oceans. The second grid is rotated with its North Pole on the geographical equator, and covers the North Atlantic and Arctic Oceans. The two grids are coupled along the Atlantic equator and at Bering Strait. At Bering Strait the Pacific and Arctic Oceans are connected by a channel model, which balances the pressure difference between either side of the strait by bottom friction in a channel of uniform width (60km), length (20km), and depth (20m). In this study only data from the second grid is used. The horizontal resolution in the Arctic Ocean on this grid is approximately $14km \times 14km$, which is fine enough to start resolving meso-scale features. The model uses depth coordinates in the vertical and has 36 levels, varying in thickness from 20m at the surface to 250m at a depth of 5500m. The model topography is derived from the $1/12°$ DBDB5 dataset (US Naval Oceanographic Office 1983). Using this topography the most important straits within the Canadian Archipelago are resolved, the Nares Strait (between Greenland and Ellesmere Island) and Lancaster Sound (eastern part of Barrow Strait). The layout of the model covering the Arctic Ocean, with overlying geographical latitude-longitude contours, is shown in figure 3.1. As the traditional latitude-longitude grid is little distorted the horizontal model grid boxes over the Arctic are almost all the same size.

The model is forced by a monthly ECMWF climatological surface stress. A set of 12 mean monthly wind stresses was calculated from data for the period 1986-1988 (Barnier et al 1995). This set is applied repeatedly for each year of the simulation. According to Proshutinsky and Johnson (1997) this is a period of negative AO index, creating an enlarged Beaufort Gyre. However there are doubts about this as Steele et al (2004) have marked this as a transition period into a strong positive AO phase. The model has no explicit treatment of sea ice, river runoff or surface fluxes of heat and freshwater. Instead the model salinity and temperature values are relaxed at the surface to the Levitus 94 climatology (Levitus and Boyer 1994, Levitus et al 1994). The salinity difference at the surface is used to derive a freshwater flux, which affects the free surface height, so the total amount of salt is conserved.

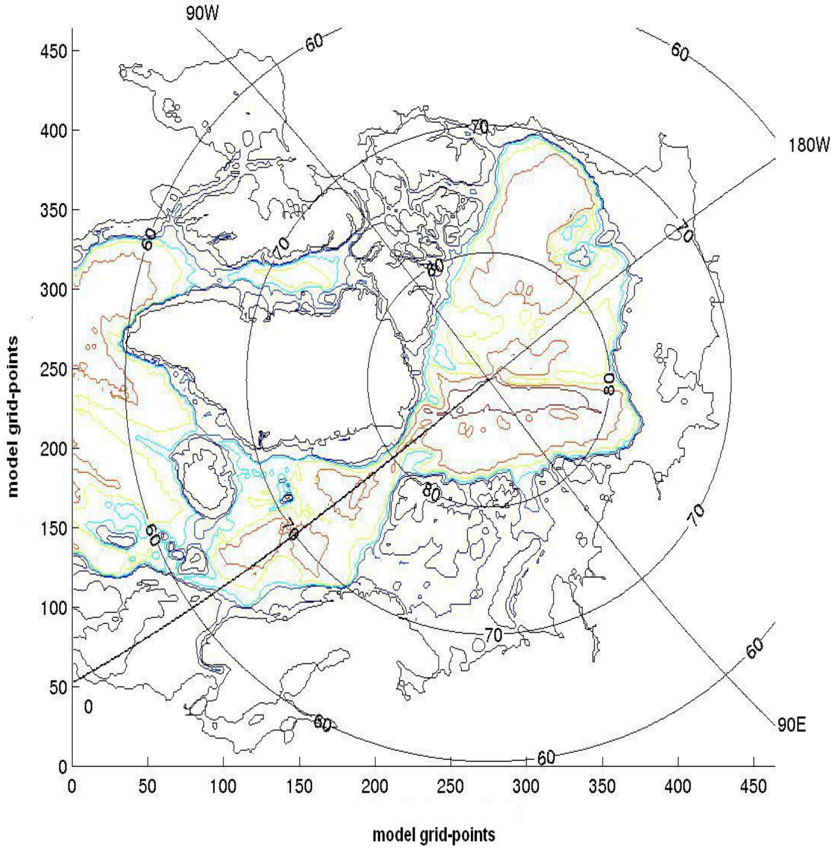

Figure 3.1: *OCCAM model over Arctic Ocean with model depth contours at 245, 508, 989, 1931, 3101, 4100 metres, and overlying geographical latitude and longitude contours.*

The initial state of the model is derived from a 8 year simulation of a similar coarser 1/4° × 1/4° resolution model. The coarser model is relaxed to Levitus 82 (Levitus 1982), and subsequently to Levitus 94 at the surface. The 1/8° × 1/8° model is then integrated for a period of 2 years from year 8. The model will not reach an equilibrium state within the integration period. However diagnostics such as the global mean kinetic energy, temperature and salinity changes suggest that the circulation patterns are generally established during a six month adjustment phase. This is followed by a slow drift towards an equilibrium state.

In this study we made use of both the 10-day instantaneous datasets and an annual mean dataset, both from the second year of the model simulation.

The Levitus climatology from which the air-sea fluxes are derived for this study has been compiled using the available observations of ocean properties. The resulting continuous temperature and salinity fields over the ocean may however be inaccurate as large parts of the Arctic Ocean have only been sparsely measured. Therefore the effects of important processes for our hypothesis, most importantly ice formation, may be missing in the data. It would be preferable to couple the ocean model to an explicit ice model in order to better represent the air-sea fluxes due to ice formation, especially in the sparsely observed regions. However at the time of this study the progress in OCCAM model development had not yet reached the stage to allow coupling to an ice model, which is a consequence of running such a high resolution model.

3.2 Model equations

The equations solved by the models are the primitive equations, which can be found in many textbooks (eg. James 1994). These consist of the horizontal momentum equations

$$\frac{\partial \mathbf{u}}{\partial t} + (\mathbf{u} \cdot \nabla)\mathbf{u} + w\frac{\partial \mathbf{u}}{\partial z} + f \times \mathbf{u} = -\frac{1}{\rho_0}\nabla p + \mathbf{D_u} + \mathbf{F_u}, \tag{3.1}$$

the advection-diffusion equations for heat and salt

$$\frac{\partial S}{\partial t} + (\mathbf{u} \cdot \nabla)S + w\frac{\partial S}{\partial z} = \mathbf{D_S} + \mathbf{F_S}, \tag{3.2}$$

$$\frac{\partial T}{\partial t} + (\mathbf{u} \cdot \nabla)T + w\frac{\partial T}{\partial z} = \mathbf{D_T} + \mathbf{F_T}, \tag{3.3}$$

and the pressure equation, continuity equation, and equation of state

$$\rho g = -\frac{\partial p}{\partial z}, \tag{3.4}$$

$$\nabla \cdot \mathbf{u} + \frac{\partial w}{\partial z} = 0, \tag{3.5}$$

$$\rho = \rho(T, S, p). \tag{3.6}$$

In the momentum equations $\mathbf{u} = (u, v)$ is the horizontal velocity vector, ∇ is the horizontal gradient operator, w is the vertical velocity, the Coriolis parameter is f $(= 2\Omega sin\phi$, where Ω is angular rotation speed of the earth and ϕ is latitude), ρ_0 is a reference density, p is pressure, $\mathbf{D_u}$ represents diffusion of horizontal momentum, and $\mathbf{F_u}$ represents the wind-stress forcing. In the advection-diffusion equations S is salinity, T is potential temperature, $\mathbf{D_S}$ and $\mathbf{D_T}$ represent diffusion of salt and temperature, and $\mathbf{F_S}$ and $\mathbf{F_T}$ represent the surface forcing of salinity and temperature. In the final three equations ρ is density and g is the gravitation. The equations (3.1), (3.2) and (3.3) are solved for the prognostic variables $\mathbf{u}$, T, S. Then the variables p and w are calculated from equations (3.4) and (3.5) respectively. The density ρ is calculated from equation (3.6) using a 3rd order polynomial fit to the equation of state.

The model uses Laplacian diffusion to represent horizontal and vertical mixing of momentum

$$\mathbf{D_u} = A_H \nabla^2 \mathbf{u} + A_Z \frac{\partial^2 \mathbf{u}}{\partial z^2}, \tag{3.7}$$

where $A_H (= 2 \cdot 10^6 cm^2/s)$ and $A_Z (= 1 cm^2/s)$ are the horizontal and vertical eddy viscosity coefficients. Horizontal mixing of tracers is also represented by Laplacian terms. Vertical mixing of tracers is represented by Pakanowski and Philander (1981) mixing, although at high latitudes the effect of this mixing scheme is to revert to a Laplacian term with a constant vertical diffusion coefficient (due to relatively small velocities). Therefore we have

$$\mathbf{D_S} = K_H \nabla^2 S + K_Z \frac{\partial^2 S}{\partial z^2}, \quad \mathbf{D_T} = K_H \nabla^2 T + K_Z \frac{\partial^2 T}{\partial z^2}, \tag{3.8}$$

where $K_H (= 1 \cdot 10^6 cm^2/s)$ and $K_Z (= 0.5 cm^2/s)$ are the horizontal and vertical eddy diffusion coefficients.

3.3 Air-sea fluxes

In this section we look at the prescribed air-sea fluxes in the model. Figure 3.2 shows the annual mean heat flux and precipitation-evaporation (P-E) fields derived from the surface forcing fields. The heat flux is dominated by a heat loss to the atmosphere by warm water in the Barents Sea and around Spitsbergen, which is probably due to inflow of warm AW into the area which creates large ice free areas. The maximum heat loss is $70W/m^2$ in the Barents Sea. If a water column over the maximum depth of the Barents Sea ($\Delta z = 200m$) were to experience this heat flux $\Delta Q = -70W/m^2$, and the heat was spread evenly over the column, then the temperature change throughout the column would be

$$\Delta T = \Delta t \frac{\Delta Q}{c_v \rho_0 \Delta z}, \tag{3.9}$$

where $c_v \approx 4200J/(kg°C)$ is the specific heat of seawater. Estimating $\rho_0 = 1000\ kg/m^3$ this would lead to a change of approximately $-2.6°C$ per year of the full 200m water column. This is a very strong cooling of AW, which flows in at a typical temperature of $6°C$.

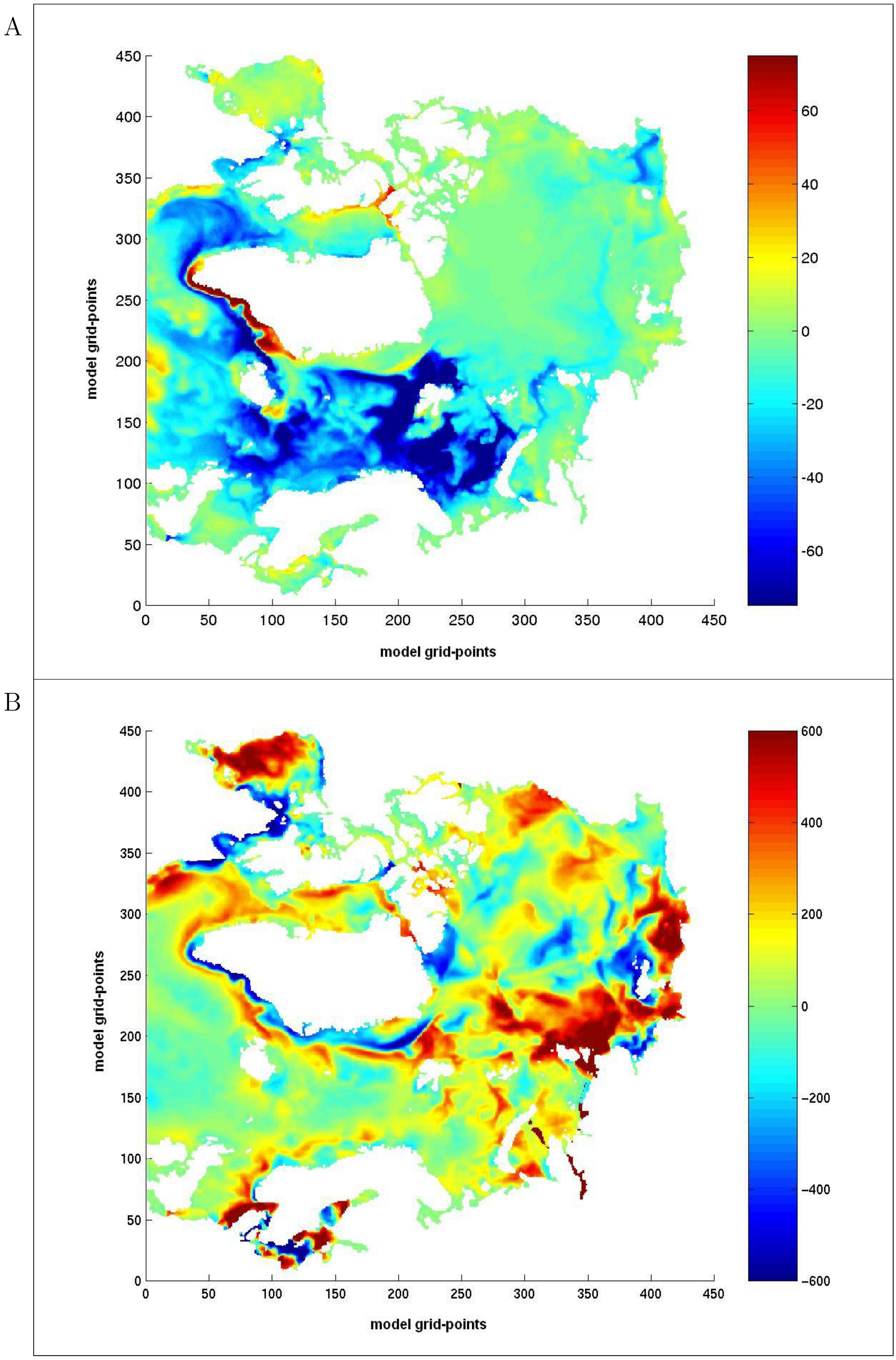

Figure 3.2: *Annual mean surface fluxes. (A) Heat flux out of ocean in* W/m^2*, (B) Precipitation-Evaporation in* $cm/year$*.*

This negative heat loss signal seems to continue along the continental slope with an approximate value of $20W/m^2$ all the way into the Canadian Basin. Another region where the ocean surface is significantly cooled is on the Chukchi shelf. This shelf is known to be mostly ice free in summer which would promote a strong cooling of the inflowing Pacific Water (Martin and Drucker 1994).

The annual mean P-E field is dominated by net precipitation on the Siberian and Canadian shelves, and smaller areas of net evaporation. The net precipitation in the model is primarily due to the freshwater flux from the large Siberian and Canadian rivers. The net 'evaporation' in the model corresponds to areas of regular ice production. These areas are relatively small in the annual mean (P-E) field, however seasonal ice production leads to larger areas of net evaporation on the Siberian and Canadian shelves in early winter.

In the Barents Sea there is a net precipitation. If an unstratified water column in the Barents Sea with salinity S_0, temperature T_0 and depth $\Delta z = 200m$ were to experience a net freshwater flux of $\Delta PE = 200cm/year$, we can estimate the associated salinity change.

The mass per unit surface area of the freshwater added to the column in a time period Δt would be $\Delta PE\rho(T_0, 0)\Delta t$. Then the new mass per unit surface area of the water column is $\rho(T_0, S_0)\Delta z + \Delta PE\rho(T_0, 0)\Delta t$. If the original amount of salt in the water column is distributed over the new mass per unit surface then the new salinity is given by

$$S = \frac{S_0\rho(T_0, S_0)\Delta z}{\rho(T_0, S_0)\Delta z + \Delta PE\rho_0\Delta t}. \tag{3.10}$$

Estimating $\rho(T_0, S_0) = 1000\ kg/m^3$ and $\rho(T_0, 0) = 1000\ kg/m^3$ the salinity change for each year is then -1%. For $S_0 = 35$PSU this gives a freshening of 0.35 PSU per year of the entire water column. The freshening is therefore less effective in than the cooling in the Barents Sea for changing water mass properties. However freshening can still play an important role, as density is much more dependent of salinity at low temperatures. This is illustrated in figure 3.3, where a Temperature-Salinity plot is shown with potential density contours (referenced to the surface). In the plot a water parcel is shown with a temperature of $3°C$ and a salinity of $34PSU$, whereby a temperature change of $-2.5°C$ and a salinity change of $+0.2PSU$ both give the same density increase.

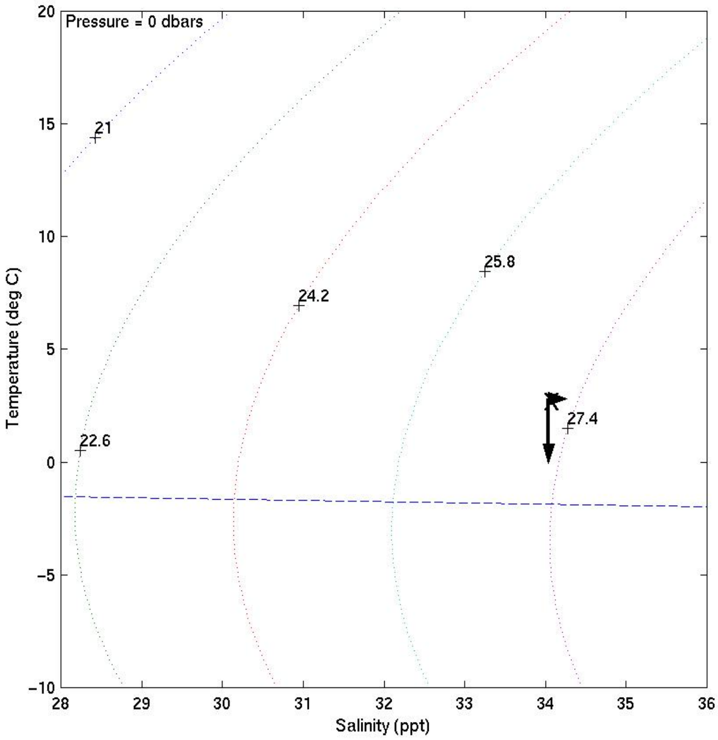

Figure 3.3: *Temperature-Salinity plot with potential density contours (referenced to the surface), showing water parcel for which temperature change of* $-2.5°C$ *and salinity change of* $+0.2PSU$ *give same density increase.*

The air-sea fluxes over the Arctic are derived from surface relaxation to the Levitus 94 climatology, which might produce unrealistic fluxes in some areas due to the sparseness of the data. The mean effect of the air-sea fluxes in the Barents Sea is to provide cooling and freshening, while this area is known to be an area of regular ice formation (eg. Middtun 1985). Ice formation acts to increase salinity of the water column through brine rejection, which increases salinity. As salinity is more important for density than temperature, this would provide a more effective way of creating dense water. However, there is little sign of these effects in the air-sea fluxes used in the OCCAM model, even in winter. Although the net freshening and cooling is consistent with the idea that the inflow of warm AW melts the ice above, which might be imported into the area from the Arctic Ocean (Aagaard and Woodgate, 2001).

A very prominent feature in the freshwater flux field is the large amount of freshwater that eminates from the Russian coast, and reaches far into the Arctic Ocean interior. This is how the river runoff from the large Siberian rivers is represented in the model, which has no explicit river inflows. The effects of ice formation near coastal areas in Greenland, Spitzbergen and on the Russian shelves can be seen through the net evaporation that is prescribed in those regions.

Investigating air-sea fluxes derived from a climatology may not provide the most accurate results, as is possibly seen in the Barents Sea, although it seems that the main effects such as ice formation and river runoff in other areas are present.

3.4 Ocean circulation

In this section we look at results from the simulation of the Arctic Ocean circulation.

A detailed comparison of transports in the model with observations has been presented by Aksenov and Coward (2001). In general the annual mean, and variability of the transports in the model are found to be in good agreement with the available observations described in chapter 2. The ocean circulation at a depth of $30m$ is shown in figure 3.4. This shows the boundary current on the Eurasian side of the Arctic, and the Beaufort Gyre, which is confined to a small part of the Canada Basin. This indicates a relatively positive index of the AO. The Trans-Arctic drift can be seen as a meandering feature flowing across the Arctic from the Beaufort Sea towards Greenland. It is found that the drift consists of several inter-connected jets, similar to those found in other high resolution models (eg. Zhang et al 1999).

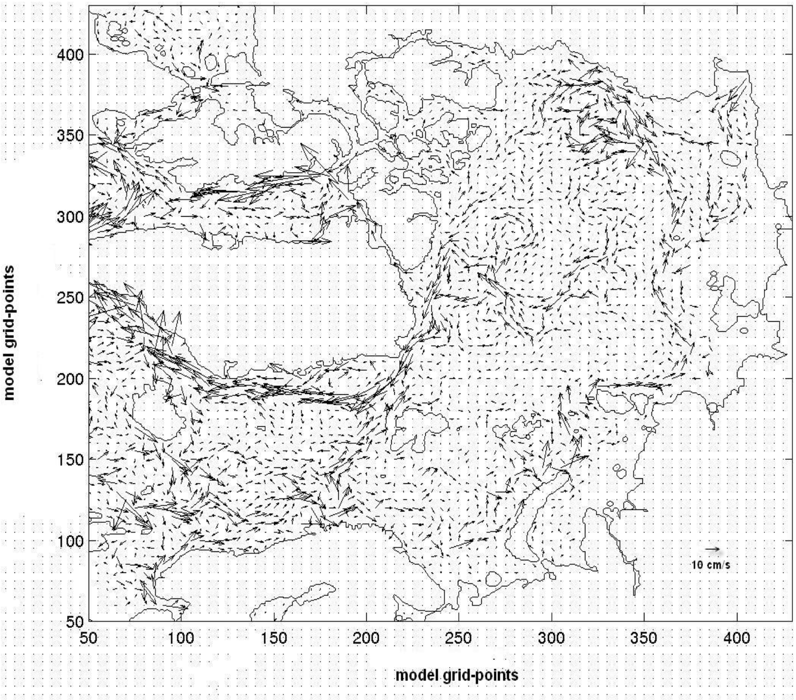

Figure 3.4: *Annual mean velocity vectors at a depth of* $30m$

The annual mean inflow of Atlantic Water through the Barents Sea in the model is 2.4

Sv, which continues into the Arctic Ocean via the St Anna Trough. Another pathway flows through the eastern part of the Fram Strait as part of the West Spitsbergen Current. This current has an annual mean transport of 5.1 Sv. A branch of AW is then found to continue as a meandering eastward current about 100 km offshore from the shelf slope. The transport of Pacific Water through the Bering Strait has an annual mean of 0.74 Sv.

There is a strong southward East Greenland Current flowing through the western part of Fram Strait in the model, and the net outflow through Fram Strait has an annual mean of 2.7 Sv. The outflow through the Canadian straits has an annual mean of 0.82 Sv.

In figures 3.5A,B the mean annual sea surface salinity and temperature of the model simulation are shown. The Arctic Ocean interior is covered by a cold and relatively fresh surface mixed layer, which is approximately 50m deep in the model. There are especially fresh waters in the Beaufort Gyre region. The warm and saline AW can be seen entering the Arctic Ocean via Fram Strait and the Barents Sea.

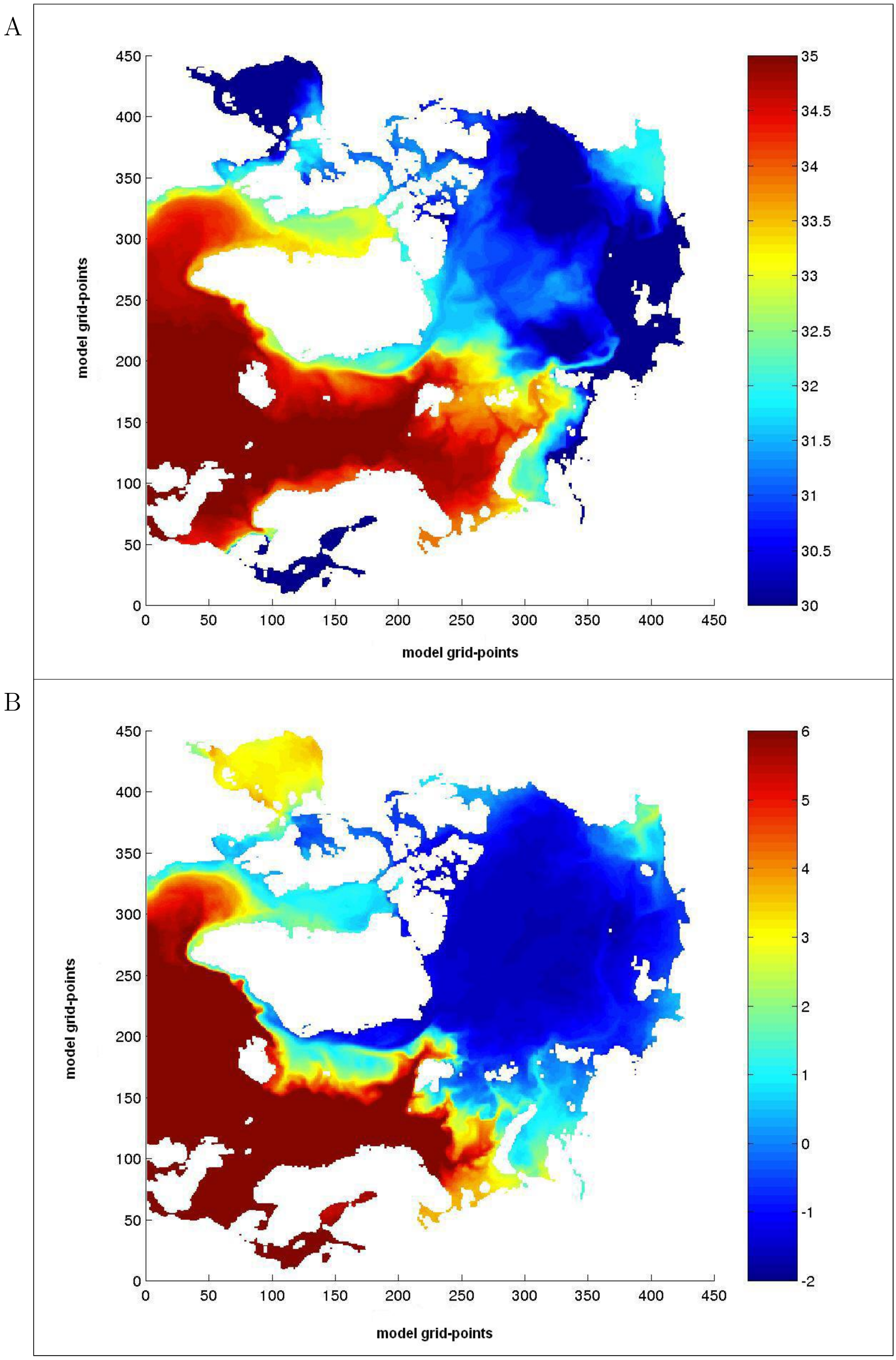

Figure 3.5: *Annual mean surface properties (A) Salinity (PSU) (B) Temperature (° C).*

The Laptev and East Siberian shelf seas are covered by a layer of cold and fresh river water, which is prescribed through the surface heat and freshwater fluxes. The Chukchi Sea is dominated by the inflow of Pacific Water.

In the model the warm and saline water of the AW inflow is found to gradually descend in the basin interior. These waters are then cooled and freshened as they flow towards the Canadian Basin, where they are found at depths of 200-800m.

Figures 3.6A,B show two velocity sections crossing the central Arctic Ocean along constant model longitude and latitude. In the first figure positive/negative values represent eastward/westward (out of/into figure) flows in model coordinates. In the second figure positive/negative values represent northward/southward (into/out of figure) flows in model coordinates. There are eastward flowing boundary currents along large parts of the continental slope, and can be traced back to the Barents Sea. The longitude section in figure 3.6A shows the current on the northern edge of the Kara Sea which reaches from the surface down to approximately 900m, with maximum velocities of up to 20cm/s reaching 100km offshore. On the other side of the basin on the southern part of the Canadian Basin slope there is only a weak subsurface current with velocities of the order of 6 cm/s at depths of 400-1100m. The latitude section in figure 3.6B shows the southwards flowing boundary current on the slope North of Greenland. Here the boundary current is stronger, and reaches from the surface to 1500m with velocities of up to 20 cm/s. The eastward flowing current on the Siberian slope has a similar structure, reaching from the surface to 900m.

There is evidence that the boundary current is stronger when flowing south-eastwards, which occurs on parts of the Kara Sea slope, East Siberian Sea slope, and around the coast of Greenland. This is probably due to westward intensification as the flow changes from being an eastern boundary current into a western boundary current.

Other important circulation features that can be seen in figures 3.6A,B are the Beaufort Gyre, the Trans-Arctic drift, and the flows along the various ridges. The Beaufort Gyre in the model consists of several anti-cyclonic meso-scale vortices which produce a net anti-cyclonic circulation. The maximum velocities in the Gyre reach up to 30cm/s. The Trans-Arctic drift can be seen flowing at depths of 0-500m towards Greenland above the Mendeleyev Ridge with velocities up to 12 cm/s. There is also a strong northwards flow along the western part of the Lomonosov ridge, which is accompanied by a southwards flow along the eastern part of the Lomonosov ridge. Both flows reach approximately from the surface to 1000m. In the ocean interior weak currents ($\pm 1 cm/s$) are produced forming complete gyres following topography. There are also small eddies found in the pycnocline of the Canadian Basin.

In order to visualize the extent of the boundary current we look at stream functions of the flow.

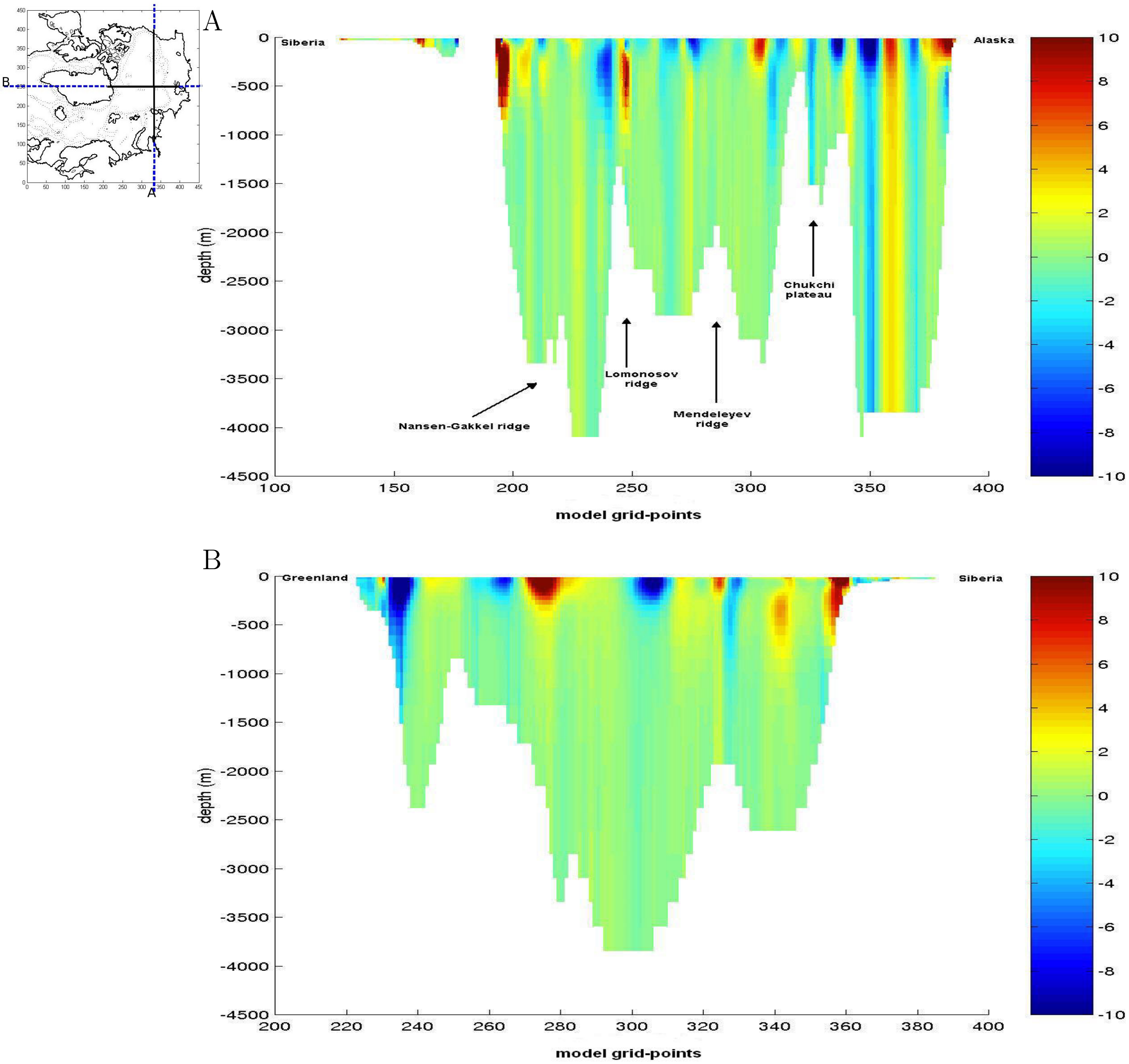

Figure 3.6: *Velocity sections in cm/s (A) Constant model longitude section at i=330 (B) Constant model latitude section at j=250.*

The annual mean circulation is seen in figure 3.7, which shows contours of the depth-integrated stream functions. The depth-integrated stream function Ψ in m^3/s is defined by

$$\begin{aligned} \frac{\partial \Psi}{\partial x} &= \int_h^0 v dz, && (3.11) \\ \frac{\partial \Psi}{\partial y} &= -\int_h^0 u dz. && (3.12) \end{aligned}$$

The contours of this function, streamlines, are then parallel to the flow, giving anti-cyclonic flow around regions with high values of Ψ and cyclonic flow around regions with low values of Ψ. In order for the stream function to exist the depth-integrated transport must be non-divergent

$$\frac{\partial U}{\partial x} + \frac{\partial V}{\partial y} = 0, \qquad U = \int_h^0 u dz, \; V = \int_h^0 v dz.$$

This condition is nearly true for the free-surface model formulation of OCCAM as the surface w is very small (order $10^{-8} m/s$). Therefore we can calculate an approximate stream function by

$$\Psi(x, y) = -\int_{y_0}^{y} U(x, y') dy' + \int_{x_0}^{x} V(x', y_0) dx', \tag{3.13}$$

using any starting point (x_0, y_0).

Figure 3.7A shows the stream function integrated from the surface down to 989m (approximating non-divergent flow). This stream function shows a strong gradient indicating cyclonic flow around the continental slope of the Eurasian Basin. This signal originates in the Barents Sea, where AW flows in from the Norwegian Sea flowing through the Barents Sea. When the signal reaches the Canadian Basin it crosses the Arctic, where the pathway of the signal seems to coincide partly with topography contours. However this figure indicates that the boundary current transport is mostly affected by the Trans-Arctic drift. Also the anti-cyclonic vortices of the Beaufort Gyre can be seen.

Figure 3.7B shows the stream function integrated up to the full depth of the ocean. This figure shows very similar features, indicating weak flow beneath 989m. One interesting feature which has not been described in observations is the anti-cyclonic flow in the western Eurasian Basin. There is also a strong cyclonic feature between the two main vortices of the Beaufort Gyre. As this is present in the annual mean field it suggests it is a stationary meso-scale feature associated with the wind-driven field.

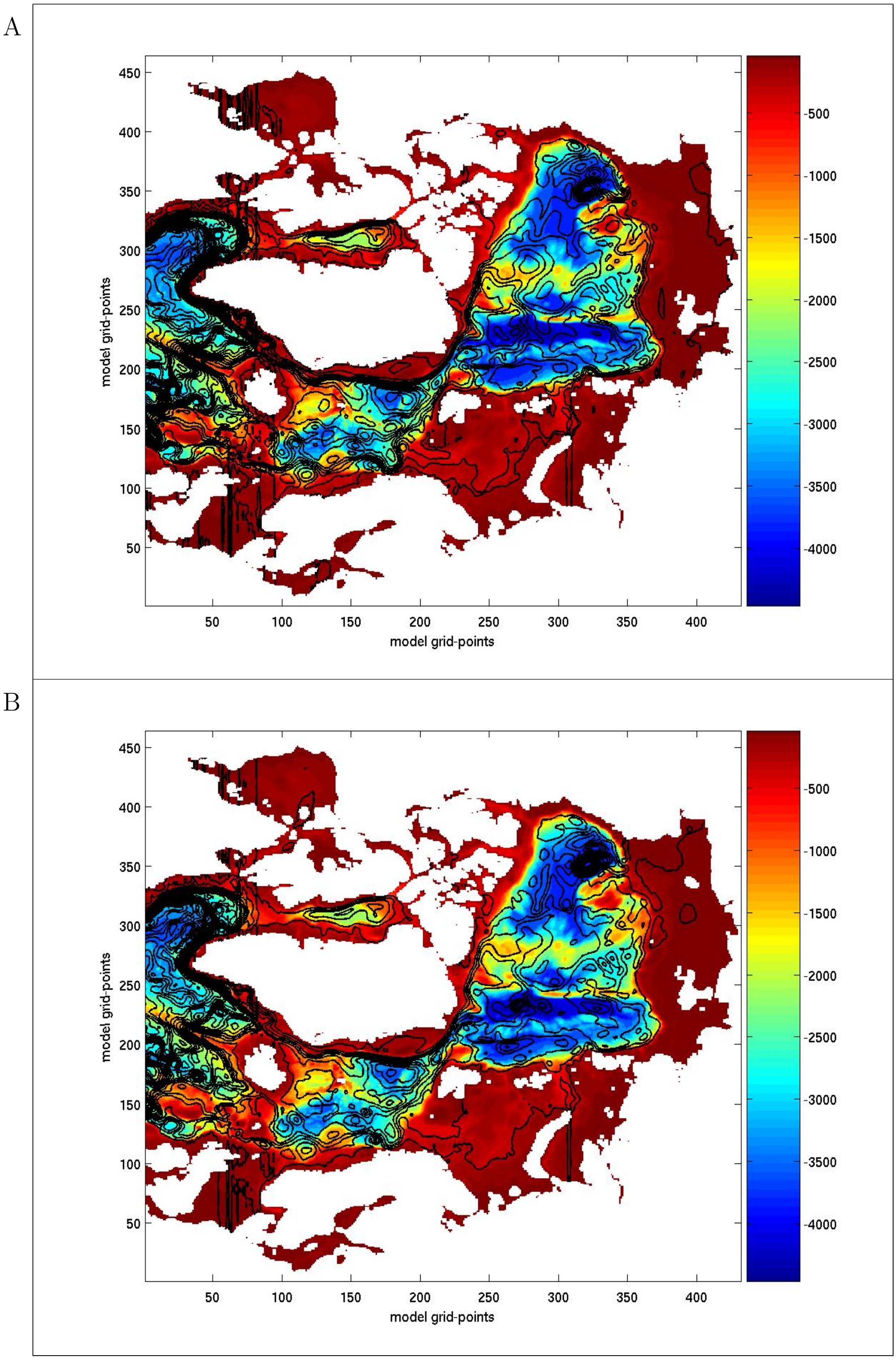

Figure 3.7: *Annual mean contours of depth-integrated streamfunctions (black) in* m^3/s *(A) Integrated to 989m (B) Integrated to full depth, with topography surfaces (m).*

Chapter 4

Boundary pressure

4.1 Introduction

In this chapter we look further at the characteristics of the circumpolar boundary current in the OCCAM model. Although the model shows a boundary current at various locations on the continental slope, it is still unclear if it is continuous. Here we would like to find the exact formation regions of the current. There are various hypotheses on the driving mechanism on the boundary current, which have been discussed in chapter 2. Here we look at the hypothesis that the current is driven by buoyancy fluxes on the shelf, which cause shelf waters to sink down the continental slope. Therefore we look at the pressure field along fixed depths on the continental slope. If the hypothesis is correct we would expect areas of high pressure on parts of the slope where dense shelf waters enter the basin. We then aim to look at the processes causing the high pressure regions on the slope.

Dense water is formed on the Arctic shelves by processes of cooling, evaporation and ice formation. A buoyancy-driven current is set up if these waters are made denser than water in the ocean interior, and manage to sink down the shelf (Shapiro et al 2003). As dense waters flow off the shelf they will mix with ambient waters and eventually sink to a stable level. The dynamics of the flow is then determined by rotation, friction and entrainment. When the dense water enters the basin it is affected by the Coriolis force and will be bound to the slope by rotation, as was observed with dense plumes on the Barents Sea slope by Schauer et al (1997).

It has been shown in various studies of numerical models that buoyancy fluxes lead to the set-up of a coastal current, via the propagation of Kelvin waves (Fennel and Mutzke 2000, Ikeda 1984). Kelvin waves travel along fixed boundaries and are dependent on rotation. In the northern hemisphere Kelvin waves travel with the boundary on the right facing the direction of wave propagation. The momentum balances for a Kelvin wave along the coast in the $y-$direction for a constant-density ocean are

$$fv = g\frac{\partial \eta}{\partial x}, \quad \frac{\partial v}{\partial t} = -g\frac{\partial \eta}{\partial y},$$

where η is the sea surface height (Gill 1982). The $x-$direction is in geostrophic balance, while the alongshore velocity is accelerated in the direction of the alongshore pressure gradient. The solution of the wave equation is then given by

$$\eta = \eta_0 \cos(\kappa y - \omega t) \exp(-fx/\sqrt{gh}),$$

where $L = \sqrt{gh}/f$ is the Rossby radius. The wave amplitude falls off exponentially from the boundary in the offshore direction with a decay scale of the Rossby radius. The wave speed is equal to the shallow water surface gravity wave speed $C = \sqrt{gh}$, which in the case of $L = 10km$ and $f = 10^{-4}/s$ is $C = 1m/s$. Internal Kelvin waves are similar and travel at the internal gravity wave speed. The presence of Kelvin waves in General Circulation Models (GCMs) such as OCCAM using an Arakawa B grid has been confirmed in various studies, although Marotzke and Klinger (2000) argue that they travel much slower in the model than in reality. Johnson and Marshall (2002) attribute this to models with horizontal resolutions that are too coarse to resolve the dimensions of the Kelvin wave.

In the next section we look at the likelihood of buoyancy fluxes around the continental slope driving the boundary current by looking at the pressure gradients along the boundary at fixed depths.

4.2 Pressure gradients

Here we look at dynamic height (pressure) fields along the boundaries of the Arctic Basin. Dynamic height in m is defined by

$$D(x,y,z) = \eta(x,y) + \frac{1}{\rho_0}\int_z^0 \rho(T(z'),S(z'),z')dz', \tag{4.1}$$

where $\eta(x,y)$ is the free surface height, and ρ_0 is a reference density. Therefore dynamic height represents the height that an unstratified water column of density ρ_0 would have if it were filled with the weight of the water column above each point. The relationship to pressure is given by

$$p(x,y,z) = g\rho_0 D(x,y,z), \tag{4.2}$$

where g is gravitational acceleration.

We have calculated the annual mean dynamic height along fixed depth contours in the model topography on the continental slope, at depths typical for the boundary current. Contours of model depth at 201m, 355m and 605m are shown in figure 4.1. They all start in the North Atlantic, and continue northwards along the continental slope along the coast of Norway. The contour at 201m enters the Arctic Basin through the St Anna Trough via the Barents Sea. The deeper contours first flow around Spitsbergen and continue eastwards. The 355m contour makes a complete loop around the St Anna Trough.

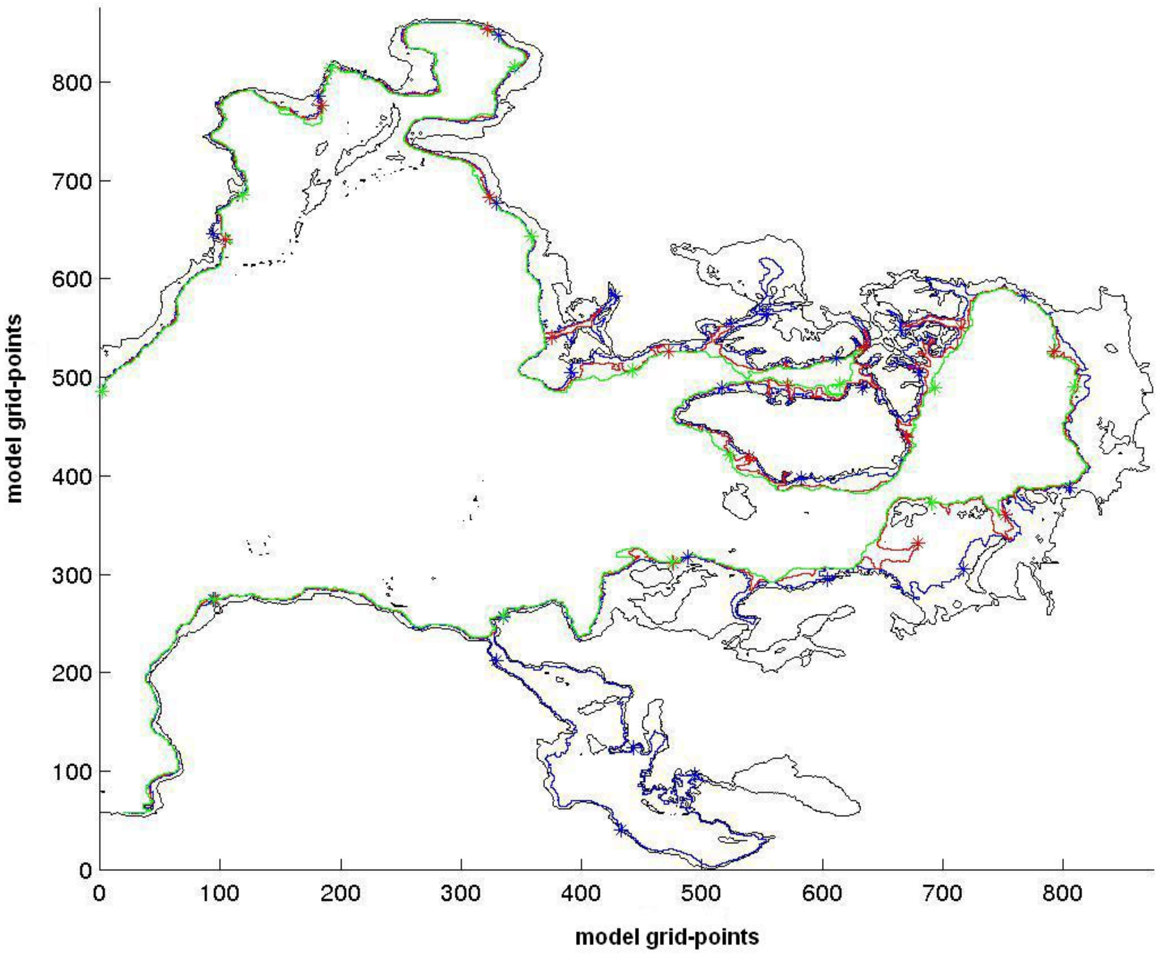

Figure 4.1: *Depth contours on extended grid at 201m,355m,605m with stars every 5000 km along boundary.*

All contours then make a loop around the outer edges of the Arctic before returning to the North Atlantic along the eastern Greenland coast. The contour at 201m makes a large loop through the Canadian Archipelago before reaching the Greenland slope. The contours remain reasonably close and are unaffected by the Lomonosov and Mendeleyev ridges, although they separate at the St Anna Trough, Chukchi plateau, and the Canadian Archipelago.

The dynamic height fields following these contours are shown in figures 4.2A,B,C. The first dynamic height field, at 201m, shows the highest pressure occurs in the southern Barents Sea. And there is then a large drop in pressure all the way up to the slope of the Chukchi Sea. This is the part of the slope in which the model has a boundary current at the slope which reaches to the surface. The surface signal of the boundary current is lost on the eastern Chukchi slope. This is due to a strong westward surface current as part of the Beaufort Gyre, which coincides with the reversal of the pressure gradient seen in figure 4.2A. Further along the contour there is a pressure rise in the direction of the East Greenland Current. This is due to the fact that the East Greenland Current is not above the slope at a depth of 201m, but forms a surface current further offshore. The lowest pressure is found further along the slope in the region of Cape Hatteras, after which there is an enormous pressure rise up to the Florida coast associated with the Gulf Stream.

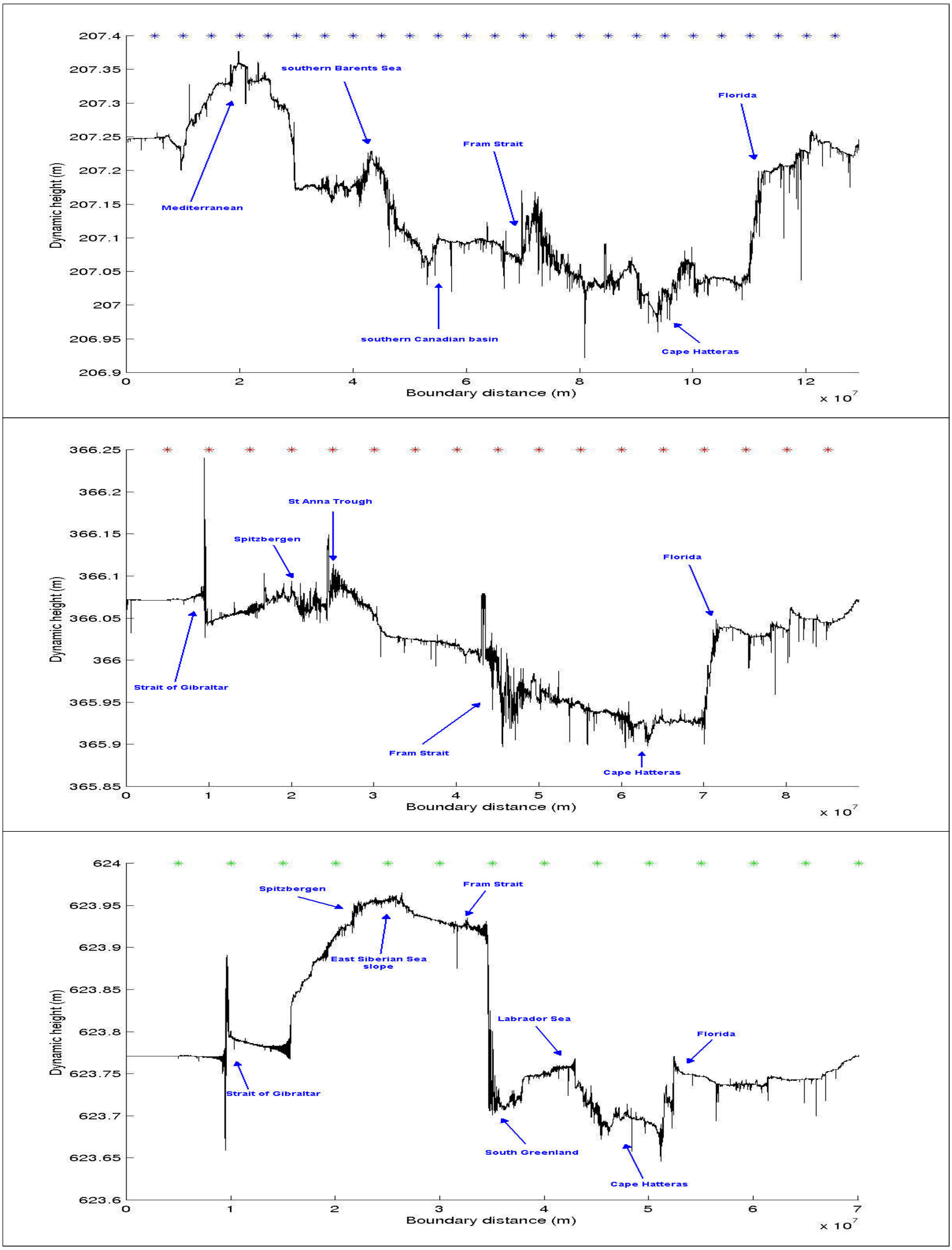

Figure 4.2: *Annual mean boundary dynamic height (A) 201m (B) 355m (C) 605m.*

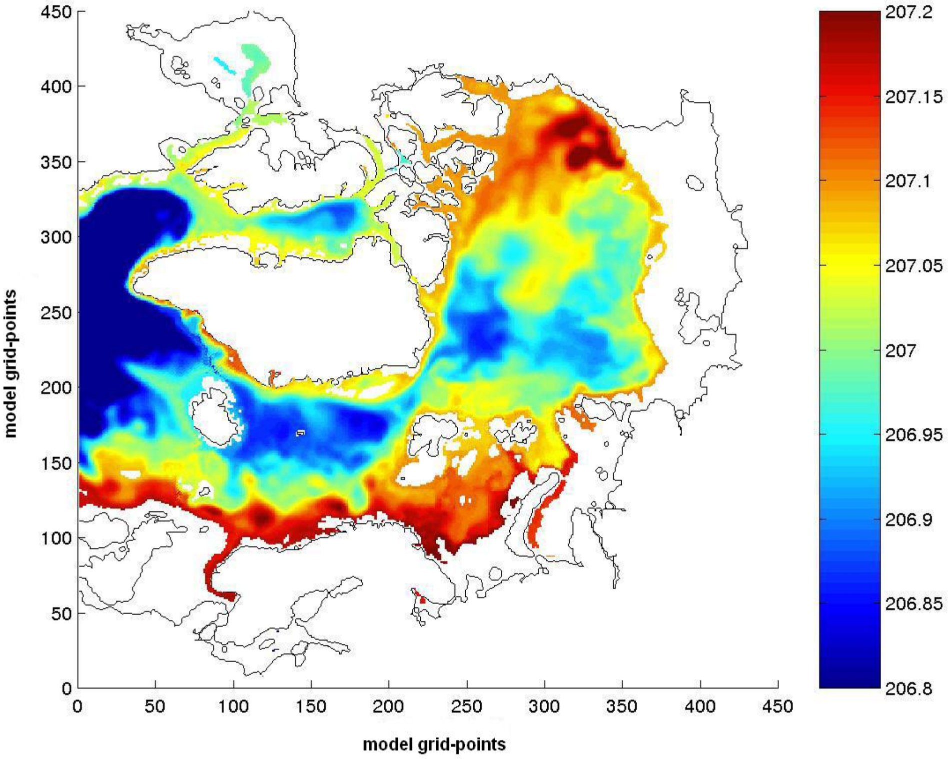

Figure 4.3: *Annual mean dynamic height at 201m.*

The dynamic height field at 355m shows the highest pressure occurs in the southern edge of the St Anna Trough. There is patchy pressure signal along the northern Barents Sea slope, where part of the AW makes it past the front north of Fram Strait (see figure 3.5) and flows eastwards along the boundary. The large pressure drop only starts from within St Anna Trough and is almost continuous until the low pressure found at Cape Hatteras. There are some large pressure variations in the region of the East Greenland Current, which could be due to the instabilities found on the interface of the East Greenland Current and the West Spitsbergen Current (Aksenov and Coward 2001).

The dynamic height field at 605m shows a large rise in pressure along the first part of the Eurasian slopes. This is associated with a reasonably weak undercurrent, which occurs at some places on the slope and extends over depths of 600-3000m flowing westwards and is shown in figure 4.4. This could be due to the fact that the wedge of AW and BSW entering the deep basin depresses the isopycnals at the slope, which has been observed by Schauer et al (1997) on the Kara Sea slope. This could lead to a reversal of the deep current due to sea surface height changes related to the surface forcing. However in the model the negative pressure gradient starts west of Greenland, where the continuation of the Gulf Stream reaches the eastern boundary of the North Atlantic. This figure also shows the intrusion of AW on the Fram Strait pathway flowing eastwards along the slope. The highest pressure is found past the Chukchi slope. There is then a general pressure drop towards Fram Strait, which coincides with the weak eastwards undercurrent. There is a huge pressure drop in the region of the East Greenland Current, as the core of this current is on the boundary at 605m.

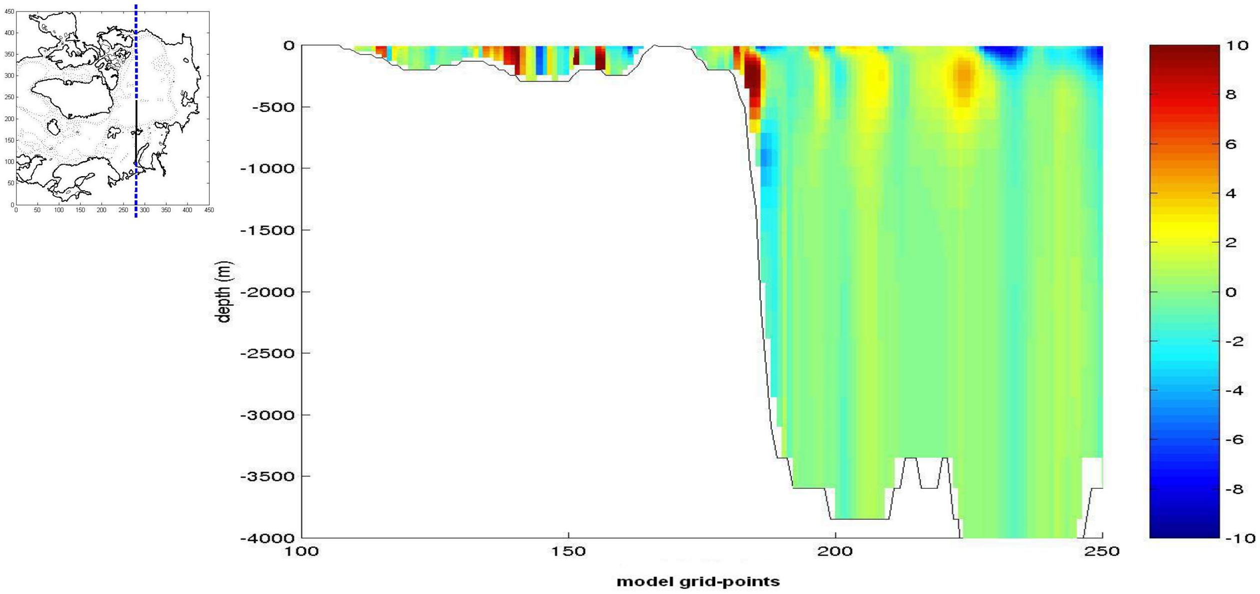

Figure 4.4: *Annual mean velocity (cm/s) on model longitude section (i=280).*

The high pressure signal occurring in/near the Barents Sea along the two shallower contours indicates the presence of relatively dense waters on the shelf. The continuous pressure gradient all the way into the North Atlantic is then a sign that these waters are involved in forming the boundary current. The downstream pressure gradient along the circumpolar boundary current is similar to the one found along the Gulf Stream. There potential energy is created in the centre of the basin by Ekman convergence and warming and is converted to kinetic energy as it is accelerated by the downstream pressure gradient (Bray and Fofonoff 1981).

The low pressure region coincides with the location where the Deep Western Boundary Current crosses under the Gulf Stream at Cape Hatteras, where low pressure could be caused by entrainment of DWBC water into the Gulf Stream or instabilities in the Gulf Stream.

Figure 4.3 shows the horizontal dynamic height field at 201m. The highest pressures occur in the coastal regions of the Barents Sea where a lot of bottom water is formed (Middtun 1985). There are also high pressure regions in the Beaufort Gyre due to Ekman convergence, which causes anti-cyclonic flow. The continuous offshore pressure gradient indicates geostrophic flow all around the slope up to the Canadian Basin. In the next section we look further at the water fluxes causing the high pressure region in the Barents Sea.

4.3 Barents Sea shelf waters

Here we look at what water mass causes the high pressure on the boundary in the St Anna Trough, and how it flows into the Arctic Ocean interior. Atlantic Water flows into the St Anna Trough from the Barents Sea as seen in the surface properties in figure 3.5 and in the stream function figure 3.7A. This is one of the two branches of AW entering the Arctic. However the boundary pressure increase at 355m in the St Anna Trough indicates the BSW water mass flowing through the St Anna Trough into the Arctic Ocean has undergone severe changes relative to the AW flowing through Fram Strait.

Figure 4.5A shows the St Anna Trough area on the model grid, which is subdivided into 16 boxes. Water flows into the trough from the Barents Sea through boxes 1, 2 and 5, and there is also a smaller inflow from the Kara Sea through boxes 2, 3, 4, 8, and 12. The annual mean of the net inflow of water into the southern boxes of the trough is 1.7 Sv, leaving 0.7 Sv of the original AW on the Barents Sea branch to flow into the Kara Sea. The AW on the Fram Strait pathway flows past the northern side of the trough in boxes 9,10, and 13. The outflow of both water masses is eastwards through box 15. Figure 4.5B shows potential temperature-salinity plots of the water in box 2 (where the largest inflow of BSW occurs) and box 15. The cores of AW and BSW in the model have very similar temperature and salinity properties, the BSW is colder and slightly fresher than AW. However density at low temperatures is mainly determined by salinity, therefore it is difficult to distinguish AW and BSW by density properties. To be able to separate AW and BSW by a single property we look at spiciness of which contours are also drawn in figure 4.5B.

Spiciness (τ) is an oceanographic variable introduced by Jackett and McDougall (1985). The variation of spiciness along isopycnals is defined to be proportional to $\int_\rho \beta dS$, where β is the saline contraction coefficient. Therefore along isopycnals

$$\int_\rho \mathrm{d}\tau = \int_\rho 2\beta \mathrm{dS}. \tag{4.3}$$

This variable is a well-defined, single-valued function of potential temperature (θ) and salinity and is independent of the scale of the $\theta - S$-diagram. τ is a conservative property as θ and S are both conserved under adiabatic change. The spiciness is calculated using a polynomial expression with coefficients a_{ij} following Jackett and McDougall (1985)

$$\tau = \sum_{i=1}^{5} \sum_{j=1}^{5} a_{ij} \theta^{i-1} S^{j-1}, \tag{4.4}$$

which gives an accurate estimation. A relatively high value of spiciness indicates a warm and salty water mass, whereas a relatively low value of spiciness indicates a cold and fresh water mass.

The core of the BSW has the potential temperature and salinity properties $1.8 - 3.2°C$ and $34.4 - 34.8$ PSU. The T-S plot of box 15 also includes BSW and very cold and fresh Polar Surface Water. The core of the AW has the properties $2.5 - 4.0°C$ and $34.2 - 35.0$ PSU. The cores of both AW and BSW have potential densities (referenced to 425m) very close to $1029.6 kg/m^3$, but the spiciness of both water masses is different. BSW has a typical spiciness of 23.6, while AW has a typical spiciness of 23.9. The BSW is therefore typically colder and fresher than AW, which is what we expect with the annual mean air-sea fluxes shown in figure 3.2.

The largest air-sea fluxes occur in the central Barents Sea, which is where we expect BSW to be formed. A model longitude section of the potential density anomaly through the central Barents Sea is shown in figure 4.6A. This shows the relatively unstratified BSW, compared to AW over a similar depth, on the shelf in the Barents Sea. The model shows AW on the continental slope covered by an insulating light surface layer. A typical column of BSW in the central Barents Sea has potential density anomalies (σ_{425m}) ranging from 29.6 to 29.7 between the surface and 201m (with potential temperature ranging from 2.7 to $2.4°C$ and salinity ranging from 34.6 to 34.7 PSU). The AW on the continental slope only reaches similar potential density anomalies below 600m. The water column on the slope has potential density anomalies ranging from 29.2 to 29.6 between the surface and 605m (with potential temperature ranging from 0.5 to $4.4°C$, and salinity ranging from 33.9 to 34.9 PSU). This indicates that BSW has the possibility to spread over a large range of depths on the slope as it reaches the Nansen Basin.

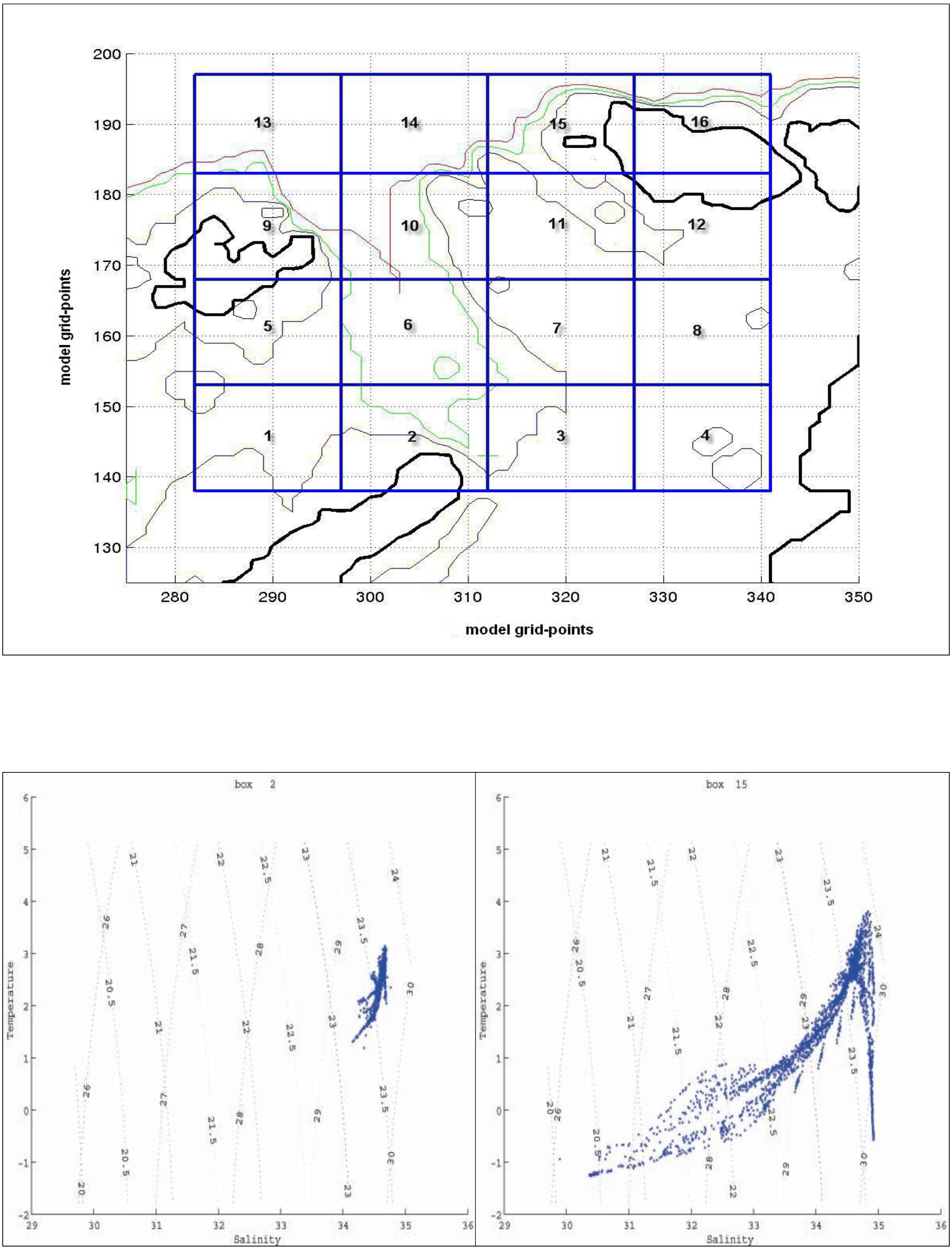

Figure 4.5: *(A) St Anna Trough box division with depth contours at 201m (blue),355m (green),605m (red). (B) Potential temperature-Salinity diagrams for boxes 2 and 15*

The potential density anomaly section also shows the isopycnals rising at the surface towards the slope, and declining at the bottom towards the slope. Schauer et al (1997) only observe this at offshore sections further east on the Kara Sea slope, which they attribute to the large intrusion of relatively unstratified BSW on the slope. This suggests the core of the AW in the model is also relatively unstratified compared to the ocean interior, and the flux of AW is large enough to displace the isopycnals at the slope.

To look at the flows and interaction of AW and BSW within the St Anna Trough figure 4.7 shows volume fluxes of spiciness classes through each box. BSW with a typical spiciness of 23.6 enters the St Anna Trough through boxes 1 and 2 at depths between 76-201m. The BSW then continues northwards along the eastern part of the trough (as described by Rudels et al (1999)) into box 6 via boxes 2-3-7 and reaches box 10 at depths between 102-508m. The net fluxes along the way indicate shelf waters mixing with each other. The AW with a typical spiciness of 23.9 can be seen flowing into the trough via boxes 9 and 10. There are large net spiciness fluxes in box 10 indicating mixing between AW,BSW and ambient waters, which evens out the spiciness distribution before flowing out through boxes 13 and 14. Further eastwards along the slope the large area under the curve of the outward flux in box 15 shows the increase in the boundary current strength compared to boxes 9 and 13. The intrusion of AW into the trough can be seen in figure 4.6B, where a large swirl of warm water enters at 245m from the North.

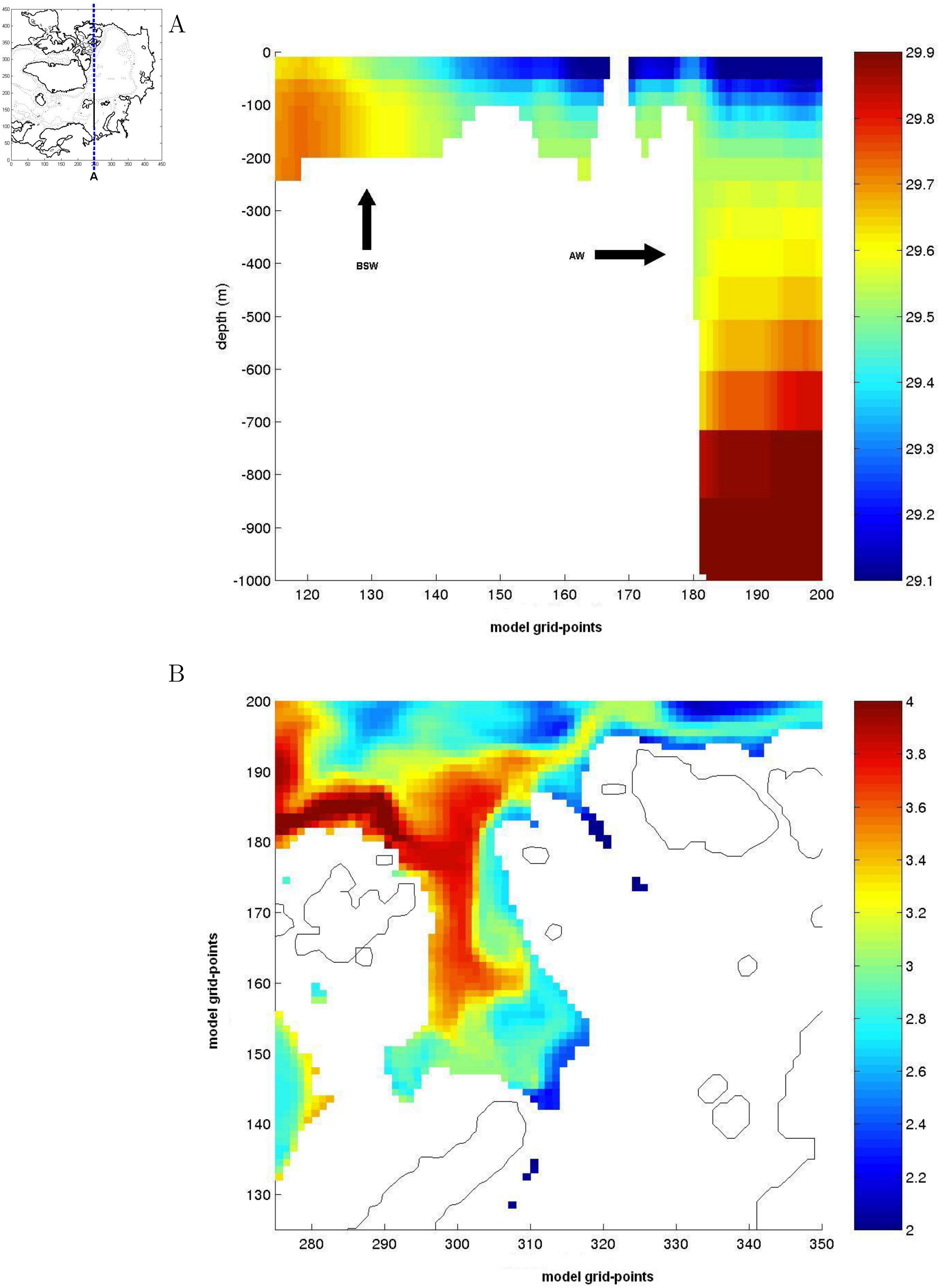

Figure 4.6: *(A) Depth-model latitude (i=250) section of potential density anomaly (kg/m^3) referenced to 425m. (B) Potential temperature (°C) at 245m. In top corner position of section A is shown.*

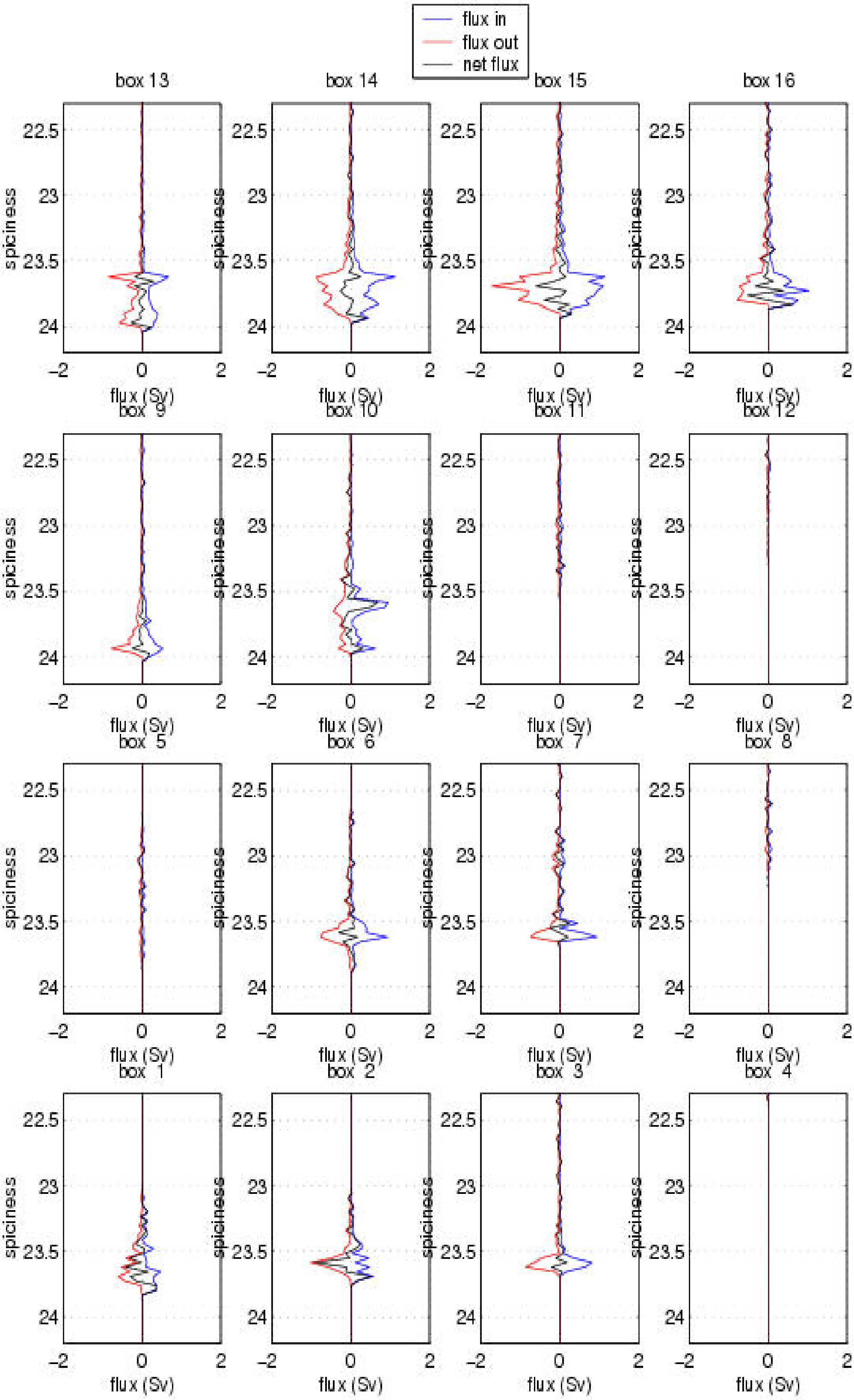

Figure 4.7: *Spiciness fluxes* ($10^6 m^3$) *through St Anna Trough boxes.*

4.4 Small-scale pressure variations

The boundary pressures in figures 4.2A, B, C show continuous small-scale variations in pressure. Partly these variations are due to convolutions in the boundary pathway, however the variations also occur on straight coastlines. The variations could be due to numerical noise associated with time-dependence, however they occur in the annual mean dynamic height in which we expect such noise to be relatively small. The annual mean datasets are calculated from a set of 36 10-daily instantaneous datasets, and therefore the noise should be reduced by a factor of order $\sqrt{36} = 6$. Also similar variations occur in the instantaneous datasets, therefore we look at other possibilities causing the pressure variations.

Figure 4.8A shows a short piece of straight coastline at level 355m, together with the boundary pathway at 508m, and the dynamic height on the boundary at 355m. The dynamic height variations along this coastline are of the order of several cm's, which is similar to the small-scale structure seen in figures 4.2A, B, C. Figure 4.8A shows some evidence of higher pressure in the presence of a deeper topographical feature (where the boundary at 508m extends offshore). Figure 4.8B shows horizontal contours of dynamic height at 355m in the same area. This suggests geostrophic flow around the deeper topographical features, which is also indicated by f/H contours given in figure 4.9B.

In order to understand the dynamics we can look at the balance of the terms in the alongshore direction of the momentum equation in the OCCAM model (3.1). The first term in (3.1) should be small in the annual mean and is ignored. The second, third, fourth, fifth and sixth terms are the horizontal advection, vertical advection, Coriolis force, pressure gradient, and diffusion. The diffusion is further divided by (3.7), where the first and second terms are the horizontal and vertical diffusion. The vertical advection and vertical diffusion terms are several orders smaller than the others and are also ignored here. The remaining four terms along the boundary at 355m are shown in figure 4.9A. In order to properly balance these terms on the Arakawa B grid we have to take the pressure as the mean of the first two offshore pressure grid points. The momentum balance is almost in completely geostrophic, whereby the pressure gradient balances the Coriolis force, and doesn't provide much information on the dynamics causing the pressure variations. However there is evidence that the a-geostrophic terms become larger (not shown) near the topographical feature acting to slow down the alongshore flow. Also the OCCAM model has a bottom friction force working to decelerate the alongshore flow on the bottom level of the water column, which only acts on the coastline at three points (i=348,349,354). So there is some evidence that there is blocking at the coast due to topographical features causing off/on-shore flow, and creating pressure variations on the coast.

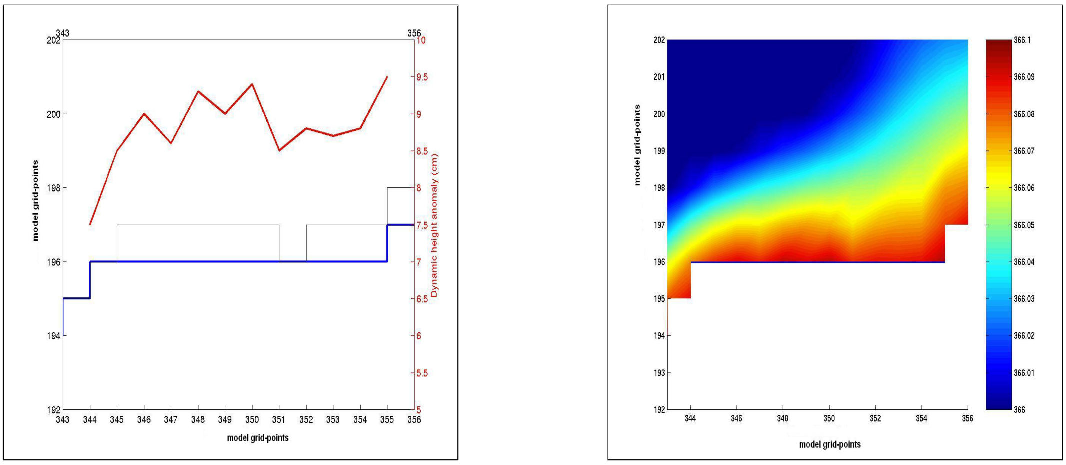

Figure 4.8: *(A) Boundary pathways at 355m (thick blue line) and 508m (thin black line) corresponding to axis on left, and dynamic height (cm) along boundary at 355m (in red) corresponding to axis on right (B) Horizontal dynamic height contours at 355m.*

Such blocking has been found in experimental and theoretical studies by Griffiths and Linden (1983), who have performed experiments with homogeneous fluids flowing over slowly varying 3D obstacles in the presence of a wall on the right-hand side of the alongshore flow. They find a large blocked region above the topographical obstacle which is what they expect from theoretical analysis, and coincides with the formation of a Taylor column. They find that the blocking only occurs for small Rossby numbers $Ro = V/fl$, which represents the importance of rotation in the flow. In the Arctic the Coriolis parameter is relatively large so we have a small Rossby number. Therefore this could be an explanation for the effect of topographical features on the alongshore flow we see, especially as the Arctic Ocean is relatively unstratified so Taylor columns can form over the full depth of the water column, although the OCCAM model has steps in topography rather than continuously varying topography. In this case the analytical solutions of Griffiths and Linden (1983) break down, although topographical blocking is known to occur in OCCAM.

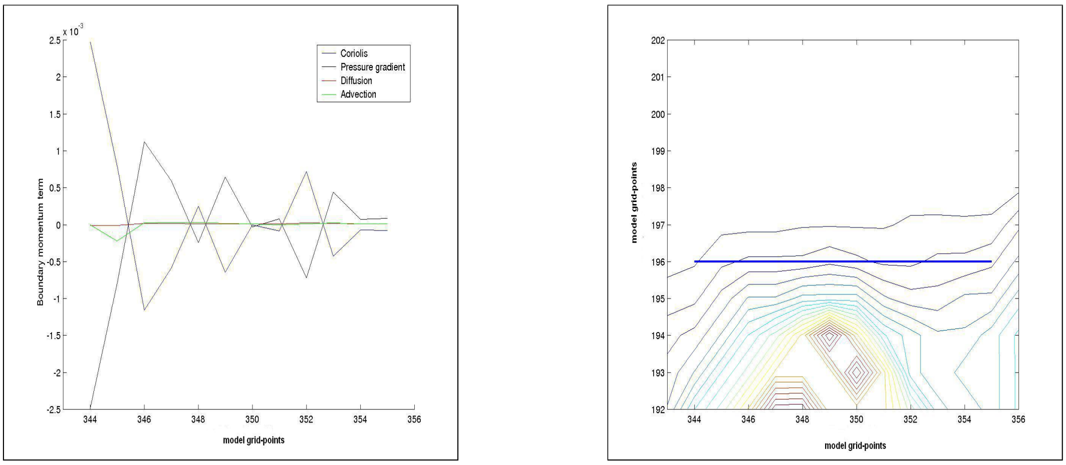

Figure 4.9: *(A) Momentum budget (terms multiplied by boundary step (dx) in* m^2/s^2*) along small section of 355m boundary (B)* f/H *contours and boundary at 355m (thick blue line).*

Chapter 5

Particle tracking - theory

5.1 Introduction

Here we introduce a method for tracing water masses that we use to determine properties of the flows in the Arctic Ocean. The main objectives are to define the pathways and time-scales for Atlantic and Pacific Water to flow through the Arctic and reach the North Atlantic. The pathways of AW will allow us to determine the origin of the density flux in the Barents Sea, and look at the interaction of the two pathways of AW at the St Anna Trough. The pathways of PW will allow us to determine whether the Bering Strait outflow is linked to the strong eddy-field in the Canadian Basin.

Döös (1995) and Blanke and Raynaud (1997) first introduced a fast and accurate method for calculating 3D time-independent trajectories of water particles. The method uses the time-averaged output of velocity from an ocean model to calculate particle trajectories off-line. This provides a much more fast and efficient method than calculating time-dependent trajectories online (ex. Maslowski et al 2000), which requires a huge amount of computer time. Therefore this method is very useful for calculating long trajectories of a large number of particles. The method is flux-conserving, making it possible to calculate volume transports of each trajectory. Other advantages of this method are the ability to follow the changes in the water mass properties along the trajectories, and the ability to calculate trajectories backwards in time.

However for studying the influence of shelf waters in the Arctic Ocean we require time-dependent trajectories to include the seasonal variations, and to reproduce meso-scale activity. Time-dependence also has the advantage of preventing particles getting stuck in stationary eddies. Blanke et al (1999) include time-dependence by using a series of monthly velocity fields. They use the original time-independent method, while keeping the velocity constant over the sample time. Here we use a more accurate method by adapting the time-independent method to use interpolation in time between two sequential velocity field samples. We also include a representation of the random diffusive effects experienced by water particles in the real ocean.

The analytical solutions for time-dependent trajectories may be derived in the same way as for time-independent trajectories, as published previously by Döös and de Vries (2001). These authors verified the accuracy of the method by calculating trajectories in an idealized 2D gyre. For the present study we have adapted the original time-independent code in order to calculate time-dependent particle trajectories which include diffusive effects.

We first describe the time-independent method introduced by Döös (1995) and Blanke and Raynaud (1997). In the following section we discuss the alterations of the method, and derive the solutions for time-dependent trajectories. Then we discuss the representation of the random diffusive effects, and the implementation of these in the new method.

5.2 Time-independent method

In the time-independent approach a 3D trajectory is calculated within a model grid-box by considering each of the three spatial directions individually. In each direction a particle can exit through two faces of the grid-box. The crossing time needed for a particle to exit through each face is calculated by interpolating the transports through each face. The minimum crossing time of all 6 faces of the grid-box then gives the face through which the particle will exit. Its position in the other two dimensions is calculated to give the exact 3D position of the particle. The trajectory is then formed by following the particle jumping through grid-boxes. As the velocity field is non-divergent this leads to a flux-conserving trajectory.

We will consider the crossing times in the x-direction for a particle in a grid-box with dimensions $(\Delta x, \Delta y, \Delta z)$. The local transports through the two faces in the x-direction of the grid-box are given by $U_{i-1} = \Delta y \Delta z u_{i-1}$ and $U_i = \Delta y \Delta z u_i$. We use the transformed coordinate for position (in non-dimensional units) and time (in units of s/m^3)

$$r_i \;=\; \frac{x_i}{\Delta x} \quad \text{and} \quad s = \frac{t}{\mathit{\Delta} x \mathit{\Delta} y \mathit{\Delta} z}. \tag{5.1}$$

The transport inside the grid-box is then estimated using linear interpolation in space

$$U(r,s) \;=\; (1 - [r - r_{i-1}])U_{i-1} + \; [r - r_{i-1}]\, U_i. \tag{5.2}$$

This can be rewritten in the following form

$$U(r,s) = -\beta r - \delta, \qquad \beta = (U_{i-1} - U_i), \qquad \delta = -U_{i-1} + r_{i-1}(U_i - U_{i-1}). \tag{5.3}$$

Now an equation for particle motion within the grid-box is formed by setting the local transport $U(r,s)$ equal to the time derivative of the position

$$\frac{dr}{ds} + \beta \cdot r + \delta = 0, \quad r(s_0) = r_0. \tag{5.4}$$

Here s_0 and r_0 give the initial time and initial position of the particle in the grid-box.

The solution of equation (5.4) is given by

$$r(s) = \left[r_0 + \frac{\delta}{\beta}\right] \exp\left(-\beta(s - s_0)\right) - \frac{\delta}{\beta}. \tag{5.5}$$

The crossing times for the particle through the faces at r_{i-1} and r_i are then calculated. The crossing time through the r_{i-1} is calculated by solving

$$r(s) = r_{i-1}. \tag{5.6}$$

The solution can be calculated analytically, and is given by

$$s = s_0 - \frac{1}{\beta} \ln\left[\frac{r_{i-1} + \delta/\beta}{r_0 + \delta/\beta}\right]. \tag{5.7}$$

.

In the next section we extend this method for time-dependent trajectories by using bilinear interpolation in space and time. The main difference is that the solutions for the crossing times must be calculated numerically.

5.3 Time-dependent method

Here we present the derivation of the solutions for time-dependent trajectories, which was performed independently from Döös and de Vries' derivation (2001). This derivation is presented in similar notation as introduced by Döös and de Vries (2001) for comparison purposes. We describe the numerical implementation for use with time-sampled velocity fields from the OCCAM global ocean model in Appendix A.

We consider the trajectory in the time interval $[s_{n-1}, s_n]$. Then the equivalent expression to (5.2) for bilinearly interpolated transport inside a grid-box is

$$U(r,s) \quad = \quad (1 - [r - r_{i-1}])(1 - \left[\frac{s - s_{n-1}}{s_n - s_{n-1}}\right])U_{i-1,n-1} \tag{5.8}$$

$$+ \quad [r - r_{i-1}] \cdot (1 - \left[\frac{s - s_{n-1}}{s_n - s_{n-1}}\right])U_{i,n-1} \tag{5.9}$$

$$+ \quad \left[\frac{s - s_{n-1}}{s_n - s_{n-1}}\right] \cdot (1 - [r - r_{i-1}])U_{i-1,n} \tag{5.10}$$

$$+ \quad [r - r_{i-1}] \cdot \left[\frac{s - s_{n-1}}{s_n - s_{n-1}}\right] U_{i,n}. \tag{5.11}$$

This can be rewritten in the following form

$$U(r, s) = -\alpha \cdot r \cdot s - \beta \cdot r - \gamma \cdot s - \delta, \tag{5.12}$$

where the constants are given by

$$\alpha = -\frac{1}{s_n - s_{n-1}} \cdot (U_{i-1,n-1} - U_{i-1,n} - U_{i,n-1} + U_{i,n}), \tag{5.13}$$

$$\beta = U_{i-1,n-1} - U_{i,n-1} - \alpha \cdot s_{n-1}, \tag{5.14}$$

$$\gamma = -\frac{1}{s_n - s_{n-1}} \cdot (U_{i-1,n} - U_{i-1,n-1}) - \alpha \cdot r_{i-1}, \tag{5.15}$$

$$\delta = -U_{i-1,n-1} + r_{i-1} \cdot (U_{i,n-1} - U_{i-1,n-1}) - \gamma \cdot s_{n-1}. \tag{5.16}$$

Now an equation for particle motion within the grid-box is formed by setting the local transport $U(r, s)$ equal to the time derivative of the position

$$\frac{dr}{ds} + \alpha \cdot r \cdot s + \beta \cdot r + \gamma \cdot s + \delta = 0, \quad r(s_0) = r_0. \tag{5.17}$$

Here s_0 and r_0 give the initial time and initial position of the particle in the grid-box.

Equation (5.17) can be solved using the Lagrange variation of constants method, by rewriting it as

$$\frac{dr}{ds} = A(s)r + B(s), \tag{5.18}$$

where $A(s) = -\alpha s - \beta$ and $B(s) = -\gamma s - \delta$. The general solution of equation (5.18) is given by

$$r(s) = r_0 \exp(\int_{s_0}^{s} A(\rho)d\rho) + \int_{s_0}^{s} B(\rho) \exp(\int_{\rho}^{s} A(\eta)d\eta)d\rho. \tag{5.19}$$

For $\alpha = 0$ this gives

$$r(s) = r_0 \exp\left(-\beta(s - s_0)\right) + \frac{1}{\beta^2}[\gamma + \gamma s\beta + \delta\beta + [\gamma - \gamma s_0\beta - \delta\beta]e^{-\beta(s-s_0)}]. \tag{5.20}$$

For $\alpha \neq 0$ the two exponential terms in (5.19) are

$$\begin{aligned}
\exp(\int_{s_0}^{s} A(\rho)d\rho) &= \exp(\int_{s_0}^{s}(-\alpha\rho - \beta)d\rho) = \exp\left(-\frac{1}{2}\alpha s^2 - \beta s + \frac{1}{2}\alpha s_0^2 + \beta s_0\right), && (5.21)\\
\exp(\int_{\rho}^{s} A(\eta)d\eta) &= \exp(\int_{\rho}^{s}(-\alpha\eta - \beta)d\eta) = \exp\left(-\frac{1}{2}\alpha s^2 - \beta s + \frac{1}{2}\alpha\rho^2 + \beta\rho\right). && (5.22)
\end{aligned}$$

The second integral in (5.19) is then given by

$$\begin{aligned}
\int B(\rho)\exp(\int_{\rho}^{s} A(\eta)d\eta)d\rho &= \int(-\gamma\rho - \delta)\exp\left(-\frac{1}{2}\alpha s^2 - \beta s + \frac{1}{2}\alpha\rho^2 + \beta\rho\right)d\rho && (5.23)\\
&= -\int \gamma\rho\exp\left(-\frac{1}{2}\alpha s^2 - \beta s + \frac{1}{2}\alpha\rho^2 + \beta\rho\right)d\rho && (5.24)\\
&- \int \delta\exp\left(-\frac{1}{2}\alpha s^2 - \beta s + \frac{1}{2}\alpha\rho^2 + \beta\rho\right)d\rho.
\end{aligned}$$

This can be rewritten to get a simpler expression for the solution by introducing $\mu = \alpha\rho + \beta\sqrt{2\alpha}$ and $\xi = \alpha s + \beta\sqrt{2\alpha}$. Then integral (5.23) becomes

$$\begin{aligned}
\int B(\rho)\exp(\int_{\rho}^{s} A(\eta)d\eta)d\rho &= -\frac{\gamma}{\alpha}\exp\left(-\xi^2 + \mu^2\right) - e^{-\xi^2}\frac{\beta\gamma\sqrt{2}}{\alpha\sqrt{\alpha}}\int_0^{\mu}\exp(x^2)dx && (5.25)\\
&- \delta\sqrt{2}\sqrt{\alpha}\exp(-\xi^2)\int_0^{\mu}\exp(x^2)dx.
\end{aligned}$$

For $\alpha > 0$ this gives the solution of (5.17)

$$\begin{aligned}
r(s) &= [r_0 + \frac{\gamma}{\alpha}]\exp\left(-\xi^2 + \xi_0^2\right) && (5.26)\\
&- \frac{\gamma}{\alpha} + \frac{(\beta\gamma - \alpha\delta)}{\alpha}\sqrt{\frac{2}{\alpha}}[D(\xi) - \exp\left(-\xi^2 + \xi_0^2\right)D(\xi_0)],
\end{aligned}$$

where $D(\xi)$ is Dawson's integral

$$D(\xi) = \exp(-\xi^2)\int_0^{\xi}\exp(x^2)dx. \tag{5.27}$$

For $\alpha < 0$ parameter ξ is complex

$$\xi = \alpha s + \beta i\sqrt{-2\alpha} = -i(\alpha s + \beta\sqrt{-2\alpha}). \tag{5.28}$$

In this case the solution can be rewritten using

$$\int_0^{\xi} \exp(x^2)dx = -i\int_0^{i\xi} \exp(-x^2)dx = -i\frac{\sqrt{\pi}}{2}\mathrm{erf}(\mathrm{i}\xi), \tag{5.29}$$

where $\mathrm{erf}(\xi)$ is the error function

$$\mathrm{erf}(\xi) = \frac{2}{\sqrt{\pi}}\int_0^{\xi} \exp(-x^2)dx. \tag{5.30}$$

The solution for $\alpha < 0$ of (5.17) is then

$$\begin{aligned} r(s) &= [r_0 + \frac{\gamma}{\alpha}]\exp\left(-\xi^2 + \xi_0^2\right) \qquad (5.31) \\ &- \frac{\gamma}{\alpha} - \frac{(\beta\gamma - \alpha\delta)}{\alpha}\sqrt{\frac{\pi}{-2\alpha}}\exp(-\xi^2)[\mathrm{erf}(\mathrm{i}\xi) - \mathrm{erf}(\mathrm{i}\xi_0)]. \end{aligned}$$

The crossing time for the particle through the face at r_{i-1} is then calculated by solving

$$r(s) = r_{i-1}. \tag{5.32}$$

In this case the solution of (5.32) must be calculated numerically due to the integrals in the function $r(s)$. The equation is solved using the Newton-Raphson root-finding algorithm. A description of the solution process is given in Appendix A. The accuracy of the code has been verified using constant velocity fields (in which $\alpha = 0$), and by comparing short-term backward and forward trajectories.

5.4 Diffusive effects

Water particles in the real ocean are subject to turbulent stresses and collisions with other particles. Therefore a particle's displacement after a certain time-step t is partly determined by random movements. Our trajectories only include the implicit diffusion due to along-trajectory changes of temperature and salinity, and by the model's parameterization of turbulent mixing in the momentum equations. However fluid inside each parcel does not mix with the ambient fluid, so the trajectory does not explicitly represent sub-grid scale diffusion.

5.4.1 Brownian motion

The particles in our case are small water parcels, and we can describe the random movements of the particle using the theory of Brownian motion, which can be found in many texts (for example Csanady 1973). The equation usually used to describe the Brownian motions is Langevin's equation

$$\frac{\mathrm{d}\mathbf{u}}{\mathrm{d}t} = \mathbf{A}(t) - \beta\mathbf{u}, \tag{5.33}$$

where $\mathbf{u}$ is the particle velocity vector relative to the ambient fluid. The function $\mathbf{A}(t)$ represents the random acceleration due to the unresolved eddies, which we want to choose to match the Laplacian viscosity terms in the momentum equations.

The second term on the right hand side of equation (5.33) represents the viscous resistance from the surrounding fluid experienced by the water particles, where β is a constant (in units s^{-1}). The constant β depends on the size and mass (m) of the water parcel, and on the viscosity (η in m^2/s) of the ambient fluid. In the case of a spherical water parcel this constant is given by Stokes' law

$$\beta = \frac{6\pi a\eta\rho}{m}, \tag{5.34}$$

where a and ρ are the radius and density of the water parcel. This can also be written in terms of the volume $V = (4/3)\pi a^3$ of the spherical particle

$$\beta = \frac{6\pi a\eta\rho}{\rho V} = \frac{8\eta}{a^2}. \tag{5.35}$$

As the water parcels are injected into the ocean they represent a small section of the transport. Therefore their volumes are infinitesimally small ($a \mapsto 0$), and β is infinitely large.

The solution of (5.33) is given by

$$\mathbf{u(t)} = \mathbf{u_0}\exp(-\beta t) + \exp(-\beta t)\int_0^t \exp(\beta t')\mathbf{A}(t')dt', \tag{5.36}$$

where $\mathbf{u_0} = \mathbf{u}(o)$ is the initial velocity of the water parcel (relative to the ambient fluid). The first term on right-hand side of (5.36), representing the persistence of the initial velocity, decays for $t \gg \beta^{-1}$. The second term is the result of a large number of independent random kicks.

5.4.2 Random walk model

Here we formulate the displacement probability function $P(x, t)$ for each separate spatial direction. The total displacement of the water parcel in a time t in the x-direction is given by

$$x = \int_0^t \mathbf{u}(t')dt'. \tag{5.37}$$

As the initial velocity decays for time-steps $\Delta t \gg \beta^{-1}$, the total displacement can be divided into $N(= t/\Delta t)$ (almost) independent steps. In each step the effect of the persistence of the velocity from previous steps is negligible if Δt is large enough. Each step is taken independently, and at random, so the water parcel executes a random walk of N steps.

A simple random walk in one dimension consists of a number of steps of unit length, in which the probability of moving forward or backward is $\frac{1}{2}$. It can be shown (see Csanady 1973) that for large N the probability that a water parcel (starting at the origin) reaches a point m is given by the following discrete Gaussian distribution

$$P(m, N) = \sqrt{\frac{2}{\pi N}} \exp\left(-\frac{m^2}{2N}\right). \tag{5.38}$$

Here m must be even/uneven if N is even/uneven. Let l be the step length and $m = x/l$, where x is the displacement from the origin. Then the total probability of finding a particle over a range Δx is approximately $P(m, N)\Delta x/(2l)$. This gives the probability of a particle reaching point x

$$P(x,t) = \frac{1}{2\sqrt{\pi D t}} \exp\left(-\frac{x^2}{4Dt}\right), \tag{5.39}$$

where t is the time needed to take N steps, and $D = nl^2/2$. This is a Gaussian distribution with the mean and the standard deviation given by

$$\begin{aligned} \mu &= 0, & (5.40)\\ \sigma &= \sqrt{2Dt}. & (5.41) \end{aligned}$$

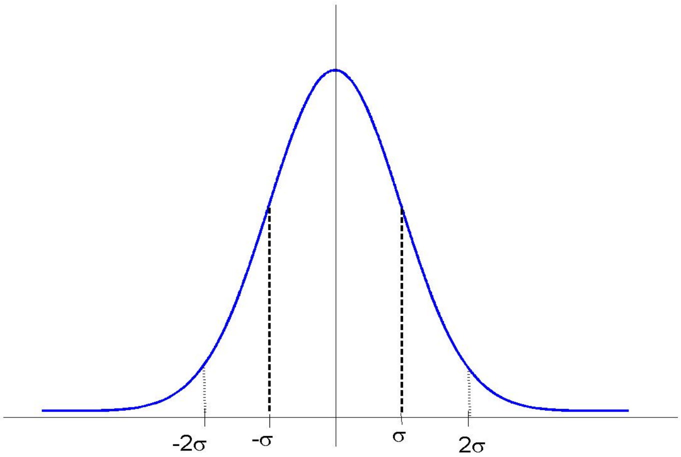

Figure 5.1: *Gaussian distribution* $P(x,t)$ *for 1D particle displacements, where* $\sigma = \sqrt{2Dt}$*. For this distribution* 68%/95% *of displacements are within range* $[-\sigma, \sigma]$ / $[-2\sigma, 2\sigma]$.

The Gaussian distribution represents an instantaneous source at the origin, which has the following limits

- for $t > 0$ fixed, $x \to \infty : P \to 0$,
- for x fixed, $t \to \infty : P \to 0$,
- for fixed $x \neq 0$, $t \downarrow 0 : P \to 0$,

- for fixed $x = 0$, $t \downarrow 0 : P \to \infty$

Also the distribution is normalized such that

$$\int_{-\infty}^{\infty} P(x,t)dx = 1. \tag{5.42}$$

The source(5.39) is a special solution of the 1D diffusion equation

$$\frac{\partial P}{\partial t} = D\frac{\partial^2 P}{\partial x^2}, \tag{5.43}$$

where D is the diffusion coefficient. This means that the random walk described is a diffusion process, which matches the Laplacian viscosity terms in the momentum terms of the OCCAM model. We therefore take D equal to the horizontal or vertical eddy viscosity, A_H and A_Z, so the random motions are on the scale of the model subgrid-scale turbulence.

5.4.3 Calculation of displacements

Here we describe the calculation of the displacements for each water parcel. The displacements in each of the three spatial directions are distributed by the $1D$ Gaussian (5.39), therefore each displacement is calculated separately. There are a large number of good algorithms available (ex. Press et al 1992) for generating uniform random numbers on the interval $[0,1]$

$$y \in [R]_0^1 . \tag{5.44}$$

The uniform distribution defines the probability of generating a number between y and $y + dy$ by

$$P(y)dy = dy \quad \text{for} \quad y \in [0,1] \tag{5.45}$$

$$P(y)dy = 0 \quad \text{for} \quad y \notin [0,1] . \tag{5.46}$$

Using a transformation of variables these uniform deviates can be used to generate random numbers following other distributions. The multi-dimensional transformation law of probabilities (eg. Feller 1950) is given by

$$P(x_1, x_2, \ldots, x_n)dx_1\, dx_2 \ldots dx_n = P(y_1, y_2, \ldots, y_n) \left| \frac{\partial(y_1, y_2, \ldots, y_n)}{\partial(x_1, x_2, \ldots, x_n)} \right| dx_1\, dx_2 \ldots dx_n. \tag{5.47}$$

For the uniform distribution on the interval $[0, 1]$ we have $P(y) = 1$, therefore in $1D$ we need to find a function $y(x)$ that satisfies the differential equation

$$\left| \frac{dy}{dx} \right| = P(x, t). \tag{5.48}$$

For $P(x, t)$ as in (5.39) the solution is given by

$$y(x) = \int_{-\infty}^{x} P(x', t)dx' \quad = \quad \frac{1}{2}\mathrm{erf}\left(\frac{x}{\sqrt{4Dt}}\right) + \frac{1}{2}, \tag{5.49}$$

where $\mathrm{erf}(x)$ is the error function as given in (5.30). This mapping is illustrated in figure 5.2.

The random deviates following distribution $P(x, t)$ are given by the inverse of (5.49)

$$x(y) = \sqrt{4Dt} \quad \mathrm{erf}^{-1} \quad (y - \frac{1}{2}). \tag{5.50}$$

This expression can be used to generate Gaussian deviates x from uniform deviates y, although the inverse of the error function (erf^{-1}) must be approximated numerically.

However in $2D$ a transformation has been introduced by Box and Muller (1958), which gives an expression for two Gaussian deviates that can be calculated analytically. A $2D$ Gaussian distribution for two independent deviates x_1 and x_2 distributed according to (5.39) is given by

$$P(x_1, x_2, t) = \frac{1}{\sqrt{4\pi Dt}} \quad \exp\left[\frac{-x_1^2}{4Dt}\right] \cdot \frac{1}{\sqrt{4\pi Dt}} \quad \exp\left[\frac{-x_2^2}{4Dt}\right]. \tag{5.51}$$

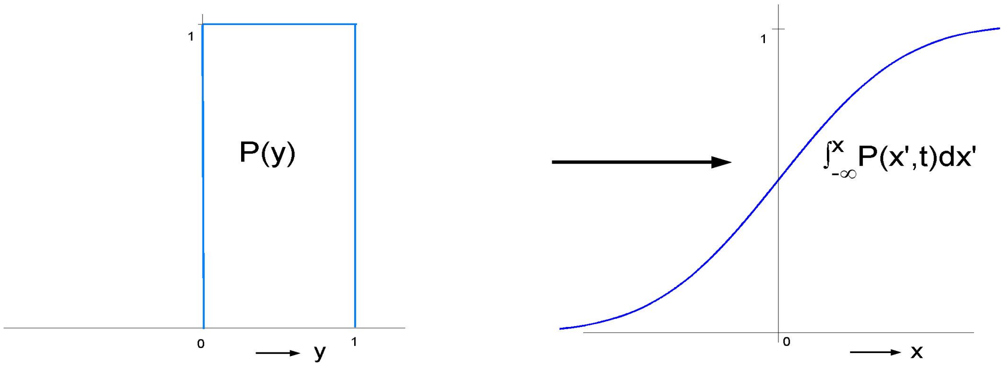

Figure 5.2: *Mapping (5.49) for generating 1D Gaussian deviates x from uniform deviates y.*

Given two uniform deviates $y_1, y_2 \in [R]_0^1$ we can use the transformation law (5.47) to generate two Gaussian deviates x_1 and x_2. In order for this we need transformations

$$y_1 = f_1(x_1, x_2), \tag{5.52}$$

$$y_2 = f_2(x_1, x_2), \tag{5.53}$$

such that

$$\left| \frac{\partial(y_1, y_2)}{\partial(x_1, x_2)} \right| = P(x_1, x_2, t). \tag{5.54}$$

This condition is satisfied by the following transformations, which are similar to those introduced by Box and Muller (1958)

$$f_1(x_1, x_2) \quad = \quad 1 - \exp\left[-\frac{x_1^2 + x_2^2}{4Dt} \right] \tag{5.55}$$

$$f_2(x_1, x_2) \quad = \quad \frac{1}{2\pi} \arctan\left[\frac{x_1}{x_2} \right]. \tag{5.56}$$

These transformations are invertible and give the following expressions for x_1 and x_2

$$x_1 = f_1^{-1}(y_1, y_2) = \sqrt{4Dt \log\left[1 - y_1\right]} \cos\left(2\pi y_2\right) \tag{5.57}$$

$$x_2 = f_2^{-1}(y_1, y_2) = \sqrt{4Dt \log\left[1 - y_1\right]} \sin\left(2\pi y_2\right). \tag{5.58}$$

Expressions (5.57) and (5.58) represent the x- and y-components of a point in the 2D plane with a distance of $\sqrt{4Dt \log\left[1-y_1\right]}$ from the origin, and an angle of $2\pi y_2$ with respect to the x-axis.

We use the transformations (5.57) and (5.58) once for the two horizontal displacements using two uniform deviates y_1 and y_2 and the horizontal eddy viscosity $D = A_H$. Then we repeat this process using two new uniform deviates y_3 and y_4 and the vertical eddy viscosity $D = A_Z$, and use only one of the resulting deviates. This leads to the following displacements

$$x_d = \sqrt{4A_H t \log\left[1-y_1\right]}\cos\left(2\pi y_2\right), \tag{5.59}$$

$$y_d = \sqrt{4A_H t \log\left[1-y_1\right]}\sin\left(2\pi y_2\right), \tag{5.60}$$

$$z_d = \sqrt{4A_Z t \log\left[1-y_3\right]}\cos\left(2\pi y_4\right), \tag{5.61}$$

which are added to to the position of the particle after each time-step of length t.

Previously a random walk model has been introduced in models for oil spill trajectories by Al-Rabeh and Gunay (1992) and Evans and Noye (1995). In these models the two horizontal dimensions are combined, and random jumps (x_d, y_d) are generated by choosing a point in the 2D plane. The distance from the starting point r_d, and the angle θ are chosen as uniformly distributed random numbers. The standard deviation of the horizontal displacement is chosen to be equal to the standard deviation of a 2D random walk

$$\sigma_{2D} = \sqrt{\sigma^2 + \sigma^2} = \sqrt{4Dt}, \tag{5.62}$$

where σ is the standard deviation found for the 1D random walk in (5.41).

For the vertical dimension Al-Rabeh and Gunay (1992) apply a 1D equivalent of this process, which we can compare to our 1D displacements. A uniform deviate in the range

$[-1, 1]$ is obtained using the following transformation

$$z = 2y - 1, \quad y \in [R]_0^1 . \tag{5.63}$$

The mean and standard deviation of z are given by

$$\begin{aligned} \mu(z) &= 2\mu(y) - 1 = 2\int_0^1 yP(y)dy - 1 = 0, & (5.64) \\ \sigma(z) &= 2\sigma(y) = 2\sqrt{\int_0^1 (y-\mu(z))^2 P(y)dy} = \frac{1}{\sqrt{3}}. & (5.65) \end{aligned}$$

The displacement z_d is then chosen such that its standard deviation is equal to (5.41), as found for the 1D random walk. This gives the displacement

$$z_d = \sqrt{3}\sigma z = \sqrt{6Dt}(2y - 1), \quad y \in [R]_0^1 , \tag{5.66}$$

which is distributed uniformly within the range $\left[-\sqrt{3}\sigma, \sqrt{3}\sigma\right]$.

The difference between our 1D displacements (5.59)-(5.61) and Al-Rabeh and Gunay's (1992) 1D displacement (5.66) is illustrated in figure 5.3. The former is a Gaussian bell curve which matches the Laplacian viscosity terms in the momentum equations, while the latter is represented by a rectangle. While the Gaussian distribution has 68%/95% of the displacements contained in the range $[-\sigma, \sigma]$ / $[-2\sigma, 2\sigma]$, the rectangle distribution has 100% of the displacements contained in the range $\left[-\sqrt{3}\sigma, \sqrt{3}\sigma\right]$.

We can approximate the magnitude of the diffusive jumps using an estimate of the time-step t needed to cross a grid-box. The dimension Δx of a horizontal grid box is approximately $14km$. A particle in a weak flow of $1cm/s$ will cross this grid box in approximately $10^6 s$. Therefore the standard deviation of the horizontal jumps is given by

$$\sigma = \sqrt{2A_H t} = 20km, \tag{5.67}$$

where A_H is equal to the horizontal eddy viscosity of $2 \cdot 10^6 cm^2/s$. Therefore in this case 68% of the jumps are within the range $[-20km, 20km]$, which is of the same order as the

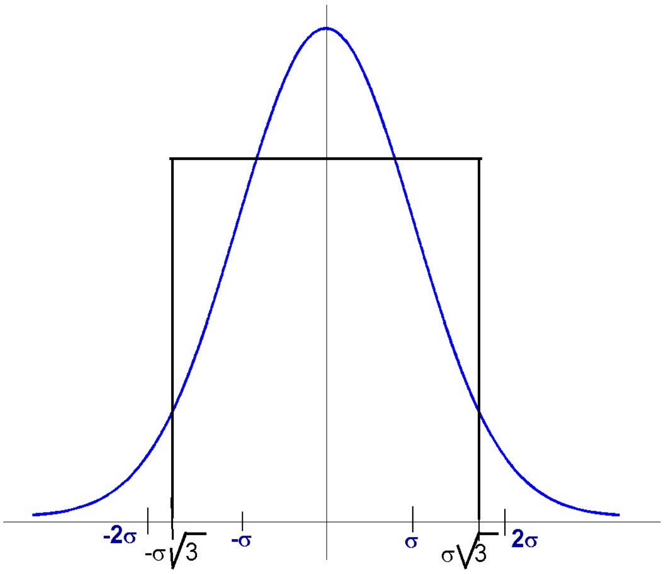

Figure 5.3: *Comparison of 1D probability distributions for particle displacements. Black: Distribution (5.66) as used by Al Rabeh and Gunay (1992). Blue: Distribution (5.39) with* $\sigma = \sqrt{2Dt}$.

horizontal grid-box size and gives us an upper estimate for the size of the horizontal random jumps.

The dimension Δz of a vertical grid box in the upper ocean is approximately $100m$. A particle in a weak flow of $10^{-4}cm/s$ will cross this grid box in approximately $10^8 s$. Therefore the standard deviation of the vertical jumps is given by

$$\sigma = \sqrt{2A_Z t} \approx 141m, \tag{5.68}$$

where A_Z is equal to the vertical eddy viscosity of 1 cm^2/s. Therefore in this case 68% of the jumps are within the range $[-141m, 141m]$, which is of the same order as the vertical grid-box size. This is a severe upper limit as the horizontal flow must be very weak for a particle to remain in the horizontal grid-box for $10^8 s$. For a more realistic crossing time t of $10^6 s$ the 68%

the range of vertical displacements is approximately $[-14m, 14m]$, which is smaller than the dimension of most vertical grid-boxes. Therefore any oscillations in the particle trajectories that are larger than the size of a horizontal or vertical grid-box are not likely to be caused by the random displacements.

Chapter 6

Particle tracking - application

6.1 Introduction

Here we apply the method described in the previous chapter to calculate pathways of shelf waters through the Arctic Ocean and assess their influence on the circulation. We start by comparing the time-independent, time-dependent, and diffusive time-dependent methods for pathways of Barents Sea Water. We then calculate pathways for the other inflows of Atlantic Water and Pacific Water. Also we assess time-scales for signals to propagate from the Barents Sea and Chukchi Sea shelves. These are two of the most important shelf seas as they directly receive and modify water from the Atlantic and Pacific Oceans.

Various observations on the Canadian side of the Lomonosov Ridge have shown the presence of AW and BSW (Schauer et al 1997, McLaughlin et al 2002). However the reach of the water masses could depend significantly on the phase of the Arctic Oscillation, as shown by Maslowski et al (2000). The OCCAM model simulation was forced by constant atmospheric conditions from 1986-1988, therefore the particle trajectories are free from atmospheric variability. Nevertheless they will give an insight into what processes determine the circumpolar boundary current pathway.

Using the method we can follow changes in water properties along pathways of the boundary current, and we also use the method to calculate backward trajectories using the inverse velocity field to determine the origin of BSW that is involved in the high pressure region at the St Anna Trough.

For each calculation we start particles flowing through a fixed vertical section. The sections for the calculations in this chapter are shown in figure 6.1. The number of particles starting from each grid-box on the section is based upon the strength of the transport such that strong, important, flows have a larger number of particles than weak flows. The process of selecting the particles is described in appendix A. Each particle is injected instantaneously, and therefore initially represents an infinitesimally small part of the transport through the starting section. As the flow is flux-conserving at each moment in time, and a current is completely determined by the particles that compose it, the flux associated with each particle (particle flux) is conserved during the integration.

Although all N particles approximately represent the same transport, there are small differences in particle fluxes as described in appendix A. Therefore statistics based on the number of particles are not accurate. In order to visualize the trajectories we use statistics that are weighted by the particle fluxes. The statistic $P(i,j)$ is defined as the percentage of the initial flux (F_T) that has passed through the horizontal grid-box (i,j) throughout the whole length of the integration, counting each particle only once for each grid-box

$$P(i,j) = \frac{\sum\limits_{p \in I} F_p}{F_T} \cdot 100\%, \tag{6.1}$$

where p is an index for each particle, I represents the set of particles that have passed through horizontal grid-box (i,j), and F_p represents the particle flux of particle p.

We also visualize the mean depths and passing times of the particles for each horizontal grid-box, which are weighted by the particle fluxes

$$\overline{D(i,j)} = \frac{\sum\limits_{p\in I} F_p D_p(i,j)}{\sum\limits_{p\in I} F_p}, \tag{6.2}$$

$$\overline{T(i,j)} = \frac{\sum\limits_{p\in I} F_p T_p(i,j)}{\sum\limits_{p\in I} F_p}, \tag{6.3}$$

where $D_p(i,j)$ and $T_p(i,j)$ represent the depth and time respectively at which particle p passes through horizontal grid-box (i,j).

In the calculations we use one year's worth of 10-daily instantaneous velocity and property fields for the time-dependent trajectories. At the end of each year we loop back to the first set of fields. We choose the starting day as the time of the maximum fluxes through the starting section.

The instantaneous datasets may contain signs of inertial oscillations, for which averaging is needed to reduce the net effect (Jayne and Tokmakian 1997). However we only have one year of data, and to reduce the inertial oscillations by a significant amount would require averaging over several datasets. This would lead to a severely reduced time resolution, and we therefore choose not to correct for this effect in this study. We also want the effect of the random motions associated with time-dependence in the trajectories, which would be severely reduced by averaging over multiple time samples. Another feature that is not corrected for is the jump from the last dataset to the first dataset at the end of each year. This can potentially lead to an odd effect.

6.2 Pathways of Atlantic Water

In the following sections we look at particle trajectories of AW and BSW in order to determine pathways, depths, and time-scales of Atlantic Water through the Arctic Ocean.

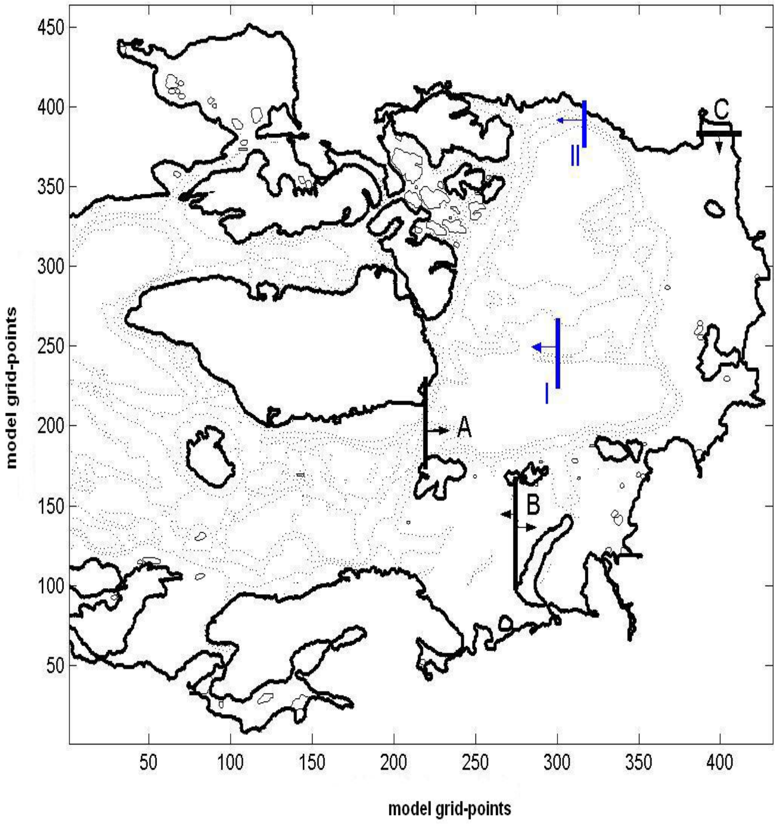

Figure 6.1: *Starting sections for trajectories of AW (A), BSW (B) and BSO (C). Depth contours at 355m,2153m,2617m.*

6.2.1 Method comparison

Here we start by comparing the time-independent, time-dependent and diffusive time-dependent methods for trajectories of BSW. We have chosen a starting section for the particles in the Barents Sea, which reaches from the surface down to 200m depth and is shown in figure 6.1.

We only track particles that flow eastwards through the section. The time-independent particles start with a transport of $2.4Sv$. The particles for the time-dependent methods are started at the time of the maximum eastward flux, which is day 680 (November 11) at which time the eastwards flux is approximately 3.5 Sv. The trajectories are all integrated for 25 years, and the transport per particle is set to be approximately 200 m^3/s.

Figure 6.2 shows flux and depth statistics of the time-independent trajectories. The time-independent pathways give a clear indication of the pathway of BSW in the boundary current, and show the boundary current is a continuous feature along the continental slope in the OCCAM model. The BSW first sinks along the eastern edge of the St Anna Trough, and then continues along the slopes of the Kara and Laptev Seas. There is a small branch of deeper water that detaches shortly from the slope of the Laptev Sea at the Nansen-Gakkel Ridge. However this branch does not form a return flow towards Fram Strait, but returns to the slope of the Laptev Sea through a gap.

There is a major bifurcation further along the current at the Lomonosov Ridge. The waters nearest the slope continue along the continental slope of the East Siberian Sea. The offshore waters are guided along the Lomonosov Ridge, where eventually they are able to pass through a gap and flow along the other side of the Ridge. After crossing the Lomonosov Ridge another small branch is guided by the Mendeleyev Ridge and flows towards Fram Strait.

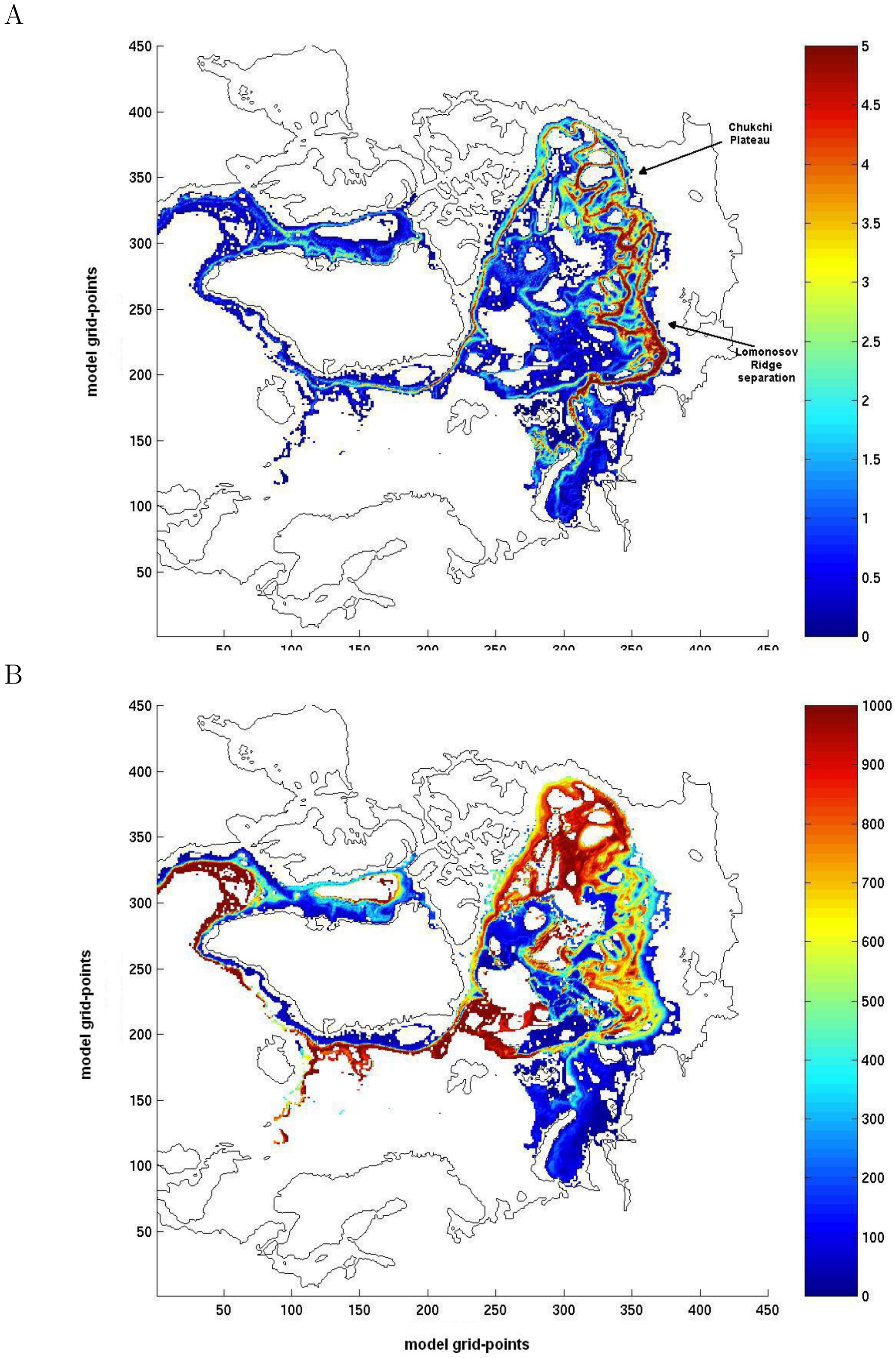

Figure 6.2: *Time-independent trajectory statistics from a 25 year integration starting from a Barents Sea section (200m in depth). Total particle flux: 2.4 Sv.. (A) Percentage of total particle flux passed through each grid-box during this period. (B) Mean depth (m) of particles when in box.*

The main branch of water reaches the Makarov and Canadian Basins. There the waters are steered by the complex topography of the Mendeleyev and Alpha ridges, and the Chukchi plateau. Swift et al (1997) have proposed that this complex topography is responsible for enhancing the double-diffusive mixing on the boundary and spreading the boundary current properties into the Makarov Basin.

Only a small part of the water continues along the slopes of the Chukchi and Beaufort Seas to make a complete loop around the Arctic. This part forms a small undercurrent as seen in figure 4.4. The other water is guided around the Chukchi Plateau. There a large number of particles get trapped in Beaufort Gyre, while flowing various loops around the gyre they sink to depths of over 1000m. Therefore it seems the BSW could play an important role in ventilating the Canadian Basin. The particles that do not get trapped flow towards the Beaufort Sea slope, joining the other particles to form a strong boundary current.

From the Beaufort Sea slope the boundary current progresses along the slope towards Fram Strait and into the North-Atlantic. There are no particles that flow through the Canadian Archipelago. By the time the BSW has reached Fram Strait it has sunk to over $1000m$ depth. Only approximately 35% of the particle flux reaches Fram Strait within the 25 year integration time. The integration is too short to see a clear separation of the deep and shallow waters flowing over the Greenland-Iceland-Scotland ridge, which are thought to follow separate pathways.

Figure 6.3 shows flux and depth statistics of the time-dependent trajectories. The time-dependent trajectories mainly follow the same main pathways as the time-independent trajectories.

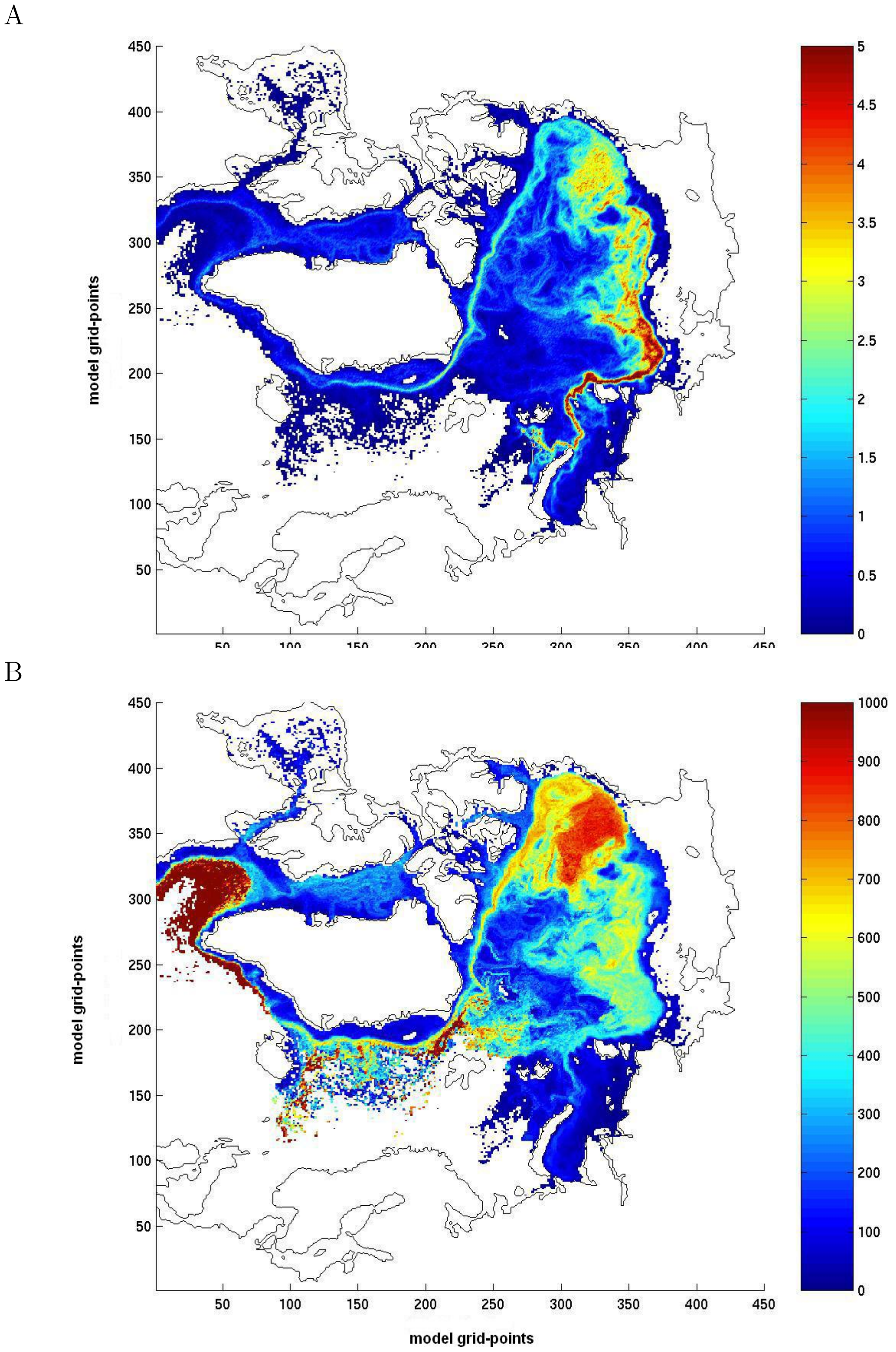

Figure 6.3: *Time-dependent trajectory statistics from a 25 year integration starting in a Barents Sea section (200m in depth). Start day: 680 (November 11). Total particle flux: 3.5 Sv.. (A) Percentage of total particle flux passed through each grid-box during this period. (B) Mean depth (m) of particles when in box.*

However there is more mixing of the water masses, and the particles now cover almost the whole Arctic Ocean, except for the Laptev, East Siberian and Chukchi Seas. The signal of the boundary current past the Lomonosov Ridge is now weaker, due to the larger spread of BSW.

A large number of BSW particles still get trapped in the Beaufort Gyre, where they sink to depths of over $1000m$. There is now a small outflow of BSW through the Canadian Archipelago. Approximately 47% of the particle flux reaches Fram Strait within the 25 year integration time. The particles that reach Fram Strait are shallower compared to the time-independent trajectories, sinking to an average depth of approximately $600m$.

Figure 6.4 shows flux and depth statistics of the diffusive time-dependent trajectories. The diffusive time-dependent pathways again follow similar pathways as the time-independent pathways, with larger horizontal spread than the time-dependent trajectories. The spread of the particles is enhanced as they are more affected by surface circulation features as the Trans-Arctic drift. The boundary current signal is now almost removed, although there are still particles completing the boundary current loop. The particles reach Fram Strait at mean depths of only $600m$, after which there is an area of large sinking past the Denmark Strait. Approximately 54% of the particle flux reaches Fram Strait within the 25 year integration time. Thus both time-dependence and diffusion reduce the residence time.

The particle trajectories calculated here reach far into the Canadian Basin, much further than similar trajectories calculated in a coarse-resolution model by Maslowski et al (2000), although these authors included the effect of annually varying wind-forcing over a 25 year period, which may alter the trajectories due to the changing phase of the AO.

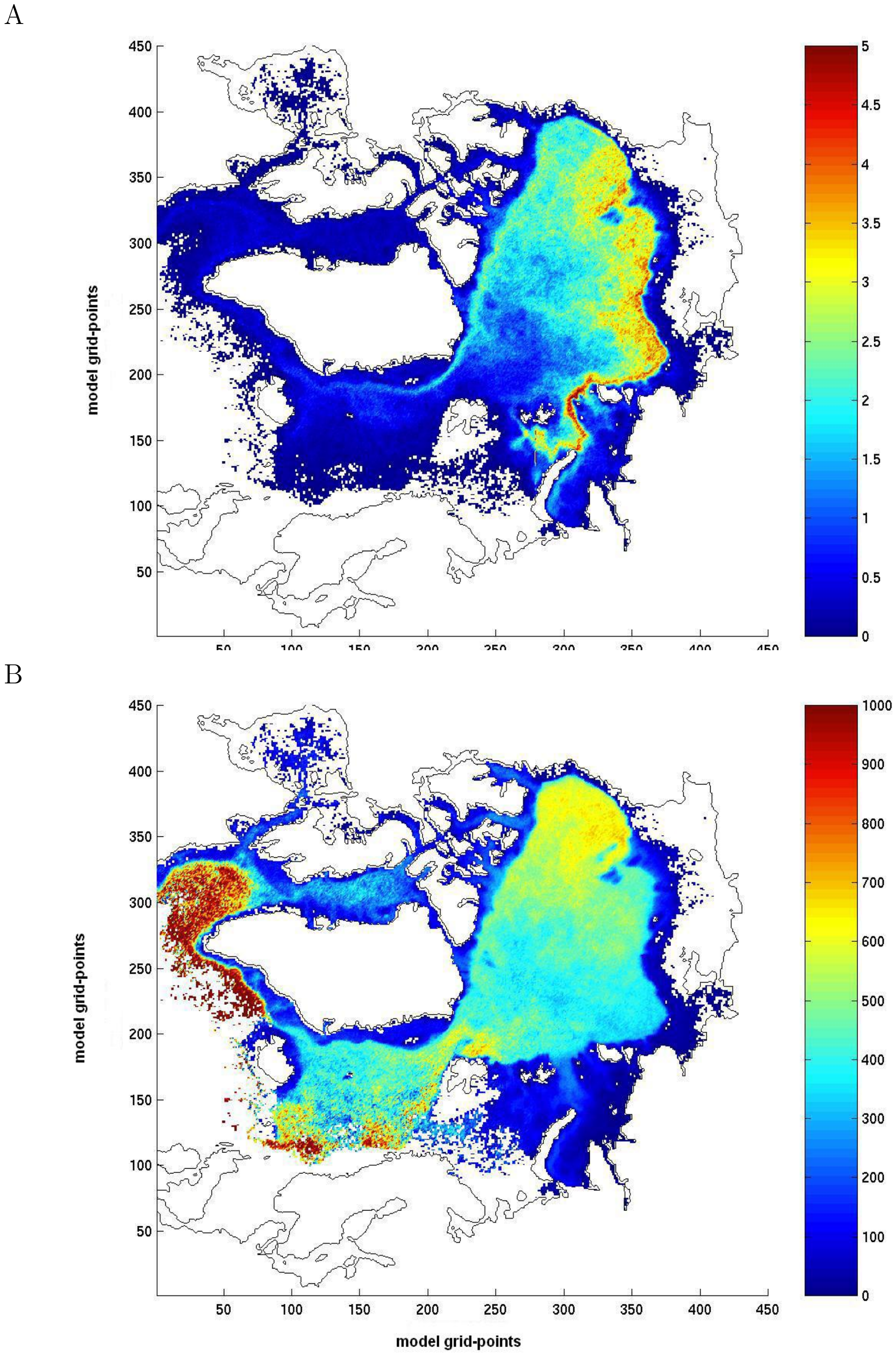

Figure 6.4: *Diffusive time-dependent trajectory statistics. 25 year integration starting from a Barents Sea section (200m in depth). Start day: 680 (November 11). Total flux: 3.5 Sv.. (A) Percentage of total particle flux passed through each grid-box during this period. (B) Mean depth (m) when in box.*

Although the time-independent trajectories provide information on the continuation of the boundary current, it is unlikely that the BSW water mass does not spread in the presence of all the meso-scale circulation features. The time-dependent trajectories show a much more realistic picture, with the water masses spreading due to meso-scale features resolved by the time-dependence and the grid-size of the model. However random motions will still be missing due to unresolved turbulence. Here we have taken the diffusivity in the random displacements equal to the eddy viscosity parameters in the OCCAM momentum equations, so the jumps hopefully resemble the randomness created by the sub-grid scale turbulence. The eddy viscosity is usually chosen as a typical length-scale of missing features (the grid-size) multiplied by a typical velocity, and gives a single value that is used at every location in the model. The distribution of tracers in the real ocean is likely to be affected by locally varying diffusion. However the constant value used for the diffusion could be validated further using observations of tracers in the real ocean, for example Argo floats or the Technetium released from the Sellafield nuclear plant, in order to find a value that most realistically reproduces trajectories in the real ocean. Later on we will see that adding our random displacements provides us with a more realistic distribution of AW and BSW in the boundary current, therefore we expect the diffusive time-dependent trajectories to represent more realistic pathways of BSW.

To identify the quickest pathways through the Arctic we have separated the particles that have made it through Fram Strait within the 25 year integration period. These pathways are shown for the time-dependent and diffusive time-dependent trajectories of BSW in figures 6.5A,B. There are two clear pathways in the time-dependent trajectories. The first is the circumpolar boundary current pathway, which is diverted offshore for a short distance by the Mendeleyev Ridge and Chukchi plateau. The second pathway is diverted along the Lomonosov

Ridge, then crosses the ridge and continues towards Fram Strait along the Makarov Basin side of the Lomonosov Ridge. It then follows the Trans-Arctic drift pathway towards Greenland. This is also a pathway for the diffusive time-dependent trajectories. The diffusive trajectories show only a very weak boundary current signal, however there are still particles that complete the full loop around the continental slope.

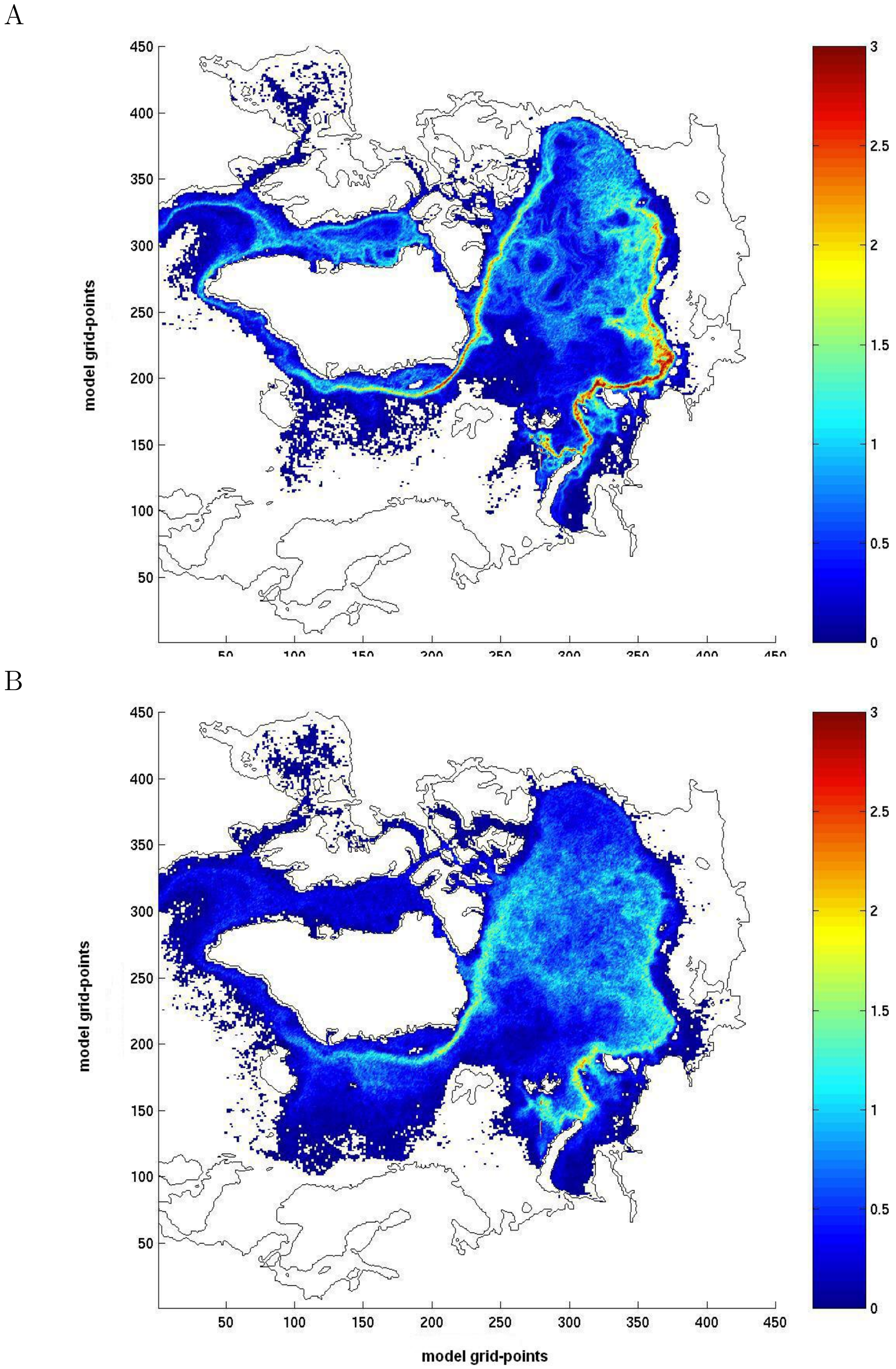

Figure 6.5: *Percentage of total particle flux that have reached Fram Strait (A) time-dependent (B) diffusive time-dependent.*

Similar diffusive time-dependent trajectories have been calculated for the inflow of AW through Fram Strait. The eastwards flowing particles start from the Fram Strait section shown in figure 6.1, and were integrated for 25 years starting at day 630 (September 22). They represent a total flux of $9.8Sv$. The flux statistic for these trajectories is shown in figure 6.6B. A large part of the AW recirculates in the West Spitsbergen Current, as discussed in chapter 2, and the pathways through the Arctic are difficult to see. Approximately 30% of the total particle flux makes it through Fram Strait and flows eastwards along the Barents Sea slope. The trajectories are not clear and therefore we have also performed similar time-independent calculation. The pathways of these trajectories provide an indication of the pathways of the diffusive time-dependent trajectories. The flux statistic for these trajectories is shown in figure 6.6A.

The time-independent trajectories show how AW enters the Arctic. There is a small inflow along the Barents Sea slope, which eventually joins up with BSW exiting through the St Anna Trough. There is also a deep branch flowing further offshore which eventually recirculates towards Fram Strait as an undercurrent on the continental slope. This undercurrent is associated with the anti-cyclonic feature in the streamfunction in figure 3.7. The branch continuing along the boundary moves offshore at the Laptev Sea slope, and appears to reach less far into the Canadian Basin than the time-independent BSW. By adding diffusion to the BSW time-dependent pathways, as seen in figure 6.5B, the BSW seems to follow the AW pathways by flowing across the Arctic before reaching the Beaufort Gyre.

Observations on the Canadian side of the Lomonosov Ridge have shown the signal of warm water of Atlantic origin (Schauer et al 1997, McLaughlin et al 2002). Schauer et al 1997 have estimated that the water that is transported towards the Canadian Basin in the boundary current above $600m$ consists of equal amounts of AW and BSW, and that the water deeper than $600m$ consists of 80% of BSW and 20% of AW. We have estimated the amount of each water mass that crosses the Lomonosov Ridge in the boundary current by calculating the amount of particle flux flowing through two vertical sections shown in figure 6.1. The first section is a fixed model longitude section across the Lomonosov Ridge, and represents the pathway that returns towards Fram Strait along the ridge. The second section is a fixed model longitude section across the Beaufort Sea slope, and represents the circumpolar boundary current pathway. A particle has passed the section if the line connecting successive particle positions crosses the section. Although more than half of the particle flux of AW and BSW still remain in the Arctic after 25 years we expect to get an indication of the distribution of the water masses in the basins. In figures 6.7A,B the pathways, and the associated fluxes, of the time-dependent and diffusive time-dependent AW and BSW particles are summarized.

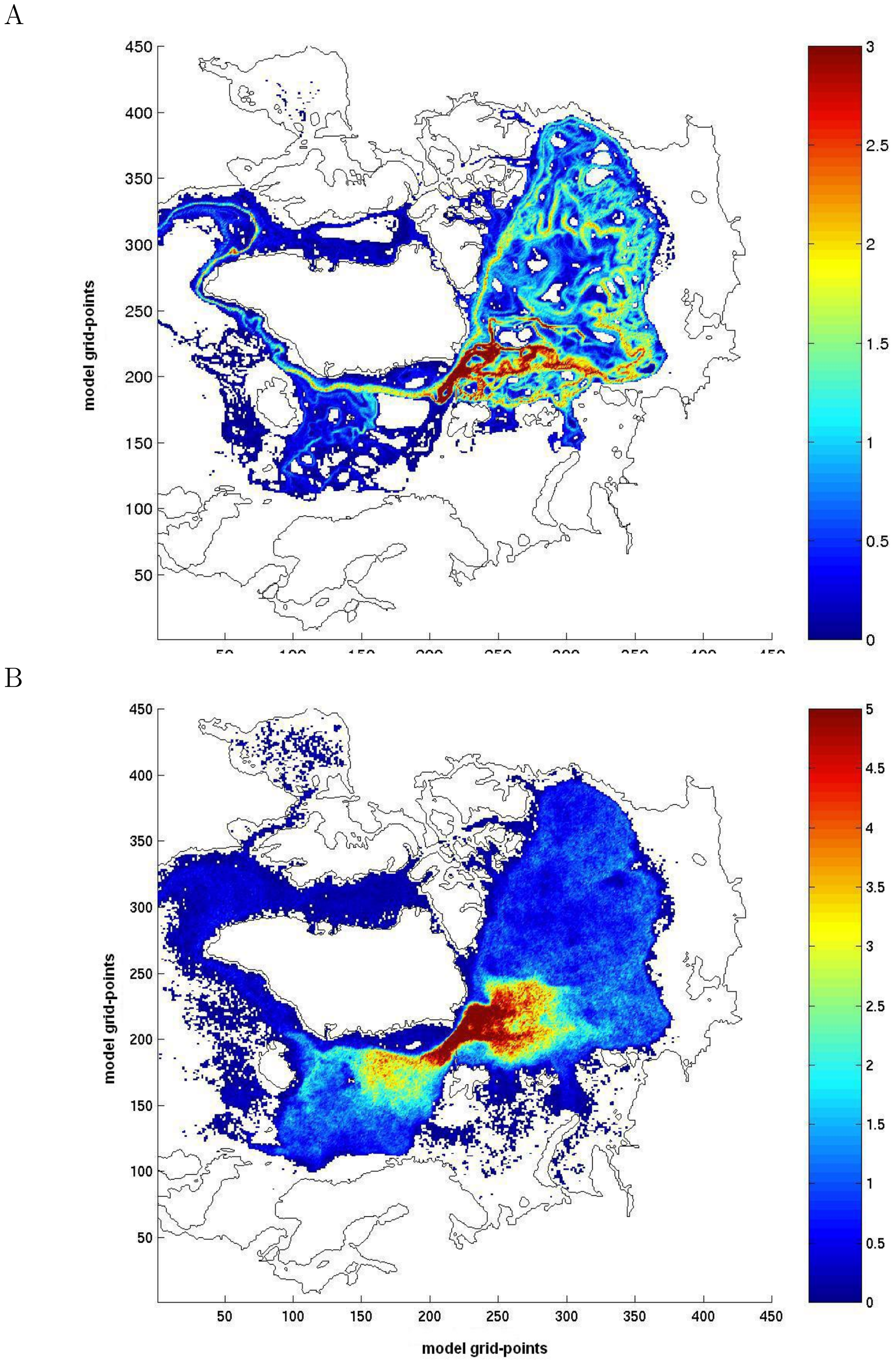

Figure 6.6: *Percentage of total particle flux passed through each grid-box for 25 year integrations starting in Fram Strait. (A) Time-independent trajectory statistics. flux:* $7.2Sv$*.(B) Diffusive time-dependent trajectory statistics. flux:* $9.8Sv$.

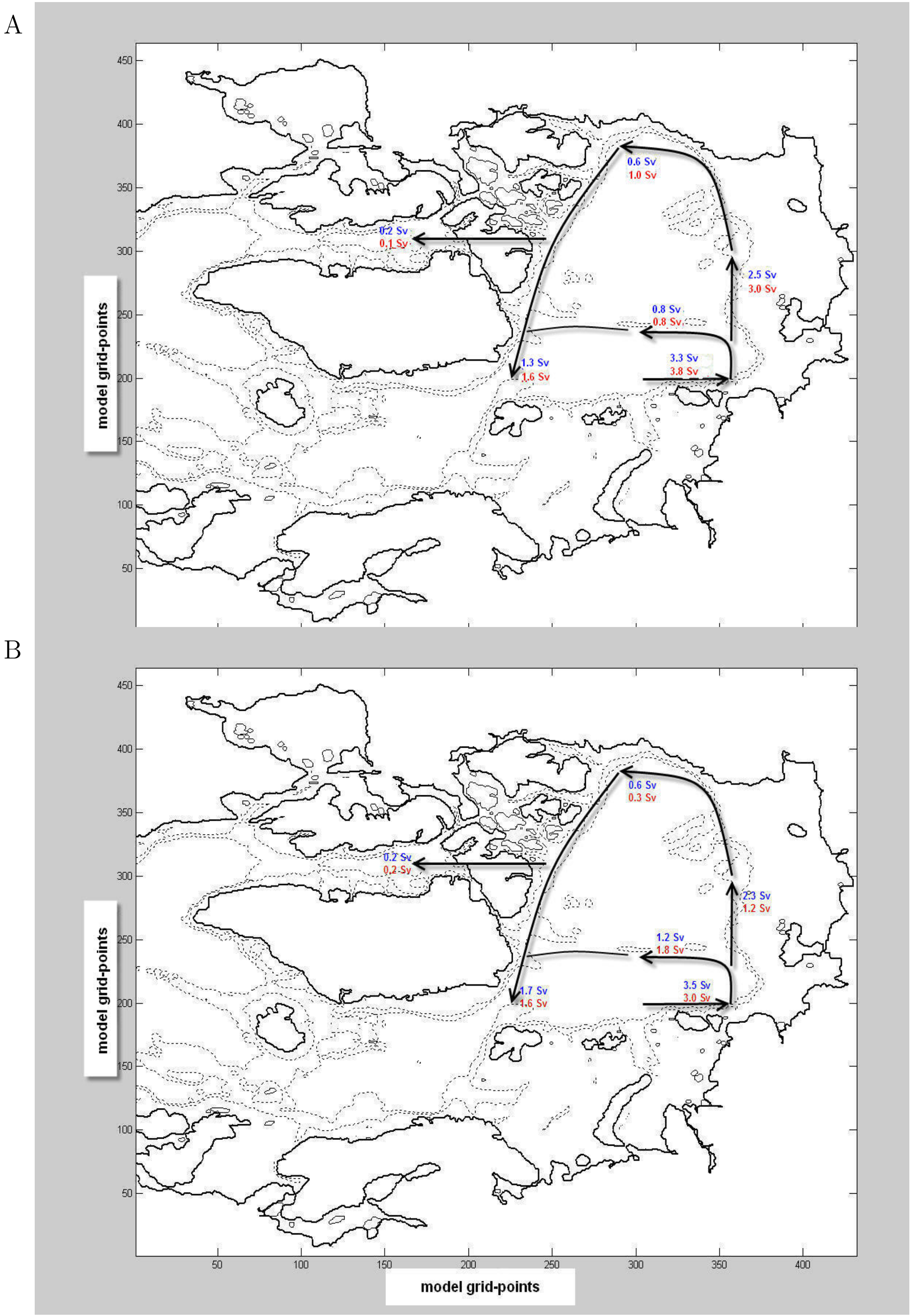

Figure 6.7: *Summary of time-dependent/diffusive time-dependent BSW (blue) and AW (red) pathways and associated particle fluxes (in Sv) after 25 year integration. At the start 3.3/3.5 Sv of BSW and 3.8/3.0 Sv of AW makes it into Arctic Ocean.*

One immediate difference between the fluxes of the time-dependent and diffusive time-dependent trajectories is the distribution of AW and BSW. It has generally been observed that BSW is the dominant water mass in the boundary current (eg. Woodgate et al 2001). Schauer et al (1997) even measured a distribution of 50% AW and 50% BSW in the upper 600m, and 20% AW and 80% BSW below 600m as the boundary current enters the Canadian Basin. In the time-dependent trajectories there is a much larger component of AW in the boundary current. The AW is located on the outer edge of the boundary current, after being pushed offshore by the BSW, and it therefore tends to mix out of the current more when diffusion is added. The branch of the boundary current returning towards Fram Strait along the Lomonosov Ridge is thought to consist of a larger part of AW, which is seen more obviously when diffusion is added. Therefore we conclude that the diffusion creates a more realistic picture of how far the AW reaches into the Canadian Basin.

Here we discuss the diffusive time-dependent fluxes in more detail. A flux of approximately $1.2 Sv$ of BSW crosses the section through the Lomonosov Ridge. The mean time for BSW to reach this section is 8.6 years, and it crosses at a mean depth of $246m$. These waters then continue to exit the Arctic Ocean via Fram Strait in a mean time of 12 years at a mean depth of $176m$. The mean crossing time for the Lomonosov Ridge section and the exit time at Fram Strait are relatively close as a large number of particles that have crossed the first section do not reach Fram Strait within the 25 year integration. Approximately $2.3 Sv$ of BSW crosses the Lomonosov ridge and flows towards the Canadian Basin.

A flux of approximately $1.8 Sv$ of AW crosses the section across the Lomonosov Ridge. The mean time for AW to reach this section is 10.1 years, and it crosses at a mean depth of $578m$. These waters then continue to exit the Arctic Ocean via Fram Strait in a mean time of 11.7 years at a mean depth of $296m$. This leaves approximately $1.2 Sv$ of AW of the original

$3.0Sv$ flowing into the Arctic along the Barents Sea slope, to cross the ridge and flow towards the Canadian Basin. This means that in the OCCAM the amount of BSW is larger than the amount of AW flowing across the Lomonosov Ridge.

The particles crossing the Beaufort Sea section towards the Canadian Archipelago are also calculated to approximate the amount of each water mass that make the (almost) full loop along the continental slope of the Arctic Ocean. Approximately $0.6Sv$ of BSW crosses this section in a mean time of 13.3 years, and at a mean depth of $498m$. Approximately $0.2Sv$ of BSW is found to flow through the Canadian Archipelago into the North Atlantic. The other waters continue to exit the Arctic Ocean via Fram Strait in a mean time of 18.3 years at a mean depth of $350m$.

Approximately $0.3Sv$ of AW crosses the section across the Beaufort Sea slope. The mean time for AW to reach this section is 14.1 years, and it crosses at a mean depth of $500m$. Approximately $0.2Sv$ of AW flows through the Canadian Archipelago. The other waters then continue to exit the Arctic Ocean via Fram Strait in a mean time of 18.1 years at a mean depth of $582m$.

This shows that BSW is the main water mass in the boundary current in the OCCAM $1/8° \times 1/8°$ model, and that the Barents Sea has a far reaching influence. Also this shows that a large part of both water masses crossing the Lomonosov Ridge do not continue in the boundary current. They are captured by the Trans-Arctic drift and the Beaufort Gyre, and are transported across the Arctic and through the Canadian Basin.

We also look at the depth distributions of both sets of particles in the Eurasian and Canadian Basins. On the boundary current route the AW is generally deeper than the BSW for the diffusive time-dependent trajectories, and provides the deepest outflows into the North Atlantic. Table 6.1 shows the percentage of time that each water mass spends in depth intervals during the full 25 year integrations of the diffusive time-dependent trajectories. This shows that the AW and BSW provide important contributions to the intermediate waters ($500 - 1500m$) and deep waters ($\geq 1500m$) of the Arctic Basins, especially in the Canadian Basin. The large amount of deep AW in the Eurasian is due to deep inflows through Fram Strait which recirculate within the Eurasian Basin.

	Eurasian	Basin	Canadian	Basin
depth	AW	BSW	AW	BSW
0-500m	25	76	46	55
500-1000m	17	20	41	34
1000-1500m	4	3	9	9
≥ 1500m	54	1	4	2

Table 6.1: *Percentage of AW and BSW particle flux in depth intervals during 25 year integration.*

6.2.2 Interaction of AW and BSW

Here we look at the interaction of the diffusive time-dependent trajectories of AW and BSW water masses along the continental slopes of the Arctic Ocean. The AW flows through the Fram Strait and continues along the Barents Sea slope, where it eventually meets the BSW which flows out through the St Anna Trough. A 3D visualization of these flows is shown in figures 6.8A,B, which shows BSW and AW particle positions in the St Anna Trough area. The first figure 6.8A shows the position of BSW particles during the 25 year integration, where the BSW can be seen falling off the continental shelf and continuing as a boundary current along the continental slope. Also a small number of particles are entrained into an undercurrent flowing towards Fram Strait. In the second figure (6.8B) the AW flowing along the continental slope is added.

We also look at vertical sections at model longitude coordinates $i = 290, 320, 350$ to view the through flow of particles at successive sections across the continental slope.The flux of particles across each section is calculated by summing particles that have crossed the section within the sample time (10 days). The depths, temperatures and salinity are then calculated by linear interpolation between the two current time samples. For the calculation of mean depths and times these interpolated values are weighted by the flux of the particles. The mixture of BSW and AW at each grid-point (k, j) on the section is also weighted by flux and defined by

$$M(k,j) = \frac{A\sum\limits_{p\in I} F_p + B\sum\limits_{q\in J} F_q}{\sum\limits_{p\in I} F_p + \sum\limits_{q\in J} F_q}, \tag{6.4}$$

where $A = 1$ represents AW, $B = -1$ represents BSW, F_p and F_q represent the AW and BSW particle fluxes, I and J represent the set of AW and BSW particles that have passed through the vertical grid-box (k, j).

Particles of AW and BSW crossing the first section are shown in figure 6.9. Figure 6.9A shows the total flux of AW and BSW crossing the section. The AW flows slowly along the slope of the Barents Sea, while the BSW is in the Barents Sea flowing eastwards towards the St Anna Trough. The total flux of AW contributing to the slow boundary current between 0-1500 metres is $3.0Sv$, at a mean depth of 347m. This is slightly less than the $3.5Sv$ of BSW on the shelf, which is at a mean depth of 120m. The mean time for AW to reach this section is 3.9 years from the Fram Strait section. The distance from its starting section is approximately 910 km, so its mean speed is less than 1 cm/s. The mean time for BSW to reach this section is 0.5 years from the Barents Sea section. Figure 6.9B shows the mixture

$(M(k,j))$ of the two water masses. It shows that the BSW and AW have not mixed, although some BSW has joined the surface of the AW pathway.

Particles of AW and BSW crossing the second section are shown in figure 6.10. At this point the BSW has entered the Arctic Basin via the St Anna Trough, and can be seen to sink down the slope. Figure 6.10A shows the large amount of AW and BSW on the slope. The total flux of water passing through this section are almost the same as in the previous section. The flux of AW contributing to the boundary current between 0-1500 metres is $3.0Sv$, at a mean depth of 352m. The flux of BSW is $3.5Sv$, which has sunk to a mean depth of 219m. The mean time for AW to reach this section is 5.2 years, compared to 1.9 years for BSW which has travelled over twice as far. Figure 6.10B shows BSW is confined to the slope, pushing AW offshore with some mixing taking place.

Particles of AW and BSW crossing the third section are shown in figure 6.11. Figure 6.11A shows that the main part of the water is on the slope. Figure 6.11B shows this water is a mixture of AW and BSW, where AW is the main component at the bottom, and BSW is the main component at the top. The total flux of water passing through this section are slightly less than the previous sections. The amount of AW contributing to the boundary current between 0-1500 metres is $2.5Sv$, at a mean depth of 353m. The amount of BSW is $3.3Sv$, which has sunk to a mean depth of 235m. The mean time for AW to reach this section from the previous section is 5.7 years, compared to 2.7 years for BSW.

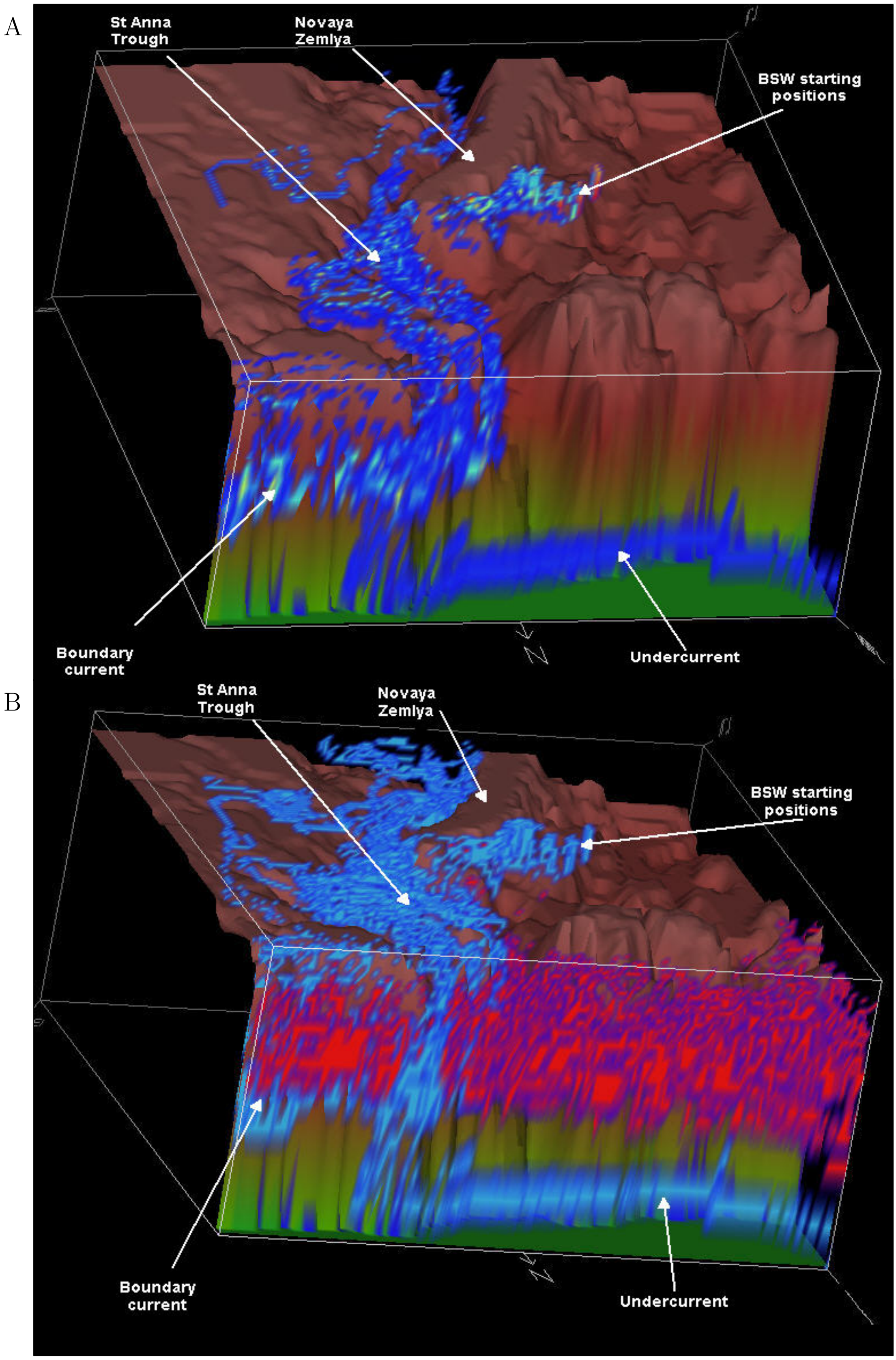

Figure 6.8: *Particle positions of BSW (blue) and AW (red) during 25 year integration in St Anna Trough area. Only positions where over 0.1 Sv flows past are shown.*

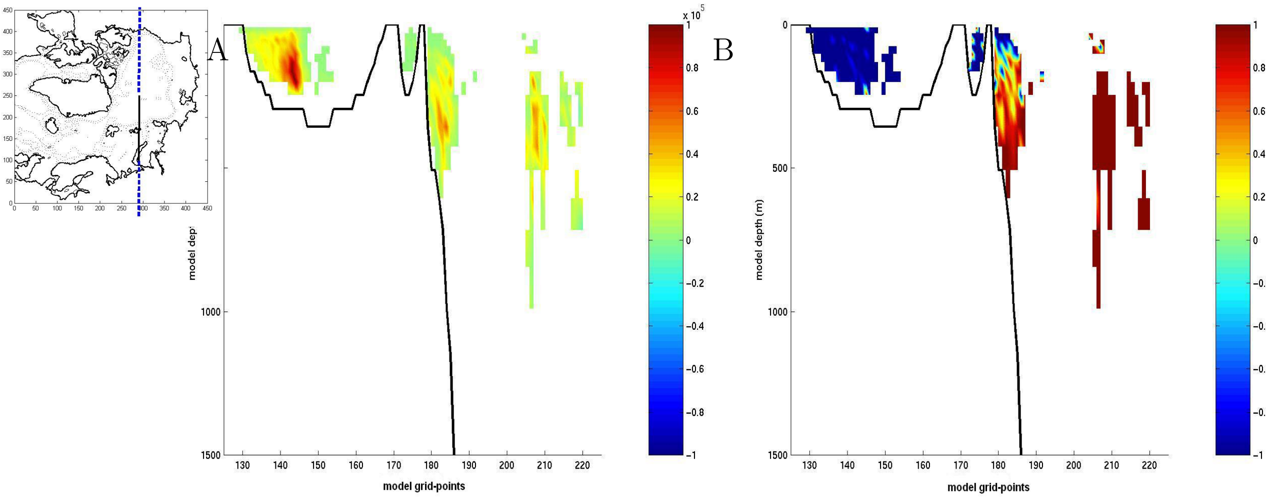

Figure 6.9: *Diffusive time-dependent trajectories at i=290 on Eurasian slope. (A) flux (m^3/s) of BSW and AW particles passing section (B) Mixture of BSW (blue) and AW (red) particles.*

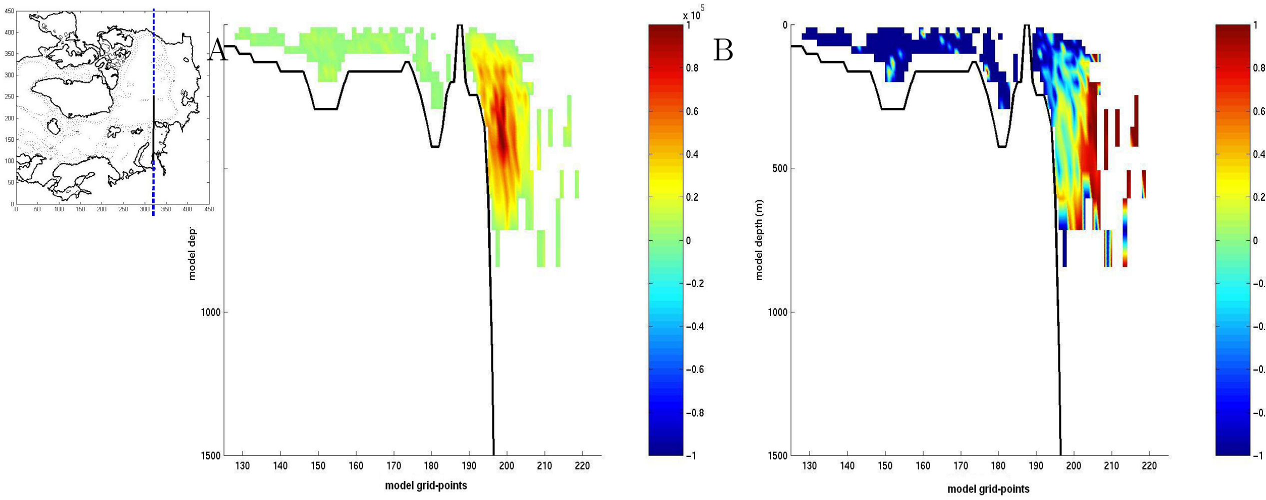

Figure 6.10: *Diffusive time-dependent trajectories at i=320 on Eurasian slope. (A) Flux (m^3/s) of BSW and AW particles passing section (B) Mixture of BSW (blue) and AW (red) particles.*

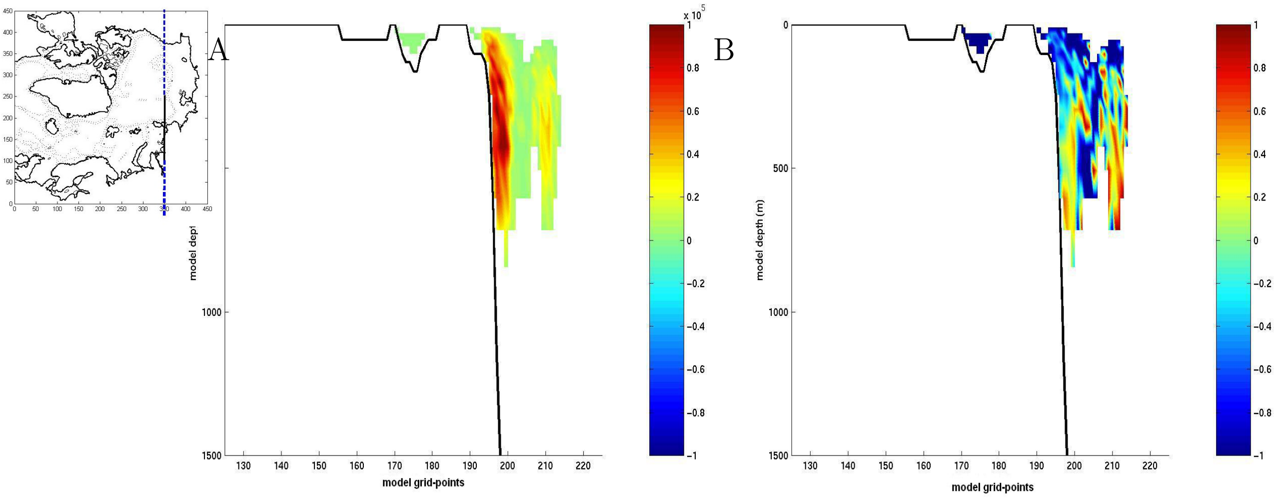

Figure 6.11: *Diffusive time-dependent trajectories at i=350 on Eurasian slope. (A) Flux (m^3/s) of BSW and AW particles passing section (B) Mixture of BSW (blue) and AW (red) particles.*

The distance from the previous section is approximately 390 km, which means the mean speed of both water masses has increased to approximately $2.5 cm/s$. These consecutive sections show that AW is pushed offshore by BSW, which is the reason that further along the slope the AW is more likely to get diverted by the Lomonosov and Mendeleyev Ridges.

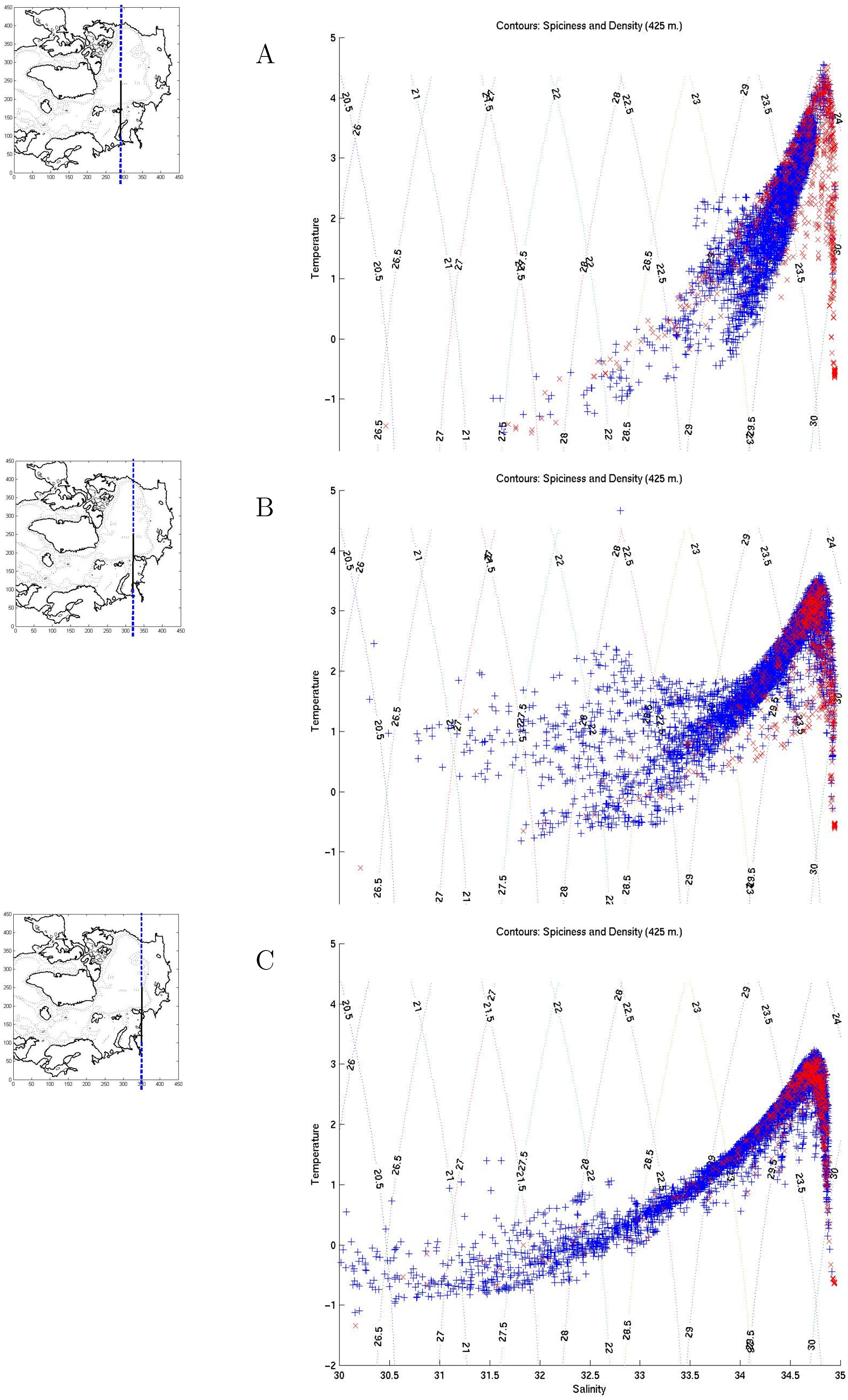

Figure 6.12: *Temperature-Salinity properties of diffusive time-dependent BSW (blue) and AW (red) particles with potential density (referenced to 425 m) and spiciness contours at (A) i=290 (B) i=320 (C) i=350 on Eurasian slope.*

The mixing of both water masses can also be seen in the particle temperature and salinity properties. Figure 6.12 shows potential temperature and salinity properties of the two water masses on the three sections of the Eurasian Basin. The first section shows the distinguishing properties of BSW and AW, where they are completely unmixed. The AW mostly is warmer, and saltier than BSW.

Further along the slope where the pathways of AW and BSW join figure 6.12C shows that the temperature maximum of AW has moved down from approximately $4.5°C$ to $3.2°C$. The property differences between BSW and AW are disappearing indicating mixing of the two water masses. Also the surface waters of BSW have been freshened compared to the previous section, indicating some mixing with surrounding Polar Surface Water.

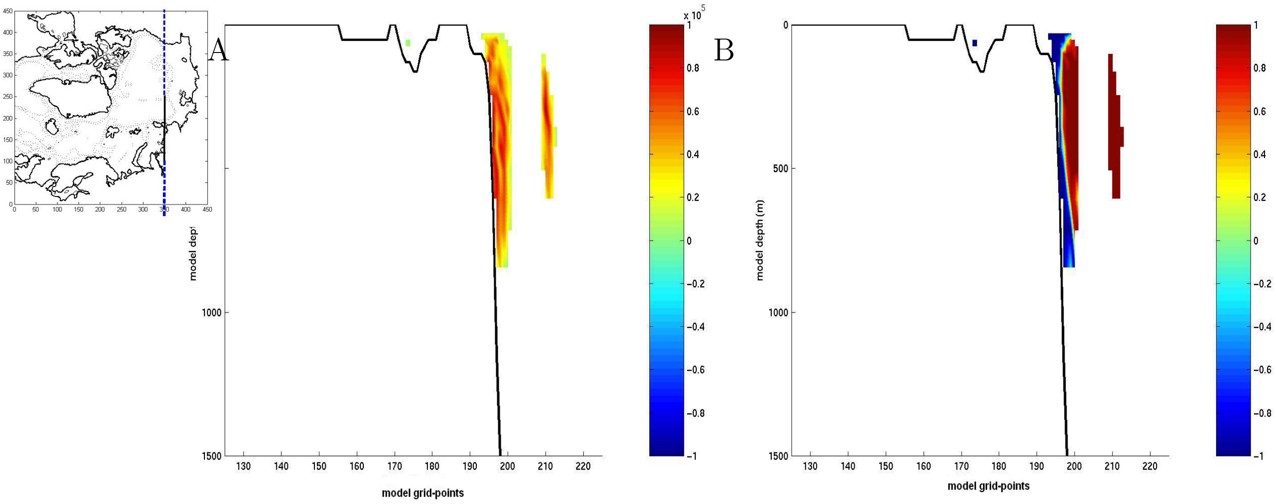

Figure 6.13: *Time-independent trajectories at i=350 on Eurasian slope. (A) flux (m^3/s) of BSW and AW particles passing section (B) Mixture of BSW (blue) and AW (red) particles.*

Figure 6.12C shows that AW and BSW are almost completely mixed further along the slope at i=350 and can not be easily distinguished from temperature and salinity properties.

In the time-independent trajectories there is no mixing at all of the two water masses. Figure 6.13 shows the crossings of time-independent AW and BSW particles through the third section at i=350. Figure 6.13A shows that the main part of the water is on the slope. In this figure the BSW can be clearly seen to sink under the AW on the slope, and to push AW offshore.

6.2.3 Water mass transformations

In this section we look at the temperature and salinity properties along the large-scale AW and BSW particle trajectories. These two water masses can be roughly divided into two groups following separate pathways. The first group of particles follows the boundary current route all along the continental slope to the Canadian Basin, where some particles are affected by the Chukchi plateau and the Beaufort Gyre. The second group of particles is forced offshore by the Lomonosov Ridge, Mendeleyev Ridge, and the Trans-Arctic drift. We have separated these groups based on particles that cross westwards through sections I and II in figure 6.1.

The main properties of the particles are set by air-sea fluxes on the continental shelves, however there are also significant air-sea fluxes in the ocean interior. Also particles can change properties due to mixing with surrounding water, or through intrusions of dense plumes. In the model these plumes are most likely to form on the East Siberian and Chukchi Sea continental shelves, where there are large seasonal air-sea fluxes that correspond to ice processes (ice formation and melting). Figure 6.14 shows the mean properties for the Eurasian and Canadian Basin interiors. These are averages of all water columns that are deeper than $1500m$. Here the Eurasian Basin includes the Nansen and Amundsen Basins, while the Canadian Basin also includes the Makarov Basin. These properties show the strong halocline on both sides of the Lomonosov Ridge, which underlies a cold and fresh surface layer.

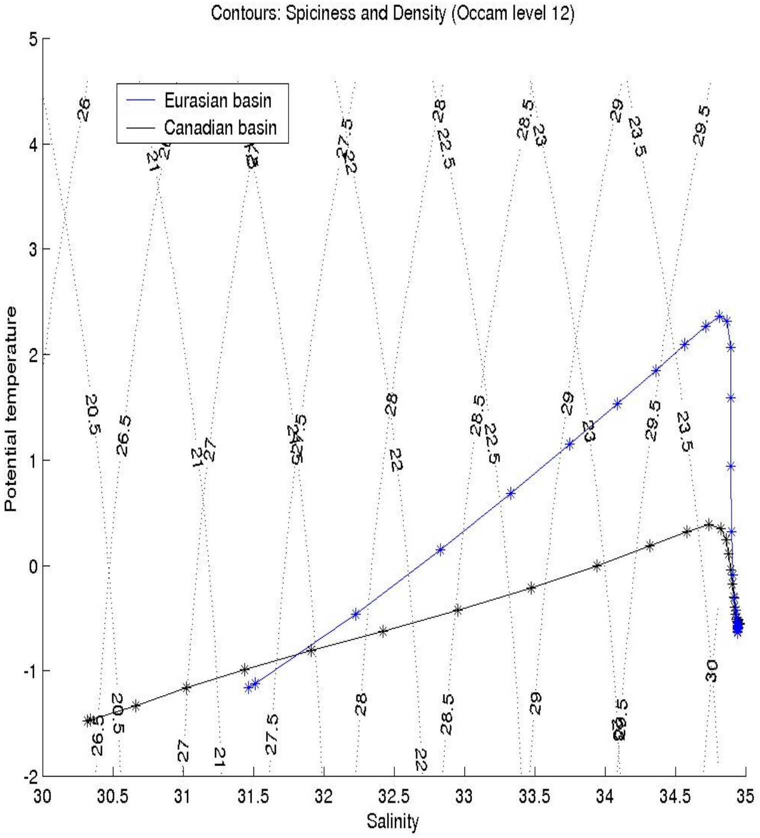

Figure 6.14: *Mean potential temperature (°C) and salinity (PSU) properties for Eurasian and Canadian Basin interior.*

The properties of the first group of particles as they cross westwards through section I (seen in figure 6.1) on the Beaufort Sea slope are shown in figure 6.15A. AW particles are shown in red, and BSW particles are shown in blue. It is mostly the deepest and densest particles flowing close to the slope that make it into the boundary current route. On the Kara Sea slope these waters have the properties of $34 < S < 35$ and $-0.5 < T < 3$. The core of the particles on the Beaufort Sea slope have the properties $33.5 < S < 35$ and

$-0.5 < T < -0.2$, which means the water particles have been significantly cooled and partly freshened as they flow along the Siberian shelves. Mixing with the Eurasian and Canadian deep waters could provide the cooling, however this water is deeper ($\geq$ 1000m) than most of the particles along the slope. The cooling and freshening can be explained by the air-sea fluxes along the current. Figure 3.2 shows that there is a constant negative heat flux along the boundary current pathway up to the Beaufort Sea slope. Estimating the heat flux out of the ocean as $\Delta Q = 30W/m^2$, the depth (Δz) of the water column of AW and BSW along the boundary as $500m$, and the time (Δt) it takes to reach the Beaufort Sea slope as 5 years gives an approximate temperature change of

$$\Delta T = \Delta t \frac{\Delta Q}{c_v \rho_0 \Delta z} = -2.3°C. \tag{6.5}$$

Here the specific heat, c_v, and reference density, ρ_0, are approximated as $4200J/(kg°C)$, $1000kg/m^3$. We have used a conservative estimate on the time Δt, however the temperature change of $-2.3°C$ over a full $500m$ water column is almost enough to provide the cooling seen in the AW and BSW particles. The Arctic Ocean is covered by a halocline, which insulates the water masses underneath from the surface cooling. However the boundary current along the continental slope of the Eurasian Basin has been seen to reach right up to the surface. The surface waters of the boundary current will be affected by the cooling, and this will be able to mix down quickly due to the turbulence in the current. Therefore we think that downward mixing along the continental slope of the changes induced by air-sea fluxes in the surface layer cause the observed water mass transformations.

There is also a large positive freshwater flux over areas of the continental slope. A similar estimate for the rate of change of salinity with $P - E = 200cm/yr$ gives $\Delta S = 0.7PSU$, which explains the freshening. Figure 6.15B shows the properties of the same group of particles as they flow through Fram Strait into the North Atlantic. Although a large part of the particles on the boundary current pathway still remain in the Arctic after 25 years, most of the particles that have made it to Fram Strait can be seen unchanged (at 0.3°C and 34.7PSU) compared to figure 6.15A.

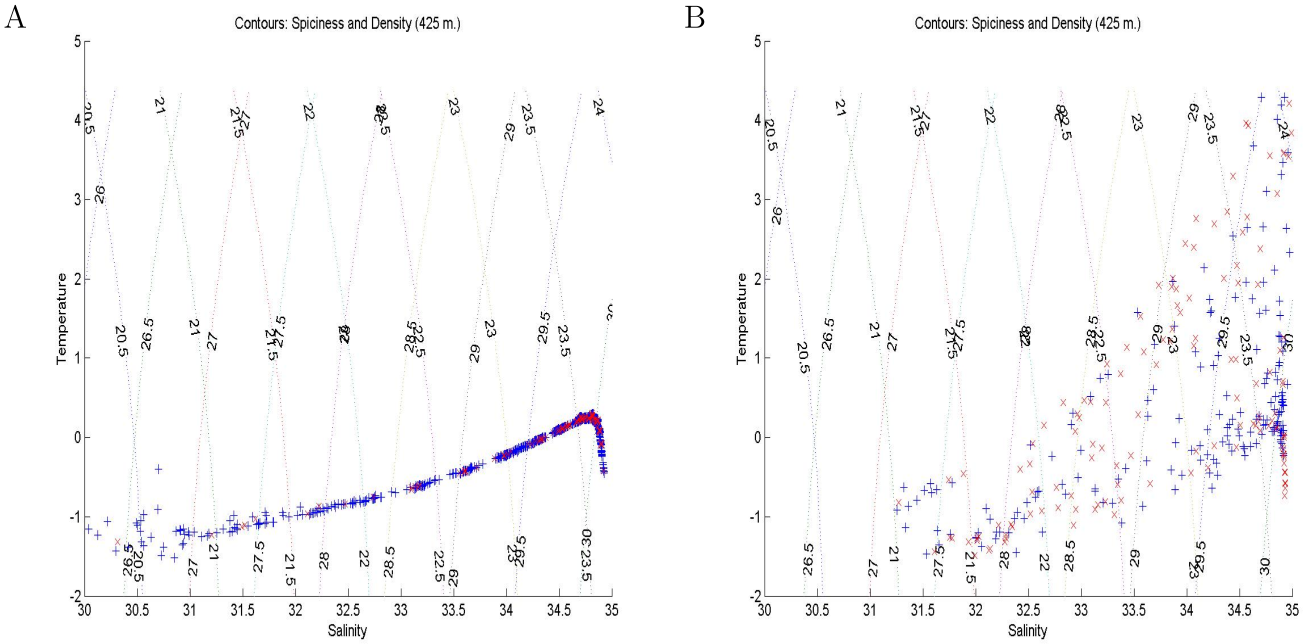

Figure 6.15: *Potential temperature (°C) and salinity properties of AW (red) and BSW (blue) particles on boundary current pathway. (A) Beaufort Sea slope (B) Fram Strait*

An example of a BSW particle following the boundary current route is given in figure 6.16, which shows the particle trajectory, and depth, potential temperature and salinity as a function of time. As the particle flows out of the St Anna Trough it becomes warmer and saltier, probably due to mixing with the warmer branch of AW. From the Laptev Sea slope onwards the particle is gradually cooled, and becomes saltier as it sinks to over 1000m depth. It then gets trapped in the Beaufort Gyre, before flowing westwards in the boundary undercurrent on the Beaufort Sea slope. There it is part of the densest waters in figure 6.15A.

The initial cooling during the first 6 years is likely to be due to air-sea fluxes, however as it sinks further in the Beaufort Gyre it mixes with the salty and cold deep waters of the Canadian Basin.

The properties of the second group of particles as they cross westwards through section II (seen in figure 6.1) along the Lomonosov Ridge are shown in figure 6.17A. It is mostly the shallower particles that are steered by the Trans-Arctic drift, and the offshore particles that are driven by the Lomonosov Ridge, that follow this route. The core of this group has been significantly freshened and cooled compared to the water properties on the Kara Sea slope.

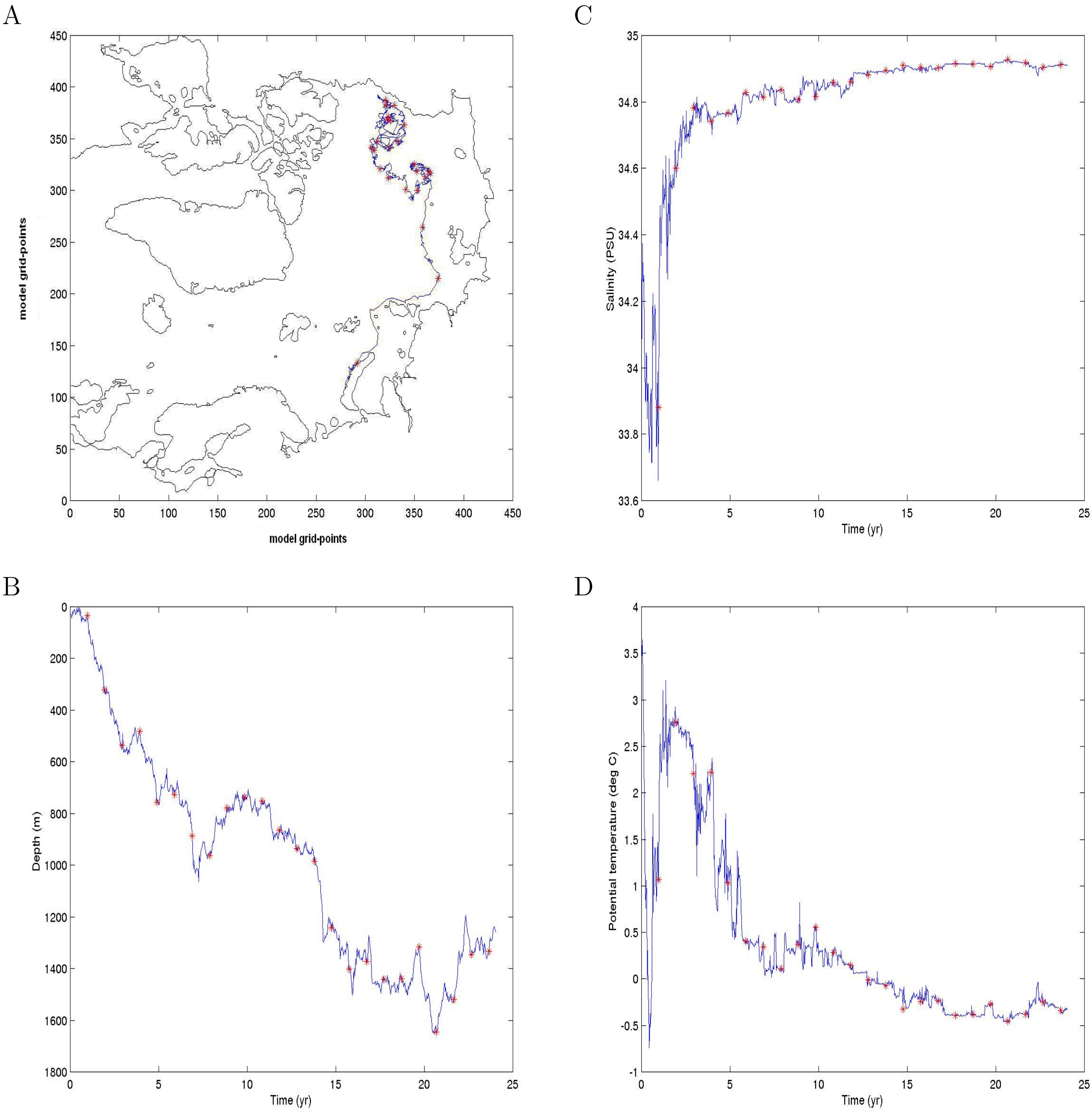

Figure 6.16: *BSW particle statistics. (A) Trajectory (B) Depth (m) (C) Salinity (PSU) (D) Potential temperature (°C).*

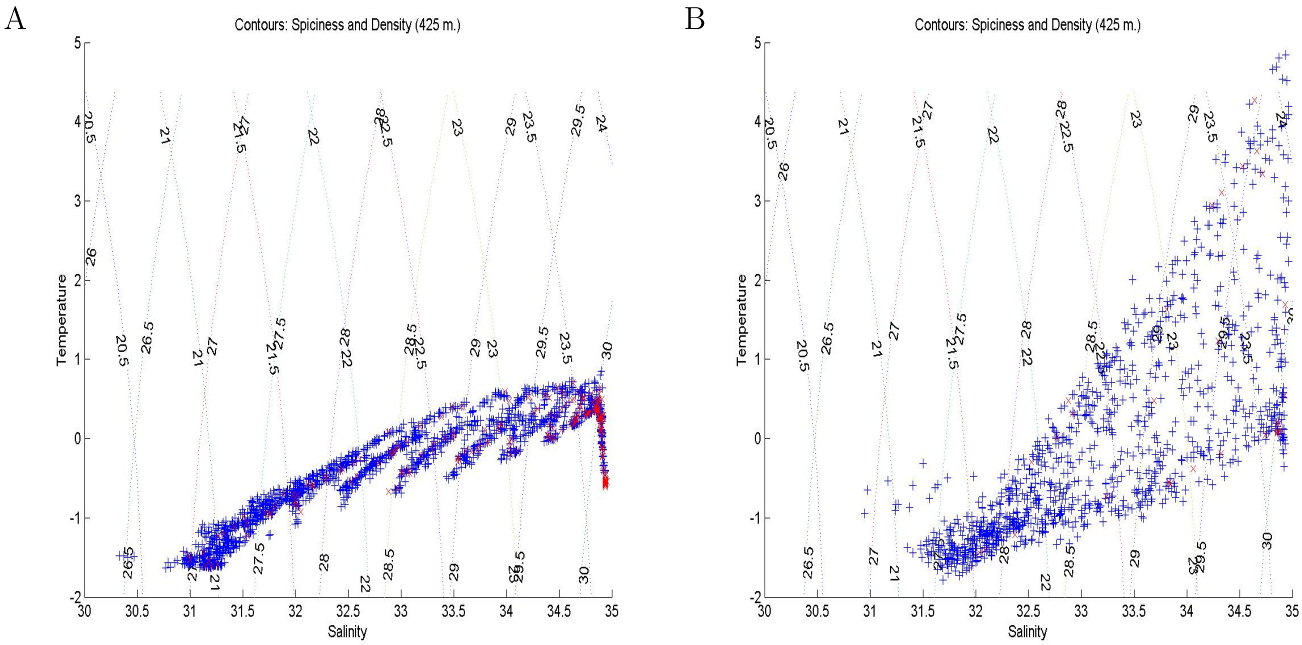

Figure 6.17: *Potential temperature (°C) and salinity properties of AW (red) and BSW (blue) particles on Trans-Arctic pathway. (A) Lomonosov Ridge section (B) Fram Strait*

Apart from the surface layer, there is no water mass cold and fresh enough beneath the halocline that would be able to provide the observed changes through mixing. However there is a very large annual mean freshwater flux in the Eurasian Basin, which originates from the mouth of a Siberian river, giving values of up to $P - E = 600 cm/yr$.

A similar calculation as for the first group of particles gives an approximate salinity change of $\Delta S = 2.0 PSU$, which is enough to transform the medium salinity waters of the AW and BSW outflow. Figure 6.17B shows the properties of the same group of particles as they flow through Fram Strait into the North Atlantic. The majority of these waters remain unchanged from the section through the Lomonosov Ridge, although some mixes in with recirculating AW from the West Spitsbergen Current.

6.3 Pathways of Pacific Water

In this section we look at particle trajectories of Pacific Water flowing into the Arctic Ocean via Bering Strait. The particle trajectories were started at day 370 (January 11), and were integrated for 20 years. After 20 years approximately 40% of the particles still remain in the Arctic, mainly in the Beaufort Gyre. The particles have a total flux of $0.5 \;\; 10^6 m^3/s$. The flux statistic of these particles is shown in figure 6.18A.

There are four branches of BSO off the shelf. The outflow is guided by the topography on the Chukchi Sea shelf, which is shown in figure 6.18B. The BSO flows towards the deep basin through the three canyons that separate the Hannah and Herald Shoals, and Wrangel Island. There are also particles that make several loops (anti-cyclonic) around Herald Shoal, which is where Martin and Drucker (1997) have shown the presence of a Taylor column in observations. The strongest branch flows through Herald Canyon, and then continues towards

Hannah Shoal where it flows off the shelf. Of the particles that flow off the shelf here there are only a few that follow the boundary current. The majority flow off the shelf and continue in the Beaufort Gyre, while some spin off in eddies as they meet the light (fresh) water in the gyre. There is another branch of BSO that flows along the shelf into the East Siberian Sea, where there is a front with the fresh Siberian shelf water. There the BSO is diverted off the shelf, and is transported offshore by the Trans-Arctic drift. The BSO exits the Arctic in almost equal quantities via the Canadian Archipelago and the Fram Strait.

During the time in the Arctic Ocean the BSO is significantly shallower than the water of Atlantic origin. Table 6.2 shows the depth distribution of the BSO particles within the Eurasian and Canadian Basins during the full 20 year integration. The water is almost entirely contained in the upper $1000m$, and does not contribute as significantly to the intermediate and deep waters as the AW and BSW. However it is dense enough to sink into the halocline.

depth	Eurasian Basin	Canadian Basin
0-500m	87	92
500-1000m	12	7
1000-1500m	0.5	0.4
$\geq$ 1500m	0	0.04

Table 6.2: *Percentage of BSO particle flux in depth intervals during 20 year integration.*

The BSO outflow is relatively fresh ($S < 33.5PSU$) compared to water of the same density in the Canadian Basin, but is still relatively salty compared to the upper waters of the Canadian Basin. There is significant dense water formation on the Chukchi Sea shelf (Cavalieri and Martin 1994). This is also represented in the annual mean prescribed air-sea fluxes in the OCCAM model, where negative heat and freshwater fluxes dominate the shelf (see figure 3.2). Therefore the BSO becomes even denser compared to the Canadian Basin surface water. D'Asaro (1988b) has proposed that the front between these two water masses can create baroclinic instabilities as the BSO flows off the shelf near Barrow Canyon. We have found particle trajectories that support this proposal.

The trajectory of a typical particle flowing through Barrow Canyon is shown in figure 6.19, which also includes the particle depth, potential temperature, and salinity. The particle trajectory shows significant depth variation, which is typical for all particles. We expect this variation is due to the model velocity field, and not due to the random jumps produced by the diffusive code, which are largely within 10m.

The particle starts flowing out onto the Chukchi Sea shelf, where it is warmed in summer. In winter it is cooled and becomes saltier as it flows through Barrow Canyon. Before it leaves the shelf the particle has a salinity of approximately $S = 32PSU$ and potential temperature $T = -1$. The particle is therefore significantly denser than the surface water in the Canadian Basin, which has typical properties of $S = 30.2$ and $T = -1.2$, as temperature does not affect density much at low temperatures. The particle flows off the shelf between the first and second year, and continues towards the basin in an eddy while sinking to 200m. As the particle reaches the central Canadian Basin it is transported in the Beaufort Gyre for several loops before leaving the Arctic through Fram Strait.

These trajectories compare relatively well to Maslowski et al (2000)'s model trajectories. For constant annual forcing they find that the BSO floods the Chukchi and East Siberian shelves, and eventually crosses the Arctic in the Trans-Arctic drift. During varying atmospheric forcing they find that there is also an outflow along the Alaskan coast. This pattern is confirmed in observations by Steele et al (2004).

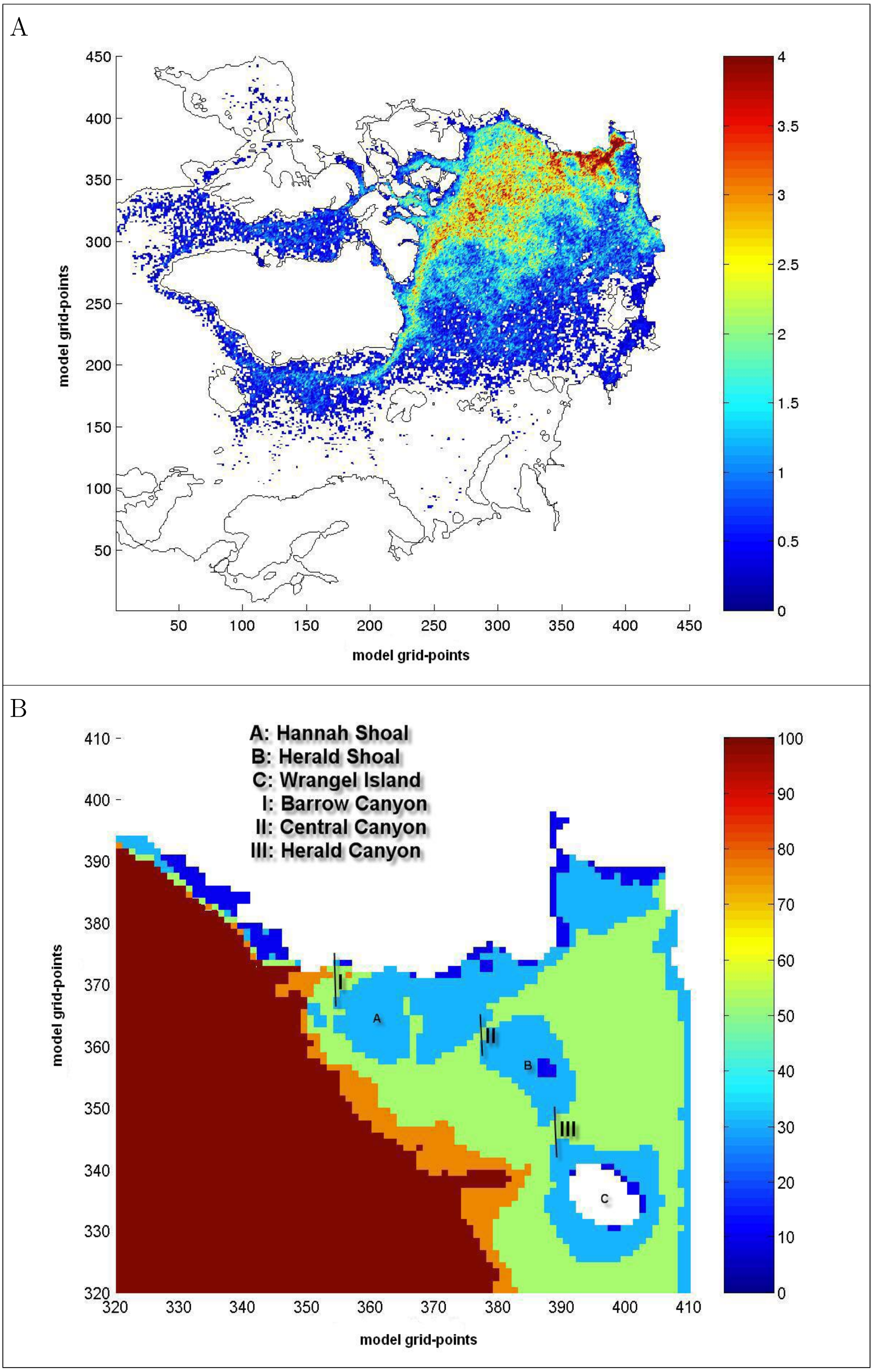

Figure 6.18: *(A) Percentage of total BSO particle flux passed through each grid-box for 20 year integration of diffusive time-dependent trajectories. Starting day: 370. Total flux* $0.5\ 10^6\ m^3/s$ *(B) Chukchi Sea bathymetry (m).*

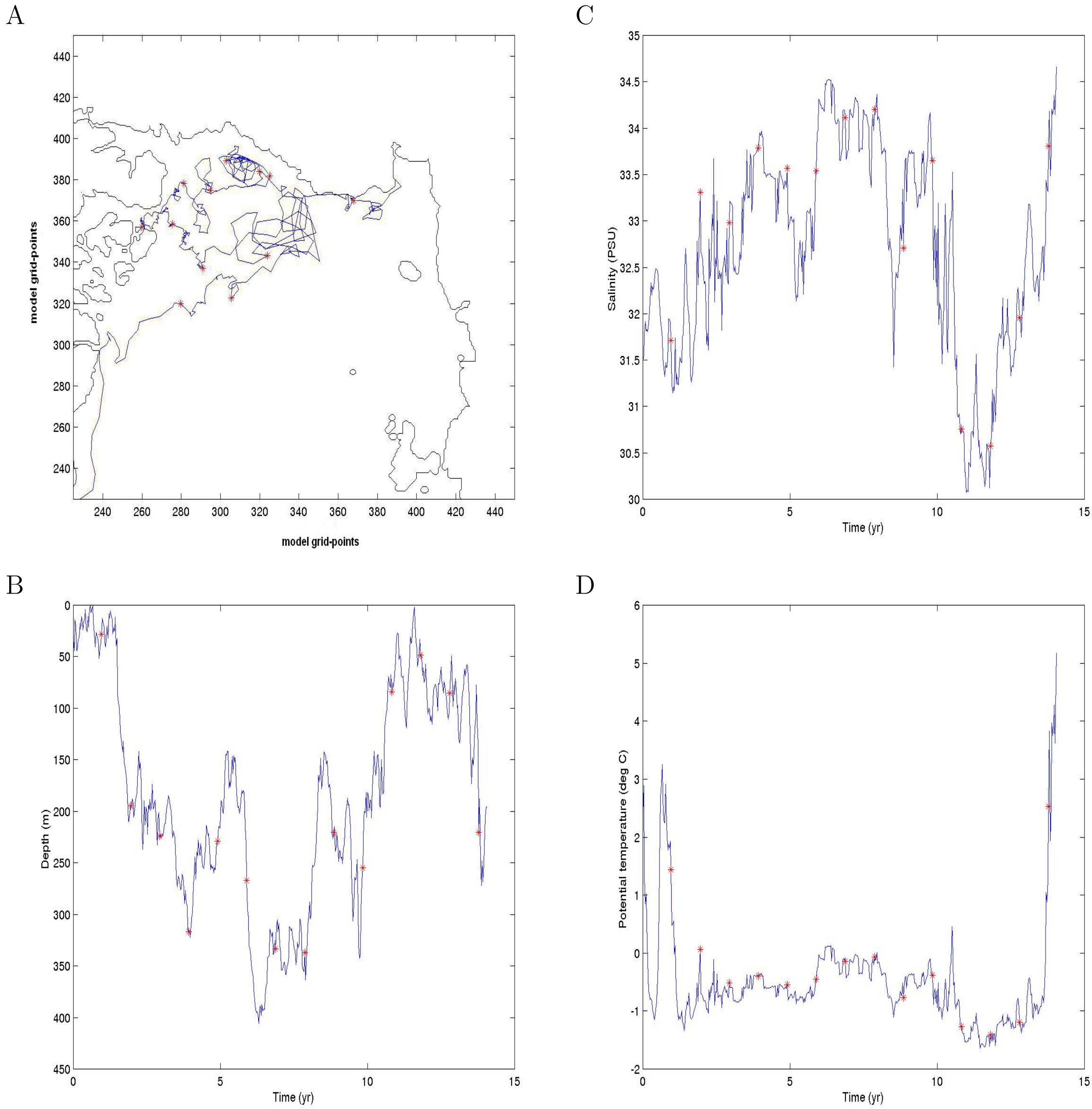

Figure 6.19: *BSO particle statistics. (A) Trajectory (B) Depth (m) (C) Salinity (PSU) (D) Potential temperature (°C).*

6.4 Signal propagation of shelf waters

Here we look at time-scales for AW and PW particles injected on the Barents and Chukchi Seas to exit the Arctic Ocean. This is an indication of the time it takes for signals to propagate from the important shelf seas into the North Atlantic Ocean. Particles exit the Arctic mainly through Fram Strait in the East Greenland current, only a small number flow through the Canadian Archipelago.

The flux of the particles that exit the Arctic have been calculated from an extended 75 year integration of diffusive time-dependent trajectories. Figure 6.20A shows the BSW particle flux that exit in yearly intervals. The graph has the shape of an asymmetric bell curve.

We expect the distribution of particles reaching the North Atlantic Ocean to resemble the solution to a diffusion or advection-diffusion equation. I start by considering a time-dependent 1D diffusion equation, which describes the evolution of a cloud of diffusing particles $P(t, x, D)$, and which is given by

$$\frac{\partial P}{\partial t} = D\frac{\partial^2 P}{\partial x^2}, \tag{6.6}$$

where D is the diffusion coefficient. The particles are injected instantaneously, therefore we expect an initial condition

$$P(0, x, D) = \delta, \tag{6.7}$$

were δ is the Dirac delta distribution representing an instantaneous source at the origin. The general solution to this problem is

$$P(t, x, D) = \frac{1}{\sqrt{4\pi Dt}} \exp\left[\frac{-x^2}{4Dt}\right], \tag{6.8}$$

which is normalized such that

$$\int_{-\infty}^{\infty} P(t, x, D)dx = 1. \tag{6.9}$$

We want to find the distribution of particles from the initial cloud reaching point a fixed point $x = x_0$, which represents the distance of an Arctic circumference. Therefore we fit the position x_0 and the diffusion parameter D of function $P(t, x_0, D)$ to the data of the diffusive time-dependent trajectories. For $t \mapsto \infty$ function $P(t, x_0, D) \mapsto 0$, and for $t \mapsto 0$ function $P(t, x_0, D) \mapsto 0$, as D is finite. Therefore this function has the required asymptotic properties to match the graph of the data.

We use the Levenberg-Marquardt method for the least squares minimization of nonlinear functions(Press et al, 1989). This method uses an initial guess to minimize

$$\chi^2(\vec{a}) = \sum_{i=1}^{N} (y_i - P(t_i, \vec{a}))^2, \tag{6.10}$$

by varying the parameter vector $\vec{a}$ (which for the 1D diffusion equation is equal to $[x_0, D]$) in the nonlinear function P. In our case the data y_i represents the percentage of the particle flux that reaches the North Atlantic during year i. We repeat this method for a series of initial guesses ($\vec{a}_0$) which are incremented within a reasonable range to obtain a global minimum.

The best fit is obtained for the values given in table 6.3. The non-dimensional variable t has been scaled as $t/360days$. The functions $P(t, x_0, D)$ and the cumulative function $\int_0^t P(t', x_0, D)dt'$ are given in figure 6.20.

Parameter	Value	Org. unit	Value	Conventional unit
x_0	12.6858	c	-	-
D	9.4724	$(c/x_0)^2/yr.$	$4.3 \cdot 10^9$	cm^2/s
χ^2	$3.91 \cdot 10^{-3}$	-	-	-

Table 6.3: *Best fit values for fitting 1D diffusion equation to propagation of diffusive time-dependent BSW particles into North Atlantic.*

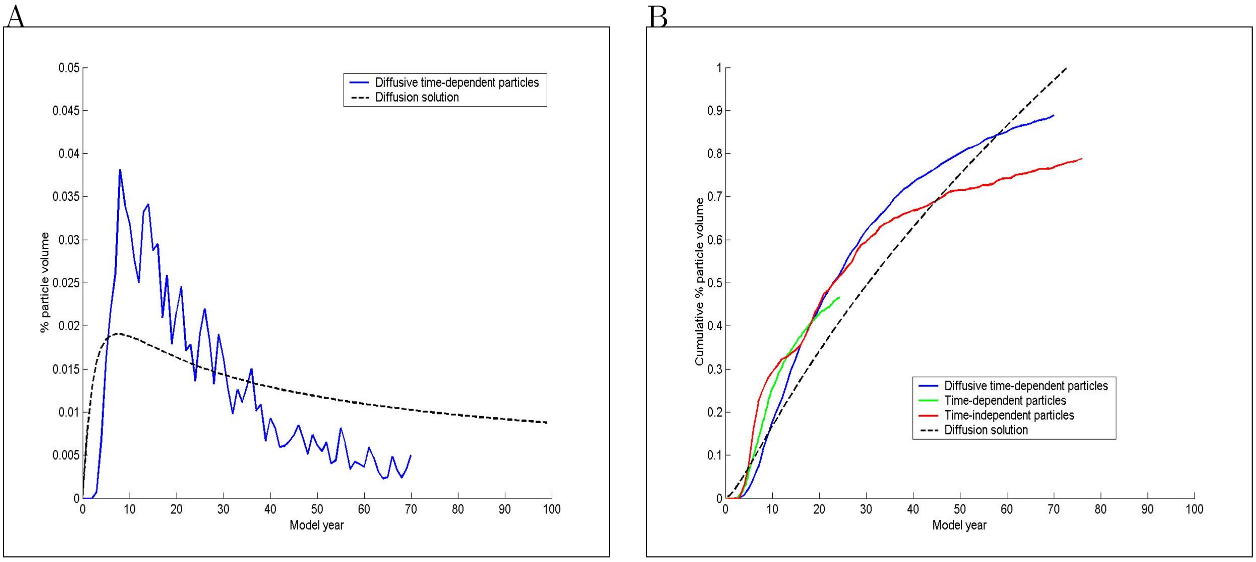

Figure 6.20: *(A).Percentage of BSW particle flux that reaches North-Atlantic in data at yearly intervals and diffusion solution (B). Cumulative percentage of BSW particle flux that reaches the North-Atlantic and diffusion solution.*

The position of x_0 measures the distance of one circumference of the Arctic, therefore the unit of D is $(c/x_0)^2/360$ days, where c represents one circumference of the Arctic. Estimating c as the distance around the boundary at level 355m gives $c = 1.5 \cdot 10^9$ cm. Then the diffusion coefficient can be converted to conventional units, which gives the high value of $D = 4.3 \cdot 10^9 \text{cm}^2/\text{s}$. As this function does not describe the data very well I next take advection into account.

The time-dependent one-dimensional advection-diffusion equation describes the evolution of a cloud of diffusing particles which are transported at constant speed V, and is given by

$$\frac{\partial P}{\partial t} + V\frac{\partial P}{\partial x} = D\frac{\partial^2 P}{\partial x^2}, \tag{6.11}$$

where D is the diffusion coefficient, and V is the speed of the transport.

The initial condition is the same as the previous model

$$P(0, x, D, V) = \delta, \tag{6.12}$$

were δ is the Dirac delta distribution representing an instantaneous source at the origin. The general solution to this problem is

$$P(t, x, D, V) = \frac{1}{\sqrt{4\pi Dt}} \exp\left[\frac{-(x - Vt)^2}{4Dt}\right], \tag{6.13}$$

which is normalized as in (6.9). In this case we fit parameters D and V of this function to the data of the diffusive time-dependent trajectories. The best fit is obtained for the values given in table 6.4.

Parameter	Value	Org. unit	Value	Conventional unit
x_0	18.4849	c	-	-
D	6.1104	$(c/x_0)^2/yr.$	$1.3 \cdot 10^9$	cm^2/s
V	1.1008	$(c/x_0)/yr.$	2.9	cm/s
χ^2	$6.4962 \cdot 10^{-4}$	-	-	-

Table 6.4: *Best fit values for fitting 1D advection-diffusion equation to propagation of diffusive time-dependent BSW particles into North Atlantic.*

The functions $P(t, x_0, D, V)$ and the cumulative function $\int_0^t P(t', x_0, D, V)dt$ are given in figure 6.21. This model is a significant improvement on the diffusion equation, reducing χ^2 by a factor of more than 5 compared to the purely diffusive solution.

Converting the parameters into conventional units gives a diffusion coefficient of $D = 1.3 \cdot 10^9 cm^2/s$ and an advection of $V = 2.9cm/s$. The diffusion coefficient is much larger than the horizontal eddy viscosity coefficient in the model of $A_H = 2 \cdot 10^6 cm^2/s$. Therefore the

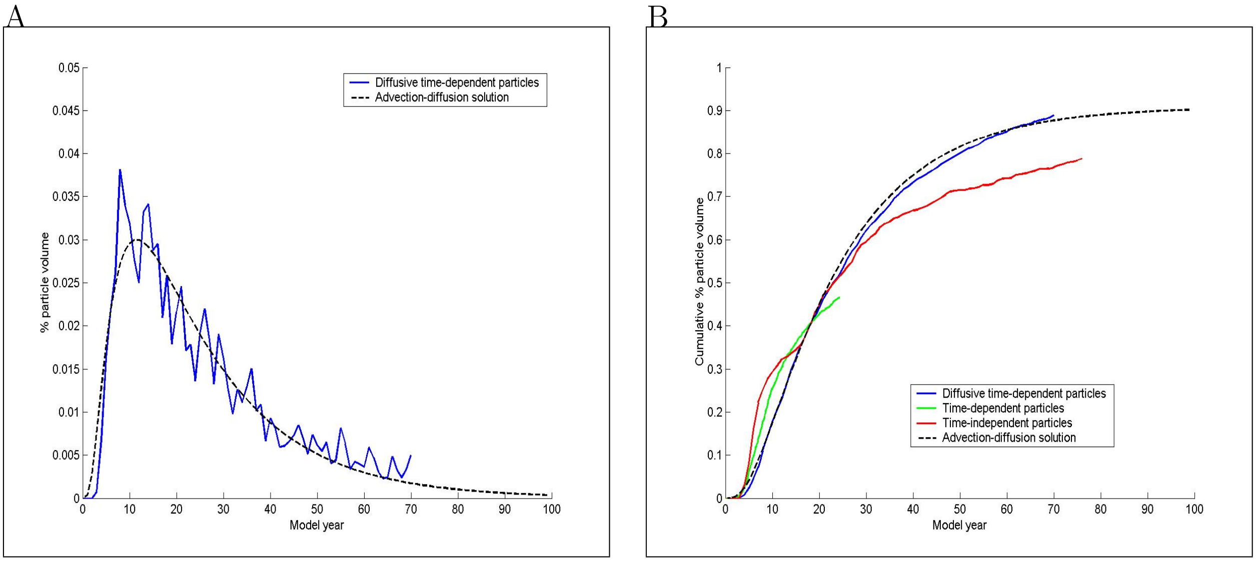

Figure 6.21: *(A).Percentage of BSW particle flux that reaches North-Atlantic in data at yearly intervals and advection-diffusion solution (B). Cumulative percentage of BSW particle flux that reaches the North-Atlantic and advection-diffusion solution.*

resolved eddies and the large-scale circulation contribute significantly to the diffusion of the particles. Taking V as the typical speed gives

$$\frac{D}{V} \approx 4483km \tag{6.14}$$

as the typical length-scale involved in diffusion. This is of the same order as the width of the Arctic Ocean (approximately 2600 km). This suggests that the 'diffusion' is primarily caused by basin-scale features such as the Beaufort Gyre, and not by meso-scale eddy features. This high value of diffusion is caused as water parcels that end up in the Beaufort Gyre tend to complete several circuits of the basin before being able to escape into the Atlantic. This agrees with views that the Beaufort Gyre is responsible for trapping water in the Canadian Basin (example Steele et al 2004).

The advection speed of $2.9cm/s$ is similar to the propagation speed found by McLaughlin et al (2002) of a large dense outflow from the Barents Sea. They found that in 1989 an atmospheric regime shift that increased cyclonic circulation in 1989 leading to a relatively large outflow of dense water from the Barents Sea could be seen 6 years later in the Canadian Basin. The signal was found approximately 5100km downstream at depths over 1000m, which leads to a mean advection speed of $2.6 cm/s$.

The time that 68% of the particle flux (the bulk) has left is approximately 33 years, which provides an estimate for the propagation time of signals from the Barents Sea into the North Atlantic. Although the strongest signal, the time of the largest outflow, occurs after approximately 10 years.

Also shown in all the cumulative distributions are the data for the 25 year integrations of time-independent, and time-dependent trajectories. The diffusive time-dependent curve shows a continuous function of particles exiting over time, while the time-independent curve indicates an unrealistic scenario of separate groups of particles exiting at different times.

The values of the best fit for the advection-diffusion solution to the outflow of the diffusive time-dependent BSO particles into the North Atlantic are given in table 6.5.

Parameter	Value	Org. unit	Value	Conventional unit
x_0	12.9097	c	-	-
D	2.6861	$(c/x_0)^2/yr.$	$5.2 \cdot 10^8$	cm^2/s
V	1.0856	$(c/x_0)/yr.$	2.7	cm/s
χ^2	$3.53 \cdot 10^{-3}$	-	-	-

Table 6.5: *Best fit values for fitting 1D advection-diffusion equation to propagation of diffusive time-dependent BSO particles into North Atlantic.*

The functions $P(t, x_0, D, V)$ and the cumulative function $\int_0^t P(t', x_0, D, V)dt$ are given in figure 6.22. Using $c = 1.0 \cdot 10^9$ cm to convert the parameters into conventional units gives a diffusion coefficient of $D = 5.2 \cdot 10^8 cm^2/s$ and an advection of $V = 2.7 cm/s$. These values are similar to the propagation of BSW, and therefore it seems the transport of the Bering Strait outflow is driven by the same processes. We can estimate the time the bulk of the signal has left the Arctic as approximately 20 years, while the largest outflow is after approximately 7 years.

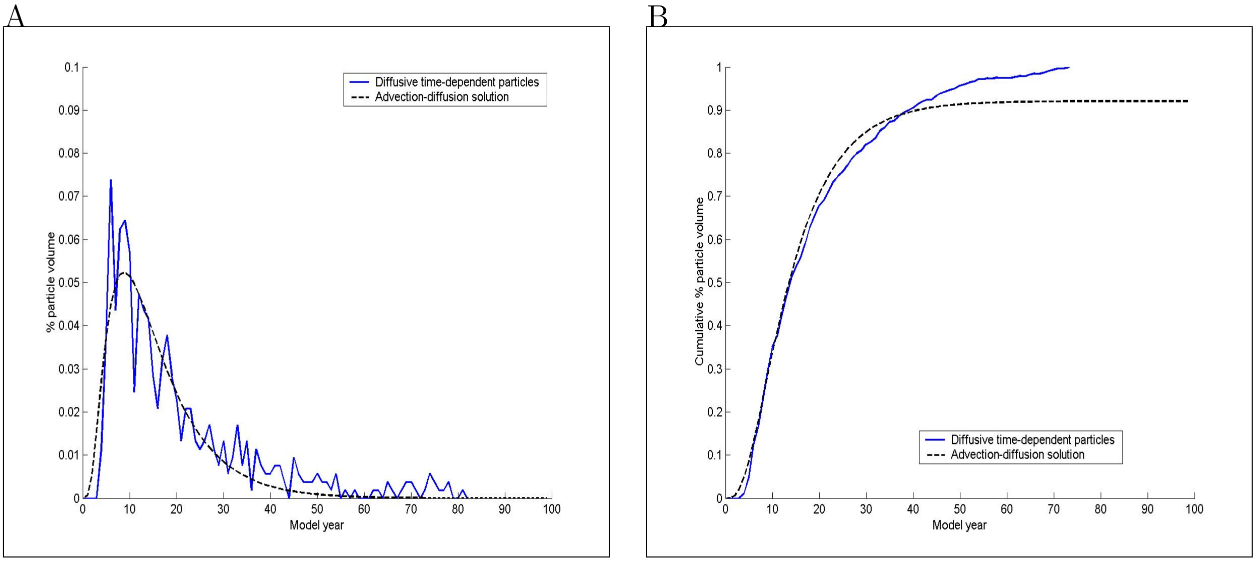

Figure 6.22: *(A).Percentage of BSO particle flux that reaches North-Atlantic in data at yearly intervals and advection-diffusion solution (B). Cumulative percentage of BSO particle flux that reaches the North-Atlantic and advection-diffusion solution.*

Chapter 7

Available Potential Energy - theory

7.1 Introduction

The purpose of this chapter is to look at the energetics to get a better feel for what physics controls the flows in the Arctic Ocean. In stratified fluids it is often convenient to discuss the energetics in terms of the available potential energy (APE). The APE of a water mass is defined as the potential energy (PE) of the water mass relative to some background state of the ocean. The standard definition of APE for the atmosphere was introduced by Lorenz (1955). He chooses the background state to be that with the minimum potential energy (PE) that can be reached by adiabatically resorting the mass of the atmosphere.

However here we are interested in values of APE in local areas of the Arctic Ocean. For this we make a new definition to calculate the APE of separate water parcels relative to the mean offshore density structure. It is this value that indicates the maximum energy that is available to drive local currents, via conversion to kinetic energy (KE). We then continue to look at the local generation of the APE due to the surface forcing. And also we look at the amount of the calculated APE that converts into kinetic energy (KE).

7.2 Previous definitions

In his definition for the atmosphere Lorenz takes the difference of total potential energy of the mass of the atmosphere and the background state. The total potential energy is the potential energy plus the internal energy. The contribution of potential energy to the APE of the ocean, also referred to as gravitational APE, is easily defined. However the contribution of the internal energy is more difficult.

The PE of a water mass in the ocean, referenced to the surface, is equal to $g\rho z$. This is used in the classic definition of the gravitational APE, which is given by

$$APE = \int\int_{V_1}\int g\rho z dV_1 - \int\int_{V_2}\int g\rho_r z_r dV_2. \tag{7.1}$$

Here (ρ_r, z_r) is the reference state. Note that adiabatically resorting the water masses can cause the free surface height to rise, which means the original state can have a different volume than the reference state.

Internal energy is the microscopic energy on atomic and molecular scale associated with the movement of molecules and atoms, and the molecular attractive forces. Changes in internal energy of the ocean between two states occur due to compression or expansion of water parcels. If salinity is assumed constant then a change of the internal energy (U) of a water mass due to a reversible process is given by (Pippard 1966)

$$dU = Tds - PdV. \tag{7.2}$$

Here V is volume, P is pressure, T is temperature, and s is entropy, which is a measure of disorder in the system. The equation of state for seawater is nonlinear, which makes it difficult to formulate the contribution of available internal energy for the ocean. Therefore in most approximations of APE the internal energy is ignored, and only the gravitational part of the APE is considered.

Reid et al.(1981) take into account the effects of compression on the internal energy in a series expansion of available total potential energy in terms of pressure, which implicitly uses the adiabatically levelled reference state. They show that the gravitational APE is the dominant term for the ocean, and find that internal energy contributes a maximum of $10-20\%$ to the total potential energy of the ocean. The contribution of internal energy is found to be negative. This means that during a readjustment process only part of the gravitational APE is converted to KE, the rest is converted to internal energy. We will see that internal energy is not relevant in our definition for the APE of separate water parcels, so we only consider gravitational terms.

For studies of limited regions (7.1) can be applied using approximations of the re-sorted local area (Bray and Fofonoff 1981). There is also a commonly used approximation of (7.1) that is derived (Bryan and Lewis 1979, Oort et al 1989) from a generalization of a formulation by Lorenz (1955), which uses the mean height over a constant density surface as a reference state

$$APE = -\frac{1}{2}g\int\int_V\int (z-z_r)^2\frac{\delta\tilde{\rho}}{dz}dxdydz. \tag{7.3}$$

This approximation shows the positive-definite character of APE. It is obtained via partial integration of (7.1), and neglecting horizontal gradients in density. In this approximation it is easy to calculate terms for generation and conversions of APE in a full energy balance (Oort et al 1994). However Huang (1998) has shown this approximation produces large errors compared to (7.1) when applied to basin-scale calculations, which he attributes to the absence of mixing in the reference state. Definition (7.3) is equivalent to the leading term in the expansion of total available potential energy found by Reid et al (1981). Although definitions (7.1) and (7.3) indicate regions of important contributions to the gravitational APE, these contributions are not accurate approximations of the energy available for separate water parcels to drive local currents.

A previous study of Arctic energetics has been performed by Uotila et al (2004) to calculate the APE for various regional coupled ocean-ice models of the Arctic Ocean. They use definition (7.3) with the mean Arctic properties as the reference state. Their main findings are the high values of APE in the Beaufort Gyre, due to light (fresh) water in the surface layers, and in the Barents Sea, due to the inflow of heavy (salty) Atlantic Water. The main conversions of APE to KE occur in the same regions. The convergence of light water in the Beaufort Gyre causes light water to rise, converting APE to KE. Inflowing AW through the Barents Sea along the Siberian continental shelf edges causes conversion of KE to APE.

In the next sections we discuss a new approach for calculating the energy available for local water parcels to sink into the offshore ocean basin.

7.3 Regional Available Potential Energy

Here we first discuss the mean offshore reference state and then derive a new definition to calculate the maximum energy available on the continental shelves for driving local currents in the Arctic Ocean.

7.3.1 Reference state

We divide the Arctic Ocean into two sets of basins, the Eurasian Basin and the Canadian Basin. The Eurasian Basin consists of the Nansen and Amundsen Basin, and the Canadian Basin also includes the Makarov Basin. For the mean offshore density we average over water columns deeper than 1500 metres over an area covering both the Eurasian and the Canadian Basins. We expect this area to be relatively quiet, so that the isopycnals are relaxed to a stable reference state. We start by comparing the mean offshore densities of the Eurasian and Canadian Basins. In figure 7.1A the positions of the areas are shown. The corresponding reference densities, and potential temperatures and salinities, are shown in figure 7.1B.

The reference densities only differ in the top 400 metres, where the Eurasian Basin is denser than the Canadian Basin. This corresponds to the salinity differences. The Eurasian Basin is saltier than the Canadian Basin due to the inflow of salty Atlantic Water (AW). The large differences in temperature in the top 800 metres do not contribute much to density. This is due to the thermal expansion coefficient, which is small at the low temperatures in the Arctic.

As the salinity dominates density, the AW is already dense enough to sink into the Arctic Ocean. Therefore it has the possibility to flood the Arctic Ocean if it makes it through Fram Strait. However only a small part of the AW watermass makes it through Fram Strait into the Arctic Ocean.

We have compared the density of inflowing AW along the continental slope with the mean offshore densities on both sides of Fram Strait. This is shown in figure 7.2. Also shown is the density for a water column in the Barents Sea on the other pathway of AW into the Arctic Ocean. There is a large temperature and salinity front between water masses at the sides of Fram Strait, which prevents the warm, salty AW from entering the cold, fresh Arctic due to geostrophy. Although a flow dominated by botttom friction, which is more important than the Coriolis force in shallow water, would be able to pass through the Arctic Front, however most AW particles recirculate before Fram Strait back into the Atlantic (as seen in chapter 6). This is also seen in the AW particle trajectories in chapter 6, which mostly recirculate in

Fram Strait back into the Atlantic. The AW also cannot sink down the slope before Fram Strait. Although the AW in the upper 200 metres on the slope is dense enough to sink into the Arctic Ocean, it is at a stable depth relative to the mean offshore state on the Atlantic side of Fram Strait. The water column of BSW in the Barents Sea is significantly cooler and fresher. This implies the cooling and freshening of AW on the Barents Sea pathway allows it to pass through the Arctic front, and this pathway therefore acts as a short circuit for AW to sink into the Arctic Ocean via a boundary current.

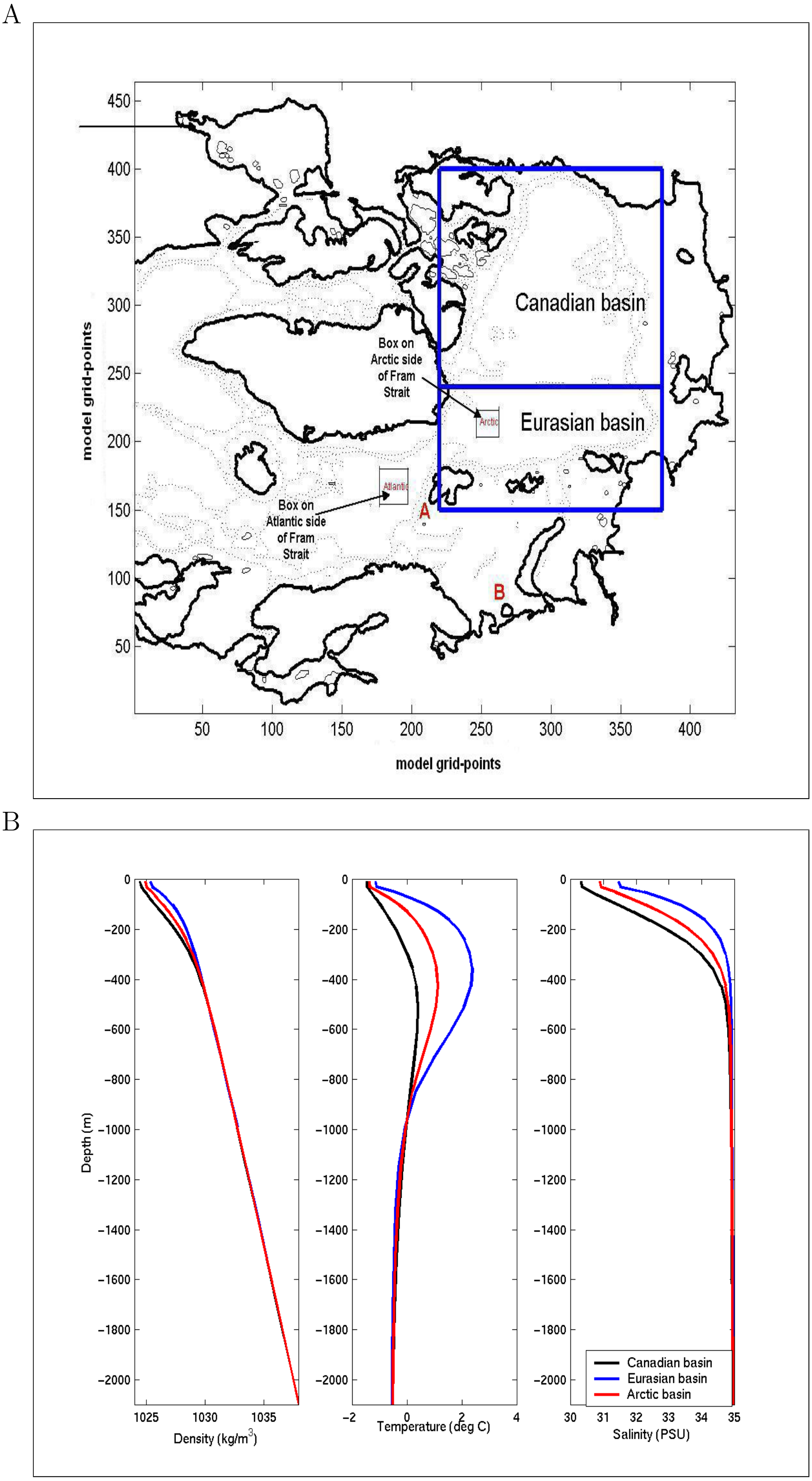

Figure 7.1: *(a) Arctic with contours at 355m and 1515m. AW columns marked by A and B. (b) Reference properties for the Eurasian Basin, Canadian Basin and Arctic (total).*

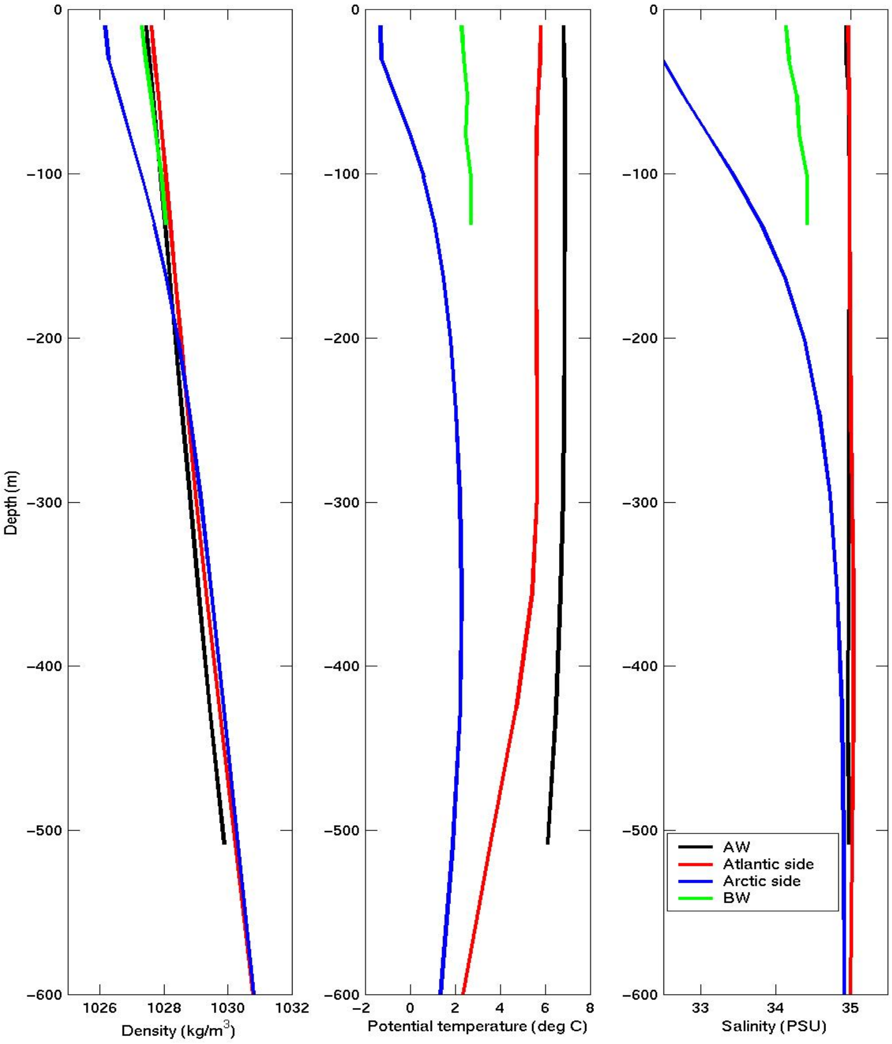

Figure 7.2: *Properties (AW) for Atlantic Water current on continental slope approaching Fram Strait, mean properties of offshore water masses on both sides of Fram Strait, and water in the Barents Sea (BW). Atlantic/Arctic side refers to box on Atlantic/Arctic side of Fram Strait as shown in figure 7.1A.*

7.3.2 2D definition of APE

One possible approach is to compare the total PE of water columns on the shelf to the total PE of the water in the reference column. Consider a water column on the continental shelf of depth H_s with a density profile $\rho_s(z)$. The energy of this column (in J/m^2) is then the PE of the shelf column minus the PE of the reference state

$$APE = \int_{H_s}^{0} g \cdot \rho_s \cdot z \cdot dz - \int_{H_o}^{0} g \cdot \rho_o \cdot z \cdot dz. \tag{7.4}$$

However this depth-integrated field of APE per water column will give a distorted view due to the differences in depths. Even a field of APE per water column per unit depth can distort the view due to differences in the mean value of depth (z). In that case a water parcel with a fixed amount of APE flowing horizontally to a deeper column would appear to lose APE, as the height of the water column increases. Therefore the best way for showing up regions of relative importance is to have a three-dimensional field of APE.

7.3.3 3D definition of APE: Equivalent to classical definition

Here we look at water parcels on the shelf and determine their stable depth in the reference column. We then compare the PE of the water parcel at its original depth on the shelf to the PE it would have if it was placed at the stable depth in the reference column. In this (adiabatic) displacement we neglect all movements of other water parcels.

We consider a water parcel with a fixed volume of δV_0 in the shelf column. The depth (z) is taken positive everywhere. The PE (per unit volume) of this parcel is

$$PE_s = g \cdot \rho_s(z) \cdot z \cdot \delta V_0. \tag{7.5}$$

The stable depth of this water parcel in the reference column is $z_o(\rho_s(z))$. The PE of the parcel at this depth in the reference column would be

$$PE_o = g \cdot \rho_s(z) \cdot z_o(\rho_s(z)) \cdot \delta V_0, \tag{7.6}$$

assuming the volume of the water parcel stays constant. The APE of this water parcel (in J/m^3) is then

$$APE_1 = g \cdot \rho_s(z) \cdot [z_o(\rho_s(z)) - z] \cdot \delta V_0. \tag{7.7}$$

This definition is equal to the integrand in the global definition (7.1).

Figure 7.3a shows a horizontal map of annual averaged APE at 30 metres depth using this definition. The main feature in this map is the large amount of energy available due to the inflowing AW. The APE along the first part of the boundary current can be clearly traced to the Barents Sea pathway. The APE of AW in the Fram Strait pathway does not make it as far along the continental slope. Other features are the APE due to the Bering Strait outflow, and there is a very small negative APE on the Siberian shelves due to the inflow of cold river water. In this definition negative energy is possible for light water whose depth on the shelf is larger than the reference depth. This represents energy that can be released if offshore water floods the shelf, which would lead to rising of the shelf water mass. Apart from the negative energies this definition shows the same features as those found by Uotila et al (2004).

This definition shows up areas of important contributions to APE, but neglects all interactions with other water parcels. When a water parcel sinks down it requires other water parcels to move up. This raises other water parcels above their stable depth and provides a negative contribution to APE. This effect is considered in the next section.

7.3.4 3D definition of APE: Including adjustment of reference state

Here we consider again a reversible adiabatic process whereby the water parcel is allowed to sink to a stable depth in the reference column. This time we include the interactions with the surrounding water in this process, but neglect the compression of the water parcel during sinking. We then define the APE as the work done on the water parcel by the buoyancy force. As the buoyancy force always works in the direction of the vertical displacement this leads to a positive-definite definition of APE. This process is equivalent to subtracting from (7.7) the gain in APE due to the opposite vertical displacements of the water parcels in the reference column.

A water parcel will have a net buoyancy force (per unit volume) acting on it at each depth z' in the column of

$$F_B = [\rho_s(z) - \rho_o(z')] \cdot g \cdot \delta V_0. \tag{7.8}$$

The work made available by letting the water parcel sink gives the following definition of APE (in J/m^3)

$$APE_2 = \int_z^{z_o(\rho_s(z))} F_B \cdot dz' = \int_z^{z_o(\rho_s(z))} [\rho_s(z) - \rho_o(z')] \cdot g \cdot \delta V_0 \cdot dz'. \tag{7.9}$$

Figure 7.3b shows a horizontal map of APE at 30 metres depth using this definition. This map shows the same overall structure as the map of the previous definition, but now the values are positive everywhere with reduced magnitude. This can be seen by the connection of APE_2 with APE_1

$$APE_2 = APE_1 - \int_z^{z_o(\rho_s(z))} [\rho_o(z')] \cdot g \cdot \delta V_0 \cdot dz'. \tag{7.10}$$

The energy on the Siberian shelves is more obvious now due to large density difference of the fresh river inflow with the offshore Arctic water. There is still energy from the Bering Strait outflow, but it is reduced in comparison to the highest APE in the Barents Sea.

This definition neglects the compressibility of the water parcel. As the water parcel sinks its volume will be compressed, and it will become denser. This will cause the water parcel to sink further in the reference column. This effect is considered in the next section.

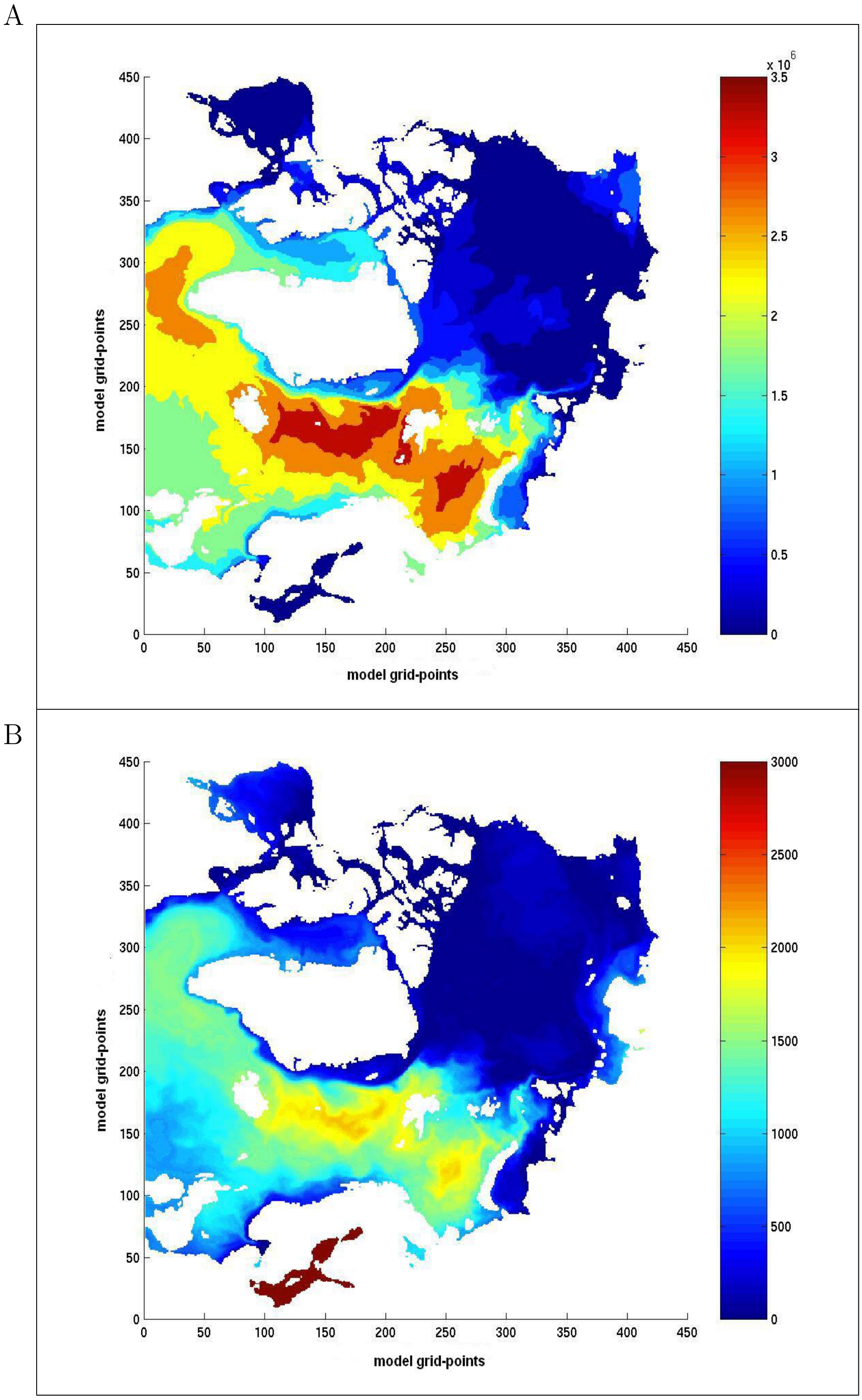

Figure 7.3: *(A) Definition 1 and (B) definition 2 of APE (J/m^3) at a depth of 30 metres. (Note change in scales).*

7.3.5 3D definition of APE: Including compressibility effects

Here we add the effects of compressibility to definition (7.9) by considering a reversible adiabatic compression process. The water parcel is allowed to sink to a stable depth in the reference column, while being compressed. As the water parcel is compressed its density will increase, its volume will decrease and its in-situ temperature will rise. The volume of the water parcel is now not conserved, and its internal energy U changes.

The change of U in a reversible process is given by (7.2). As the water parcel sinks it does not exchange heat with the surroundings so the change in heat $dQ = Td\eta = 0$. The only change is therefore due to the change in volume of the ocean (PdV) due to the net effect of compression of the sinking water parcel, and expansion of the rising water parcels in the reference column. As the water parcel sinks it is replaced at each depth by a water parcel from the reference state. The compression is performed by the global pressure field, and the energy comes from a slight fall in sea surface height. This does not change the APE of the water parcel, but is important when considering the APE of the global ocean.

The density of the water parcel at each depth can be written as

$$\rho_s^c(z') = \rho_s(z) \cdot [1 + \alpha(z')] \,, \tag{7.11}$$

where $\alpha(z)$ is the change in density due to adiabatic changes in temperature and changes in pressure. As the water parcel is compressed its volume will decrease. The volume of the water parcel at each depth can be written, using conservation of mass, as

$$\delta V(z') \quad = \quad \left[\frac{1}{1 + \alpha(z')}\right] \cdot \delta V_0. \tag{7.12}$$

The depth to which the water parcel will sink is $z_o(\bar{\rho_s}(z)$, where $\bar{\rho_s}$ is the potential density of the water parcel referenced to its stable depth in the reference column. Using these values in definition (7.9) gives

$$APE_3 = \int_{z}^{z_o(\bar{\rho}_s(z))} \left[\rho_s^c(z') - \rho_o(z')\right] \cdot g \cdot \left[\frac{1}{1+\alpha(z')}\right] \cdot \delta V_0 \cdot dz'. \tag{7.13}$$

This definition can be separated into contributions from the compressibility of the water parcel, and a contribution from the density differences between the water parcel and the reference column. The reference density can be written as

$$\rho_o(z') = \rho_s(z) \cdot \left[1 - \beta(z')\right], \tag{7.14}$$

where $\beta(z')$ is the change in density due to the stratification of the reference column. The integral in (7.13) can then be separated into 3 components

$$\begin{aligned} APE_3 &= \int_{z}^{z_o(\rho_s(z))} \rho_s(z) \cdot \left[\frac{\beta(z')}{1+\alpha(z')}\right] \cdot g \cdot \delta V_0 \cdot dz' \\ &+ \int_{z}^{z_o(\rho_s(z))} \rho_s(z) \cdot \left[\frac{\alpha(z')}{1+\alpha(z')}\right] \cdot g \cdot \delta V_0 \cdot dz' \\ &+ \int_{z_o(\rho_s(z))}^{z_o(\bar{\rho}_s(z))} \rho_s(z) \cdot \left[\frac{\alpha(z')+\beta(z')}{1+\alpha(z')}\right] \cdot g \cdot \delta V_0 \cdot dz'. \end{aligned} \tag{7.15}$$

The coefficients $\alpha(z)$ and $\beta(z)$ are of the order of 10^{-3} or smaller. By approximating $1+\alpha(z) \approx 1$ in the denominator we can separate the APE into a contribution from incompressibility (first term on right-hand side (RHS) of (7.15)) and contributions from compressibility (second and third terms on RHS of (7.15)).

Figure 7.4 shows density profiles for a column in the Barents Sea, with three areas representing different contributions. In this diagram we can approximate

$$APE \approx g \cdot \delta V_0 \cdot \left[A + B + C\right]. \tag{7.16}$$

Here area A represents the first term on the RHS of (7.15), area B represents the second term on the RHS of (7.15), and area C represents the third term on the RHS of (7.15).

This figure shows that typical density differences between waters in the Barents Sea and water from the reference state are of the order of $2kg/m^3$. The vertical acceleration, or reduced gravity, is then equal to

$$\frac{\partial w}{\partial t} = g \cdot \frac{\Delta \rho}{\rho} \approx 0.02m/s^2. \tag{7.17}$$

Assuming a typical boundary current speed is of the order of $0.1m/s$, then the time needed to gain this velocity from a stationary position is 5 seconds, which is equivalent to vertical sinking of only $0.5m$. Therefore a typical water parcel in the Barents Sea would only have to sink $0.5m$ to reach the boundary current speed, in the absence of turbulence and mixing. It should be noted that the density difference between the Barents Sea water mass and the reference state will reduce during sinking, although this is insignificant in the initial $0.5m$ of sinking.

Figure 7.5a shows a horizontal map of APE at 30 metres depth using this definition, and figure 7.5b shows only the compressibility contribution (B+C). We can see that the compressibility gives a significant contribution to the values of APE at the surface in the Barents Sea. Compressibility of seawater is largest for cold and fresh water so this an important contribution for Arctic Ocean water. The coldest and freshest water is the river water on the Siberian shelves, however compressibility has little effect on the APE of this water mass as it is very close to its stable depth at the surface.

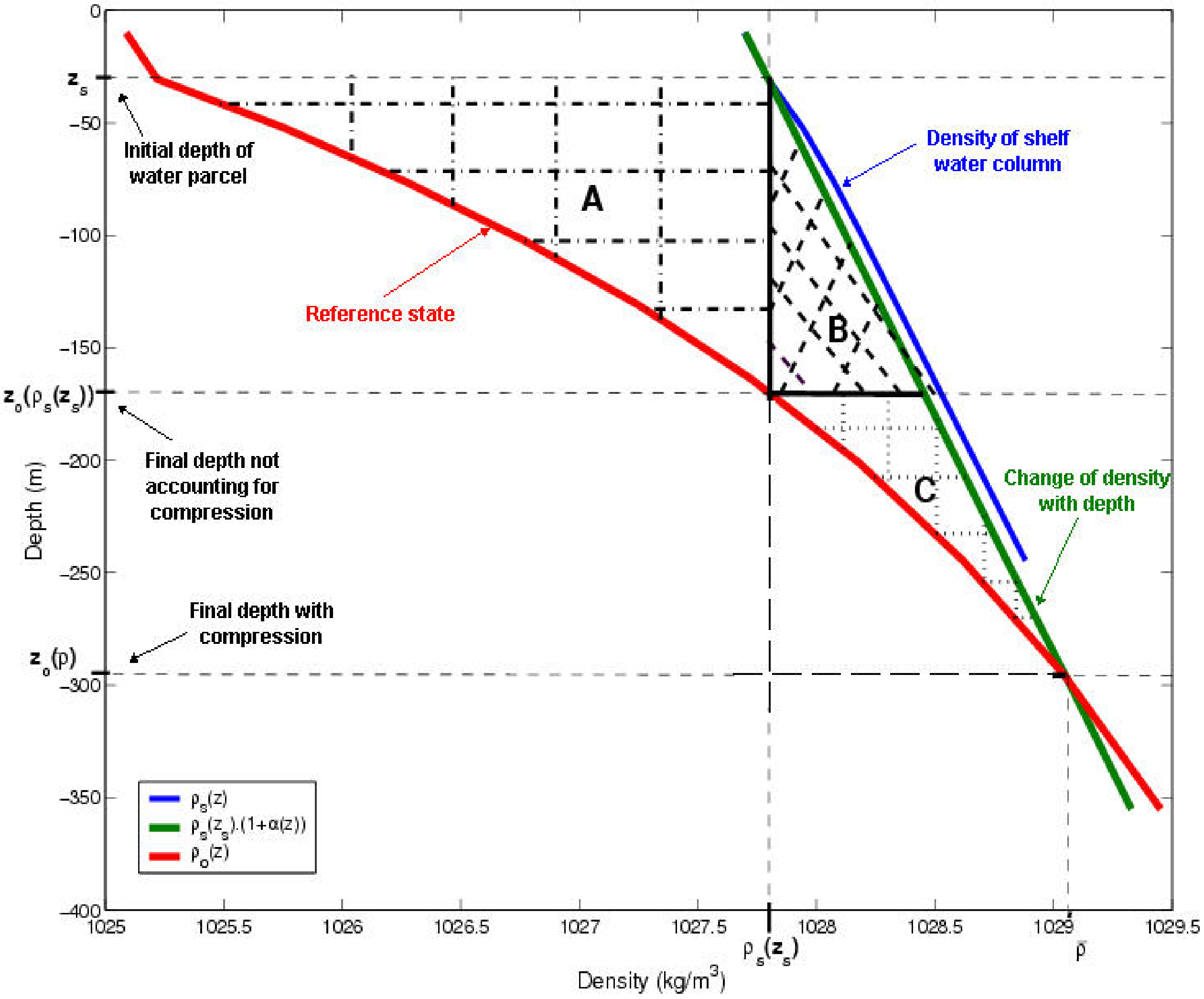

Figure 7.4: *Profiles of* $\rho_s(z')$,$\rho_s^c(z')$ *for a column in the Barents Sea, and* $\rho_o(z')$ *for an averaged area in the central Arctic Ocean. The APE of the water parcel at depth* z *is approximately* $g \cdot \delta V_0 \cdot [A + B + C]$. *Area* A *represents the contribution from incompressibility. Areas* $B + C$ *represent the contributions from compressibility.*

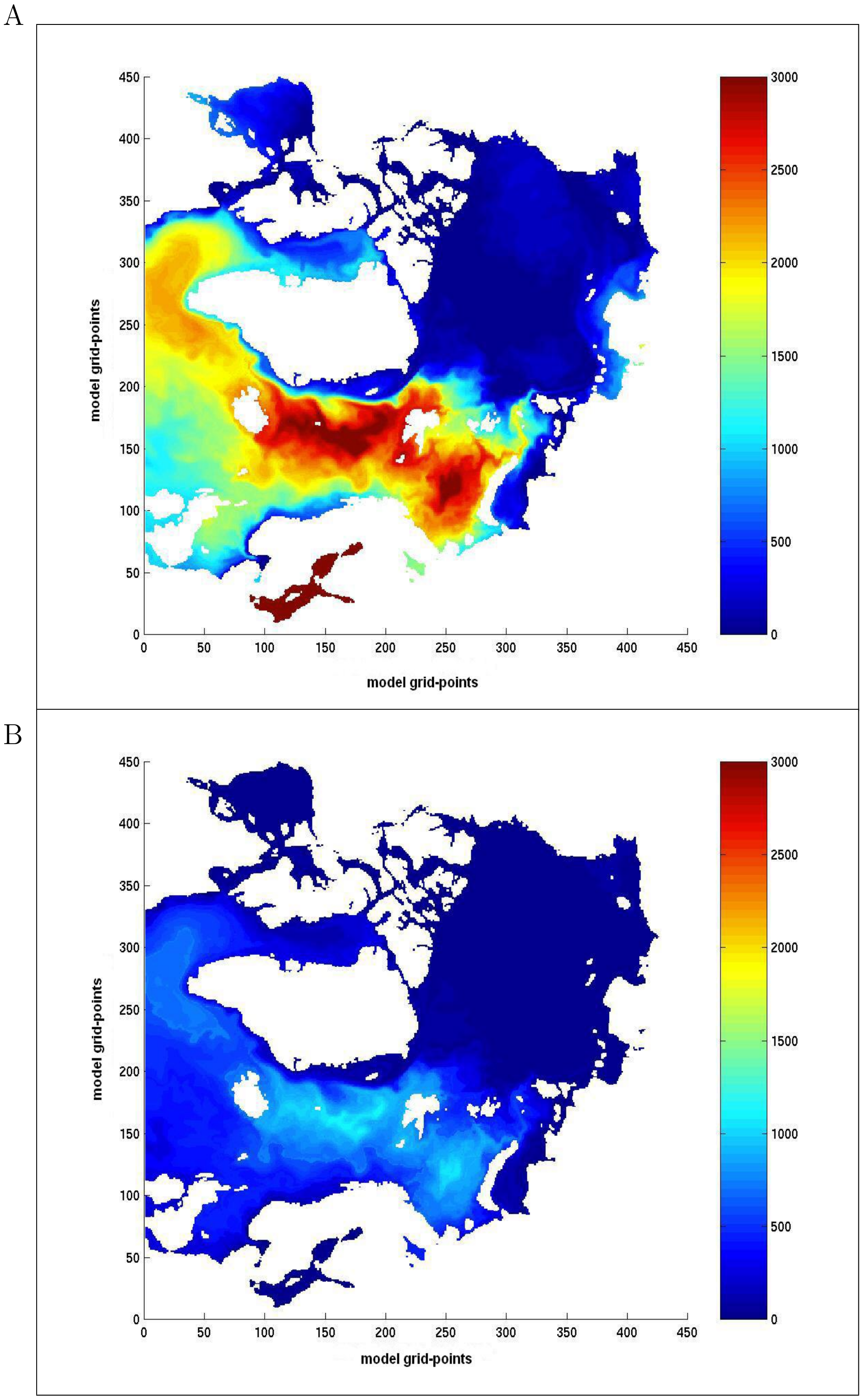

Figure 7.5: *(A) Definition 3 and (B) compressibility contribution of APE* (J/m^3) *at a depth of 30 metres.*

7.4 Available Potential Energy balance

In this section we look at energy conservation laws, and formulate a balance by listing conversion terms for losses and gains of APE.

7.4.1 Conservation laws

Water parcels in the ocean are subject to advection and diffusive mixing. Here we aim to determine whether the APE is conserved under these processes.

The APE has been defined as the work done in letting a water parcel sink adiabatically to its stable depth in the reference column. However a water parcel can take any number of pathways from its original position on the continental shelf to the deep basin. In the following consideration we determine whether the work done in letting the water parcel sink is independent of its pathway through the ocean, whereby we assume there is no mixing that affects the potential temperature and salinity of the water parcel.

We compare two pathways, which are shown in figure 7.6. The first is the original pathway in our definition of APE, whereby the water parcel moves across to the reference column ($\rho_o(z)$) at depth z and is allowed to sink to its stable depth $z_o(\bar{\rho})$. In the second pathway the water parcel first sinks in the original column ($\rho_s(z)$) to depth $z_o(\bar{\rho})$, before moving across to the reference column.

Up to now we have ignored the work done against the horizontal pressure gradient in moving across from the original column to the reference column. Defining the pressure profiles in the shelf and reference columns as $P_s(z)$ and $P_o(z)$, the work (per unit volume) done in moving a water parcel from the original column to the reference column at depth z is given

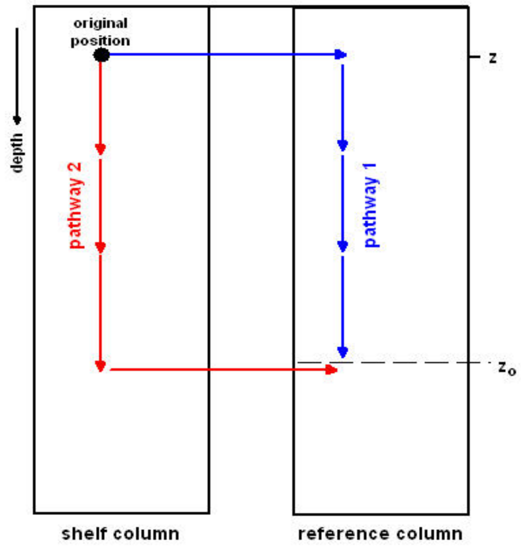

Figure 7.6: *Two pathways for water parcel to reach stable depth in reference column. The first pathway (as used in APE definition) crosses to reference column first, and then sinks to stable depth. The Second pathway sinks in shelf column first, and then crosses to reference column.*

by

$$W_P = [P_s(z) - P_o(z)] \cdot \delta V_0 \cdot \left[\frac{1}{1+\alpha(z)}\right]. \tag{7.18}$$

The last factor on the right-hand side is negligible, as $\alpha(z)$ (defined in (7.11)) is of the order of 10^{-3}, and is therefore ignored in the following analysis. The work done on the first pathway is then equal to the sum of the APE of the water parcel and the work done against the horizontal pressure gradient at depth z, which is given by

$$W_1 \quad = \quad g\int_z^{z_o(\bar{\rho})} [\rho_s^c(z') - \rho_o(z')] \cdot \delta V_0 \cdot dz' \quad + \quad [P_s(z) - P_o(z)] \cdot \delta V_0. \tag{7.19}$$

The corresponding expression for the work done on the second pathway is given by

$$W_2 \;=\; g\int_z^{z_o(\bar{\rho})} [\rho_s^c(z') - \rho_s(z')] \cdot \delta V_0 \cdot dz' \;+\; [P_s(z_o(\bar{\rho})) - P_o(z_o(\bar{\rho}))] \cdot \delta V_0 \quad (7.20)$$

The last term on the right-hand side of (7.20) can be rewritten using the hydrostatic equation for pressure as

$$[P_s(z_o(\bar{\rho})) - P_o(z_o(\bar{\rho}))] \cdot \delta V_0 \;=\; [P_s(z) - P_o(z)] \cdot \delta V_0 \;+\; g\int_z^{z_o(\bar{\rho})} [\rho_s(z') - \rho_o(z')] \cdot \delta V_0 \cdot dz'.$$

Substituting this into equation (7.20) gives

$$W_2 \;=\; g\int_z^{z_o(\bar{\rho})} [\rho_s^c(z') - \rho_o(z')] \cdot \delta V_0 \cdot dz' \;+\; [P_s(z) - P_o(z)] \cdot \delta V_0, \quad (7.21)$$

which is equal to the work done on the first pathway. The second pathway has been chosen arbitrarily, which implies the work done is independent of the pathway of the water parcel, as long as we assume there is no mixing.

Therefore in this case APE is conserved under advection if we take into account the changes of APE due to vertical motion, and any work done against horizontal pressure gradients. The total work done in moving the water parcel is available for conversion to kinetic energy (KE) as along any pathway dx

$$\begin{aligned} \frac{dKE}{dx} &= \rho \cdot v \cdot \frac{dv}{dx} \cdot \delta V_0 & (7.22)\\ &= \rho \cdot v \cdot \frac{dv}{dt}\frac{dt}{dx} \cdot \delta V_0, & (7.23) \end{aligned}$$

which is equal to a force $F = \rho \cdot dv/dt \cdot \delta V_0$. Therefore any change in KE is equal to the total work done

$$\delta KE = \int F dx, \quad (7.24)$$

where the KE here includes the large scale kinetic energy of the flow plus any losses to internal energy of the fluid due to turbulence. This leads to the following conservation law for APE following a water parcel (ignoring work against viscosity)

$$\delta APE + \delta KE + W_P = 0, \tag{7.25}$$

which is equivalent to Bernoulli's law (eg. Gill 1982) as $P_o(z)$ is constant.

Next we look at conservation of APE under horizontal mixing, starting for a simple case with a linear equation of state. We compare the APE of two adjacent water parcels, with densities ρ_1 and ρ_2, that are both at depth z before and after they mix with each other, assuming that there are no other exchanges occurring. The original amounts of APE are given by (ignoring changes in volume)

$$APE_1 = g\int_z^{z_o(\overline{\rho_1})} [\rho_1(z') - \rho_o(z')] \cdot \delta V_0 \cdot dz', \tag{7.26}$$

$$APE_2 = g\int_z^{z_o(\overline{\rho_2})} [\rho_2(z') - \rho_o(z')] \cdot \delta V_0 \cdot dz'. \tag{7.27}$$

Assuming $\rho_1 < \rho_2$ the densities at depth z of both water parcels after mixing using a linear equation of state will be $\rho_1 - d\rho$ and $\rho_2 + d\rho$. These changes will affect the stable depth of the water parcels in the reference column and also the entire density profile from the original depth to the stable depth. The new density profiles are given by $\overline{\rho_1}(z)$ and $\overline{\rho_2}(z)$, which leads to the following amounts of APE after mixing

$$\overline{APE}_1 = g\int_z^{z_o(\overline{\rho_1+d\rho})} [\overline{\rho_1}(z') - \rho_o(z')] \cdot \delta V_0 \cdot dz', \tag{7.28}$$

$$\overline{APE}_2 = g\int_z^{z_o(\overline{\rho_2-d\rho})} [\overline{\rho_2}(z') - \rho_o(z')] \cdot \delta V_0 \cdot dz'. \tag{7.29}$$

The changes in APE of both water parcels, $\overline{APE}_1 - APE_1$ and $\overline{APE}_2 - APE_2$, do not necessarily compensate as z_o is a nonlinear function of ρ. This can be seen in the (red) reference density profile in figure 7.7. Also in the case of a nonlinear equation of state the density profiles $\rho(z)$ and $\overline{\rho}(z)$, representing the changes in density with depth due to adiabatic changes in temperature and pressure, are very nonlinear. An example showing that the changes in the APE of two water parcels do not compensate during horizontal mixing is given in figure 7.7. Here the changes in density of both water parcels $d\rho$ compensate, whereas the gain in APE of water parcel 1 (area A) is not equal to the loss in APE of water parcel 2 (area B).

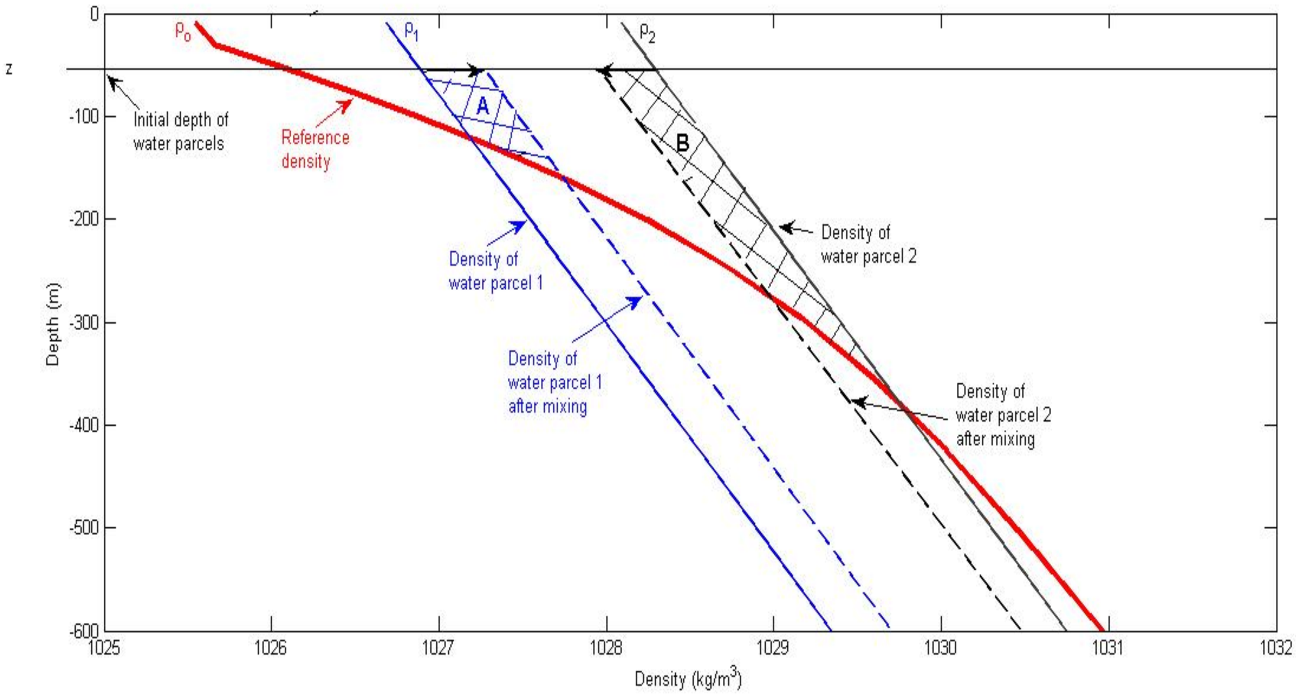

Figure 7.7: *Density profiles of two mixing water parcels. Area A represents the APE gained by water parcel 1 due to mixing, and area B represents the APE lost by water parcel 2 due to mixing.*

The density profiles of the water parcels in figure7.7 have been calculated using the following linear equation of state

$$\rho(z) = \alpha T + \beta S + \gamma z + \delta, \tag{7.30}$$

where $\alpha, \beta, \gamma, \delta$ are constants. For the calculation of the reference density profile the temperature and salinity in this equation are replaced by $T = T_o(z)$ and $S = S_o(z)$, which are the properties at each depth in the reference column. Using this equation the change in density due to mixing of heat and salt is given by

$$d\rho = \alpha dT + \beta dS. \tag{7.31}$$

The change in APE due to mixing for the first water parcel becomes

$$\Delta APE_1 \; = \; g \int_{z}^{z_o(\overline{\rho_1})} d\rho \cdot \delta V_0 \cdot dz' + g \int_{z_o(\overline{\rho_1})}^{z_o(\overline{\rho_1 + d\rho})} \left[\rho_1(z') + d\rho - \rho_o(z')\right] \cdot \delta V_0 \cdot dz'.$$

This can be rewritten using equation (7.30) as

$$\begin{aligned} \Delta APE_1 \; &= \; g \int_{z}^{z_o(\overline{\rho_1})} \left[\alpha dS + \beta dT\right] \cdot \delta V_0 \cdot dz' \\ &+ \; g \left[z_o(\overline{\rho_1 + d\rho}) - z_o(\overline{\rho_1})\right] (\alpha T_1 + \beta S_1) \delta V_0 \\ &- \; g \int_{z_o(\overline{\rho_1})}^{z_o(\overline{\rho_1 + d\rho})} \left[\alpha T_o(z') + \beta S_o(z')\right] \cdot \delta V_0 \cdot dz'. \end{aligned} \tag{7.32}$$

If $d\rho$ is an infinitesimally small change, and using the fact that $z_o(\rho)$ is a continuous function, the third term on the right-hand side can be approximated by

$$g \left[z_o(\overline{\rho_1 + d\rho}) - z_o(\overline{\rho_1})\right] (\alpha T_o(z_o(\overline{\rho_1})) + \beta S_o(z_o(\overline{\rho_1}))) \cdot \delta V_0 \cdot dz' + \mathcal{O}(d\rho \cdot dz_o). \tag{7.33}$$

This term then approximately cancels out the second term on the right-hand side of (7.32) as

$$\alpha T_1 + \beta S_1 - \alpha T_o(z_o(\overline{\rho_1})) - \beta S_o(z_o(\overline{\rho_1})) = 0, \tag{7.34}$$

which is equivalent to the requirement that the density of the water parcel and the reference column are equal at the stable depth $z_o(\overline{\rho_1})$. Considering only the first term on the right-hand side of (7.32), the changes in APE of water parcels 1 and 2 will only cancel out if the stable depths of the two water parcels are equal $(z_o(\overline{\rho_1}) \neq z_o(\overline{\rho_2}))$. Even when considering all three terms in the right-hand side of (7.32) these changes do not necessarily compensate.

Therefore even using a linear equation of state mixing can create or destroy APE, meaning there is no conservation law possible. In the next section we look at the contribution of mixing to APE in a fixed volume, which can become relatively large. This is due to the fact that it is not only mixing on the boundaries that affects the total APE of the volume of water, but also (especially) mixing within the volume that can create or destroy APE.

7.4.2 Conversion terms

Here we identify terms for losses and gains of APE. The APE of a fixed water parcel can change due to air-sea fluxes, such as heating, cooling, precipitation, evaporation. The APE can also be converted into kinetic energy (KE) during sinking, however not all APE is turned into large scale ocean currents as some of the KE is quickly lost as turbulence due to bottom friction. Another conversion term is the loss, or gain, of APE due to mixing with neighbouring water masses. The APE of a fixed volume also changes due to advection. Therefore for a volume V

$$\int\int_V\int \frac{\partial APE}{\partial t} dV + \int\int_V\int \left[u\frac{\partial APE}{\partial x} + v\frac{\partial APE}{\partial y} + w\frac{\partial APE}{\partial z}\right] dV \tag{7.35}$$

$$= C(FF, APE) + C(HF, APE) - C(APE, KE) - C(APE, MX), \tag{7.36}$$

where the terms $C(FF, APE), C(HF, APE)$ are the conversion to APE from freshwater and heat fluxes, and the terms $C(APE, KE), C(APE, MX)$ are the conversion of APE to kinetic energy and mixing. The advection terms can be written as fluxes through the boundaries b using the divergence theorem and the continuity equation

$$\int\int_V\int \left[u\frac{\partial APE}{\partial x} + v\frac{\partial APE}{\partial y} + w\frac{\partial APE}{\partial z}\right] dV = \int\int_b APE\,\mathbf{u}\,\mathbf{n} db = C(FL, APE), \tag{7.37}$$

where $\mathbf{n}$ is the vector normal to the boundary, and $C(FL, APE)$ is the conversion to APE from fluxes through the boundaries. If we assume the ocean is in a steady state the conversion terms must balance

$$-C(FL, APE) + C(FF, APE) + C(HF, APE) - C(APE, KE) - C(APE, MX) = 0. \quad (7.38)$$

In the next sections we derive expressions for the contributions from the air-sea fluxes and kinetic energy to APE.

7.4.3 Surface forcing

Fluxes of heat and freshwater at the surface of the ocean cause changes in density, and therefore APE, in the surface layer. The process in the case of a loss of APE is represented in figure 7.8. This shows that any change in density (due to air-sea fluxes or mixing) affects the entire density profile in the APE diagram. Let $(P - E)$ be the rate of precipitation minus evaporation per unit surface area in units of m/s. The original amount of salt in the surface box $(\Delta x, \Delta y, \Delta z)$ is $S_0\rho(T_0, S_0)\Delta x\Delta y\Delta z$, where T_0, S_0 are the surface temperature and salinity. The mass of the freshwater added to the surface box in a time period Δt is $(P - E)\rho(T_0, 0)\Delta t\Delta x\Delta y$. If the original amount of salt is distributed over the new mass of the surface box $\rho(T_0, S_0)\Delta z\Delta x\Delta y + (P - E)\rho(T_0, 0)\Delta t\Delta x\Delta y$, then the new salinity S_1 is

$$S_1 = \frac{S_0\rho(T_0, S_0)\Delta z}{[\rho(T_0, S_0)\Delta z + (P - E)\rho(T_0, 0)\Delta t]}. \quad (7.39)$$

Let Q be the net heat flux into the ocean per unit surface area in units of W/m^2. If the energy from the heat flux is distributed over the depth of the surface box Δz then the new temperature is

$$T_1 = T_0 + \Delta t \frac{Q}{c_v\rho(T_0, S_0)\Delta z}, \quad (7.40)$$

where c_v is the specific heat of seawater ($\approx 4200 J/(kg^\circ C)$).

The rate of change of APE due to separate contributions from surface heat and freshwater fluxes in W/m^3 are given by

$$C(HF, APE) = \frac{g}{\Delta t}\left[\int_{z_o(\rho(T_1,S_0))}^{z} (\rho(T_1, S_0) - \rho_o)\delta V_0 dz' - \int_{z_o(\rho_0(z))}^{z} (\rho_0 - \rho_o)\delta V_0 dz'\right], \quad (7.41)$$

$$C(FF, APE) = \frac{g}{\Delta t}\left[\int_{z_o(\rho(T_0,S_1))}^{z} (\rho(T_0, S_1) - \rho_o)\delta V_0 dz' - \int_{z_o(\rho_0(z))}^{z} (\rho_0 - \rho_o)\delta V_0 dz'\right]. \quad (7.42)$$

Figure 7.9 shows the gain in APE due to separate contributions of annual average freshwater and heat fluxes. There is a great deal of heat lost to the atmosphere as the inflowing AW enters the Arctic in areas with no ice coverage. This creates a lot of APE in the Barents Sea. Although the Barents Sea and the Kara Sea are areas with a large amount of ice formation the net annual effect is a loss of APE, indicating that freshwater increase from ice melt dominates over the brine rejection associated with ice formation.

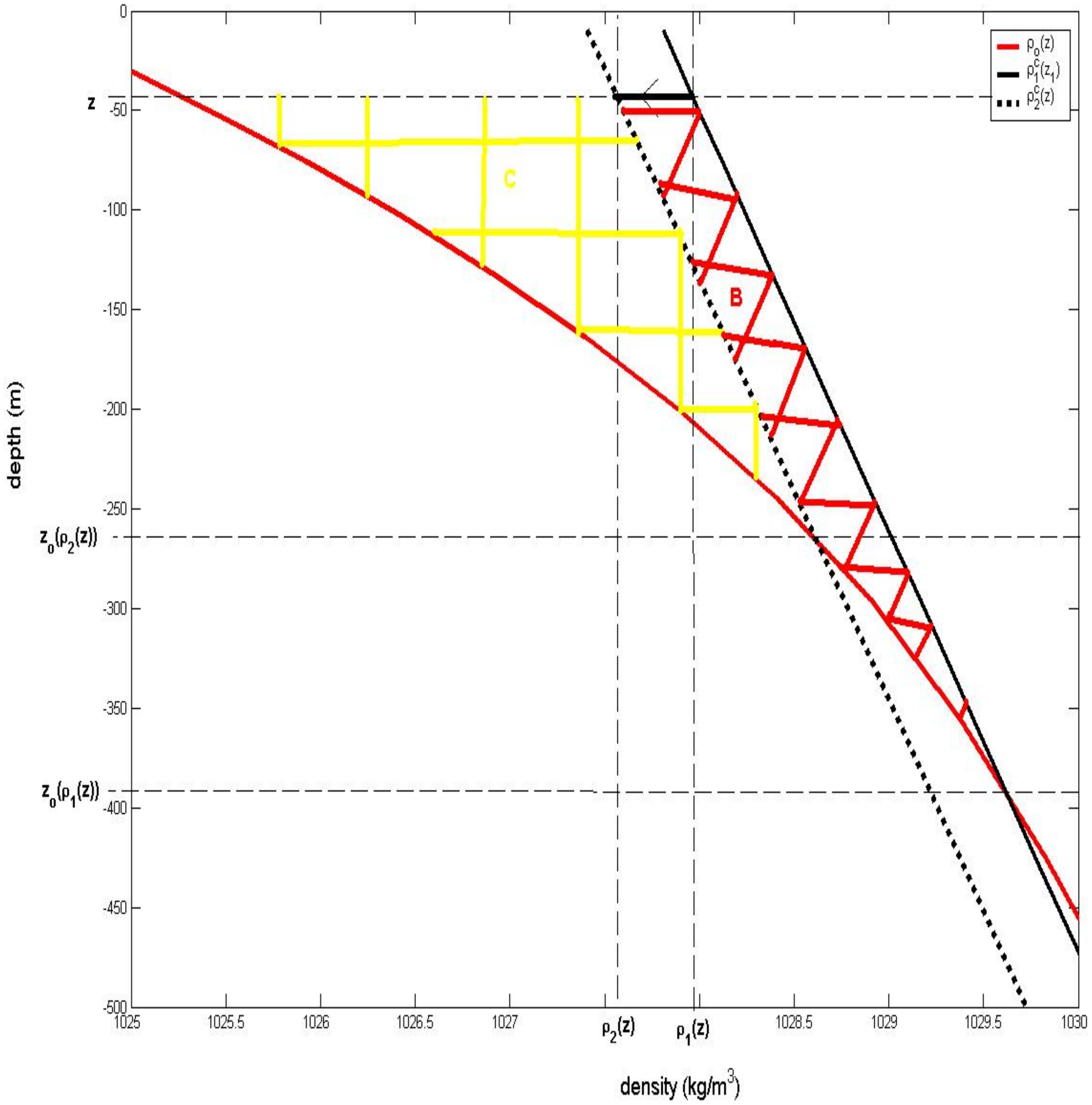

Figure 7.8: *Loss of APE due to surface forcing represented by area B. Area C represents the remaining APE.*

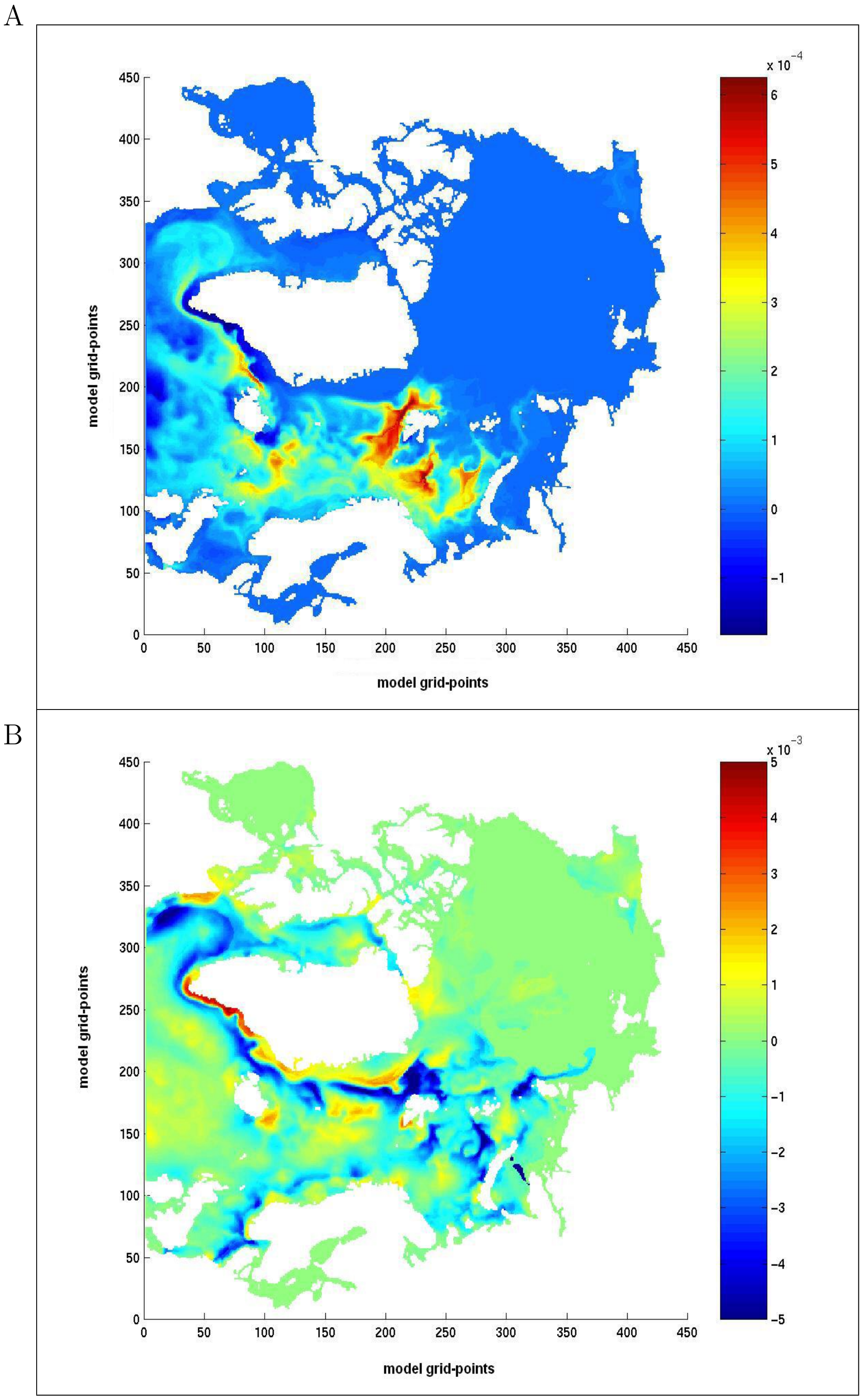

Figure 7.9: *Annual average gain of APE* (W/m^3) *from (a) Surface heat flux and (b) P-E.*

Although the effect of temperature on density is very small at low temperatures, this increases with pressure (thermobaric effect). This is seen in figure 7.10 which shows contours of isopycnals in a temperature-salinity diagram at two pressure levels, where the slope of the isopycnals is larger at higher pressure. Therefore cooling at the surface can have a large impact, as the effect on density increases as water parcels sink towards their stable depth.

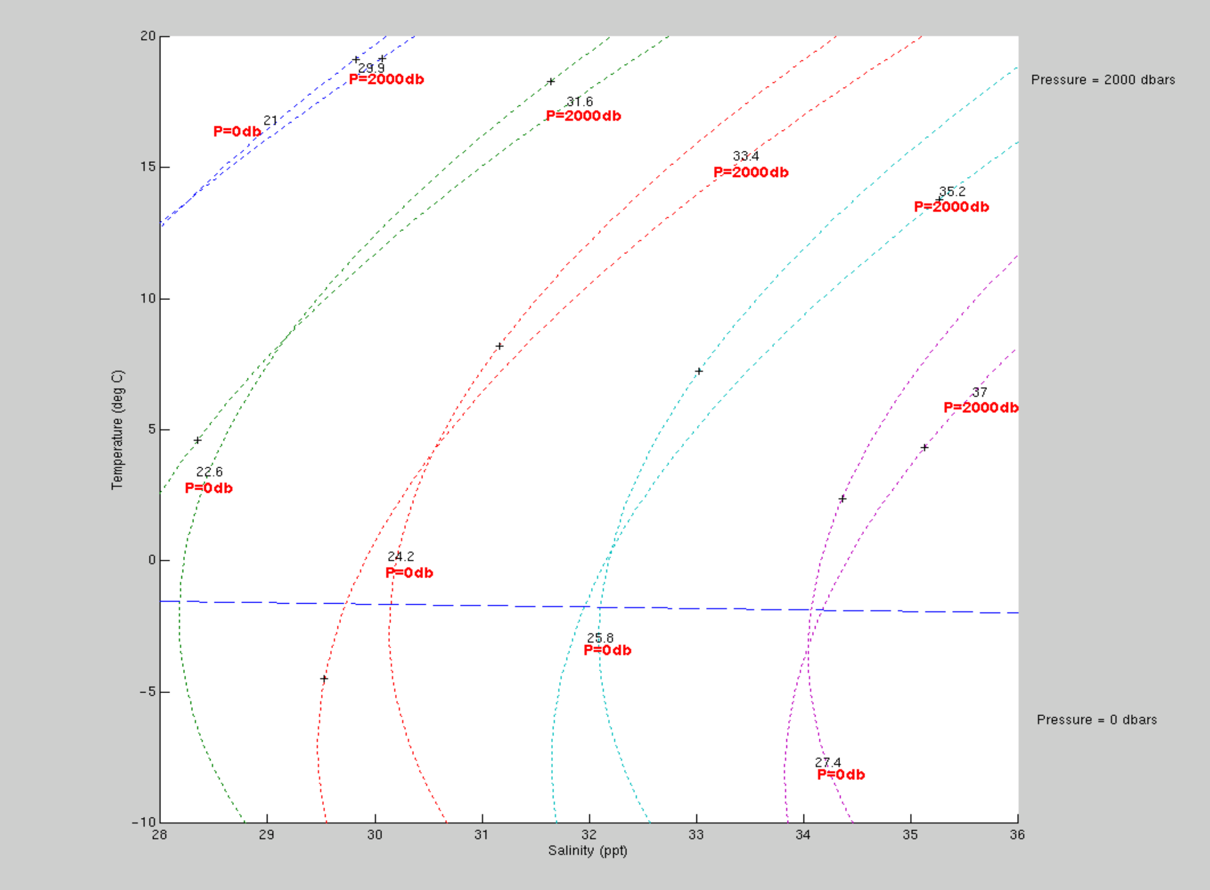

Figure 7.10: *T-S diagram with isopycnals at pressure 0db and 2000db.*

7.4.4 Kinetic Energy

A water parcel converts APE to KE when it moves vertically towards its stable depth. Vertical movement in the opposite direction converts KE to APE. An example of conversion of APE to KE is given in figure 7.11. As the water parcel sinks it can mix with other water parcels which changes its density and the amount of remaining available energy.

The rate at which APE is converted to KE in W/m^3 is given by

$$C(APE, KE) = g\frac{\Delta z}{\Delta t}(\rho - \rho_o)\delta V_0 = gw(\rho - \rho_o)\delta V_0, \tag{7.43}$$

Therefore conversion of APE to KE takes place due to sinking of relatively heavy water and rising of relatively light water.

7.4.5 Mixing

Water parcels in a volume can lose or gain APE due to diffusive mixing of tracers. The amount of energy lost during conversion of APE to KE due to mixing with other water parcels in an example of a sinking process is shown in 7.11. The rate at which this happens is given by

$$C(APE, VMX) = w\frac{\partial APE}{\partial z} - C(APE, KE). \tag{7.44}$$

The total mixing term is calculated as a residual by assuming a steady state.

$$\begin{aligned} C(APE, MX) &= C(FL, APE) + C(FF, APE) + C(HF, APE) \qquad (7.45) \\ &- C(APE, KE). \end{aligned}$$

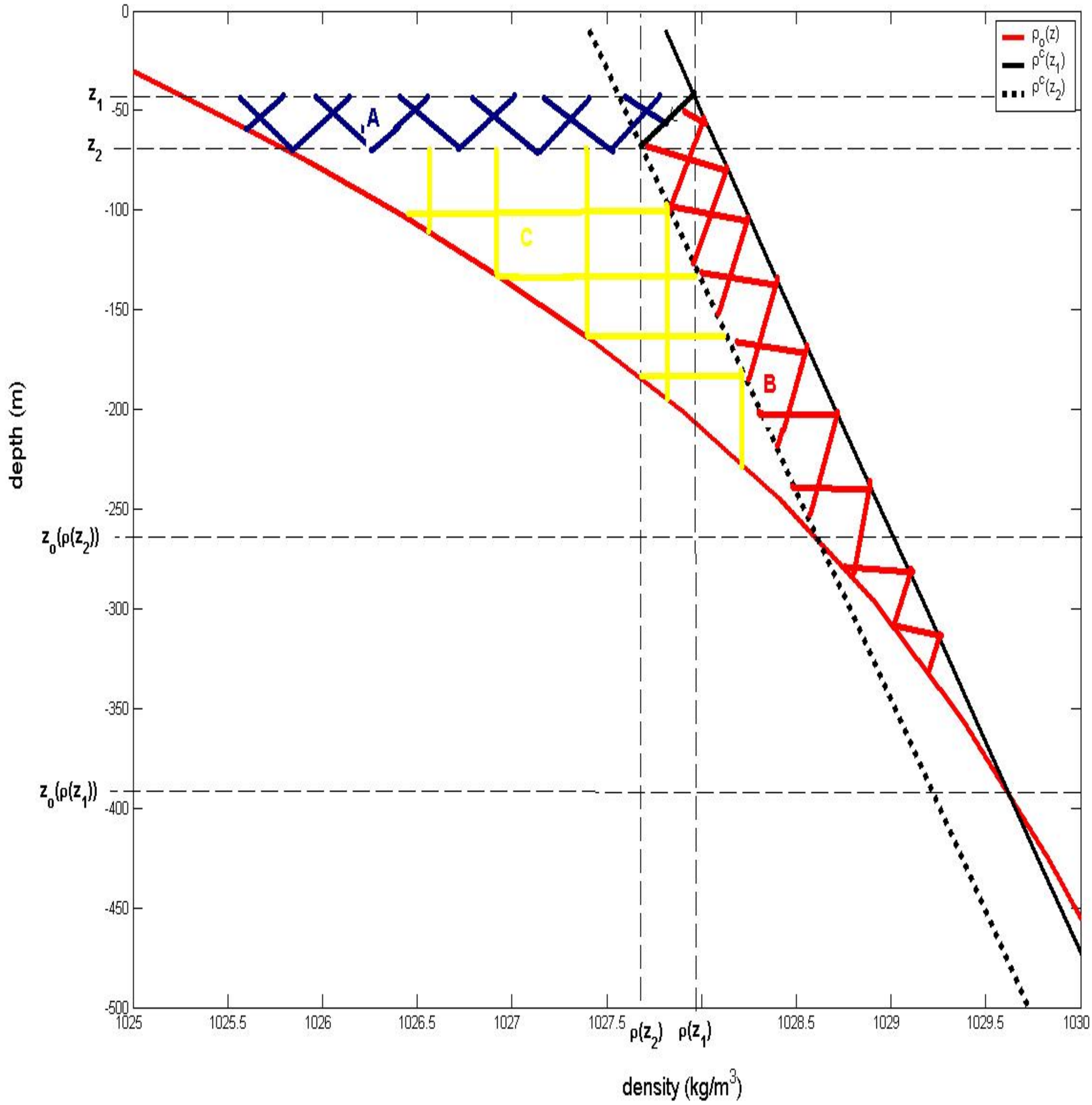

Figure 7.11: *Vertical movement of a water parcel leading to conversion of APE to KE (represented by area A) and a loss of APE to vertical mixing (represented by area B). Area C represents the APE remaining after the vertical displacement.*

Chapter 8

Available Potential Energy - application

8.1 Introduction

In this chapter we apply the energetics theory from chapter 7 to calculate the energy balances for the continental shelf regions of the Arctic. We focus on the amount of APE gained on the shelves by the throughflow of Atlantic Water and Pacific Water due to air-sea fluxes. We have already seen that the largest amount of APE on the shelves is in the Barents, Laptev, East Siberian and Chukchi Seas. The areas that directly receive AW and PW, the Barents and Chukchi Seas, are dominated by large negative surface heat fluxes due to relatively ice free areas, which increase the APE of the inflowing water.

First we look at the energetics of the Barents Sea region in order to determine the source of energy for the increase in PE later available for driving the boundary current. Then we look at the similar problem in the Chukchi Sea area, in order to determine what energy is available for driving the meso-scale eddies seen offshore.

The conversion of APE to KE is a difficult term to calculate in ocean models. This term is generally several orders smaller than other conversion terms, and has been shown to be very sensitive to the balance of horizontal and vertical viscosity coefficients (Oort et al 1994). Energy distributions, and conversions of APE to KE in regional models of the Arctic Ocean have been calculated by Uotila et al (2004), who use the energy definition (7.3). Although this is a different definition to our regional definition of APE (7.13), the conversion term $C(APE, KE)$ is the same, and is given by (7.43). The sign of this conversion term depends on the reference state and on the vertical velocity field, which can be patchy in ocean models. In most models Uotila et al (2004) surprisingly find conversion of KE to APE all along the Eurasian Basin slope.

In the following sections we also look at fluxes of KE through the boundaries of shelf areas. In a steady state the sum of these fluxes $C(FL, KE)$ gives the total increase of KE inside the area. KE is defined as

$$KE = \frac{1}{2}\rho_0(u^2 + v^2 + w^2), \tag{8.1}$$

and the term $C(FL, KE)$ is given by

$$C(FL, KE) = \int\int_b KE\,\mathbf{u}\,\mathbf{n}db, \tag{8.2}$$

where b is the boundary.

8.2 Barents Sea region

Here we look at the APE balance in the areas around the Barents Sea. These areas (A,B,C,D) are shown in figure 8.1. Tables 8.2 and 8.3 show the fluxes of APE and KE through

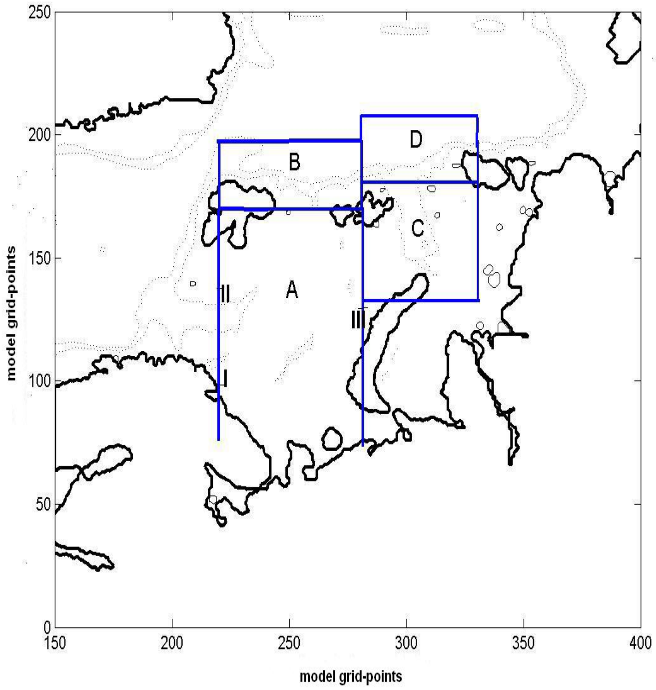

Figure 8.1: *Areas (A,B,C,D) for APE balance in Barents Sea region. Points on Barents Sea boundaries: I (ρ_{ncc}),II ρ_{nac} ,III ρ_{bar}.*

the boundaries of these areas. Generally the fluxes of KE are 2 or 3 orders of magnitude smaller than fluxes of APE, and are relatively unimportant in a full energy balance.

The Barents Sea is represented by area A. A large amount of APE, due to the salty AW, flows into this area from the west. As seen from table 8.2, the APE on the western boundary already has a large amount of APE, compared to the net gain in the Barents Sea, relative to the Arctic Ocean. This net gain is dominated by the heat flux contribution. In the Barents Sea this water gains energy from the heat flux contribution, adding approximately 50% of the original amount flowing in. The majority of this then flows out to the east into the St Anna Trough (area C). There is a very small negative contribution from $C(APE, KE)$ in

Area	A	B	C	D
$C(FL, APE)$	-1123	680	1102	1000
$C(HF, APE)$	3455	661	241	43
$C(FF, APE)$	-2146	-1189	-594	-607
$C(APE, KE)$	-7	-1	6	-1
$C(APE, VMX)$	-524	152	370	-30
$C(APE, MX)$	717	1	373	467

Table 8.1: *Conversion terms of APE (in* 10^6 *W) in Barents Sea areas.*

Area		APE	KE	Area		APE	KE
A	West	2130	3.6	B	West	2600	5.9
	South	0	0		South	561	0.9
	East	-2683	-5.4		East	-611	-4.7
	North	-561	-0.9		North	-1870	-1.4
	Net Gain	1123	2.7		Net Gain	-680	-0.7

Table 8.2: *Fluxes of APE and KE (in* 10^6 *W) into Barents Sea areas A and B.*

this area, which is due to the uphill pathway towards the St Anna Trough. The fluxes of KE show a significant increase in KE, which occurs due to the start of the boundary current in the eastern part of the Barents Sea (see table 8.2).

The APE of water masses at $30m$ depth on the western boundary of the Barents Sea are shown in figure 8.2, which also includes a water mass on the eastern boundary that has been transformed in the Barents Sea. These water masses correspond to points I,II and III in figure 8.1. The water that flows into the Barents Sea originates from the Norwegian Coastal Current, and is indicated by ρ_{ncc}. This water is lighter, and has less APE than the water further offshore in the North Atlantic Current that continues towards Fram Strait. This water mass is indicated by ρ_{nac}. At the other side of the Barents Sea the water from the NCC has gained APE due to the strong cooling. The difference in APE of BSW and the AW flowing towards Fram Strait is small. However the particle trajectories in chapter 6 demonstrate that all the APE of the BSW will make it into the Arctic Ocean, whereas a large part of the energy of the AW flowing towards Fram Strait will recirculate back into the North Atlantic as the AW reaches the Arctic front.

The Area on the Barents Sea slope (area B of figure 8.1) receives the part of AW that has made it through Fram Strait through the western boundary. The amount of APE associated with this flow is still significant, of the same order as the Barents Sea inflow. Within area B there is a large loss of APE due to the freshwater flux contribution, which loses almost 25% of the original amount flowing in. The remaining energy mainly exits through the northern boundary. This is due to a branch of AW that follows the deeper topography, flowing offshore before joining the boundary current on the Kara Sea slope. Part of this water also recirculates along the coast as seen in the anti-cyclonic flow feature in chapter 3.

In this box there is a negative contribution from $C(APE, KE)$, which agrees with the

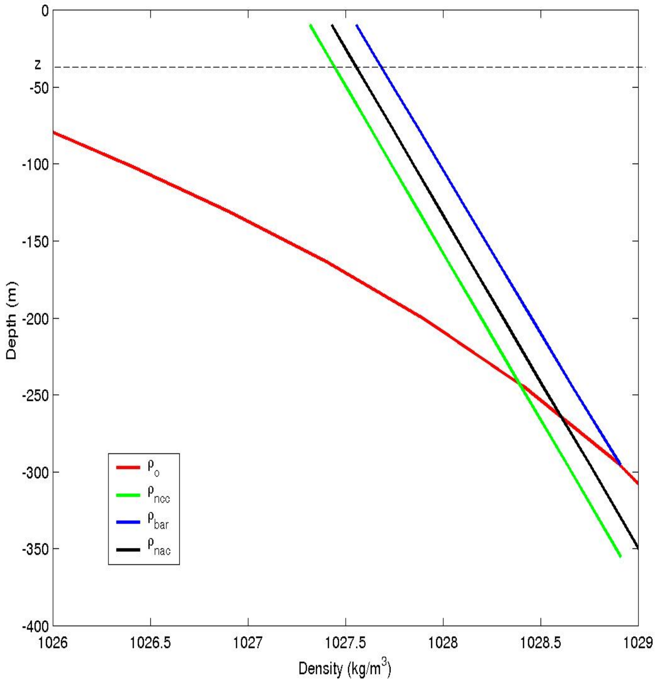

Figure 8.2: *Density profiles for water masses at* $30m$ *on the Barents Sea boundaries. Water masses* ρ_{ncc}, ρ_{nac}, ρ_{bar} *refer to points I, II, III in figure 8.1*

results from Uotila et al (2004). The conversion of KE to APE is due to relatively light water found at the bottom of the current. This water is below its stable depth and therefore can release APE by rising. The APE on a section across the slope through area B is shown in figure 8.3A. There is a layer of APE in the upper part of the current due to relatively heavy AW, and a layer of APE in the lower part of the current due to the depressed isopycnals seen in figure 4.6B. Figure 8.3B shows the $C(APE, KE)$ term on the same section, which indicates that the whole current is sinking on the slope. However the increase in APE due to the sinking of the light water at the bottom dominates over the decrease in APE due to the sinking of the heavy water at the top.

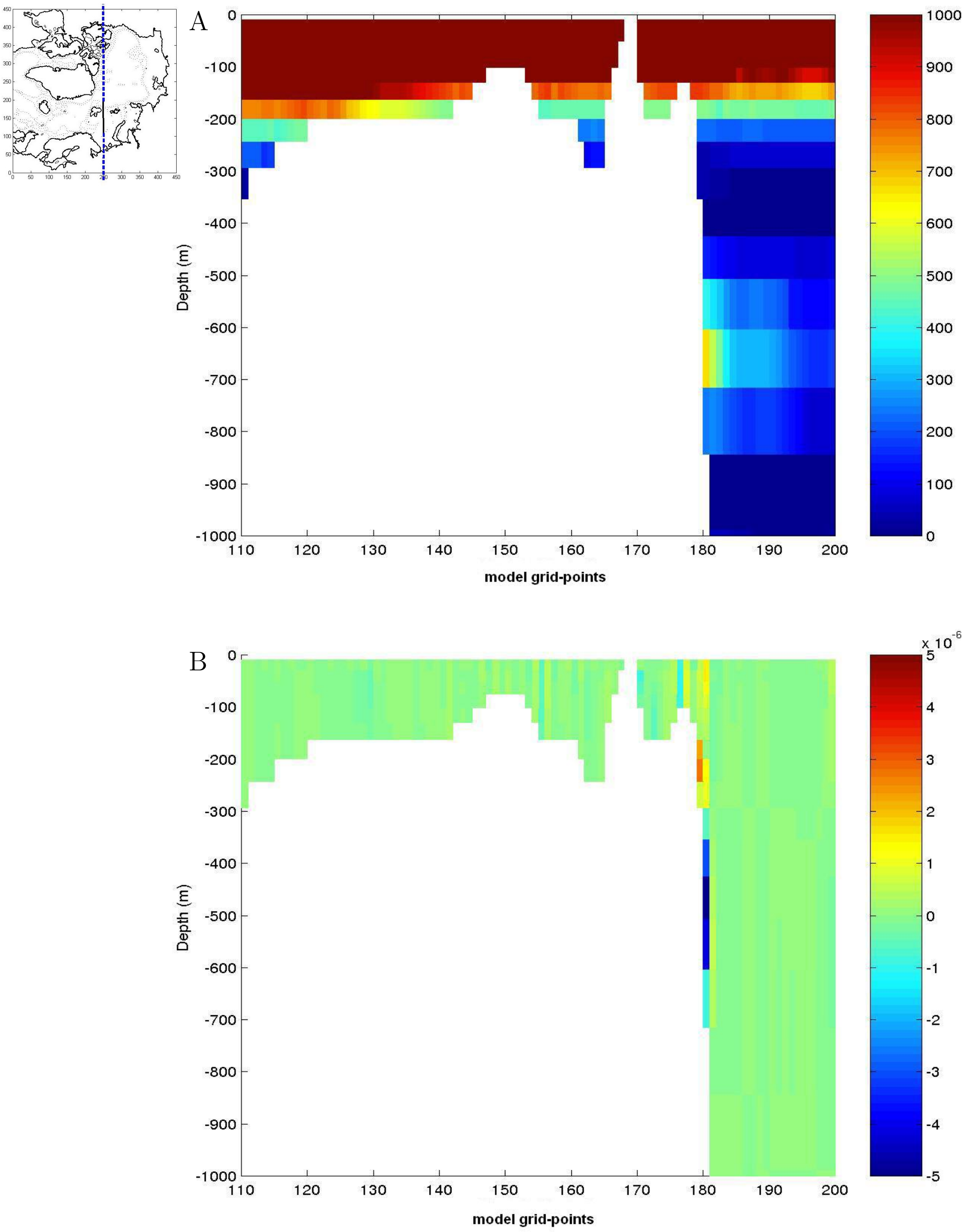

Figure 8.3: *Model longitude section* $(i = 250)$ *(A)* APE *in* J/m^3*.(B)* $C(APE, KE)$ *in* W/m^3.

The depression of the isopycnals towards the coast at the bottom of the current is an adjustment that is necessary for the strength of the flow to decrease with depth, and is probably set-up by transient features during the spin-up phase of the model. Figure 8.4 shows the dynamic height, $\bar{D}$, referenced to the offshore Arctic reference state

$$\bar{D}(x, y, z) = \eta(x, y) + \frac{1}{\rho_0} \int_z^0 \left[\rho(T(z'), S(z'), z') - \rho_o(z')\right] dz'. \tag{8.3}$$

The relatively high pressure region at the slope indicates a positive offshore pressure gradient, and implies large alongshore geostrophic flow. The pressure on the slope slowly decreases with depth, which implies the strength of the geostrophic flow decreases with depth.

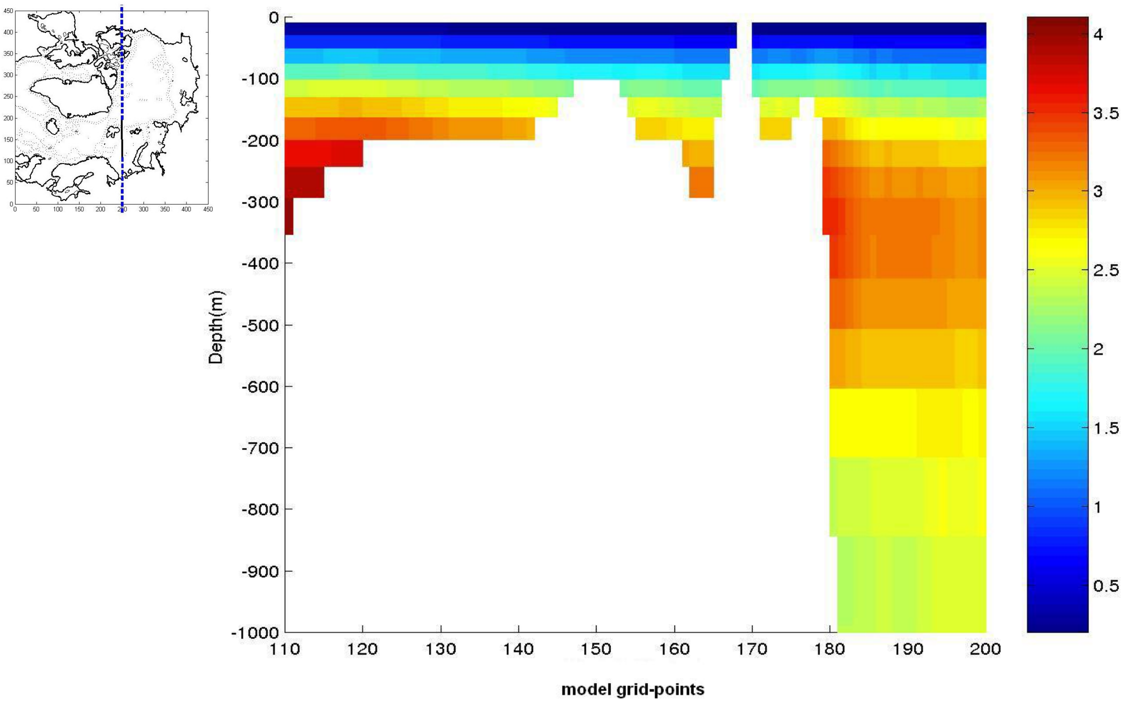

Figure 8.4: *Dynamic height $\bar{D}$ referenced to mean offshore state along model longitude section ($i = 250$).*

The St Anna Trough (area C) receives a large amount of APE from the Barents Sea (see

Area		APE	KE	Area		APE	KE
C	West	2229	5.1	D	West	811	5
	South	214	0.3		South	1225	9.4
	East	-101	0.4		East	-1180	-41.0
	North	-1220	-9.4		North	161	0.3
	Net Gain	-1122	3.6		Net Gain	-1017	23.6

Table 8.3: *Fluxes of APE and KE (in* 10^6 *W) into Barents Sea areas C and D.*

table 8.3), and also some from the Kara Sea through the southern boundary. Approximately half of the APE received from the Barents Sea is lost in this relatively small area. There is a positive $C(APE, KE)$ due to sinking of heavy water along the eastern part of the trough, and a large loss to mixing. This mixing coincides with a large gain in KE, which is due to the formation of the boundary current. There is also a loss of APE due to the contribution from the freshwater flux. The remaining APE flows northwards with the boundary current into area D.

The area on the Kara Sea slope (area D) receives APE from the St Anna Trough, from the AW along the Barents Sea slope, and also from the offshore branch of AW which reaches the slope. There is another large loss of APE here, which is partly due to the contributions from the freshwater flux and mixing. This is also a region of large sinking of the BSW, and there is a large increase of KE indicating that APE is being converted to KE. However the $C(APE, KE)$ term is negative overall, as is the case along the Barents Sea slope. Again this is due to the whole of the current sinking on the slope, whereby the increase in APE due to light water sinking at the bottom of the current dominates over the decrease in APE due to heavy water sinking at the top of the current.

The energetics in this region (A+B+C+D) of the Arctic are dominated by the inflowing AW. This water already has a large amount of APE relative to the Arctic Ocean interior. However only a small part of this water is able to pass through the Arctic front at Fram Strait due to geostrophy. The water that does make it through Fram Strait loses a large amount of APE on the Barents Sea slope as it sinks and is freshened by the surface freshwater flux, which dominates over the cooling from the surface heat flux. The AW that flows through the Barents Sea gains a large amount of APE as it is cooled by the loss of surface heat, which dominates over the surface freshening. This gain in APE is then converted to KE as the newly formed BSW sinks along the boundary of the St Anna Trough, forming the boundary current. As all the water flowing through the Barents Sea makes it into the Arctic Ocean, while a large part of AW flowing through Fram Strait recirculates, the Barents Sea pathway acts as a short circuit for AW into the Arctic Ocean via a boundary current.

A time series of the gain in APE from the air-sea fluxes in the Barents Sea for the second year of the OCCAM model simulation is shown in figure 8.5A. The maximum contributions of $C(FF, APE)$ and $C(HF, APE)$ occur in winter, with a minimum loss from the freshwater flux and a maximum gain from the heat flux. This indicates the effects of ice melt in the prescribed air-sea fluxes. In the summer there is a net loss from the air-sea fluxes, which coincides with a maximum loss from the freshwater flux. This indicates the effects of warming and precipitation in the prescribed air-sea fluxes. The maxima in the gain in APE correspond to the time of maximum AW transport into the Barents Sea. A time series of the net volume fluxes through the western boundary of the Barents Sea is shown in figure 8.5B. Ingvaldsen et al (2004) have shown from observations that this variability is driven by changes in wind stress, which mostly cause an increase of transport in winter. These high transports then provide more warm AW to melt ice in the Barents Sea, promoting heat loss to the atmosphere, which causes the large APE increase. This cooling in the Barents Sea could be crucial for the formation of the boundary current, by reducing the front between BSW and the Arctic Ocean interior.

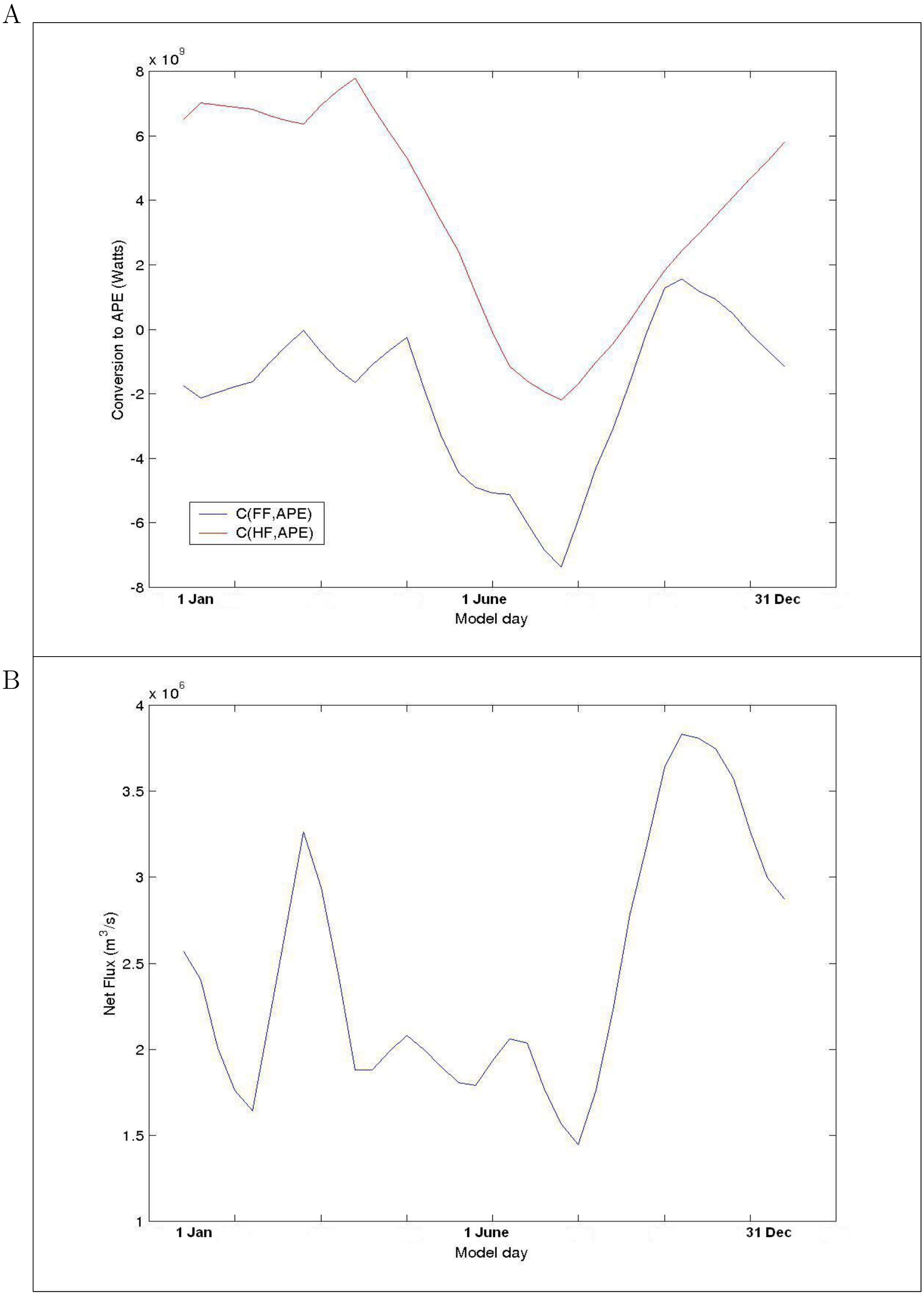

Figure 8.5: *Time series of (A) Conversion terms $C(FF, APE)$ and $C(HF, APE)$ (B) Net volume fluxes through western boundary of Barents Sea.*

8.3 Bering Strait region

Here we look at the APE balance in the areas around the Bering Strait. These areas (E,F,G,H) are shown in figure 8.6. Table 8.4 shows the balance terms from chapter 7 in these areas, and tables 8.5 and 8.6 show the fluxes of APE and KE through the boundaries of these areas. In the energy balance for this region we have used the reference state of the Canadian Basin, as this is the basin where the BSO water masses flow off the shelf. The Canadian Basin reference state is lighter than the Eurasian Basin reference state, and therefore the BSO has more energy relative to the Canadian Basin.

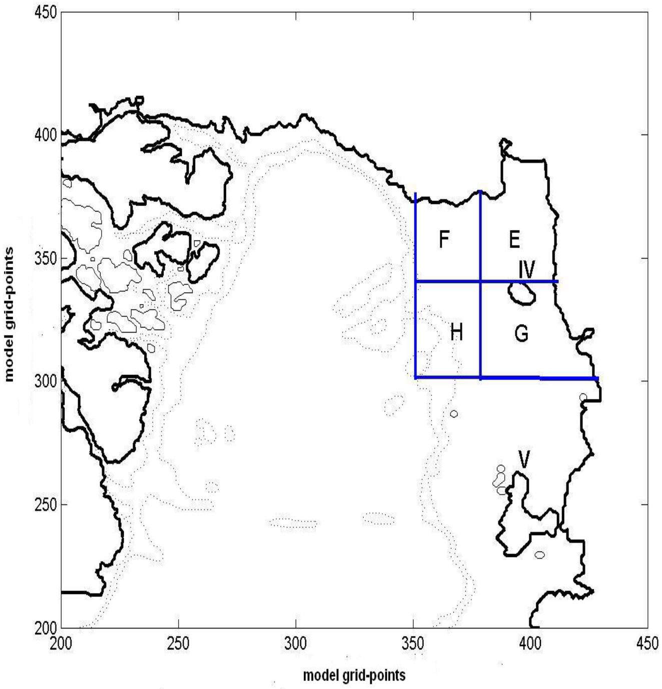

Figure 8.6: *Areas (E,F,G,H) for APE balance in Bering Strait region. Points in Chukchi and East Siberian Seas: IV, V.*

Figure 8.7 shows the APE for a water parcel at $30m$ depth in the Chukchi Sea. This water

Area	E	F	G	H
$C(FL, APE)$	-243	127	236	209
$C(HF, APE)$	71	17	23	4
$C(FF, APE)$	81	-109	-65	-60
$C(APE, KE)$	1	1	0	0
$C(APE, VMX)$	65	-5	1	-14
$C(APE, MX)$	-157	39	193	169

Table 8.4: *Conversion terms of APE (in* 10^6 *W) in Bering Strait areas.*

Area		APE	KE	Area		APE	KE
E	West	-104	-0.1	F	West	7	6.5
	South	-365	-1.5		South	16	-58.8
	East	0	0		East	104	0.1
	North	226	6.3		North	0	0
	Net Gain	243	-4.7		Net Gain	-127	52.2

Table 8.5: *Fluxes of APE and KE (in* 10^6 *W) into Bering Strait areas E and F.*

Area		APE	KE	Area		APE	KE
G	West	-126	-1.0	H	West	-295	-16.2
	South	-3	0		South	126	12.9
	East	0	0		East	394	1.0
	North	365	1.5		North	-16	58.8
	Net Gain	-236	-0.5		Net Gain	-209	-56.5

Table 8.6: *Fluxes of APE and KE (in* 10^6 *W) into Bering Strait areas G and H.*

parcel corresponds to point IV in figure 8.6. The APE of this water parcel relative to the full Arctic reference state is represented by area A in figure 8.7, while the APE relative to the Canadian Basin is represented by areas A+B in figure 8.7, which is over double the former amount. Also shown is the APE for a water parcel (point V) in the East Siberian Sea, which consists of very fresh and cold water. This water is below its stable depth in the reference state and has the possibility to rise, its APE is represented by area C in figure 8.7.

The Chukchi Sea is represented by areas E and F. A large amount of APE, due to the relatively salty PW, flows into area E from the model north, from the Bering Strait. This water gains energy from the heat and freshwater flux contributions, adding approximately 67% of the original amount flowing in. This energy then flows out through the western and southern boundaries. In the northern part of the Chukchi Sea (area F) there is a large loss of APE, and a smaller gain of KE, which coincides with the region where the BSO flows off the shelf. In chapter 6 we have seen particles here flowing offshore in eddies (see figure 6.19).

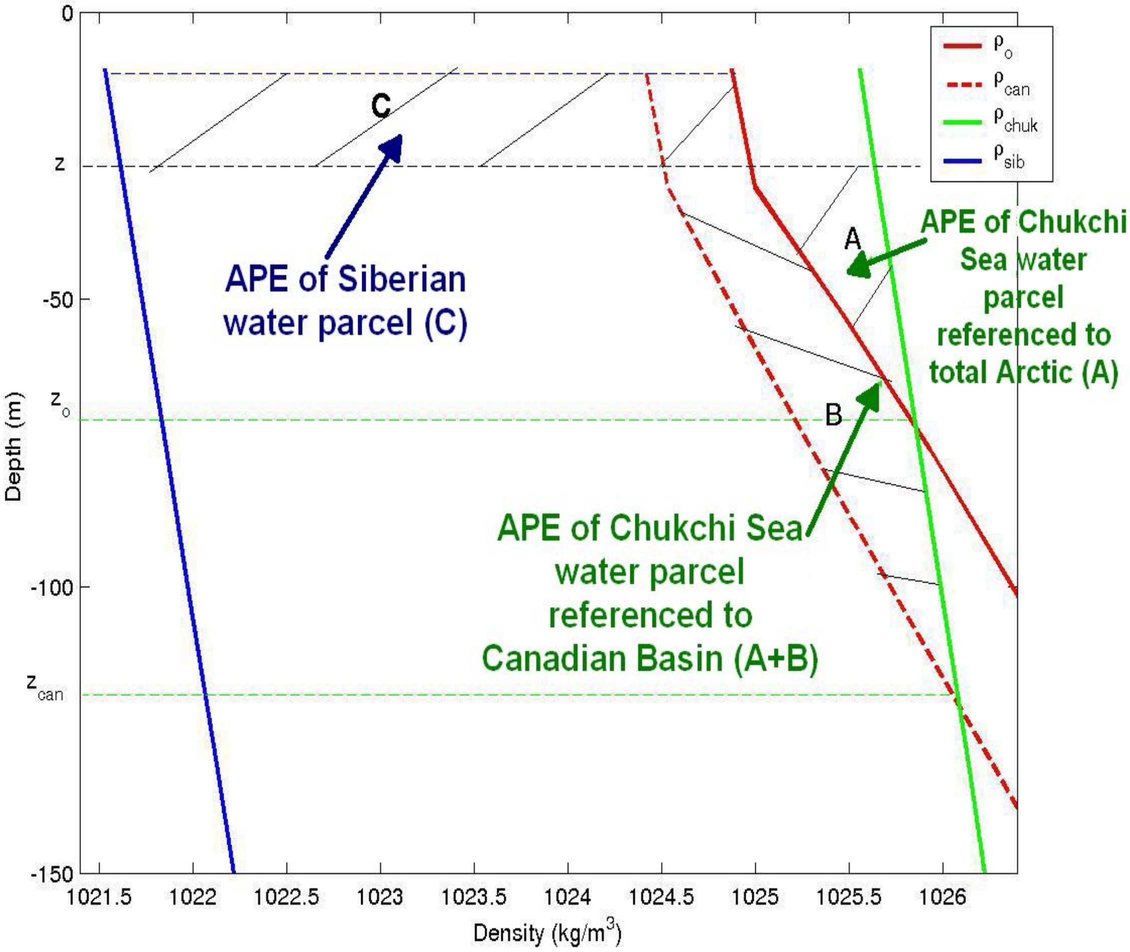

Figure 8.7: *Density profiles for water masses at 30m in the Chukchi Sea and East Siberian Sea.* ρ_o/ρ_{can} *are mean total Arctic/Canadian Basin densities,* ρ_{chuk}, ρ_{sib} *are densities of water parcels on Chukchi/Siberian shelves.* ρ_{chuk}, ρ_{sib} *correspond to pionts IV and V in figure 8.6. This figure shows it is important to take into consideration which ocean basin the water parcel is likely to flow into. The energy of a Chukchi Sea water parcel, which is more likely to flow into the Canadian Basin, has only little energy referenced to the entire Arctic (area A), but significantly more energy referenced to only the Canadian Basin (areas A+B).*

However the amount of $C(APE, KE)$ is only small, indicating the APE is lost to mixing rather than sinking. A section of APE across the slope of the Chukchi Sea is shown in figure 8.8, which shows the APE is lost immediately as the BSO flows towards the slope.

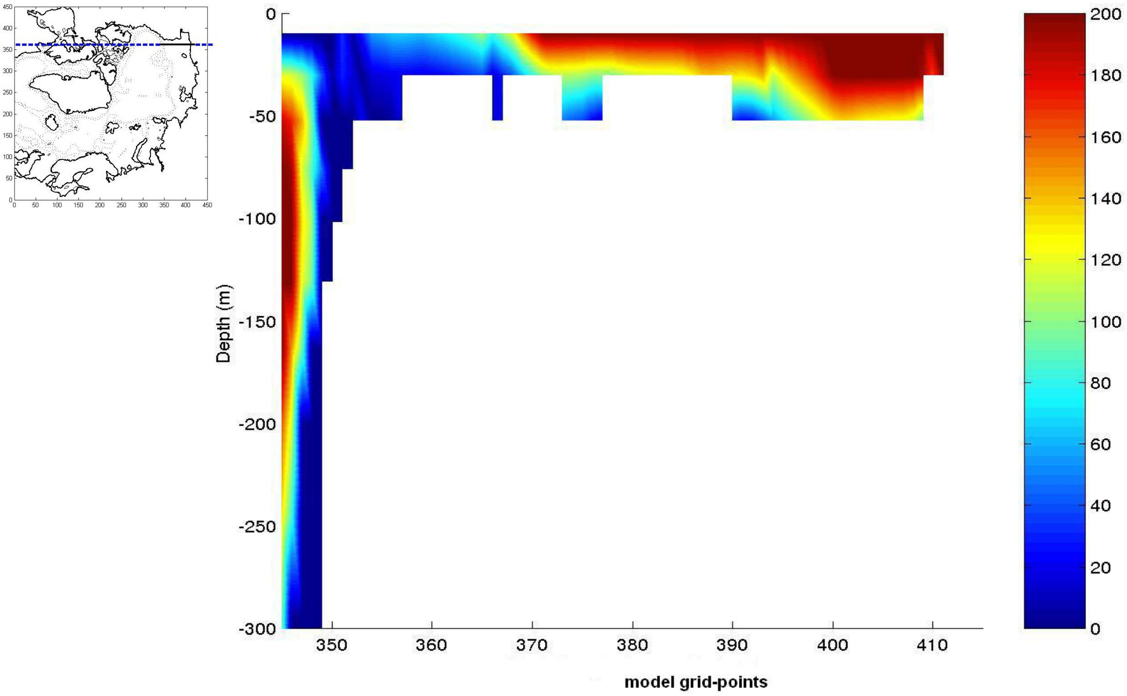

Figure 8.8: *APE (J/m^3) along model latitude section on Chukchi Sea slope ($j = 360$)*

The East Siberian Sea (area G) receives a large amount of APE through the northern boundary. This is due to the relatively salty BSO water that has been made saltier and colder in the Chukchi Sea. The East Siberian Sea is dominated by cold and fresh river water. The large loss of APE to mixing indicates mixing between the BSO and the river water. The BSO is above its stable depth, and the river water is below its stable depth, therefore mixing destroys the energy of both water masses. The remaining energy, which has the properties of the river water after mixing, flows through the western boundary off the shelf. There it has the possibility to create instabilities, generating eddies, as it meets the relatively dense

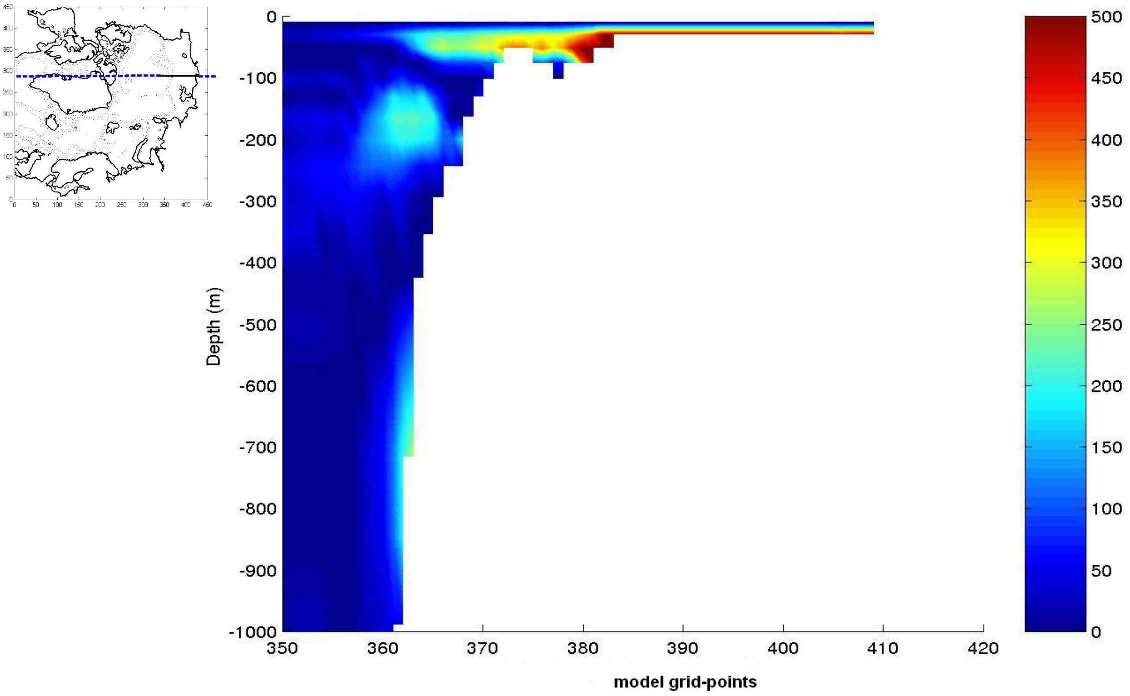

Figure 8.9: *APE* (J/m^3) *along model latitude section on East Siberian Sea slope* ($j = 280$)

surface water of the boundary current. A section of APE across the slope of the East Siberian Sea is shown in figure 8.9, which shows the APE flowing off the shelf near the surface. This shallow energy is the major inflow to area H, which also has a large loss of energy, with the remainder flowing out westwards in the Trans-Arctic drift.

A time series of the gain in APE from the air-sea fluxes in the eastern Chukchi Sea (area E) for the second year of the OCCAM model simulation is shown in figure 8.10A. The freshwater flux contribution dominates over the heat flux contribution, with large positive contributions of $C(FF, APE)$ in winter. This indicates the effect of ice formation in the prescribed model air-sea fluxes. A time series of the net volume fluxes through the northern boundary of the Chukchi Sea is shown in figure 8.10B. The maxima in the gain in APE correspond to the time of minimum PW transport into the Chukchi Sea.

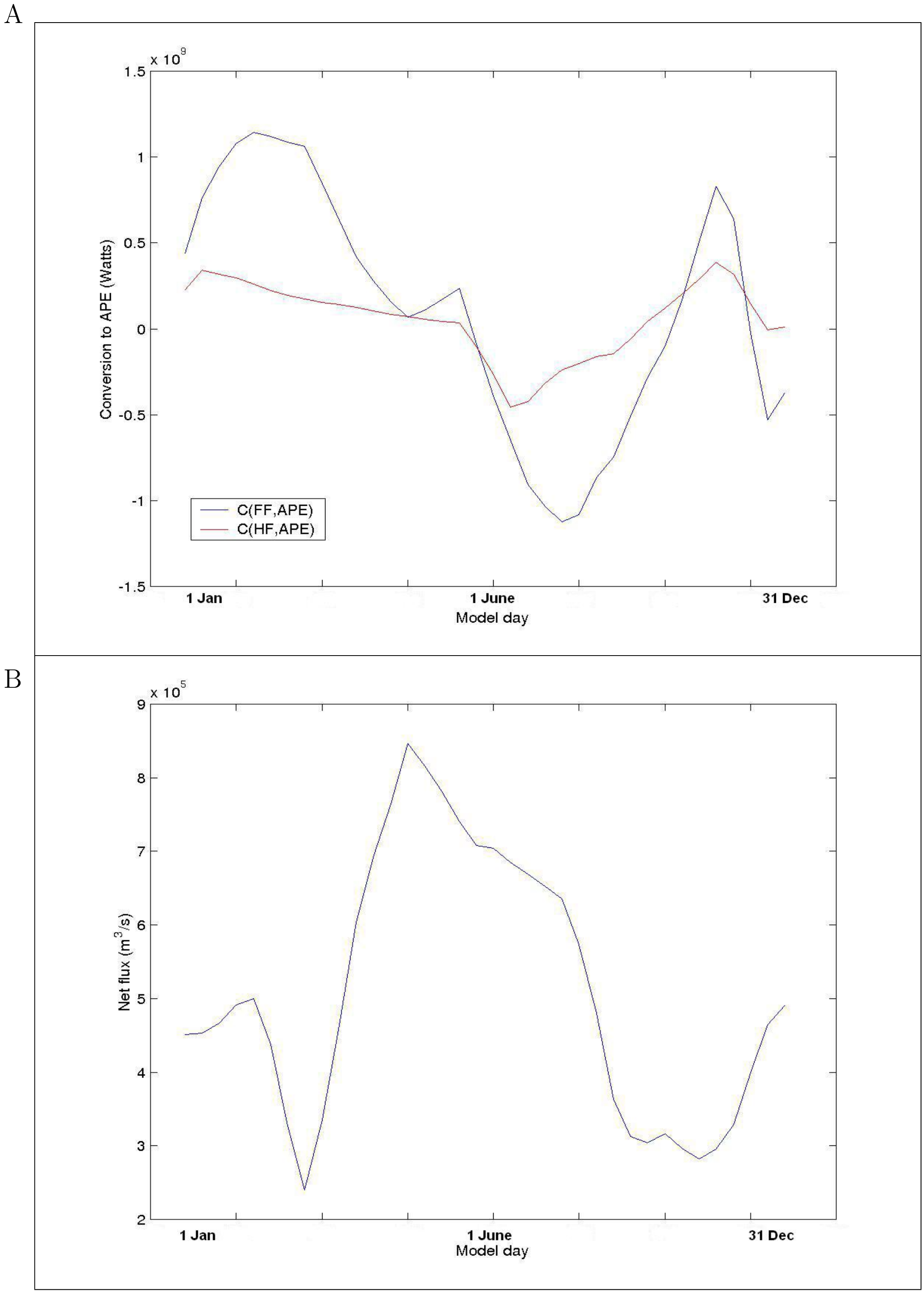

Figure 8.10: *Time series of (A) Conversion terms* $C(FF, APE)$ *and* $C(HF, APE)$ *(B) Net volume fluxes through northern boundary of Chukchi Sea.*

Chapter 9

Discussion and conclusions

In this thesis we have discussed the circumpolar boundary current in the Arctic Ocean, as seen in the OCCAM global ocean model. In particular we have used the model results to understand the dynamics of the boundary current through a study of sources and sinks of energy, and have tried to evaluate the effects of buoyancy forcing due to air-sea fluxes on the continental shelves. We were also able to calculate and visualize pathways of the main water masses in the boundary current using particle tracking techniques, helping to find the formation region and the downstream extent of the boundary current.

In reality, the boundary current has been observed at a number of sites along the Arctic continental slopes (Newton and Sotirin 1997, Schauer et al 1997, Woodgate et al 2001). Historically it was thought that the boundary current started as Atlantic Water entered the Arctic Ocean through Fram Strait (Aagaard 1989), however recently it has been shown that another source, that may be more important, is another branch of the AW inflow that flows through the Barents Sea and enters the Arctic Ocean further along the continental slope (Rudels et al 1994, Schauer et al 1997).

Although there has been improvement in observational evidence of the boundary current recently (eg. Woodgate et al 2001), the Arctic is still a sparsely observed region. Therefore it is still unclear how the boundary current is forced. Up to now most studies (eg. Woodgate et al 2001, Nazarenko et al 1998, Uotila et al 2004) have mentioned the Neptune effect (Holloway 1987) as a potential driving force. This effect is based on theory of statistical mechanics, whereby an along-shore current is generated along depth contours as off-shore meso-scale eddies interact with the shelf break. The Neptune effect can only occur in ocean models if the grid-box is smaller than the Rossby radius (5-10km for the Arctic), allowing the models to resolve meso-scale eddies. However even most regional models of the Arctic have grid-boxes that are several times the size of the Rossby radius, and therefore parameterizations of the Neptune effect have been used (eg. Nazarenko et al 1998). In this paramaterization the traditional eddy-diffusion, which damps the velocity out at the boundaries, is replaced in order to generate along-shore flows at the shelf breaks. This leads to increased cyclonic circulation in the Arctic along depth contours and helps force Atlantic Water into the Arctic Ocean. However Zhang and Zhang (2001) find that although the parameterization improves the strength of the boundary current, it causes incorrect stratification of the Arctic Ocean due to increased heat transport into the Arctic Ocean associated with the enhanced inflow of AW. They conclude that producing the correct stratification is very important in simulating the correct cyclonic circulation, something which is aided by the inflow of dense water from the Barents Sea.

Here we have used results from a recent two year run of the high-resolution ($1/8^\circ \times 1/8^\circ$) OCCAM global ocean model (Aksenov and Coward 2001). While Aksenov and Coward (2001) have reported on the in- and out-flows through the various straits in the Arctic, here we have focused on the boundary current. It is important to note that the model was forced by surface relaxation to the Levitus 94 climatology (Levitus and Boyer 1994) for heat and freshwater fluxes, and by ECMWF wind-stresses calculated from the period of 1986-1988 (Barnier et al 1995). As measurements are sparse in the Arctic Ocean, the full effects of regional and seasonal buoyancy fluxes due to processes such as ice formation may be missing in the air-sea fluxes used to force the model. These processes might be better represented by the inclusion of an explicit sea-ice model, as especially the heat and freshwater fluxes in the Barents Sea show little effect of ice processes, while this is known to be an important area of sea-ice formation (Middtun 1985). Another short-coming of the model is the short integration period, and the consequent use of wind-stresses from a limited period. The Arctic Ocean is subject to significant variability (the Arctic Oscillation) affecting the wind-driven flow at periods of 5-7 years, therefore this simulation only provides us with a snap-shot of the Arctic Ocean circulation during one phase of the oscillation. However the model seems to provide a realistic flow field at very high-resolution, and can be used to study mechanisms behind flow features. We believe that this is the first model to produce a continuous boundary current following the continental slope, as a very high-resolution grid is needed to resolve the small Rossby radius at high latitudes. The model does not include a parameterization of the Neptune effect, therefore this effect can only occur due to the resolved eddy-field in the model.

The model shows many of the known and suspected features of the Arctic Ocean circulation, such as the inflow of Atlantic Water along the eastern boundary of the Norwegian Sea, strong flows near Fram Strait, an anti-cyclonic wind-driven gyre in the Beaufort Sea, a boundary current around most of the Arctic Ocean, inflow of Pacific Water through Bering Strait, a complex eddy-field north of Alaska, the Trans-Arctic Drift, and the East Greenland Current carrying water from the Arctic into the Atlantic. One interesting feature is that the horizontal model grid-box size is approximately 13km, which means the Rossby radius is not quite resolved, however still a narrow boundary current is produced. This is possibly the result of the low stratification of the Arctic Ocean, which will tend to result in barotropic currents following contours of f/H in order to conserve potential vorticity. Therefore the currents tend to be steered by topography, and depending on how they are formed, may have a width determined by the scale of the topography. In this case a realistic boundary current may be produced as long as the model resolves topography.

By studying the simulated velocity field we have traced the formation area of the boundary current back to the Barents Sea. Here it appears that a major source of the energy of the current is dense water that flows off the continental shelves. If water on the shelf becomes denser than water at the same depth in the ocean interior it tends to flow off the shelf as a density driven current (Shapiro et al 2003). The turbulent boundary current that is produced tends to mix with surrounding water masses, before spreading out at a stable depth in the ocean interior. Such behaviour has been observed on the Barents and Kara Sea shelf edges by Schauer et al (1997), however it has not been reported before in modelling studies, probably due to resolution limitations. It is known that such buoyancy fluxes can set up boundary currents in primitive equation models, as reported by Fennel and Mutzke (1997), through the initial propagation of Kelvin waves that set up a boundary current in their wake.

In order to determine if this mechanism occurs in the OCCAM model we have looked at pressure fields following the continental slope at constant depths. This has lead to the discovery of a continuous pressure gradient all around the Arctic Ocean continental slope at depths of 201m and 355m, which are typical depths for the boundary current in the model. Another interesting feature is that these along-shore pressure gradients extend into the Atlantic Ocean, where the lowest pressures occur in the Cape Hatteras area, indicating a connection between the pressure fields of these two oceans. High values of pressure are found outside of the Arctic, for example as the 201m depth contour reaches the Mediterranean, however the values along the NW European shelf remain approximately constant before an increase along the 201m contour as it crosses the Barents Sea. Here a dynamic height increase of approximately 5cm is seen, which is equivalent to a pressure increase of 500 N/m^2. A similar picture is seen along the 355m contour, which enters the Artic through Fram Strait, with a dynamic height increase of 5cm as the contour enters the St Anna Trough. We associate the high pressure areas in the Barents Sea and the St Anna Trough with the formation of extra dense water masses in the Barents Sea, and the sinking of these dense water masses down the slope of the St Anna Trough into the Arctic Ocean. It is well known that in reality dense water formation occurs in the Barents Sea through cooling, evaporation and ice formation (Middtun 1985), although in the OCCAM model the dominant term contributing to dense water formation appears to be cooling. This dense water formation will increase the pressure at depth, explaining the results in the Barents Sea. As this water then tends to sink down the St Anna Trough it will spread out, pushing other water masses away. This will be countered by the inertia and the Coriolis force which will lead to a high pressure region, which explains the pressure maximum in the St Anna Trough at 355m.

To further determine and visualize the extent of the boundary current we have developed a time-dependent variant of an ”off-line” particle tracking technique, that was originally introduced by Döös (1994) for time-independent calculations. A similar extension for time-dependent trajectories has been previously published by Döös and de Vries (2001), however this method was only applied to 2D idealized gyres. Here we have deduced the method independently, and applied it to simulated 3D velocity fields from the OCCAM global ocean model. We have also extended the method with a representation for the random diffusive effects that are experienced by water parcels in the real ocean, using the theory of Brownian motion. The resulting probability distribution used to generate the random displacements is a Gaussian, which is the solution of the 1D diffusion equation and is of the same form as the eddy viscosity terms used in the momentum equations of the OCCAM model. Therefore we chose to take the diffusion coefficient in the random displacements to be equal to the eddy viscosity parameters of the OCCAM model, as this will lead to the particles being displaced on the scale of the model sub-grid scale turbulence. This choice of the diffusion coefficient may however not be the best choice for representing the dispersion of water parcels in the real ocean, although our results show significant resemblance to the propagation of observed features in the ocean.

A comparison of the time-independent, time-dependent, and diffusive time-dependent methods has lead us to believe that the diffusive time-dependent trajectories are most consistent with observations, especially the distributiom of Atlantic Water and Barents Sea water in the boundary current. The time-dependent trajectories show AW is the dominant water mass in the boundary current, however it has been observed that most of AW recirculates within the Eurasian Basin along the Lomonosov Ridge (Schauer et al 1997), and that BSW is the dominant water mass in the boundary current as it enters the Canadian Basin. This distribution is better observed in the diffusive time-dependent trajectories.

We have shown pathways of the waters in the boundary current, and conclude that the OCCAM model only has a weak true circumpolar boundary current. The boundary current waters are severely affected by the wind-driven flow features in the Canadian Basin. The Beaufort Gyre acts to trap water in the Arctic, while the Trans-Arctic drift and the Lomonosov and Mendeleyev Ridges are responsible for diverting water offshore out of the boundary current.

There are two pathways for AW into the Arctic Ocean. One branch flows through Fram Strait (total of 9.8Sv), but most of this branch recirculates due to the Arctic front, leaving only 3Sv to flow eastwards along the Barents Sea slope. The other branch flows through the Barents Sea, where it is cooled and freshened, forming Barents Sea Water (BSW). This water mass has been found to flow through the southern part of the Barents Sea, where it gets denser through cooling. The BSW, originally at depths of 10-200m on the shelf, eventually sinks down the eastern boundary of the St Anna Trough. It enters the Arctic Ocean at depths of up to 1000m as an eastward flowing boundary current, while it is seen to push the AW on the Fram Strait pathway offshore. Approximately 3.5 Sv. of BSW enters the ocean interior in this manner. Both AW and BSW are found to provide significant contributions to the intermediate and deep waters of the Arctic Ocean.

The outflow rate of the diffusive time-dependent particles from the boundary current into the Atlantic can be accurately described by a 1D advection-diffusion equation, where the particles are advected at a speed of approximately $2.9cm/s$ and diffused at a rate of $1.3 \cdot 10^9 cm^2/s$. This large diffusion coefficient is caused by the Beaufort Gyre which traps water masses for several circuits around the Canadian Basin. This confirms that diffusion is caused by basin-scale features such as the Beaufort Gyre and the Trans-Arctic drift, while the advection rate of almost $3cm/s$ corresponds to the propagation speed found for an extra dense outflow from the Barents Sea found along the continental slope of the Canadian Basin by McLaughlin et al (2002). We have also estimated that the bulk of changes in the Barents Sea outflow will propagate into the North Atlantic on a time-scale of the order of 30 years, while the strongest signal occurs after 10 years, indicating the time-scales on which changes in the Barents Sea outflow will impact the deep convection regions in the Atlantic.

The particle trajectories of BSW confirm that dense water flows off the shelf in the St

Anna Trough, where the boundary current starts. We therefore considered the potential energy available to drive the flows down the slope and the boundary current. As OCCAM is one of the first ocean models to simulate a realistic high-resoltion Arctic Ocean circulation, there have been no studies yet on energetics of specific processes on the continental shelves and slopes in this region, and we have found this requires a new approach. Potential Energy (PE) is not an absolute quantity, so it is necessary to define it relative to a suitable reference state. In the case of the atmosphere, Lorenz (1955) used a reference state in which the atmosphere was adiabatically resorted so that it had the lowest possible value of PE. Then the Available Potential Energy (APE) was defined as the potential energy difference between the two states. Studies of the ocean energetics have used a reference state which is the lowest possible PE state of the ocean (eg. Huang 1998), which is known in the literature as the classic definition of APE, giving a single value for the total APE of the global ocean. However regional processes in the Arctic are more likely to be affected by nearby water masses and their stratification. Therefore we have defined the APE as the potential energy relative to the mean offshore density structure in the Arctic Ocean interior. In a study of Arctic Ocean model energetics by Uotila et al (2004) a reference state is chosen of the mean stratification for the whole model domain using an approximation of the original APE definition, and the authors discuss depth-integrated fields of APE. However for our purpose of finding the amount of available energy for a water parcel to fall off the shelf and create a boundary current, it was necessary to use a 3D field of APE, as a 2D field of depth-integrated APE creates a distorted view due to changes in topography. We found that using the classic definition of APE with a reference state in the deep offshore ocean basin did not give an accurate estimate for the amount of energy of a single water parcel on the shelf. Therefore we included terms accounting for the adjustment of the reference state, and the compressibility of sea-water, defining the APE of each water parcel as the work done by moving it from the original depth to its stable depth in the reference column. We think this provides an accurate estimate of the amount of energy available on the continenatal shelves and slopes for driving local currents in the Arctic Ocean.

The energetics in the Barents Sea region are dominated by the inflowing AW. We have found that this water already has a large amount of APE relative to the Arctic Ocean interior. However, as dicussed previously, only a small part of this water is able to enter the Arctic Ocean on the Fram Strait branch even though there is enough energy available for the AW to flood the Arctic basin. The currents in the Fram Strait region are very complicated (Aksenov and Coward 2001), however it seems that a large branch of AW turns back towards the Atlantic due to the strong Arctic Front between the warm Atlantic and the cold Arctic. The flow through the Fram Strait is then prevented by geostrophy. Water is only able to pass through the strait if the flow is dominated by bottom friction, which is more important than the Coriolis force in shallow water, therefore there is only a small branch close to the Spitzbergen coast that is able to enter the Arctic Ocean. The preferred route for AW to enter the Arctic is via a friction dominated route through the Barents Sea, that therefore acts as a short-circuit for AW into the Arctic Ocean. Through a study of the APE balance we have found that there is approximately 2000 W of APE flowing into the Barents Sea associated with AW. In the Barents Sea approximately 1000 W of energy is gained due to cooling by the surface heat flux, which dominates over the effects of freshening from the surface freshwater flux. The majority of this energy is lost as the newly formed BSW sinks along the boundary of the St Anna Trough, while some remains to help counter turbulence further along the boundary current. It is found that only a small part of this energy loss is due to conversion to kinetic energy (KE), while the majority of the APE is lost due to turbulence and mixing. We have found that the amount of potential energy available is of the order of 100-1000 times greater than the kinetic energy in the boundary current, indicating that the conversion process is very inefficient. This large difference has been reported on before in estimates of global APE by Oort et al (1994), who find that there is 50 times more APE than KE in the worlds oceans.

We have also looked at the APE on the Chukchi Sea shelf, where waters flow into the eddy-rich region offshore. These eddies have been studied in the real ocean by D'Asaro (1988a,b), and are thought to consist of waters from the Chukchi Sea, and formed by baroclinic instability at the shelf break. Therefore we have investigated whether dense water formation plays any role here. The Chukchi Sea is dominated by inflowing Pacific Water that gains a large amount of energy in equal amounts from the air-sea fluxes of heat and fresh water. Part of this water appears to flow off the shelf towards the Beaufort Sea, where there is a large loss of APE and a large gain of KE. This coincides with eddying motions of simulated water particles as they flow off the shelf, indicating that there may be instabilities that convert APE to KE as the dense PW meets the very light Beaufort Sea surface water. Another part of the PW inflow flows into the East Siberian Sea, where it loses most of its energy due to freshwater fluxes associated with river inflow and mixing with fresh Siberian shelf water. The light Siberian shelf water can be seen to flow off the shelf into the Makarov Basin, where it has the possibility to create instabilities near the surface.

In conclusion, we have shown that dense water in the form of inflowing AW, and changes in AW due to air-sea fluxes on the Barents Sea shelf, are important in providing energy for the Arctic circumpolar boundary current. The fact that the sinking in St Anna Trough seems so important, and that the current slowly sinks as it makes its way through the Arctic, contradicts the Neptune effect. This is the mechanism proposed most frequently in the literature, however it would only act to drive flows along depth contours.

This work has opened up several opportunities for further work. There are still open questions on what role the Neptune effect plays in ocean models, and how fine the resolution and how strong the eddy-field must be before resolving the Neptune effect. Therefore it would be interesting to see what happens to the boundary current in the OCCAM 1/12° resolution OCCAM model, which is currently being run. It would be especially of interest to see if the inflow of AW through Fram Strait is enhanced, which would occur if the Neptune effect is better resolved, even though the resulting 8km grid-box size may still not completely resolve the Rossby radius of 5-10km. The most challenging problem however is to estimate the contribution of the Neptune effect to the boundary current in ocean models that do not use a specific parameterization for the effect.

The forcing mechanism for the boundary current presented in this thesis presents the need to investigate the effects of using more accurate forcing fields in ocean models. As the Arctic is only sparsely observed, particularly the central Arctic, using surface relaxation to the Levitus 94 climatology may not provide an accurate simulation of the effects of air-sea fluxes on the ocean circulation. Particularly it seems the seasonal signals of ice formation in the Barents Sea are missing, while this is known to be an important area for ice formation in winter. Therefore it would be desirable to see the effects of regional and seasonal ice processes by coupling an ice-model to OCCAM, to see if there are any significant changes in the boundary current and the contributions from the resulting surface fluxes of heat, brine and freshwater. Another improvement in the ocean forcing could be obtained by using annually varying wind fields to properly see the effects of the Arctic Oscillation, which has been shown to have a large impact on how far Atlantic Water reaches into the Arctic (Maslowski et al 2000), especially as our results have shown that if a water particle reaches the Canadian Basin it is likely to be affected by the wind-driven circulation. However in order to simulate the boundary current through several phases (each phase is 5-7 years) a much longer simulation of the OCCAM model is required, which at present is not feasible due to computing limitations.

There are also processes that occur in the boundary current that are of interest, and can be investigated in OCCAM. As the current progresses through the Arctic, its direction is constantly changing. The current can be thought of as an eastern boundary current, except for when it flows in a south-eastwards direction. Then it acts as a western boundary current, and it can be seen to intensify when this occurs, for example on the Kara Sea shelf edge. It would be interesting to understand the dynamics of the change-over from western boundary current to eastern boundary current, which is most likely to occur only in circumpolar currents. Another important issue is the impact of the boundary current water masses on the deep convection regions in the Atlantic. These water masses are thought to play an important role (Mauritzen 1996a,b, Andersson et al 1999), and therefore the pathways of the boundary current are of interest as it leaves the Arctic as part of the East Greenland Current for the Atlantic. Preliminary work (not reported on) shows the possibility that there is a split in pathways between deeper water masses of the boundary current that follow a pathway through the Faraeo-Shetland channel and shallower water masses that follow a pathway across the Greenland-Iceland ridge.

Another area for further study is the impact the Arctic boundary current has on climate, as it acts as a heat pump by drawing warm Atlantic waters to high latitudes. There has been much talk lately of a collapse of the overturning circulation in the Atlantic, maybe leading to a new ice age. Therefore it would be interesting to know if the Arctic boundary current could continue to form in glacial conditions, and whether it is responsible for enough northwards heat transport in the Atlantic to maintain Europe's mild climate. This is especially relevant to our forcing mechanism as it is thought that the Barents Sea was covered by a grounded ice sheet during the last glacial maximum (Siegert and Dowdeswell, 2004), which would shut off the short-circuit pathway for Atlantic Water into the Arctic Ocean.

There is also opportunity to further develop the methods introduced in this thesis. For example, the diffusion value used in the random displacements in our particle trajectories was simply taken to match the sub-grid scale turbulence in the OCCAM model, however this might not be the best value for representing the spread of water parcels in the real ocean. There are several radioactive tracers in the real ocean that are used for studying the circulation in the Nordic Seas and the shelf seas around the UK, such as the release of Technetium-99 from the Sellafield nuclear power plant in the UK (eg. Gao et al 2005). This comparison could provide a validation of the diffusion value, and also for the OCCAM simulated velocity fields. Also the energetics of the strong eddy-field in the Canadian Basin require further thought, as this is by nature a time-dependent problem, and therefore it is necessary to extend the study of this region by looking at sources of the eddy kinetic energy, rather than the annual mean KE.

Bibliography

[1] K. Aagaard. The Beaufort undercurrent. *The Alaskan Beaufort Sea: ecosystems and evironments, edited by P.W. Barnes, D.M. Schnell and E. Reimnitz. Academic Press Inc.*, pages 47–71, 1984.

[2] K. Aagaard. A synthesis of the Arctic Ocean circulation. *Rapp. P. V. Reun. Cons. Int. Explor. Mer.*, 188:11–22, 1989.

[3] K. Aagaard and E.C. Carmack. The role of sea ice and other fresh water in the Arctic circulation. *Journal of Geophysical Research*, 94:14485–14498, 1989.

[4] K. Aagaard and E.C. Carmack. The Arctic Ocean and climate: a perspective. *The Polar Oceans and their role in the shaping the global environment, edited by Johannessen, Muench, Overland, Geophysical Monograph Series, Vol 85. AGU.*, pages 4–20, 1994.

[5] K. Aagaard, L.K. Coachman, and E.C. Carmack. On the halocline of the Arctic Ocean. *Deep-Sea Research*, 28:529–545, 1981.

[6] K. Aagaard, J.H. Swift, and E.C. Carmack. Thermohaline circulation in the Arctic Ocean. *Journal of Geophysical Research*, 90:4833–4846, 1985.

[7] K. Aagaard and R.A. Woodgate. Some thoughts on the freezing and melting of sea ice and their effects on the ocean. *Ocean Modelling*, 3:127–135, 2001.

[8] Ye. Aksenov and A.C Coward. The Arctic Ocean circulation as simulated in a very high resolution global ocean model (OCCAM). *Annals of Glaciology*, 33:567–576, 2001.

[9] A.H. Al-Rabeh and N. Gunay. On the application of a particle dispersion model. *Coastal engineering*, 17:195–210, 1992.

[10] L.G. Anderson, G. Bjork, O. Holby, E.P. Jones, G. Kattner, K.P Koltermann, B. Liljeblad, R. Lindegren, B. Rudels, and J. Swift. Water masses and circulation in the Eurasian basin: Results from the *Oden 91* expedition. *Journal of Geophysical Research*, 99:3273–3283, 1994.

[11] L.G. Anderson, E.P. Jones, and B. Rudels. Ventilation of the Arctic Ocean estimated by a plume entrainment model constrained by CFCs. *Journal of Geophysical Research*, 104(C6):13423–13429, 1999.

[12] L.G. Anderson, S. Jutterstrom, S. Kaltin, E.P. Jones, and G.R. Bjork. Variability in river runoff distribution in the Eurasian basin of the Arctic Ocean. *Journal of Geophysical Research*, 109(C1):art no: 1016, 2004.

[13] J.O. Backhaus, H. Formann, J. Kampf, and A. Rubino. Formation and export of water masses produced in Arctic shelf polynyas - process studies of oceanic convection. *ICES Journal of Marine Science*, 54:366–382, 1997.

[14] B. Barnier, L. Siefridt, and P. Marchesiello. Thermal forcing for a global ocean circulation model using a three-year climatology of ECMWF analyses. *Journal of Marine Systems*, 6:363–380, 1995.

[15] B. Blanke and S. Raynaud. Kinematics of the Pacific Equitorial Undercurrent: an Eulerian and Lagrangian approach from GCM Results. *Journal of Physical Oceanography*, 27:1038–1053, 1997.

[16] G.E.P. Box and M.E. Muller. A Note on the Generation of Random Normal Deviates. *Annals of Mathematical Statistics*, 29:610–611, 1958.

[17] N.A. Bray and N.P. Fofonoff. Available potential energy for MODE eddies. *Journal of Physical Oceanography*, 11:30–47, 1981.

[18] K. Bryan and L.J. Lewis. A water mass model of the world ocean. *Journal of Geophysical Research*, 84:2503–2517, 1979.

[19] E.C. Carmack, R.W. MacDonald, R.G. Perkin, F.A. McLaughlin, and R.J. Pearson. Evidence for warming of Atlantic water in the southern Canadian basin of the Arctic Ocean: Results from the Larsen-93 expedition. *Geophysical Research Letters*, 22:1061–1064, 1995.

[20] D.J. Cavalieri and S. Martin. The contribution of Alaskan, Siberian, and Canadian polynyas to the cold halocline layer of the Arctic Ocean. *Journal of Geophysical Research*, 99(C9):18343–18362, 1994.

[21] D.C. Chapman. Dense water formation beneath a time-dependant coastal polynya. *Journal of Physical Oceanography*, 29(4):807–820, 1999.

[22] D.C. Chapman and D.B. Haidvogel. Formation of Taylor caps over a tall isolated seamount in a stratified ocean. *Geophysical and Astrophysical Fluid Dynamics*, 64:31–65, 1992.

[23] L.K. Coachman and K. Aagaard. Physical oceanography of Arctic and Subarctic seas. *Marine Geology and Oceanography of the Arctic Seas, edited by Y. Herman, Springer-Verlag, New York*, pages 1–72, 1974.

[24] G.T. Csanady. *Turbulent Diffusion in the Environment*. D. Reidel Publishing Company, 1973.

[25] E.A. D'Asaro. Observations of small eddies in the Beaufort Sea. *Journal of Geophysical Research*, 93(C6):6669–6684, 1988a.

[26] E.A. D'Asaro. Generation of submesoscale vortices: a new mechanism. *Journal of Geophysical Research*, 93(C6):6685–6693, 1988b.

[27] T.L. Delworth and K.W. Dixon. Implications of the recent trend in the Arctic/North Atlantic oscillation for the North Atlantic thermohaline circulation. *Journal of Climate*, 13(21):3721–3727, 2000.

[28] R. Dewey, R. Muench, and J. Gunn. Mixing and vertical heat flux estimates in the Arctic Eurasian basin. *Journal of Marine Systems*, 21:199–205, 1999.

[29] K. Döös. Interocean exchange of water masses. *Journal of Geophysical Research*, 100:13499–13514, 1995.

[30] K. Döös and P. de Vries. Calculating Lagrangian Trajectories Using Time-Dependent Velocity Fields. *Journal of Atmospheric and Oceanic Technology*, 18(6):1092–1102, 2001.

[31] K. Döös, P. Killworth, A. Coward, R. Marsh, M. Lee, B. Blanke, S. Speich, M. Valdivieso, R. Santoleri, D. Iudicone, S. Drijfhout, P. de Vries, V. Artale, V. Rupolo, and

S. Marullo. Tracing water masses of the North Atlantic and the Mediterranean. *Final report of the EU project TRACMASS*, 2001.

[32] B. Ekwurzel, P. Schlosser, R.A. Mortlock, R.G. Fairbanks, and J.H. Swift. River runoff, sea ice meltwater, and Pacific water distribution and mean residence times in the Arctic Ocean. *Journal of Geophysical Research*, 106(C5):9075–9092, 2001.

[33] P.L. Evans and B.J. Noye. A model for fast oil spill prediction in shallow gulfs. *PACON '94 Proceedings: Recent Advances in Marine Science and Technology, O. Bellwood, H. Choat, N. Saxena eds.*, 1995.

[34] W. Feller. *An Introduction to Probability Theory and its Applications (Vol. 1).* John Wiley and Sons, 1950.

[35] W. Fennel and A. Mutzke. The initial evolution of a buoyant plume. *Journal of Marine Systems*, 12:53–68, 1997.

[36] Y. Gao, H. Drange, M. Bentsen, and O.M. Johannessen. Tracer-derived transit time of the waters in the eastern nordic seas. *Tellus*, 57B:332–340, 2005.

[37] A.E. Gill, M.K. Davey, E.R. Johnson, and P.F. Linden. Rossby adjustment over a step. *Journal of Marine Research*, 44(4):713–738, 1986.

[38] A.L. Gordon. Interocean Exchange. *Ocean Circulation and Climate, edited by Siedler, Church and Gould, International Geophysics Series Volume 77, Academic Press.*, Chapter 4.7:303–314, 2001.

[39] R.W. Griffiths and P.F. Linden. The influence of a side wall on rotating flow over bottom topography. *Journal of Fluid Dynamics*, 27:1–33, 1983.

[40] S. Häkkinen and A. Proshutinsky. Freshwater content variability in the Arctic Ocean. *Journal of Geophysical Research*, 109(C3):art no: 3051, 2004.

[41] I.H. Harms. Water mass transformation in the Barents Sea - application of the Hamburg Shelf Ocean Model (HamSOM). *Journal of Marine Science*, 54:351–365, 1997.

[42] I.H. Harms. Modeling the seasonal variability of hydrography and circulation in the Kara Sea. *Journal of Geophysical Research*, 104(C6):13431–13448, 1999.

[43] J.E. Hart and P.D. Killworth. On open ocean baroclinic instability in the Arctic. *Deep-Sea Research*, 23:637–645, 1975.

[44] D.M. Holland, L.A. Mysak, and J.M. Oberhuber. Simulation of the mixed-layer circulation in the Arctic Ocean. *Journal of Geophysical Research*, 101(C1):1111–1128, 1996.

[45] G. Holloway. Systematic forcing of large-scale geophysical flows by eddy-topography interaction. *Journal of Fluid Mechanics*, 184:463–476, 1987.

[46] R.X. Huang. Mixing and Available Potential Energy in a Boussinesq Ocean. *Journal of Physical Oceanography*, 28:669–678, 1998.

[47] M. Ikeda. Coastal Flows Driven by a Local Density Flux. *Journal of Geophysical Research*, 89:8008–8016, 1984.

[48] R.B. Ingvaldsen, L. Asplin, and H. Loeng. The seasonal cycle in the Atlantic transport to the Barents Sea during the years 1997-2001. *Continental Shelf Research*, 24:1015–1032, 2004.

[49] D.R. Jackett and T.J. McDougall. An oceanographic variable for the characterization of intrusions and water masses. *Deep-Sea Research*, 32A(10):1195–1207, 1985.

[50] I.N. James. *Introduction to circulating atmospheres.* Cambridge University Press, 1994.

[51] S.R. Jayne and R. Tokmakian. Forcing and sampling of ocean general circulation models: impact of high-frequency motions. *Journal of Physical Oceanography*, 27(6):1173–1179, 1997.

[52] H.L. Johnson and D.P. Marshall. A theory for the surface Atlantic response to thermohaline variability. *Journal of Physical Oceanography*, 32(4):1121–1132, 2002.

[53] E.P. Jones, L.G. Anderson, and J.H. Swift. Distribution of Atlantic and Pacific waters in the upper Arctic Ocean: Implications for circulation. *Geophysical Research Letters*, 25:765–768, 1998.

[54] E.P. Jones, B. Rudels, and L.G. Anderson. Deep waters of the Arctic Ocean: origins and circulation. *Deep Sea Research I*, 42:737–760, 1995.

[55] E.P. Jones, J.H. Swift, L.G. Anderson, M. Lipizer, G. Civitarese, K.K. Falkner, G. Kattner, and F. McLaughlin. Tracing Pacific water in the North Atlantic Ocean. *Journal of Geophysical Research*, 108 (C4):art. no: 3116, 2003.

[56] J.H. Jungclaus, J.O. Backhaus, and H. Fohrmann. Outflow of dense water from the Storfjord in Svalbard: a numerical study. *Journal of Geophysical Research*, 100(C12):24719–24728, 1995.

[57] R. Kwok. Recent changes in Arctic Ocean sea ice motion associated with the North Atlantic Oscillation. *Geophysical Research Letters*, 27:775–778, 2000.

[58] S. Levitus. Climatological Atlas of the World Ocean. *NOAA Prof. Paper, 13, GFDL, Princeton University, N.J.*, page 173pp, 1982.

[59] S. Levitus. World Ocean Atlas, Volume 3 Salinity. *NOAA Atlas NESDIS 3*, page 99pp, 1994.

[60] S. Levitus. World Ocean Atlas, Volume 4 Temperature. *NOAA Atlas NESDIS 4*, page 117pp, 1994.

[61] P.F. Linden and J.E. Simpson. Gravity-driven flows in a turbulent fluid. *Journal of Fluid Mechanics*, 172:481–497, 1986.

[62] H. Loeng, V. Ozhigin, B. Adlandsvik, and H. Sagen. Current measurements in the northeastern Barents Sea. *ICES, Contribution to Statutory Meeting, Hydrography Committee*, C:41:22pp., 1993.

[63] H. Loeng, V. Ozhigin, and B. øAdlandsvik. Water fluxes through the Barents Sea. *Journal of Marine Science*, 54:310–317, 1997.

[64] E.N. Lorenz. Available potential energy and the maintenance of the general circulation. *Tellus*, 7:157–167, 1955.

[65] E.N. Lorenz. *The nature and general circulation of the atmosphere.* World Meteorological Orginization, 1967.

[66] R.W. MacDonald, E.C. Carmack, F.A. McLaughlin, K.K. Falkner, and J.H. Swift. Connections among ice, runoff and atmospheric forcing in the Beaufort Gyre. *Geophysical Research Letters*, 26:2223–2226, 1999.

[67] T.O. Manley. Branching of Atlantic Water within the Greenland-Spitzbergen Passage: An estimate of recirculation. *Journal of Geophysical Research*, 100:20627–20634, 1995.

[68] T.O. Manley and K. Hunkins. Mesoscale eddies of the Arctic Ocean. *Journal of Geophysical Research*, 90(C3):4911–4930, 1985.

[69] J. Marotzke and B.A. Klinger. The dynamics of equatorially asymmetric thermohaline circulations. *Journal of Physical Oceanography*, 30(5):955–970, 2000.

[70] J. Marshall and F. Schott. Open-ocean convection: observation, theory and models. *Reviews of Geophysics*, 37(1):1–64, 1999.

[71] S. Martin and R. Drucker. The effect of possible Taylor columns on the summer ice retreat in the Chukchi Sea. *Journal of Geophysical Research*, 102(C5):10473–10482, 1997.

[72] W. Maslowski, B. Newton, P. Schlosser, A. Semtner, and D. Martinson. Modeling recent climate variability in the Arctic Ocean. *Geophysical Research Letters*, 27(22):3743–3746, 2000.

[73] C. Mauritzen. Production of dense overflow waters feeding the North Atlantic across the Greenland Sea - Scotland Ridge: Part 1. Evidence for a revised circulation scheme. *Deep-Sea Research*, 43:796–806, 1996a.

[74] C. Mauritzen. Production of dense overflow waters feeding the North Atlantic across the Greenland Sea - Scotland Ridge: Part 2. An inverse model. *Deep-Sea Research*, 43:807–835, 1996b.

[75] C. Mauritzen and S. Häkkinen. Influence of sea ice on the thermohaline circulation in the Arctic-North Atlantic Ocean. *Geophysical Research Letters*, 24:3257–3260, 1997.

[76] T.J. McDougall. Thermobaricity, Cabbeling and Water Mass conversion. *Journal of Geophysical Research*, 92 (C5):5448–5464, 1987.

[77] F. McLaughlin, E. Carmack, R. MacDonald, A.J. Weaver, and J. Smith. The Canada Basin, 1989-1005: Upstream events and far-field effects of the Barents Sea. *Journal of Geophysical Research*, 107(C7):3082–3102, 2002.

[78] F.A. McLaughlin, E.C. Carmack, R.W. MacDonald, and J.K.B. Bishop. Physical and geochemical properties across the Atlantic/Pacific water mass front in the southern Canadian basin. *Journal of Geophysical Research*, 101(C1):1183–1197, 1996.

[79] H. Melling. Hydrographic changes in the Canada Basin of the Arctic Ocean, 1979-1996. *Journal of Geophysical Research*, 103 (C4):7637–7645, 1998.

[80] L. Middtun. Formation of dense bottom water in the Barents Sea. *Deep Sea Research*, 32:1233–1241, 1985.

[81] L. Nazarenko, G. Holloway, and N. Tausnev. Dynamics of transport of 'Atlantic signature' in the Arctic Ocean. *Journal of Geophysical Research*, 103 (C13):31003–31015, 1998.

[82] J.L. Newton, K. Aagaard, and L.K. Coachman. Baroclinic eddies in the Arctic Ocean. *Deep-Sea Research*, 21:707–719, 1974.

[83] J.L. Newton and B.J. Sotirin. Boundary undercurrent and water mass changes in the Lincoln Sea. *Journal of Geophysical Research*, 102:3393–3403, 1997.

[84] O.A. Nost and P.E. Isachsen. The large-scale time-mean ocean circulation in the Nordic Seas and Arctic Ocean estimated from simplified dynamics. *Journal of Marine Research*, 61(2):175–210, 2003.

[85] A.H. Oort, L.A. Anderson, and J.P. Peixoto. Estimates of the energy cycle of the oceans. *Journal of Geophysical Research*, 99 (C4):7665–7688, 1994.

[86] A.H. Oort, S.C. Ascher, S. Levitus, and J.P. Peixoto. New estimates of the available potential energy in the world ocean. *Journal of Geophysical Research*, 94 (C3):3187–3200, 1989.

[87] R.C. Pacanowski and S.G.H. Philander. Parameterisation of vertical mixing in numerical models of tropical oceans. *Journal of Physical Oceanography*, 11:1443–1451, 1981.

[88] R.S. Pickart and W.M. Smethie Jr. How does the Deep Western Boundary Current cross the Gulf stream? *Journal of Physical Oceanography*, 23:2602–2616, 1993.

[89] A.B. Pippard. *Classical Thermodynamics.* Cambridge University Press, 1966.

[90] W.H. Press, B.P. Flannery, S.A. Teukolsky, and W.T. Vetterling. *Numerical recipes in Fortran 77: the art of scientific computing.* Cambridge University Press, 1992.

[91] A. Proshutinsky, V. Pavlov, and R.H. Bourke. Sea level rise in the Arctic Ocean. *Geophysical Research Letters*, 28(11):2237–2240, 2001.

[92] A.Y. Proshutinsky and M.A. Johnson. Two circulation regimes of the wind-driven Arctic Ocean. *Journal of Geophysical Research*, 102(C6):12493–12514, 1997.

[93] D. Quadfasel, B. Rudels, and K. Kurz. Outflow of dense water from a Svalbard fjord into the Fram Strait. *Deep-Sea Research*, 35A(7):1143–1150, 1988.

[94] D. Quadfasel, A. Sy, and B. Rudels. A ship of opportunity section to the North Pole: Upper ocean temperature observations. *Deep Sea Research I*, 40:777–789, 1993.

[95] R.O. Reid, B.A. Elliott, and D.B. Olson. Available potential energy: A clarification. *Journal of Physical Oceanography*, 11:15–29, 1981.

[96] A.T. Roach, K. Aagaard, C.H. Pease, S.A. Salo, T. Weingartner, V. Pavlov, and M. Kulakov. Direct measurements of transport and water properties through the Bering Strait. *Journal of Geophysical Research*, 100:18443–18457, 1995.

[97] B. Rudels, L.G. Anderson, and E.P. Jones. Formation and evolution of the surface mixed layer and halocline of the Arctic Ocean. *Journal of Geophysical Research*, 101(C4):8807–8821, 1996.

[98] B. Rudels, H.J. Friedrich, and D. Quadfasel. The Arctic circumpolar boundary current. *Deep-Sea Research*, II 46:1023–1062, 1999.

[99] B. Rudels, E.P. Jones, L.G. Anderson, and G. Kattner. On the origin and circulation of the Atlantic layer and intermediate depth waters in the Arctic Ocean. *The Polar Oceans and their role in the shaping the global environment, edited by Johannessen, Muench, Overland, Geophysical Monograph Series, Vol 85. AGU.*, pages 33–46, 1994.

[100] B. Rudels, R.D. Muench, J. Gunn, U. Schauer, and H.J. Friedrich. Evolution of the Arctic Ocean boundary current north of the Siberian shelves. *Journal of Marine Systems*, 25:77–99, 2000.

[101] P.M. Saunders. The Dense Northern Overflows. *Ocean Circulation and Climate, edited by Siedler, Church and Gould, International Geophysics Series Volume 77, Academic Press.*, Chapter 5.6:401–417, 2001.

[102] U. Schauer. The release of brine-enriched shelf water from Storfjord into the Norwegian Sea. *Journal of Geophysical Research*, 100 (C8):1601516028, 1995.

[103] U. Schauer, R.D. Muench, B. Rudels, and L. Tomokhov. Impact of eastern Arctic shelf waters on the Nansen Basin intermediate waters. *Journal of Geophysical Research*, 102(C2):3371–3382, 1997.

[104] U. Schauer, B. Rudels, E.P. Jones, L.G. Anderson, R.D. Muench, G. Bjork, J.H. Swift, V. Ivanov, and A.M. Larsson. Confluence and redistribution of Atlantic Water in the Nansen, Admundsen and Makarov basins. *Annales Geophysicae*, 20(2):257–273, 2002.

[105] P. Schlosser, D. Grabitz, R. Fairbanks, and G. Bönisch. Arctic river-runoff: mean residence time on the shelves and in the halocline. *Deep Sea Research*, 41:1053–1068, 1994.

[106] G.I. Shapiro, J.M. Huthnance, and V.V. Ivanov. Dense water cascading off the continental shelf. *Journal of Geophysical Research*, 108 (C12):art no: 3390, 2003.

[107] M.J. Siegert and J.A. Dowdeswell. Numerical reconstructions of the eurasian ice sheet and climate during the late weichselian. *Quaternary Science Reviews*, 23:1273–1283, 2004.

[108] S.R. Signorini and D.J. Cavalieri. Modeling dense water production and salt transport from Alaskan coastal polynyas. *Journal of Geophysical Research*, 107(C9):art no: 3136, 2002.

[109] M.A. Spall. Dynamics of the Gulf stream/Deep Western Boundary Current crossover. Part I: entrainment and recirculation. *Journal of Physical Oceanography*, 26:2152–2168, 1996.

[110] M. Steele and T. Boyd. Retreat of the cold halocline layer in the Arctic Ocean. *Journal of Geophysical Research*, 103:10419–10435, 1998.

[111] M. Steele, J. Morison, W. Ermold, I. Rigor, M. Ortmeyer, and K. Shimada. Circulation of summer Pacific halocline water in the Arctic Ocean. *Journal of Geophysical Research*, 109(C2), 2004.

[112] M. Steele, J.H. Morison, and T.B. Curtin. Halocline water formation in the Barents Sea. *Journal of Geophysical Research*, 100:881–894, 1995.

[113] J.H. Swift, E.P. Jones, K. Aagaard, E.C. Carmack, M. Hingston, R.W. MacDonald, F.A. McLaughlin, and R.G. Perkin. Waters of the Makarov and Canada basins. *Deep-Sea Research II*, 8:1503–1529, 1997.

[114] P. Uotila, D.M. Holland, S. Häkkinen, G. Holloway, N. Steiner, M. Steele, J. Zhang, and A. Proshutinsky. An energy-diagnostics intercomparison of coupled ice-ocean Arctic models. *Ocean Modelling*, in press, 2004.

[115] U.S. Naval Oceanographic Office and and the U.S. Naval Ocean Research and Development Activity. DBDB5 (Digital Bathymetric Data Base-5 minute grid). *U.S.N.O.O., Bay St. Louis, Mississippi*, 1983.

[116] D.J. Webb, B.A. de Cuevas, and A.C. Coward. The first main run of the OCCAM global ocean model. *Southampton Oceanography Centre Internal document*, 34, 1996.

[117] T.J. Weingartner, D.J. Cavalieri, K. Aagaard, and Y. Sasaki. Circulation, dense water formation, and outflow on the northeast Chukchi shelf. *Journal of Geophysical Research*, 103(C4):7647–7661, 1998.

[118] K.B. Winters, P.N. Lombard, J.J. Riley, and E.A. D'Asaro. Available Potential Energy and mixing in density-stratified fluids. *Journal of Fluid Mechanics*, 289:115–128, 1995.

[119] R.A. Woodgate, K. Aagaard, R.D. Muench, J. Gunn, G. Bjork, B. Rudels, A.T. Roach, and U. Schauer. The Arctic Ocean Boundary Current along the Eurasian slope and the adjacent Lomonosov Ridge: Water mass properties, transports and transformations from moored instruments. *Deep-Sea Research I*, 48:1757–1792, 2001.

[120] A.E. Yankovsky and D.C. Chapman. A simple theory for the fate of buoyant coastal discharges. *Journal of Physical Oceanography*, 27:1386–1400, 1997.

[121] X. Zhang and J. Zhang. Heat and freshwater budgets and their pathways in the Arctic Mediterranean in a coupled Arctic ocean-sea ice model. *Journal of Oceanography*, 57:207–234, 2001.

[122] Y. Zhang, W. Maslowski, and A.J. Semtner. Impact of mesoscale ocean currents on sea ice in high-resolution Arctic ice and ocean simulations. *Journal of Geophysical Research*, 104(C8):18409–18429, 1999.

Appendix A

Time-dependent particle tracking - solution process

A.1 Introduction

Here we describe the solution process for calculating the crossing times of the particles. We discuss the numerical solution process, the series expansions used for the evaluation of functions, how the boundaries are handled when performing random jumps, and how the particles are selected at the start.

The method described in the chapter 5 can be used to calculate a huge number of particles. The main limitation for calculating the time-dependent trajectories is the time it takes to load the 3D velocity and property fields after each time-interval.

A.2 Numerical solution

Here we calculate the crossing time s from equation (5.32). The equation is solved numerically using the hybrid Newton-Raphson root-finding algorithm from Press et al (1992) to solve

$$r(s) - r_i = 0. \tag{A.1}$$

Valid solutions must be within the grid-box $[r_{i-1}, r_i]$, and within the time-interval $[s_0, s_n]$. Here $s_0 \geq s_{n-1}$ is the starting time.

To start the solution process a bracket $[s_a, s_b]$ is needed that contains the solution s. Then a combination of the Newton-Raphson method and the bisection method is used to calculate the root. The Newton-Raphson method is given by

$$s_{t+1} = s_t - r(s_t) \left[\frac{dr}{ds}(s_t) \right]^{-1}. \tag{A.2}$$

The derivative in this method is calculated using equation (5.17). Locally this method converges quadratically, however it does not converge globally. In the case that it does not converge the linearly converging bisection method is used, which is guaranteed to converge (if a root exists). In this method the function $r(s)$ is evaluated at the midpoint of the bracket, and the bracket is halved so it contains the root.

An initial bracket is obtained from the time sample interval $[s_{n-1}, s_n]$. However usually this bracket is not sufficient. A more exact approximation of the lower limit is given by the earliest time the particle could reach the exit face, which is

$$s_a = s_0 + \frac{r_i - r_0}{u_m}, \tag{A.3}$$

where u_m is the maximum flow rate, and is taken as the maximum of the absolute values of the transports at the surrounding points $(r_0, s_0), (r_i, s_0), (r_0, s_n), (r_i, s_n)$.

The bracket can be improved by looking at the time-averaged acceleration rates at both sides of the grid-box. In the case that the initial transport at the exit face $U(r_i, s_0) < 0$, the particle cannot pass through the face unless the transport changes sign within the time-interval. Therefore if the transport at the end of the time-interval $U(r_i, s_n) > 0$ then it is possible for the particle to pass through r_i, and an estimate of the earliest time of positive transport is given by

$$s_a = s_0 - U(r_i, s_0)\left[\frac{d^2r}{ds^2}(r_i)\right]^{-1}, \qquad \frac{d^2r}{ds^2}(r_i) = \frac{U(r_i, s_n) - U(r_i, s_0)}{s_n - s_0}. \tag{A.4}$$

Equivalently if the initial transport at the exit face $U(r_i, s_0) > 0$, while the transport at the end of the time-interval $U(r_i, s_n) < 0$, we can estimate an earliest time of negative transport

$$s_b = s_0 + U(r_i, s_0)\left[\frac{d^2r}{ds^2}(r_i)\right]^{-1}. \tag{A.5}$$

After this time it is not possible for the particle to pass through r_i.

Another estimate is obtained by looking at sign of the transport at the initial position. If the initial transport at the exit face $U(r_0, s_0) < 0$, the particle can not move in the right direction (towards r_i) until the transport becomes positive. An estimate of the earliest time of positive transport at r_0 is

$$s_a = s_0 - U(r_0, s_0)\left[\frac{d^2r}{ds^2}(r_0)\right]^{-1}. \tag{A.6}$$

These estimates are used to find the smallest bracket possible before entering the numerical solution process.

It is also possible to identify the case that there are no solutions. A solution is only possible if the transport $U(r_i, s) > 0$ at either s_0 or s_n. If this is not the case then the flow is always in the wrong direction for the particle to cross the wall at r_i. Equivalently the transport at the initial position r_0 must be positive for either s_0 or s_n for the particle to move in the right direction.

Also a particle can only cross through the wall at r_i if the flow is strong enough. This is the case when a particle moving at the maximum flow rate u_m towards r_i does not reach the exit face within the time-interval. Therefore if

$$x_0 + u_m \cdot (t_n - t_0) < x_i, \tag{A.7}$$

a solution is not possible.

If there is no solution in all three spatial directions then we calculate the exact position of the particle in the grid-box at s_n, and move to the next time interval.

A.3 Series expansions

The evaluation of function $r(s)$ requires the calculation of error functions, and Dawson's integral. The error function $erf(\zeta)$ is calculated using the series expansion of Press et al (1992). The error function can be written in terms of the incomplete gamma function

$$P(a,x) = \frac{\gamma(a,x)}{\Gamma(a)} = 1 - \frac{\Gamma(a,x)}{\Gamma(a)}, \quad \Gamma(a) = \int_0^\infty t^{a-1}\exp(-t)dt, \tag{A.8}$$

where and $\Gamma(a,x)$ and $\gamma(a,x)$ are given by

$$\Gamma(a,x) = \int_x^\infty t^{a-1}\exp(-t)dt, \quad \gamma(a,x) = \int_0^x t^{a-1}\exp(-t)dt. \tag{A.9}$$

Then $erf(\xi)$ is given by

$$erf(\xi) = \frac{2}{\sqrt{\pi}}\int_0^\xi \exp(-t^2)dt = P(\frac{1}{2},\xi^2). \tag{A.10}$$

Then we compute $P(\frac{1}{2},\xi^2)$ using a series expansion. If $\xi^2 < \frac{3}{2}$ the fastest conversion is obtained using the series

$$P(\frac{1}{2},\xi^2) = \exp(-\zeta^2)\xi\sum_{n=0}^{\infty}\frac{1}{\Gamma(\frac{3}{2}+n)}\xi^{2n}. \tag{A.11}$$

Using $\Gamma(1/2) = \sqrt{\pi}$ the other values are calculated using the identity $\Gamma(a+1) = a\Gamma(a)$.

If $\xi^2 \geq \frac{3}{2}$ the fastest conversion is obtained using a continued fraction development

$$P(a,\xi^2) = 1 - \left[\Gamma(\frac{1}{2})\right]^{-1} \exp(-\xi^2)\xi \left[\frac{1}{x+1-a-} \; \frac{1(1-a)}{x+3-a-} \; \frac{2(2-a)}{x+5-a-} \; \cdots\right], \quad \text{(A.12)}$$

where $a = 1/2$.

Dawson's integral is also calculated following Press et al (1992). For $|\xi| < 0.2$ $D(\xi)$ converges to zero, and a simple power series is used. For $|\xi| \geq 0.2$ Rybicki's formula is used

$$D(\xi) = \lim_{h\to 0} \frac{1}{\sqrt{\pi}} \sum_{n \text{ odd}} \frac{1}{n} \exp(-(\xi - nh)^2). \quad \text{(A.13)}$$

.

A.4 Implementation of random displacements

The implementation of the random displacements representing the diffusive effects discussed in chapter 5 requires some exceptions due to the presence of topography. A random displacement can cause a particle to move onto land, or jump into or from an isolated area of water, or move out of the model domain. Therefore the calculations of the random displacements are repeated until a suitable displacement is found. The particle is assumed to be stuck if a large number of repeats are necessary, in which case the trajectory is halted.

A.5 Selection of initial particles

The initial particles all start on a vertical section. In order to get a larger number of particles starting in areas with stronger flow the particles are distributed on the starting section so they all have similar transports.

Here we consider a vertical starting section in (y, z) space, along a constant model longitude x. We define a transport U_n, which will approximately be the transport represented by each particle. The total volume transport through each vertical grid-box on the starting section is given by

$$U_T = u(x, y, z) \cdot \Delta y \Delta z. \tag{A.14}$$

The number of sub-boxes per grid-box N is then set by

$$N = \left[\frac{U_T}{U_n}\right]. \tag{A.15}$$

Then a subdivision of $K \times K$ sub-boxes within the grid-box is chosen where K is an integer such that

$$K \approx \sqrt{N}. \tag{A.16}$$

Then each particle in one of the K^2 sub-boxes transports

$$\left[\frac{U_T}{K^2}\right] \approx \left[\frac{U_T}{N}\right] = U_n \ \ m^3/s \tag{A.17}$$

at the start of the trajectory.

Figure A.1A shows an example of the particle distribution on a vertical section associated with the volume flux through the section given in figure A.1B.

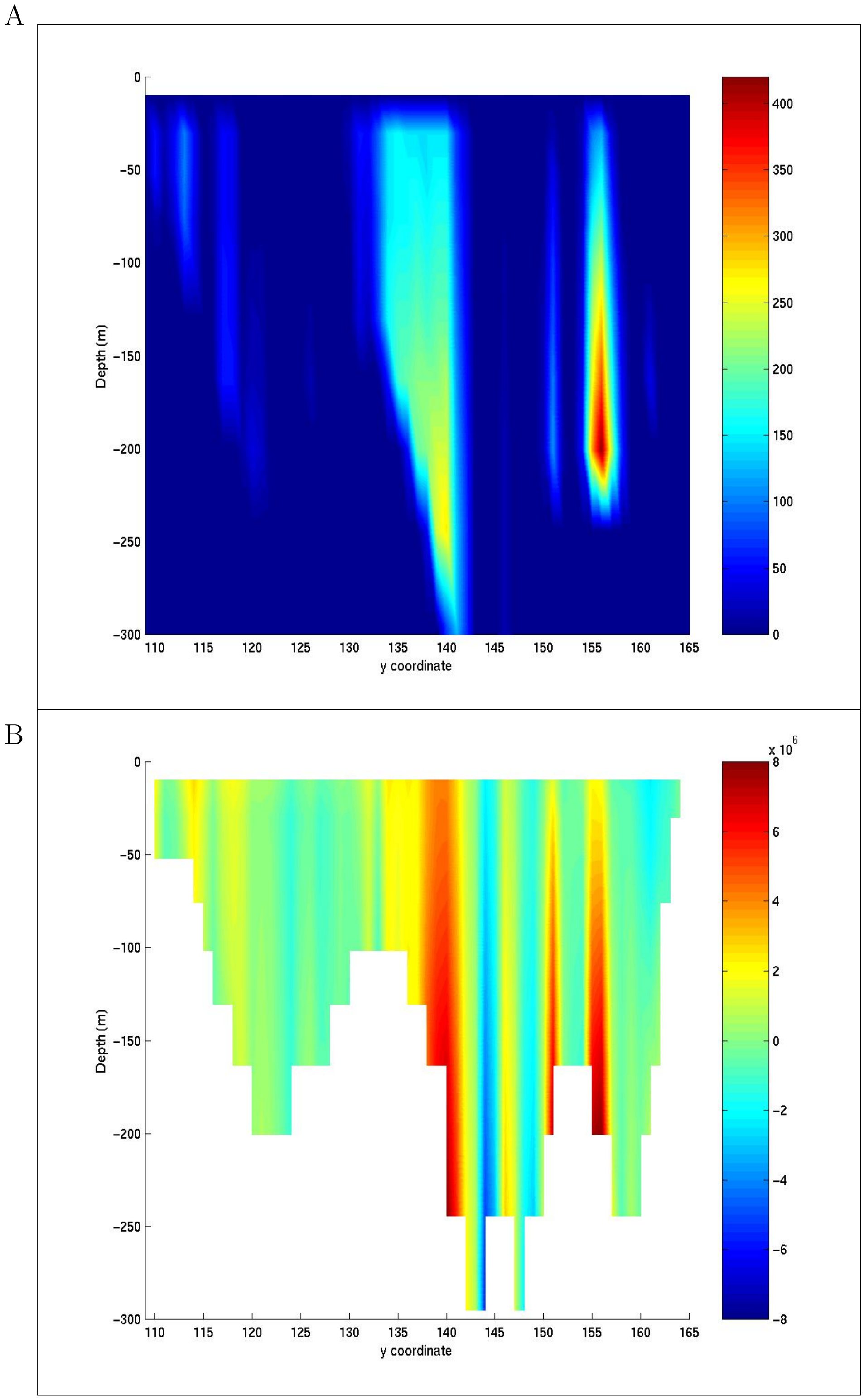

Figure A.1: *(A) Initial particle distribution on vertical section (B) Volume flux* (m^3/s) *through vertical section.*